University College of Southeast Norway
Faculty of Technology

Doctoral dissertation no. 4
2016

Lu Li

One-step Conversion of Ethylene to Propylene by a $NiSO_4$-ReO_X/γ-Al_2O_3 Catalyst

Lu Li

One-Step Conversion of Ethylene to Propylene by a $NiSO_4$ -$ReOx/\gamma$-Al_2O_3 Catalyst

A PhD dissertation in
Process, Energy and Automation Engineering

Faculty of Technology
University College of Southeast Norway
Kongsberg, 2016

Doctoral dissertations at the University College of Southeast Norway no. 4

ISSN: 2464-2770 (print)
ISSN: 2464-2483 (electronic)
ISBN: 978-82-7206-413-5 (print)
ISBN: 978-82-7206-414-2 (electronic)

Print: **University College of Southeast Norway**

Preface

This dissertation is submitted to the University College of Southeast Norway in partial fulfilment of the requirements for the degree of Doctor of Philosophy (Ph.D.). The work has been carried out between August 2012 and December 2015, under the supervision of Professor Klaus Joachim Jens and Professor Dag Eimer.

In June 2011, I participated in the project “Olefin transformation catalysts”, which was a part of the main project “Ethylene oligomerization and metathesis (OLGOM). Before starting, the scope of the project already gained my interest and attention. When really working on that project, I found myself learning a lot, not only in the science but also the personal skills. Consequently, I applied for the research fellow position without any hesitation since this continued the work of the project.

As mentioned, this Ph.D. work is a part of a main project entitled “Ethylene oligomerization and metathesis (OLGOM)”. In the three and a half years, the process of the research was hard, but definitely a happy one filled with achievements.

Porsgrunn, February 10, 2016

Lu Li

Acknowledgements

I have profited greatly from the assistance and encouragement of many people, so let me express my gratitude to all those who helped me to complete this project.

First of all, a special acknowledgement is sent to my supervisor Prof. Klaus J.Jens, who offered me an opportunity to join his team and to enter the field of catalysis. To compensate for my lack of background in catalysis, he patiently taught me anything from basic theories to deep mechanisms of catalytic reaction. I cannot remember how many times he drew and deduced possible reaction pathways to help me with the research difficulties. He enjoyed telling the interesting stories of his previous work, which kept my optimism and enthusiasm for the Ph.D. work at hand. I would like to thank him for being my supervisor. I must extend my thanks to Prof. Dag Eimer for his guidance and encouragement in the project meetings.

This project was in cooperation with the Centre for Material Science and Nanotechnology (SMN), Department of Chemistry, University of Oslo. Honestly, without their support on the experimental instruments, the project would have undergone a very difficult time. The pulse reactor testing, in-situ FT-IR studies and TGA measurements were carried out there. It is a pleasure to acknowledge my sincere thanks to Prof. Unni Olsbye for her supporting interest in this work. I am thankful to Dr. Radostina D. Palcheva and Dr. Sachin M. Chavan, who assisted me with the lab work. I am also grateful to Gloria Bostick for arranging my stay in Oslo and Sharmala Aravinthan for her experimental assistance.

In-situ UV-Vis-NIR spectroscopy studies were conducted at the Department of Chemistry, NIS and INSTEM reference centre, University of Turin, Italy. I would like to express my appreciation to Prof. Silvia Bordiga and Dr. Elena Groppo. They provided valuable expertise and shared their knowledge with me for interpreting FT-IR and UV-Vis-NIR spectra as well as the manuscript writing.

I would like to express my sincere gratitude to Prof. Einar. Sagstuen from the Department of Physics, University of Oslo for the EPR measurements. I would also like

to thank Dr. Martin. F. Sunding from SINTEF, Oslo for the SEM measurements and XPS analysis. I am grateful to Dr Maela Manzoli from the Department of Chemistry, University of Turin for the HRTEM measurements.

My hearty gratitude goes to the laboratory managers and technicians (former and present) working in HSN, including Joachim Lundberg, Morten Pedersen, Per. M. Hansen, Arve Lorentzen, Nora. C. I. Furuvik, Eivind Fjelddalen and Hildegunn. H. Haugen. I enjoyed the work in HSN very much. I am thankful to my colleagues, Bo Li, Christian Ahoba-Sam, Gamunu L. Samarakoon and Zulkifli. B. Idris.

I am grateful to my friends, who make my life much more enjoyable in Norway. Special thanks go to my boyfriend, Nick Hor, who gave me unlimited support throughout the journey. Last but not least, I would like to express my love and gratitude to my parents, Yueru Cao and Fuping Li for their encouragement and caring.

Lu Li

Porsgrunn, February, 2016.

Abstract

The demand for propylene has dramatically increased due to the discovery of propylene's derivatives (e.g. polypropylene). The propylene production from the conventional processes (steam cracking process and a refinery fluid catalytic cracking process (FFC)) cannot satisfy the demand. Moreover, if shale gas is going to be a future energy, the products from a steam cracker will be largely limited and the propylene production will be less. Therefore, to fill the increasing supply/demand gap, so called "on-purpose" technologies have to be developed. Today's 'on-purpose' propylene technologies such as propane dehydrogenation, olefin metathesis and enhanced FFC are already of interest. However, a one-step reaction from ethylene to propylene (ETP) has gained attention since the technology of bio-ethanol dehydration allows provision of a renewable and sustainable ethylene source.

In this project, a series of $NiSO_4$-ReO_x/Al_2O_3 catalysts were synthesized by a co-impregnation method using an aqueous solution of $NiSO_4$ and $[NH_4][ReO_4]$, which catalyzed direct conversion of ethylene to propylene at mild conditions (323K, 1atm). To optimize propylene yield, a systematical catalytic test has been carried out by varying and adjusting the operating windows. The yield of the catalyst for propylene could reach approximately 29%, which is superior to other metal based catalysts. It is concluded that the two catalyst functions work independently for dimerization and metathesis.

The results of the TGA analysis indicate that the catalysts are quite stable below 950 K and decomposition of $NiSO_4$ may take place at above 1003 K. Elemental analysis revealed that the material loss is minor during the catalyst preparation. Morphology and texture of the catalysts were examined by SEM and HRTEM techniques. $NiSO_4$ and ReO_x dispersed well on γ-Al_2O_3, but their element distributions were heterogeneous.

The $NiSO_4$-ReO_x/Al_2O_3 catalysts were then thoroughly characterized by FT-IR, DR UV-Vis-NIR, XPS and EPR spectroscopies. In particular, the attention was focused on the $NiSO_4$ function, which is directly involved in ethylene dimerization/isomerization to 2-butylene, but also drives the catalyst deactivation. It was found that the sulfate anions

increase the surface acidity of alumina, and simultaneously influence the electronic properties of the Ni sites. Indeed, thermal activation of the catalyst promotes the formation of covalent bonds between the sulfate anions and the Ni^{2+} or Al^{3+} cations, while keeping constant the +2 oxidation state of the Ni sites. The initial steps of the ETP reaction were investigated by FT-IR spectroscopy in the presence of ethylene, which revealed the initial acid-catalyzed formation of branched hydrocarbons. The sulfate anions are involved in the reaction. Catalyst deactivation could be due to formation and absorption of long-chain hydrocarbons oligomers, or slow displacement of sulfate anions from their initial position connected to the Ni ions.

This project also investigated oxidative regeneration of the NiSO4/γ-Al2O3 part of the $NiSO_4$-ReOx/γ-Al_2O_3 catalyst. An attempt was made to regenerate the deactivated catalyst by purging with synthetic air in the temperature range of 298 to 673 K. The entire regeneration process was monitored and recorded by FT-IR and TG-MS. Long chain hydrocarbons deposited on the catalyst evolve and convert to highly condensed coke species, which need temperature higher than 673 K to be burned. However, higher regeneration temperatures may destroy catalyst surface texture and cause decomposition of nickel sulfate. Hence, the catalyst could not be regenerated by purging synthetic air. It appears that the failure of catalyst regeneration could also be due to the destruction of the active nickel dimerization site. HRTEM measurement was also applied in order to observe morphology of the deactivated catalyst after the re-activation process.

Content

List of Figures

List of Tables

Nomenclature

Symbols

Symbols	Description
V_a	Amount of gas adsorbed at a standard temperature and pressure (273.15K and the atmospheric pressure)
P	Equilibrium pressure
P_0	Saturation pressure of adsorbed gas
C	Dimensionless constant
V_m	Gas quantity of monolayer adsorption on the sample
N_s	Avogadro constant ($6.022 \cdot 10^{23}$ mol^{-1})
V	Molar volume of gas
a	Mass of the solid sample
E_K	Kinetic energy of an emitted photoelectron
h	Plank's constant
v	Frequency of a radiation
E_B	Binding energy of a core-level electron
ϕ	Instrument's spectrometer work function
E	Energy of a magnetic moment of an electron in a magnetic field
g	Landé factor (g factor)
μ_B	Bohr magneton
B_o	magnetic field intensity
α or β	Two states of an electron spin
S	Spin vector
ΔE	Energy difference
θ	CO coverage

Abbreviations

ADH	Autothermal dehydrogenation
EA	Equilibrium adsorption
EPR	Electron paramagnetic resonance
ESCA	Electron spectroscopy for chemical analysis
EPR	Electron spin resonance
ETP	Conversion of ethylene to propylene
FCC	Fluid catalytic cracking process
FID	Flame ionization detector
FT-IR	Fourier transform infrared spectroscopy
GC	Gas chromatography
GHSV	Gas hourly space velocity
HRTEM	High resolution transmission electron microscope
MOI	Mobil olefin interconversion
MS	Mass spectrometry
MTG	Methanol go gasoline
MTP	Methanol to propylene
OCP	Olefin cracking process
OCT	Olefin conversion technology
OCU	Olefin conversion unit
ODH	Oxidative reaction
SCH	Selective combustion of hydrogen
SEM	Scanning electron microscope
TCD	Thermal conductivity detector
TGA	Thermogravimetric analysis
TIE	Template ion exchange method
UHV	Ultra-high Vacuum
UV-Vis-NIR	Ultraviolet-visible-Near infrared spectroscopy
USY	Ultra-stabilized zeolite Y
VGO	Vacuum gas oil

XPS	X-ray photoelectron spectroscopy
C-2-butene	Cis-2-butene
T-2-butene	Trans-2-butene
8-Ni-1-Re	8wt%-$NiSO_4$/1wt%-ReO_x/γ-Al_2O_3
8-Ni-3-Re	8wt%-$NiSO_4$/3wt%-ReO_x/γ-Al_2O_3
8-Ni-5-Re	8wt%-$NiSO_4$/5wt%-ReO_x/γ-Al_2O_3
8-Ni-8-Re	8wt%-$NiSO_4$/8wt%-ReO_x/γ-Al_2O_3
8-Ni-11-Re	8wt%-$NiSO_4$/11wt%-ReO_x/γ-Al_2O_3
8-Re-8-Ni	8wt%-ReO_x/8wt%-$NiSO_4$/γ-Al_2O_3
3-Re-8-Ni	3wt%-ReO_x/8wt%-$NiSO_4$/γ-Al_2O_3
5-NiS	5wt%-$NiSO_4$/γ-Al_2O_3
8-NiS	8wt%-$NiSO_4$/γ-Al_2O_3
11-NiS	11wt%-$NiSO_4$/γ-Al_2O_3
8-NiS (A)	8wt%-$NiSO_4$/Al_2O_3-SiO_2
8-S	8wt%-$(NH_4)_2SO_4$/γ-Al_2O_3
10-Re	10wt%-Re_2O_7/γ-Al_2O_3
8-NiO	8wt%-NiO/γ-Al_2O_3

Chapter 1

1 Introduction

This chapter gives an overview of ethylene and propylene production in the past decades and their developing trends in the future. The limitation of traditional processes for propylene production is described as well. The last part of this chapter describes the objectives and the outline of the thesis.

1.1 Market of Ethylene and Propylene

Ethylene and Propylene are the two key chemical building blocks in the petrochemical industry, which are derived from both natural gas and petroleum[1]. Ethylene is the feedstock for approximately 30% of all petrochemicals. Therefore, it is no surprise that ethylene production always dominates the olefins production. However, the discovery of propylene's derivatives and their continuous development changes the demand for propylene. Propylene is a reactive alkene having a methyl group adjacent to a carbon-carbon double bond and the unique reactivity of its allylic methyl group allows to create important materials. Propylene can be produced to polymers and chemicals such as polypropylene, ethylene-propylene copolymers, isopropanol, allyl alcohol, glycerol and acrylonitrile[2]. Figure 1.1 shows the global consumptions of polypropylene and polyethylene between 1997 and 2010. Consumption of polyethylene is the largest in the international polymer industry[3] and approximately 80% of ethylene was produced for this purpose. Undoubtedly, ethylene is still the most important raw material in the petrochemicals in terms of its demand and production. However, as shown in Figure 1.1, the growth rate for propylene has largely exceeded ethylene's growth rate. The consumption of polypropylene has increased more than five times during 40 years from 1970 to 2010. Moreover, it is forecast that the demand of propylene will still keep this rapidly increasing trend and the demand will be around 100 million metric tons by 2020.

The continuously increasing demand for propylene cannot be satisfied by the supply because the production of propylene is relegated to a by-product from the ethylene production. 60%-65% of the global propylene production comes from the steam

cracking process that is designed for maximum production of ethylene with propylene being produced as a by-product[4]. Propylene manufacture via a refinery fluid catalytic cracking (FCC) process accounts for around 30% of its production[5].

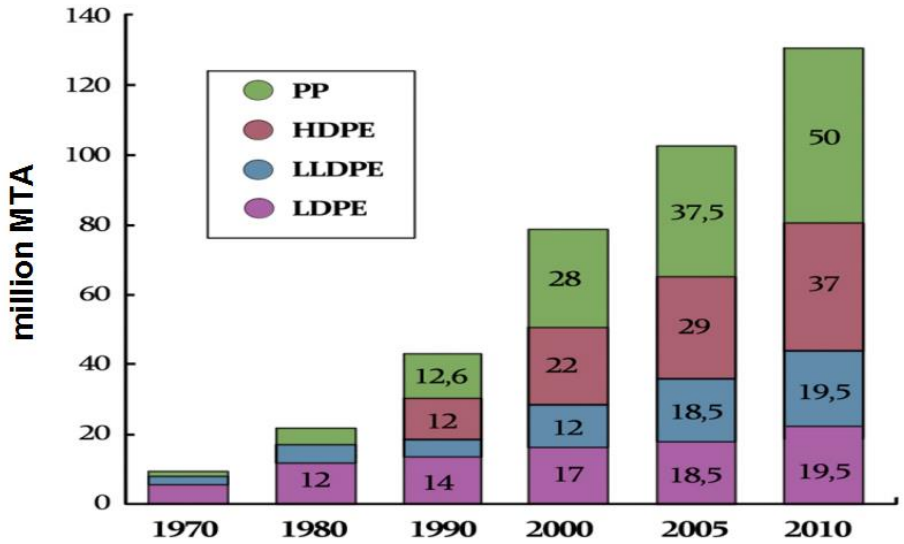

Figure 1.1: Polypropylene and polyethylene consumption between 1997 and 2010[6].

The steam cracking technology is an uncatalyzed radical cracking leading to a high proportion of olefins. The basic mechanism is to break the molecular bonds of hydrocarbons so as to form free radicals that are very reactivity and can be involved in chemical reactions such as dehydrogenation, olefin polymerization alkylation and so on. As mentioned, propylene is produced as a by-product from the steam cracking process and thus its amount is crucially dependent on the cracking feedstock[1]. The heavier the feedstock is, the more propylene is produced. For example, if ethylene is the feedstock, proportion of propylene is only 0.019. However, if naphtha and gas oil are applied, the proportion increases to 0.4 or even higher. Producers prefer light feedstocks in the United States and Middle East while manufacturers use heavy feedstocks in Asia-Pacific. In addition, shale gas has gained attention as an important potential source of natural gas due to large shale gas reserves. The technology of extraction of shale gas has been dramatically improved by a Texas gas producer, Mitchell Energy and Development[1]. If it is going to become a future energy, the propylene production as a by-product from the traditional steam cracking process will be less. Therefore, to a large extent, the amount of produced propylene is constrained by the type of feedstocks and operating severity of feedstock changes from gas to liquid in some crackers. Moreover, FCC is currently the

most important technology in petroleum refineries and propylene is also produced as a by-product from this process. The FCC unit is wildly used to convert large molecules of gas oil to smaller molecules for gasoline and olefinic gas production with the help of catalysts[7]. Although some refineries have worked for maximizing the propylene production, there is still a big gap between supply and demand which needs to be filled. Figure 1.2 shows propylene supply/demand and its forecast in the future. It can be clearly seen that the conventional propylene production cannot match the growth rate of propylene demand and this difference will become larger if no action is taken. Therefore, one must consider and address an effective solution for this imbalance of propylene demand and supply. Furthermore, the price ratio of ethylene to propylene has had an upward trend between 1978 and 2008, and has reached parity in 2010, which is another driving force leading efforts on new technologies[1].

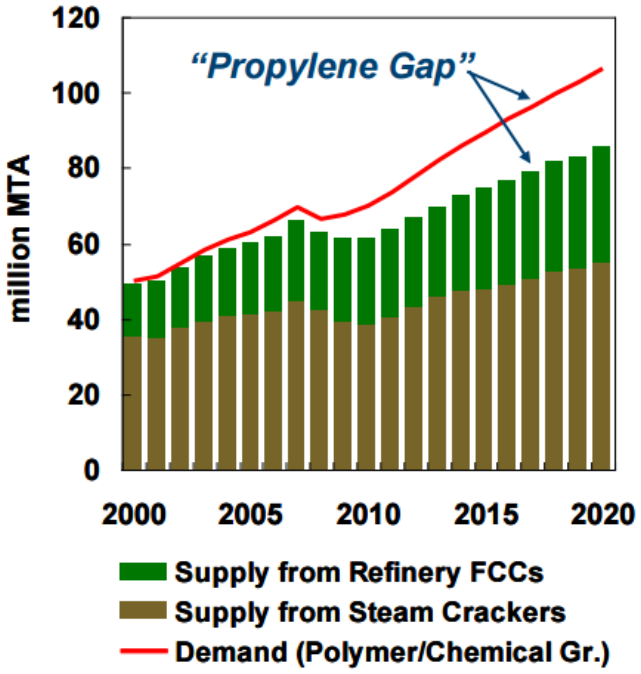

Figure 1.2: Propylene supply and demand gap between 2000 and 2020[5].

1.2 Objectives of the Project

To make-up the shortfall between propylene supply and demand, it is necessary to develop the so-called "on purpose" technologies. The current on-purpose technologies such as propane dehydrogenation, enhanced FCC process, selectivity C_4/C_5 catalytic cracking and olefin metathesis are already of interest. However, it is known that

propane dehydrogenation requires large capital investment for the heating source. Moreover, zeolites, even having a special pore shape, still result in diverse olefinic products in the enhanced FCC process and C_4/C_5 catalytic cracking. Besides, propylene production by olefin metathesis between ethylene and butene may face a problem of shortage of butene if light feedstock such as ethane is used. Therefore, additional hydrogenation and ethylene dimerization units have to be built to provide sufficient butene for the following metathesis (e.g. olefin conversion unit (OCU) developed by Borouge). To save investments on such processes, a new way of one-step conversion of ethylene to propylene arouses our interest because 1) Ethylene is easily obtained since its production is well-developed; 2) With the development of dehydration technology, converting from bio-ethanol to ethylene provides a renewable and sustainable ethylene source[8].

This projects aims to discover a proper catalyst for the conversion of ethylene to propylene. As mentioned, propylene could be produced by metathesis between ethylene and butene, and this technology already has many applications such as the famous ABB Lummus olefin conversion technology (OCT) as well as IFP-CPC Meta-4 process. However, considering the limitation of the butene source, an idea based on a combination of ethylene dimerization reaction and metathesis reaction was considered.

Commercial catalysts for olefin metathesis have been available for decades whereas the catalysts for dimerization reaction have not been widely investigated and reported. Accordingly, the purpose of the project was to synthesis a dual-function (dimerization and metathesis) catalyst by incorporating two functional compounds into one support material. Support materials of metal oxides such as alumina and silica-alumina were chosen in this project due to their high abundance and inexpensive price. Optimizing experimental conditions and yield of ethylene were the other goals that were expected to be achieved, which are important in relation to economy. Moreover, the emphasis was on understanding the activation and deactivation mechanism of the dually functional catalyst by several effective characterization methods, especially on the dimerization part.

1.3 Outline of the Thesis

The thesis consists of seven chapters. In chapter 2, a brief description of current on-purpose technologies for propylene production is given and a detailed literature review forces on the one-step reaction for conversion of ethylene to propylene (ETP) in terms of different types of support materials as well as on the available catalysts for dimerization and metathesis reaction, respectively.

Chapter 3 describes a screening process of a series of prepared catalysts relating to their performance. The synthesized Ni based dimerization catalysts were tested in a continuous flow reactor and the best catalysts with the highest yield of 2-butene were chosen for subsequent synthesis by mixing with a metathesis catalyst. One Re modified metathesis catalyst was also made for both physically and chemically mixing with the dimerization catalysts in order to combine the dual functions. In addition, Ni-MCM-41 and Ni-ZSM-5 catalysts, which have been reported for the ETP reaction, were also prepared by repeating the published procedures [9, 10]. Testing of all the catalysts for the ETP reaction was then performed in the same continuous flow reactor by varying the experimental conditions. Finally, to investigate the induction period of the ETP reaction, a pulse reactor testing of $NiSO_4$-ReO_x/Al_2O_3 (our best catalyst) was carried out. This chapter also introduces the methods of the catalyst synthesis and discusses the results of catalytic testing.

The main $NiSO_4$-ReO_x/Al_2O_3 catalysts had been characterized by BET surface area, element analysis, thermogravimetric analysis (TGA), scanning electron microscope (SEM) and high resolution transmission electron microscope (HRTEM). In chapter 4, the experimental instruments and methods for the characterizations are generally described. Moreover, thermal property, element distribution and surface structure of the catalyst are discussed based on the results of the characterizations.

The nature of active sites on the $NiSO_4$-ReO_x/Al_2O_3 catalyst, especially on the $NiSO_4$ responsible dimerization reaction, were investigated by using Fourier transform infrared spectroscopy (FT-IR), Ultraviolet-visible-Near infrared spectroscopy (UV-Vis-NIR), X-ray photoelectron spectroscopy (XPS) and electron paramagnetic resonance (EPR). CO was used to probe the catalyst in an in-situ FT-IR experiment at both room temperature and

a low temperature (100K). Moreover, adsorption of ethylene on the main catalysts was carried out by means of both in-situ FT-IR and UV-Vis-NIR, which enables monitoring of the course of the catalytic reactions and elucidation of catalyst deactivation. Last, active catalysts were measured by XPS and EPR in-situ for further investigation on the oxidation state of the active Ni sites. Information about experimental instruments and set-up, including four types of self-designed cell for in-situ measurements, are given in chapter 5. In addition, the collected spectra for each experiment are demonstrated and analyzed.

In chapter 6, re-activation of the deactivated catalyst was conducted by purging synthetic air at a high temperature in order to burn the deposited hydrocarbons on the catalyst. TG-MS and in-situ FT-IR were employed to analyze and monitor the process of catalyst re-activation after deactivation. HRTEM was used to observe the morphology of the catalyst.

Chapter 7 summarizes the conclusions for all the above chapters and gives some suggestions for the future work.

Reference

1. Wittcoff, H.A., Reuben, B.G., Ploktin, J.S., *Industrial Organic Chemicals.* 3rd ed., John Wiley & Sons Ltd, Chicester, 2012.
2. Matar, S., Hatch, L.F., *Chapter Eight - Chemicals Based on Propylene*, Chemistry of Petrochemical Processes, Gulf Professional Publishing, Woburn, 2001, 213-237.
3. Vasile, C., Pascu, M., *Practical guide to polyethylene.* Rapra Technology Limited, Shrewsbury, 2005.
4. Plotkin, J.S., *Catal. Today*, 106 (2005) 10-14.
5. Akah, A., Al-Ghrami, M., *Appl.Petrochem.Res.*, 5 (2015) 377-392.
6. Galli, P., Vecellio, G., *J. Polym. Sci., Part A: Polym. Chem.*, 42 (2004) 396-415.
7. Souza, J.A., Vargas, J.V.C., Ordonez, J.C., Martignoni, W.P., von Meien, O.F., *Int. J. Heat Mass Transfer*, 54 (2011) 1187-1197.
8. Zhang, M., Yu, Y., *Ind. Eng. Chem. Res.*, 52 (2013) 9505-9514.
9. Lin, B., Zhang, Q., Wang, Y., *Ind. Eng. Chem. Res.*, 48 (2009) 10788-10795.
10. Lehmann, T., Wolff, T., Hamel, C., Veit, P., Garke, B., Seidel-Morgenstern, A., *Microporous Mesoporous Mater.*, 151 (2012) 113-125.

Chapter 2

2 Literature Review

Propylene is mostly produced as a by-product from the thermal cracking process and the refinery unit, as described in the previous chapter. However, the supply of propylene from this conventional processes is not sufficient to keep pace with the demand of propylene. “On-purpose” technologies have been developed to satisfy the demand of propylene. In the first section, five “On-purpose” technologies- dehydrogenation of propane, enhanced fluidized catalytic cracking, selective C_4/C_5 cracking, metathesis between ethylene and butene, and methanol to olefins, are introduced. Moreover, their industrial applications and limitations are described. In the second section, the most attractive “on-purpose” technology, direct conversion of ethylene to propylene, is reviewed in detail in terms of the support materials (metal oxides, zeolites and mesoporous materials) of the catalysts. In the last two sections, Ni modified catalysts for ethylene dimerization reaction and Re-based catalysts metathesis reaction are introduced, since our dual-functional catalyst was synthesized on a basis of these two reactions.

2.1 On-purpose Technologies

2.1.1 Dehydrogenation of Propane

The technology of dehydrogenation of propane have been available for decades. In 1947, E. J. Houdry and the co-workers built a process for dehydrogenation of aliphatic hydrocarbons aiming to produce butadiene. A Cr_2O_3/Al_2O_3 catalyst was used in this process[1]. However, at this early stage, investors had little interest in the propane dehydrogenation process due to unfavourable economics. As the price of propylene rose, this process gained the attention of investors. With the development of this technology and improvement of the catalyst, the first propane dehydrogenation line was established in Thailand in 1990 and the second production line was founded in Northwest Europe in 1991. Several licensors possess the technology of propane dehydrogenation including licensors such as UOP Oleflex, ABB/Catofin, Snamprogetti, Phillips STAR and Krupp Uhde[2]. The catalysts used for dehydrogenation were developed

at the beginning of the 20th century[3] and noble metals, particularly Pt modified catalysts, are commercially available for propane dehydrogenation.

However, this process has high operationing costs. The reason for this is that the reaction of propane to propylene is strongly endothermic therefore requiring an external heating source. The dehydrogenation reaction converting propane to propylene is shown as follows:

$$C_3H_8 \rightleftharpoons C_3H_6 + H_2 \quad (\Delta H^0 = 124 \text{ kJ/mol}) \qquad (2.1)$$

According to the chemical equilibrium, to obtain maximum propylene, a high reaction temperature (above 600 °C), low pressure or strong dilution is needed[4]. Moreover, propylene as a product is very difficult to separate with propane as a reactant because of a small boiling point difference. Furthermore, high reaction temperature leads to major side reactions such as cracking and hydrogenation, which, in turn, accelerates formation of coke that quickly deactivates the catalyst.

As a whole, the current technology presents major problems, high cost for the heating source and fast deactivation of the catalyst. Therefore, some new technologies have been recently discovered to improve the process of propane dehydrogenation and are briefly introduced below.

- Oxidative reaction (ODH): Oxygen is involved in the propane dehydrogenation reaction and this oxidative reaction is exothermic[5].
- Autothermal dehydrogenation (ADH): Combusting hydrogen produced from the propane dehydrogenation reaction compensates the heat for the reaction. Various processes have been developed for ADH by mixing steam, hydrogen or oxygen with propane to make up the energy demand[6].
- Selective combustion of hydrogen (SCH): only part of the produced hydrogen is burned for the necessary reaction heat and the rest of the hydrogen is used to reduce coke in the presence of O_2 or steam[7].

2.1.2 Enhanced Fluidized Catalytic Cracking

Besides the thermal cracking process, fluidized catalytic cracking (FCC) is another important source of propylene production. Traditional FCC is used to produce additional gasoline in the refining process, which is a complex process unit designed for cracking long molecules from vacuum gas oil (VGO) and residue into shorter fuel molecules[8]. However, this process has been recently improved to maximize propylene production since propylene supply cannot match the demand[9]. By adjusting operating conditions and reconfiguring the process, the propylene production can be increased by up to 20%-25%[2]. In addition, a special catalyst has also been discovered which increase the selectivity of propylene[10].

This enhanced FFC was firstly developed in China, where research was conducted over 10 years on a zeolite catalyst for producing propylene and other light olefins. Initially several production lines were built in China followed by the establishment of a plant in Thailand in 1997. Other companies including KBR, Petrobras, Lummum Technology/Indian Oil, Shell, ExxonMobil, UoP, Axens, KFUpm/Saudi Aramco/Nippo oil, and Fortum Oy have also developed similar technologies[2].

Ultra-stabilized zeolite Y (USY)[11] is the most used catalyst in the traditional FCC process and ZSM-5[12-14] has been developed for light olefin production, especially for maximizing propylene production. These catalysts are spherical particles containing large voids and pores, in which zeolite crystals, clay particle, porous material such as alumina or silica-alumina are well distributed. The design of the catalyst must satisfy the need of physical strength and mass transport of the heavy feedstock[15-18]. In the FCC technology, a high temperature above 500 °C and mediate pressure, ranging from 1 to 3 bars is applied. Olefin production and the speed of catalyst deactivation (coke formation) are mainly determined by reaction variables in terms of catalyst circulation rate, reaction temperature, ratio of C/O, feed quality and hydrocarbon partial pressures[9].

2.1.3 Selective C_4/C_5 Cracking

A selective C_4/C_5 cracking aims to convert low value hydrocarbons (e.g.C_4 and C_5) to high value olefins (e.g. propylene and ethylene) over specially formulated shape-selective zeolite catalysts[2]. The feed can be obtained from steam cracker by-products, FFC low value refinery stem or naphtha cracker. To achieve maximum propylene/ethylene production, the feed needs to be pre-treated by selective hydrogenation of all dienes and the selective C_4/C_5 cracking technology process needs to be conducted at a high reaction temperature in the range of 600 – 650 °C. The Combination of olefin oligomerization, cracking and metathesis is the basic mechanism of this technology. However, besides these reactions, the unfavourable secondary hydrogen transfer reaction leads to aromation, cyclization and protolytic cracking.

Recently, many companies have developed this type of technology. KBR has licensed their SUPERFLEX^{TM} technology, which was developed by ARCO Chemical. Moreover, this technology is known as the Mobil Olefin Interconversion (MOI) process in ExxonMobil and Lurgi's process of this technology is named Propylur. Furthermore, UOP and Total cooperatively built a process called Olefin cracking Process (OCP).

Beside the most famous ZSM-5, the medium-pore size zeolites ZSM-22, ZSM-23, ZSM-35 and small-pore sized zeolite SAPO-34 could also achieve selective production of ethylene and propylene[19-21]. Pore size of the zeolites determines the yield of light olefins (propylene and ethylene) due to an influence of the secondary reaction of hydrogenation and cyclization reaction forming undesired paraffins and aromatic compounds[22, 23]. Catalysts with smaller pore size could suppress the secondary reaction to some extent, so they are able to exhibit high selectivities for propylene. Moreover, the selectivity of propylene and ethylene are also dependent on the Si/Al ratio of the zeolite catalysts that affect the acidity. Furthermore, the stability of the catalysts is largely controlled by both the pore size and Si/Al ratio.

2.1.4 Metathesis between Butene and Ethylene

The discovery of the olefin metathesis reaction provides a flexibility for production of various olefins and it also satisfies the market demand for olefins[24, 25]. This reaction interconverts C=C bonds in hydrocarbons and is shown below[25]

$$2\ R\text{-}CH{=}CH\text{-}R' \rightleftharpoons R\text{-}CH{=}CH\text{-}R + R'\text{-}CH{=}CH\text{-}R' \qquad (2.2)$$

Where R and R´ are alkyl groups or hydrogen. The first industrial application of this reaction was cross-metathesis of propylene to ethylene and butene in order to turn propylene into more valuable products. This first olefin metathesis industrial process (Phillips Triolefin Process) was built in 1964 and a heterogeneous, silica-supported tungsten oxide catalyst was utilized in the process. The catalysts were originally discovered by Banks and Bailey of Philips Petroleum[26]. As the demand of propylene increased, ABB Lummus Globlal, Houston (USA) purchased Philips' technology and developed the olefins conversion technology (OCT) in a reverse direction for propylene production. The process could reach above 60% conversion of butene and above 90% selectivity for propylene at around 260 °C and 30-35 bar[27]. The Meta-4 process was developed by the Institut Français du Pétrole (IFP) and the Chinese Petroleum Corporation (Kaoshiang, Taiwan) for propylene production also by metathesis between ethylene and 2-butene. Conversion of butene is 63% per pass in the presence of Re_2O_7/Al_2O_3 at 35 °C and 60 bar. Yet, this process is not commercialized due to the high cost of the catalyst and requirement of high purity of feedstock[28].

The typical heterogeneous metathesis catalysts used in industrial processes are oxides of transition metals (rhenium, molybdenum and tungsten) supported metal oxides (Al_2O_3, SiO_2, and SiO_2-Al_2O_3) catalysts[26, 29-32]. Among these, Re based metathesis catalysts that consist of rhenium oxide impregnated over a highly porous support could perform a high activity and high selectivity even at room temperature[32-34]. The structure of the catalyst, both in active and deactivated statuses, and the oxidation state of the rhenium ion has been reported widely. This will be reviewed in more detail later in this chapter, since rhenium oxide is believed to play a role of metathesis in our dual-functional catalyst. Molybdena-based catalysts are active for olefin metathesis at a broad temperature range from 25 °C to 200 °C[35]. It has been reported that SiO_2[36, 37], ECl_4

(E=Si or Ge)[38], CoO[39] and $(CH_2)_4Sn$[40] could act as promoters in this catalyst system. WO_x/SiO_2 catalyst is a famous catalyst for olefin metathesis due to its use in the Triolefin Process and Olefin Conversion Technology for decades. This catalyst requires a high temperature (350-450 °C) to activate and is typically prepared by an impregnation method[41].

2.1.5 Methanol to Olefins

Thanks to the methanol to gasoline (MTG) process, its catalyst ZSM-5 was also found to make light olefins from methanol[2]. In the mid-1990s, UOP and Norsk Hydro developed a catalytic process for methanol to light olefins[42]. Instead of ZSM-5 catalyst, SAPO-34 with a smaller pore size (around 0.38 nm) was utilized and can exhibit about 78% selectivity to total ethylene and propylene based on a hydrocarbon calculation[43-45]. The production ratio of ethylene to propylene could be changed according to market demand and the overall reaction may be written, despite the intermediate formation of dimethyl ether and CH_2 radicals[46].

$$2CH_3OH \rightarrow CH_2 = CH_2 + 2H_2O \quad (2.3)$$

$$3CH_3OH \rightarrow CH_2 = CH - CH_3 + 3H_2O \quad (2.4)$$

As shown in the equations above, hydrocarbons and water are the main products. Hence, this process must be designed to accommodate enough aqueous flow. Lurgi's methanol to propylene (MTP) employs a special formulated zeolite for higher propylene production. Moreover, Honeywell's UOP and Total have built a Methanol-to-olefin unit in Belgium showing commercial viability.

2.2 Direct Conversion of Ethylene to Propylene

2.2.1 Metal Oxides

In 1972, P. O'Neill and co-workers for the first time observed a direct transformation of ethylene to propylene on a $Mo(CO)_6$-Al_2O_3 catalyst in a olefin metathesis experiment[47]. The catalyst was prepared by dry mixture of pre-treated alumina and molybdenum hexacarbonyl followed by evacuation at 90 °C for 2 hours

before use. This catalyst was expected to express metathesis function and convert propylene to equal amount of ethylene and butane in a static reactor test. However, it turned out that the C_2/C_4 ratio was less than one and it changed with the reaction time as well as the temperature. An immediate increase of propylene after dosing more ethylene into the reactor finally proved the occurrence of the ETP reaction as a side-reaction. Later, A.K.Ghosh et al. discovered the ETP reaction over reduced MoO_3 catalysts based on a group of metal oxides (SiO_2-Al2O_3, Al_2O_3, SiO_2, ZrO_2 and TiO_2), in which MoO_3-SiO_2-Al_2O_3 (28.61% Al_2O_3) showed the best propylene yield[48]. T.Suzuki et al. reported that the yield of propylene from ethylene could be improved over a MoO_x-SiO_2 catalyst in presence of cobalt[49] or H_2[50] in 1990 and 1991, respectively.

Besides MoO_x based metal oxides, T.Yamaguchi et. al. reported propylene production from an ethylene reaction over a partially reduced WO_3-TiO_2 catalyst at 200 °C in a closed recirculation system in 1980[51]. The catalysts were obtained by wet-impregnation of an aqueous solution of $(NH_4)_{10}W_{12}O_{41}$ into TiO_2.

A tri-functional single-site catalyst, W(H_3)/Al_2O_3, was found to transform ethylene into propylene in 2007[52]. This catalyst could perform constantly high propylene selectivity (95%) in a continuous flow reactor test at 150 °C by feeding ethylene at a flow rate of 4ml/min. However, the conversion of ethylene decreased dramatically from 40% to below 20% in the first two hours. The precursor of the catalyst [(Al-O)W(≡CtBu)(Cu_2tBu)$_2$], which was synthesized by grafting [W(≡CtBu)(CH_2tBU)$_3$] onto γ-Al_2O_3, was reduced at 150 °C in the presence of H_2. Initiation and propagation reactions were investigated by identifying the products formed during the reaction at 150 °C as shown in Figure 2.1. They concluded that propylene formed through three steps, dimerization of ethylene to 1-butene, isomerization 1-butene to 2-butene and cross-metathesis between ethylene and 2-butene. In other words, this catalyst possessed three functions, dimerization, isomerization and metathesis in one single site.

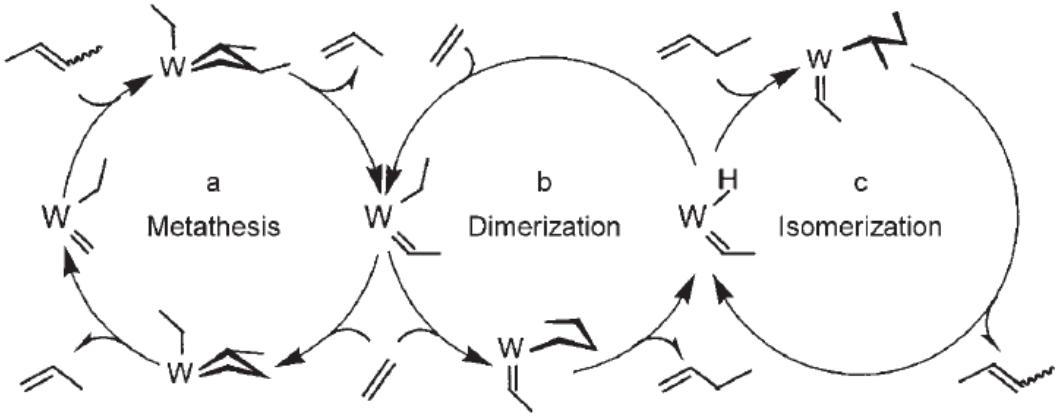

Figure 2.1: A proposed scheme of mechanisms of the ETP reaction over $W(H_3)$-Al_2O_3[52].

A Russian patent claimed a high efficiency of single-step synthesis of propylene from ethylene over a NiO-Re_2O_7/B_2O_3-Al_2O_3 catalyst[53]. Similar to our work, their idea was to develop a bimetallic catalyst based on a Ni responsible dimerization/oligomerization reaction and a Re_2O_7 dominated metathesis reaction. The borate-containing alumina was prepared by mixing a hydrate of alumina oxide with ortho-boric acid as the support material. Then an impregnation method was applied then to saturate the borate-containing alumina with an aqueous solution of perrhenic acid and nickel nitrate. The catalytic performance was determined in a fix-bed reactor by passing an ethylene flow at 40-150 °C and atmospheric pressure. The conversion of ethylene and selectivity of propylene were approximately 15% and 65%, respectively. Later, they reported that using a Pd-Re_2O_7/B_2O_3-Al_2O_3 catalyst it was possible to achieve a high propylene yield of up to 77%-83%[54, 55].

M.Iwamoto et al. studied Sc-In_2O_3 and Y-CeO_2 catalysts for the conversion of ethanol to ethylene and propylene[56, 57]. Compared with Sc-In_2O_3, Y-CeO_2 expressed a more steady activity for the ETP reaction in fix-bed reactor tests. The conversion of ethylene was close to 100% and the yield of propylene was around 25% at 420-430°C. They suggested possible reaction pathways including formation of acetaldehyde and acetone followed by a hydrogenation-dehydration activity to produce propylene as listed below.

$$CH_3CH_2OH \rightarrow CH_3CHO + H_2 \quad (2.5)$$

$$CH_3CHO + CH_3CH_2OH + H_2O \rightarrow CH_3COCH_3 + CO_2 + 3H_2 \quad (2.6)$$

$$CH_3CHO + H_2O \rightarrow CH_3COCH_3 + CO + 2H_2 \quad (2.7)$$

$$CH_3COCH_3 + H_2 \rightarrow CH_2 = CHCH_3 + H_2O \quad (2.8)$$

2.2.2 Mesoporous Material (MCM-41)

A nickel-loaded mesoporous material used for the ETP reaction has been found and investigated mainly by two research teams from Japan and Germany. M. Iwamoto et al. reported that a Ni-MCM-41 prepared with a template ion exchange (TIE) method could perform ethylene conversion of 68% and propylene selectivity of 48% in a direct ETP reaction at 400 °C[58, 59]. The catalysts were tested in a fix-bed continuous flow reactor at atmospheric pressure. In addition, Y. Kato et al. found that an introduction of water into the reactant gas and slowing the feed rate could promote the stability and activity of the catalysts synthesized by this TIE method[60]. Otherwise, carbon deposition on the catalyst would lead to a fast deactivation of the catalyst. Considering reaction mechanisms, regularly arranged mesopores of this catalyst eliminate the possibility of the sharp selectivity that takes place on acidic zeolites in a cracking reaction for propylene production due to the narrow pore sizes of the zeolites. Therefore, to understand the reaction pathways, a systematic experimental design was carried out by varying the feeding gases and the experimental conditions. Two ethylene molecules dimerize to generate 1-butene (2.9) accompanied by an isomerization to 2-butene (2.10) and then a cross-metathesis occurs between 2-butene from the previous reaction and one more ethylene molecule to form two propylene molecules (2.11). Thus, the acidity of MCM-41 and Ni active sites were the two essential factors for this reaction. Moreover, it was confirmed for the first time that Ni active sites in this reaction expressed not only the dimerization function but also the metathesis function.

$$C_2H_4 + C_2H_4 \rightarrow CH_2 = CH - CH_2 - CH_3 \quad (2.9)$$

$$CH_2 = CH - CH_2 - CH_3 \rightarrow CH_3 - CH = CH - CH_3 \quad (2.10)$$

$$CH_3 - CH = CH - CH_3 + C_2H_4 \rightarrow CH_3 - CH = CH_2 + CH_3 - CH = CH_2 \quad (2.11)$$

Next, the effects of pore size and the Si/Al ratio for the reaction rate were investigated. Smaller pore sizes and increased Si/Al ratio could result in an enhancement of the catalyst activity[61]. Moreover, FT-IR spectra of Ni-MCM-41 indicated that the formation of 2:1 layered nickel phyllosilicate-like species was independent of the pore size and the Si/Al ratio. Furthermore, the catalytically active sites seemed to be composed of three-coordinated Ni^{2+} ions situated on five- and six-membered Si-O rings of the MCM-41 framework in UV-Vis-NIR experiments of C_2H_4 and NO adsorbed on the activated catalysts.

The other group utilized an equilibrium adsorption (EA) method to prepare the Ni-MCM-41with different nickel precursors, among which nickel citrate and nickel nitrate exhibited the best performance for the ETP reaction above 250 °C and at atmospheric pressure in a fix-bed flow reactor[62]. Maximum ethylene conversion (36%) was obtained at 400 °C with a high dilution of reactant gas (5% C_2H_4 in N_2) while the selectivity of propylene kept at 45%. It is notable that high feed concentrations of ethylene lowered the propylene selectivity and increased the 2-butene selectivity. Therefore, to achieve a high propylene yield, a low feed concentration of ethylene is necessary. In addition, a high temperature and a long resident time could also improve the selectivity to propylene, although this slightly increased coke formation on the catalyst. Kinetic product measurements demonstrated the same reaction pathways on this catalyst as the mechanisms proposed by M. Iwamoto on template ion-exchanged Ni-MCM-41. No dedicated pre-treatment or introduction of water vapour was needed to activate this catalyst, which indicated that active nickel sites of this equilibrium adsorbed Ni-MCM-41 was different from that of template-ion exchanged catalysts. In their next publication, Ni-MCM-41, prepared by the TIE method, was extensively characterized by means of nitrogen physisorption, XRD, ADS, TEM, EDS, XPS, TPR and FT-IR[63]. Ni(II) phase was confirmed to be a 2:1 type phyllosilicate but there was a disagreement about the generation of the Ni phase. Its formation occurred on the external surface instead of on

the Si-O rings and underwent a dissolution of the mesoporous support. Moreover, it had three types of acid sites in presence of the catalysts. Two of them were due to the nickel phyllosicicate and the remaining one was from the original support MCM-41. Lastly, Ni-AlMCM-41 catalysts with different Si/Al ratios were synthesized by TIE methods and tested for the ETP reaction[64]. The acidity of the catalysts was well controlled by adjusting the Si/Al ratio. These catalysts showed higher activity and propylene selectivity than the other Ni-MCM-41 catalysts. The catalyst with a Si/Al ratio of 60 achieved a maximum propylene yield. In the TEM measurement, Ni particles were observed on the spent catalyst. Consequently, Ni^+ was suggested to be an acid site of the Ni-AlMCM-41 catalyst, which was formed during the reaction and stabilized by a suitable acidity. A serious deactivation of the catalysts at high temperature (450 °C) was due to the deposition of various carbon species.

Recently, V. Hulea and his co-workers[65] reported a new method to achieve a high conversion of ethylene to propylene through cascade oligomerization/isomerization/metathesis reactions over two heterogeneous catalysts. The catalysts, Ni-AlSBA-15 and MoO_3-SiO_2-Al_2O_3, were employed for the reactions and they worked in a single flow reactor under identical conditions.

Ni-FSM-16 and Ni-MCM-41 are attractive catalysts for the direct conversion of ethanol to ethylene and propylene[66, 67]. S. Sugiyama et al. showed this conversion to proceed more favorably on FSM-16 and Ni-FSM-16 than on MCM-41 and Ni-MCM-4[66]. The catalytic testing was carried out in a fix-bed reactor. FSM-16 achieved ethanol conversion of above 99%, but the main product was ethylene (95% ethylene selectivity at 400 °C). When Ni was loaded to FSM-16, the ethanol conversion (above 99%) was unchanged whereas the propylene selectivity was increased to 35%.

2.2.3 Zeolites (ZSM-5 and SAPO-34)

H-ZSM-5 and SAPO-34 have been employed for the ETP reaction due to their sharp selectivity and acidity[68-71]. B. Lin et al. studied a series of molecular sieves, among which H-ZSM demonstrated the highest activity, with 25% ethylene conversion and 42% propylene selectivity at 723 K[70]. The experiment was conducted in a fixed-bed flow reactor operated at atmospheric pressure. It was found that the ethylene conversion

was dependent on the degree of H^+ exchange in the H-Na-ZSM-5 samples as well as the Si/Al ratio. Brønsted acidity of the catalyst was crucial for the ethylene conversion. Phosphorus or Boron modified H-ZSM-5 gave a higher propylene selectivity but a lower ethylene conversion. H. Oikawa et al. reported a selective ETP reaction over SAPO-34[71]. Yields of light olefins were calculated with respect to conversion level of ethylene controlled by adjusting contact time. The result showed that the maximum selectivity (73.3%) was obtained when the ethylene conversion was 71.2%. They also concluded that a shape selectivity effect of the small pore sizes and modest acid strength contributed to this reaction. The effect of SAPO-34 particle size for the ETP reaction was investigated by Y. Iwase et al[68]. The propylene yield and catalyst lifetime were greatly affected by the crystal size of the catalyst. The highest selectivity of propylene (80%) and a high conversion of ethylene (70%) were achieved in a continuous-flow reactor test at 200 °C when the particle size of SAPO-34 was approximate 2.5 μm.

Reaction mechanisms for this kind of zeolite suggest that ethylene undergoes oligomerization and the resultant oligomers crack to light hydrocarbons. The chain-length of the products is strongly constrained by the pore size of the zeolite.

Conversion of ethanol to propylene over these two zeolites has been widely studied[72-77]. Catalytic performances of HZSM-5, SAPO-34, hydrothermal synthesized HZSM-5/SAPO-34 (ZS-HS) and mechanical mixed HZSM-5/SAPO-34 (HS-MM) were reported by C. Duan et al in catalytic testing of a fixed-bed continuous flow reactor[72]. The ZS-HS catalyst exhibited a relatively high propylene yield (25.3%) at 500 °C in comparison to the other three catalysts. The high propylene production was due to proper acidity strength and distribution resulting from the significant interaction and modification between two catalysts during the synthesis. K. Inoue found La modified H-ZSM-5 with a Si/Al_2 ratio of 280 and La-Mg co-modified H-ZSM-5 with a Si/Al_2 ratio of 150 showed propylene selectivity of 31% and 32% respectively at 0.1MPa and 550 °C[73, 74]. Z. Song reported that P/Zr/ZSM-5 resulted in a yield of 29.2% propylene at 550 °C, 0.1Mpa, which was higher than non-modified ZSM-5 and Zr/ZSM-5[75, 76].

2.3 Ni-based Catalysts for Ethylene Oligomerization

2.3.1 NiO and $NiSO_4$ on Metal Oxides

The first report of NiO supported silica for the ethylene oligomerization reaction occurred in 1938 by K. Morikawa[78]. G. C. Bailey and J.A. Reid discovered that NiO based silica-alumina exhibited a high activity for ethylene oligomerization even at room temperature[79]. They suggested that the catalyst activity could be improved with modification of alumina and a pre-treatment of the catalyst was needed to activate the catalyst (e.g. at 400-500°C, an oxidizing atmosphere). NiO-SiO_2 was found to show the dimerization reaction of ethylene at room temperature by A. Ozaki and T. Shiba in 1953[80] as well as H. Uchida and H. Imai in 1962[81, 82]. Later, K. Kimure et al investigated the ethylene dimerization reaction by means of a deuterium tracer[83]. NiO, supported with various support materials (γ-Al_2O_3, SiO_2, SiO_2-Al_2O_3, TiO_2, TiO_2-MgO, TiO_2-ZnO), was studied with regard to its function in ethylene dimerization. It turned out that only catalysts supported on acidic silica and/or alumina showed activity for the ethylene dimerization reaction. Moreover, the number of active sites was influenced by the content of alumina in the support material. J. R. Sohn et al. reported a series of NiO based metal oxides catalysts for ethylene dimerization at room temperature and low pressure. Acid strengths of the metal oxides, including TiO_2[84, 85], ZrO_2[86-89] Al_2O_3[90, 91] and SiO_2-Al_2O_3[92-94], were examined in relation to the catalytic activities. Structural and catalytic properties of NiO/Al_2O_3-SiO_2 were characterized by G. Wendt et al[95, 96]. Later, T. Cai et al. and J. R. Sohn et al. studied the catalytic activity of $NiSO_4$/γ-Al_2O_3 for ethylene dimerization in 1992 and 2002, respectively. Surface acidity of this catalyst has a crucial influence on the catalytic activity.

Table 2.1 lists the catalytic performance of a series of NiO or $NiSO_4$ supported metal oxides for ethylene dimerization/oligomerization reactions. These catalysts were prepared by impregnation or precipitation methods. The ethylene dimerization reaction favours near room temperature. From literature data, it is known that the product distribution of ethylene oligomerization reaction highly depends on the reaction temperature[97]. Even-number oligomers (olefins) are produced exclusively over weak-medium acid catalysts under mild experiment conditions[98-100]. On the contrary, a broad

spectrum of products including aromatics, alkanes and alkene with both odd and even carbon numbers are formed at high reaction temperatures, especially on strongly acidic catalysts[101-103]. Pressure, from the thermodynamic point of view, effects chain-length of the products from the ethylene oligomerization reaction which become longer as the reaction pressure increases. Therefore, most experiments of ethylene dimerization are carried out at near or lower than atmospheric pressure.

Table 2.1: Catalytic performance in the ethylene dimerization/oligomerization of Ni-based catalysts.

Catalyst	Experimental setup	T (°C)	P (bar)	Feed	Main oligomers
NiO/SiO_2-Al_2O_3 [83, 104-106]	Continuous flow reactor [a]	40	20	C_2H_4:H_2 45:55	C_4, C_6, C_8, C_{10}
	Circulatory flow system [a]	40-100	0.47	C_2H_4	C_4
	Continuous flow reactor [a]	25	0.53	C_2H_4	C_4
	Tubular flow reactor [b]	150	1	C_2H_4	C_4
$NiSO_4$/γ-Al_2O_3 [90, 107]	Closed circulating system [a]	25	2.67 [c]	C_2H_4	C_4
	Static system [a]	20	0.39 [c]	C_2H_4	C_4
NiO-SiO_2 [108, 109]	Static system[a]	20	0.31 [c]	C_2H_4	C_4
NiO-ZrO_2/SO_4^{2-} [86]	Static system [a]	20	0.38 [c]	C_2H_4	C_4
NiO-ZrO_2/WO_3 [87]	Static system [a]	20	0.4 [c]	C_2H_4	C_4
NiO-TiO_2/WO_3 [110]	Static system [a]	20	0.4 [c]	C_2H_4	C_4
NiO-ZrO_2/MO_3 [89]	Static system [a]	20	0.4 [c]	C_2H_4	C_4
NiO/Al_2O_3-SiO_2 [93]	Static system [a]	20	0.4 [c]	C_2H_4	C_4

[a] Catalysts were synthesized by an impregnation method. [b] Catalysts were made by a precipitation method. [c] Initial pressure of ethylene.

Many studies have been devoted to the nature of Ni active sites and the role of acid sites due to their significance for catalytic performance in ethylene dimerization and oligomerization reactions[97]. G. Wendt et al. concluded that catalytically active sites are formed during the process of thermal activation of NiO/SiO_2-Al_2O_3 catalysts. The active sites consisted of acid sites in conjunction with coordinatively unsaturated nickel (II) ions in different coordinative environments (C_{3v}, C_{4v} or T_d symmetry)[111]. $NiSO_4$/γ-Al_2O_3 for ethylene dimerization has been studied by T. Cai et al[107]. They concluded that active sites involved in the ethylene dimerization reaction were Ni^+ activated by acid sites. Ni^+ on the activated catalyst, which was pretreated at 600°C for 1 hour at vacuum, was demonstrated by FT-IR and EPR techniques. Moreover, formation of Ni^+ was also found in the EPR measurement after introduction of ethylene to the catalyst calcinated in an oxygen atmosphere at 500 °C. Hence, the reduction of Ni^{2+} was suggested to occur both in the course of high-temperature evacuation and after dosage of ethylene on the

calcinated catalyst. The need for an acid strength of $H_0 \leq 3$ for ethylene dimerization reaction was deduced in a NaOH poisoning experiment. J. R. Sohn et al. investigated the active sites of a series of catalysts consisting of NiO/$NiSO_4$ on metal oxdies[84, 88, 90, 92-94]. For these catalysts, they reported a low valent Ni site combined with surface acidity as the active catalyst site responsible for the dimerization reaction. The ethylene dimerization reaction over $NiSO_4$/γ-Al_2O_3 was also studied by them. Ni^+ was observed on the thermal-activated catalyst (500 °C, under vacuum) by FT-IR and XPS experiments. Brønsted and Lewis acid sites were found on the catalyst surface in a FT-IR study by adsorption of ammonia. A recent report investigated active sites of a $NiSO_4$/γ-Al_2O_3 catalyst for the oligomerization of isobutene[112]. It was concluded that the oxidation state of Ni remained +2 after calcination but was reduced to low valence (≤1) during the course of isobutene oligomerization. They also found sulfate ions increased the acidity of the Lewis acid sites on the surface and assisted in the adsorption of isobutene.

The deactivation of the catalysts for ethylene oligomerization has been evaluated in a vast number of publications. In general, the reason for deactivation is the strong adsorption of formed products blocking or deactivating the active sites[97].

2.3.2 Ni-based Zeolite and Mesoporous Materials

Employing Ni-containing zeolites or mesoporous materials for an effective ethylene dimerization/oligomerization reaction has been the topic of a considerable number of publications. Nickel exchanged X and Y zeolites could show high activities for ethylene dimerization/oligomerization at mild conditions[113-118]. However, these materials always accompanied severe deactivation during the reaction since their microporses were rapidly blocked by a limitation of intracrystalline diffusion[119]. To tackle this problem, Nickel exchanged mesoporous materials (e.g. MCM-41, MCM-36 and MCM-22) were used and showed attractive properties for ethylene dimerization/oligomerization[120-122]. In addition, Ni-containing dealuminated Y zeolite, with its large supercages and pore volume, provided an alternative way to alleviate fast deactivation of the catalysts[119, 123, 124].

2.4 Re-based Metathesis Catalysts

Typical Re-based metathesis catalysts are rhenium oxide supported on a high-surface-area metal oxide support (e.g. Al_2O_3, SiO_2, SiO_2-Al_2O_3)[24]. To synthesise the catalysts, generally, the support is impregnated by an aqueous solution of a rhenium salt such as NH_4ReO_4 or $HReO_4$ followed by drying at 110-120 °C and calcination at 500-500 °C in air. The catalyst could show a high activity and high selectivity for metathesis reaction at low temperatures (20-100 °C)[31, 125-129].

The formation of a metal carbene species is generally accepted as the initial step of the metathesis reaction[29]. The formed transition-metal carbene species with a vacant coordination site participates in the propagation of the metathesis. Figure 2.2 shows the cycle of self-metathesis of propylene to 2-butene and ethylene proposed by Y. Chauvin[130]. One propylene molecule interacting with one active specie generates a metallacyclobutane, which cleaves to a new metal carbene complex and one 2-butene. Subsequently, the new complex continues to react with one propylene forming another metallacyclobutane to produce one ethylene.

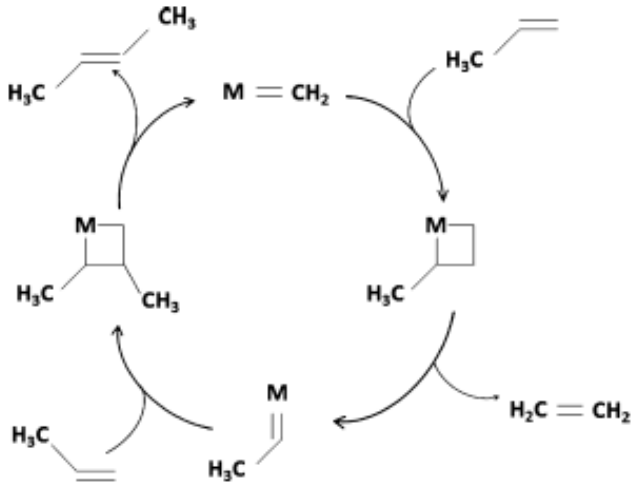

Figure 2.2: Olefin metathesis for self-metathesis of propylene to 2-butene and ethylene proposed by Y. Chauvin[130].

Figure 2.3 demonstrates the four proposed initiation mechanisms of the formation of metal carbine complex: (A) formation of a π-complex between the reacting alkene and the transition metal (1-2 hydrogen shift mechanism)[131, 132], (B) a π-ally complex formed by a hydride transfer (π-ally mechanism)[127, 133], (c) a hydrogen shift from a surface Brønsted acid site to form a π-complex (H-assisted mechanism)[134], (D) formation

of a π-ally complex by elimination of a carbonyl compound (Pseudo-Wittig mechanism)[135].

The results of many characterization methods reveal that rhenium oxide is homogeneously dispersed on the alumina support after calcination at high temperature (~500 °C) due to its low melting temperature[29]. Characterization of Re_2O_7/γ-Al_2O_3 with electron microscopy was carried out by A. Olsthoorn and C. Boelhouwer in 1976[136]. They concluded that no Re_2O_7 crystal was observed and if it was present, the mean diameter of the crystals would be smaller than 2nm. Later, J. Okal et al. undertook a detailed investigation on the microstructural changes during oxidation and re-dispersion of a Re/γ-Al_2O_3 catalyst[137]. Small clusters, less than 1nm, were observed after oxidation of the Re/γ-Al_2O_3 catalyst in a HRTEM measurement. These clusters were suggested to be aggregates of $(ReO_4)^-$ tetrahedral grouped around special sites on γ-Al_2O_3 or Re clusters formed inside the electron microscope under the influence of the electron beam. It was discovered during an in-situ FT-IR experiment that ReO_4^- first reacts with basic surface hydroxyl groups at low loadings of Re_2O_7 and at high converges of Re_2O_7, moderate and acidic hydroxyl groups are consumedt[138, 139]. L. Wang and W. Hall reported that the symmetry of ReO_4^- on the alumna is lower than the tetrahedral symmetry of free ReO_4^- ions after comparing their UV-Vis spectra[140]. Later, in-situ Raman and FT-IR studies were carried out to test the Re_2O_7/γ-Al_2O_3 catalyst with high loadings of Re_2O_7 in dehydrated form. The results show two distinct isolated surface rhenium $(O=)_3$-Re-O-Al species on the alumina and the terminal Re=O is slightly different for the two species[139, 141].

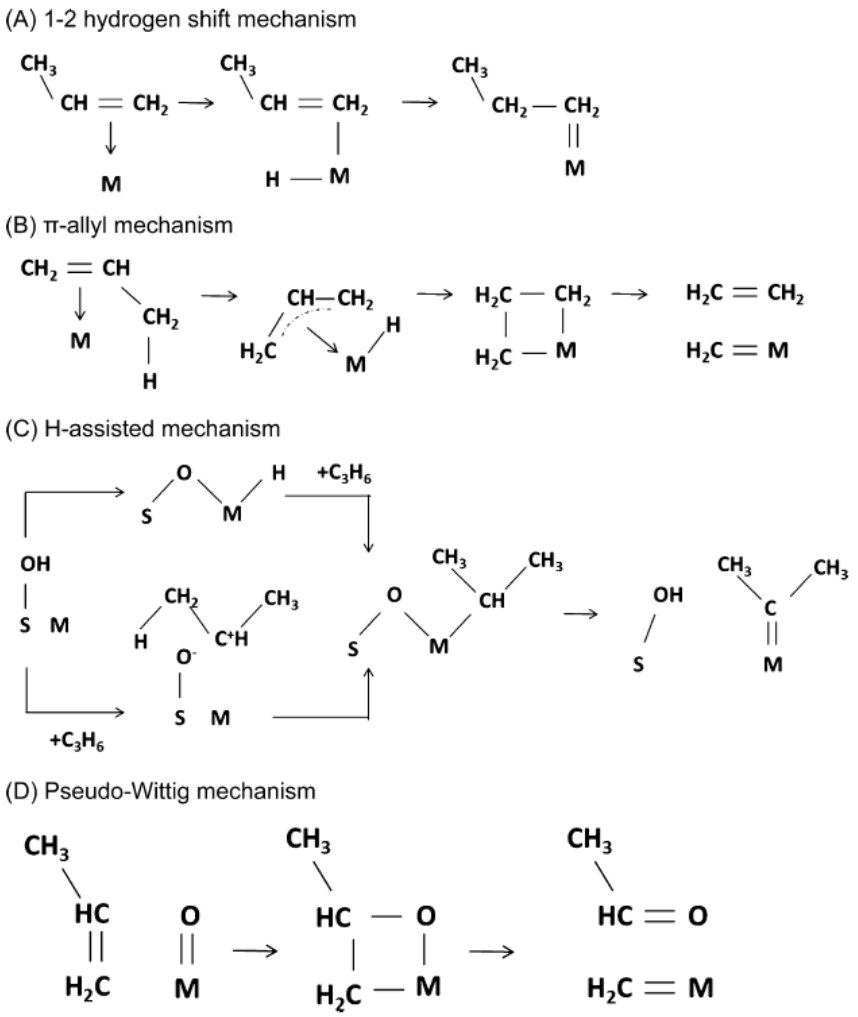

Figure 2.3: Proposed olefin metathesis activation mechanisms. M represents the catalytic active sites and S represents the oxide support[29, 135, 142].

2.5 Summary

This chapter gives an overview of the development of the "on purpose" technologies for propylene production and one step ETP reaction. Among these technologies, one step ETP reaction gains our attentions by considering the availability of ethylene resource and industrial applicability in the future. Therefore, this project aims to investigate a catalyst for ETP reaction.

In this project, the effort has been made on synthesizing a dual-functional catalyst for ETP reaction. As mentioned in chapter 1, the first idea is to combine the two functional sites (dimerization and metathesis) onto one support material. Therefore, the research first focused on synthesizing dimerization catalysts. A series of Ni-based metal oxide catalysts were synthesized and the one with the highest butene production was

chosen further tests. As the dimerization catalyst ($NiSO_4$/γ-Al_2O_3) has been chosen, the next step is to screen metathesis catalysts. Since $NiSO_4$/γ-Al_2O_3 shows a high dimerization activity at mild condition, the metathesis catalyst, Re_2O_7/γ-Al_2O_3, which also shows a high activity at mild reaction temperatures and has the same support material, is therefore selected. Consequently, the $NiSO_4$-ReO_x/ γ-Al_2O_3 catalyst was synthesized and tested for ETP reaction. Detail descriptions of testing methods and results are given in the next chapter.

References

1. Houdry, E.J., 1947, US patent 2.419.997.
2. Wittcoff, H.A., Reuben, B.G., Ploktin, J.S., *Industrial Organic Chemicals.* 3rd ed., John Wiley & Sons Ltd, Chicester, 2012.
3. Lee, D.H., Lee, W.J., Lee, W.J., Kim, S.O., Kim, Y.-H., *Phys. Rev. Lett.*, 106 (2011) 175502.
4. Låte, L., Rundereim, J.I., Blekkan, E.A., *Appl. Catal. A- Gen*, 262 (2004) 53-61.
5. Beretta, A., Piovesan, L., Forzatti, P., *J. Catal.*, 184 (1999) 455-468.
6. Beretta, A., Forzatti, P., Ranzi, E., *J. Catal.*, 184 (1999) 469-478.
7. Grasselli, R.K., Stern, D.L., Tsikoyiannis, J.G., *Appl. Catal. A- Gen*, 189 (1999) 1-8.
8. Jiménez-García, G., Aguilar-López, R., Maya-Yescas, R., *Fuel*, 90 (2011) 3531-3541.
9. Akah, A., Al-Ghrami, M., *Appl.Petrochem.Res.*, 5 (2015) 377-392.
10. Li, X., Li, C., Zhang, J., Yang, C., Shan, H., *J. Nat. Gas Chem.*, 16 (2007) 92-99.
11. Perego, C., Millini, R., *Chem. Soc. Rev.*, 42 (2013) 3956-3976.
12. Buchanan, J.S., *Catal. Today*, 55 (2000) 207-212.
13. Degnan, T.F., Chitnis, G.K., Schipper, P.H., *Microporous Mesoporous Mater.*, 35–36 (2000) 245-252.
14. Zhao, X., Roberie, T.G., *Ind. Eng. Chem. Res.*, 38 (1999) 3847-3853.
15. Mao, R.L.V., Al-Yassir, N., Nguyen, D.T.T., *Microporous Mesoporous Mater.*, 85 (2005) 176-182.
16. Al-Khattaf, S., *Energy Fuels*, 17 (2003) 62-68.
17. Von Ballmoos, R., Hayward, C.-M.T., *Matrix vs Zeolite Contributions to the Acidity of Fluid Cracking Catalysts*, Stud. Surf. Sci. Catal., Elsevier, 1991, 171-183.
18. Yan, H.T., Le Van Mao, R., *Appl. Catal. A- Gen*, 375 (2010) 63-69.
19. Zhu, X., Liu, S., Song, Y., Xu, L., *Appl. Catal. A- Gen*, 288 (2005) 134-142.
20. Zhu, X., Liu, S., Song, Y., Xie, S., Xu, L., *Appl. Catal. A- Gen*, 290 (2005) 191-199.
21. Corma, A., González-Alfaro, V., Orchillés, A.V., *Appl. Catal. A- Gen*, 187 (1999) 245-254.
22. Komatsu, T., Ishihara, H., Fukui, Y., Yashima, T., *Appl. Catal. A- Gen*, 214 (2001) 103-109.
23. Wang, B., Gao, Q., Gao, J., Ji, D., Wang, X., Suo, J., *Appl. Catal. A- Gen*, 274 (2004) 167-172.
24. Mol, J.C., *Catal. Today*, 51 (1999) 289-299.
25. Mol, J.C., *J. Mol. Catal. A: Chem.*, 213 (2004) 39-45.
26. Banks, R.L., Bailey, G.C., *I&EC Product Research and Development*, 3 (1964) 170-173.
27. Parkinson, G., *Chem.Eng.*, 108 (2001) 27.
28. Amigues, P., Chauvin, Y., Commereuc, D., Lai, C.C., Liu, Y. H., Pan, J.M., *Hydrocarbon process*, 69 (1990) 79.
29. Lwin, S., Wachs, I.E., *ACS Catal.*, 4 (2014) 2505-2520.
30. Mol, J.C., *NATO ASI Ser., Ser. C*, 326 (1990) 247-269.
31. El-Sawi, M., Iannibello, A., Morelli, F., Catalano, G., Intrieri, F., Giordano, G., *J. Chem. Technol. Biotechnol.*, 31 (1981) 388-394.
32. Sang, L., Chen, S.-L., Yuan, G., Zheng, M., You, J., Chen, A., Li, R., Chen, L., *J. Nat. Gas Chem.*, 21 (2012) 105-108.
33. Yuan, G., Wang, H., Chen, S., Sang, L., Ma, R., *Shiyou Huagong*, 39 (2010) 151-156.

34. Wang, H., Yuan, G., Hou, Y., Jin, H., Chen, S., Xia, Y., *Shiyou Huagong*, 37 (2008) 1127-1132.
35. Zhu, X., Li, X., Xie, S., Liu, S., Xu, G., Xin, W., Huang, S., Xu, L., *Catal. Surv. Asia*, 13 (2008) 1-8.
36. Debecker, D.P., Stoyanova, M., Rodemerck, U., Gaigneaux, E.M., *J. Mol. Catal. A: Chem.*, 340 (2011) 65-76.
37. Domínguez, M.I., Sánchez, M., Centeno, M.A., Montes, M., Odriozola, J.A., *J. Mol. Catal. A: Chem.*, 277 (2007) 145-154.
38. Bykov., V.I., Belyaev, B. A., Butenko, T. A., Finkel'shtein, E. S., *Kin.Catal.*, 53 (2012) 353-356.
39. Hardee, J.R., Hightower, J.W., *J. Catal.*, 83 (1983) 182-191.
40. Handzlik, J., Ogonowski, J., *Catal. Lett.*, 88 119-122.
41. Ross-Medgaarden, E.I., Wachs, I.E., *J. Phys. Chem. C*, 111 (2007) 15089-15099.
42. Vora, B.V., Marker, T. L., Nilsen, H. R., 1998, US5714662A.
43. Salmasi, M., Fatemi, S., Hashemi, S.J., *Scientia Iranica*, 19 (2012) 1632-1637.
44. Li, J., Wei, Y., Liu, G., Qi, Y., Tian, P., Li, B., He, Y., Liu, Z., *Catal. Today*, 171 (2011) 221-228.
45. Sun, Q., Wang, N., Guo, G., Yu, J., *Chem. Commun.*, 51 (2015) 16397-16400.
46. Stöcker, M., *Microporous Mesoporous Mater.*, 29 (1999) 3-48.
47. O'Neill, P.P., Rooney, J.J., *J. Am. Chem. Soc.*, 94 (1972) 4383-4384.
48. Ghosh, A.K., Tanaka, K., Toyoshima, I., *J. Catal.*, 105 (1987) 530-535.
49. Suzuki, T., Hirai, T., Hayashi, S., *Chem. Express*, 5 (1990) 877-880.
50. Suzuki, T., Hirai, T., Hayashi, S., *Int. J. Hydrogen Energy*, 16 (1991) 345-348.
51. Yamaguchi, T., Tanaka, Y., Tanabe, K., *J. Catal.*, 65 (1980) 442-447.
52. Taoufik, M., Le Roux, E., Thivolle-Cazat, J., Basset, J.-M., *Angew. Chem. Int. Ed.*, 46 (2007) 7202-7205.
53. Lavrenov, A.V., Mikhailova, M.S., Buluchevskii, E.A., 2011, RU 2427421, C1 20110827.
54. Buluchevskii, E.A., Mikhailova, M.S., Lavrenov, A.V., *Khim. Interesakh Ustoich. Razvit.*, 21 (2013) 55-59.
55. Buluchevskii, E.A., Lavrenov, A.V., Saifulina, L.F., *Khim. Interesakh Ustoich. Razvit.*, 22 (2014) 561-567.
56. Iwamoto, M., Mizuno, S., Tanaka, M., *Chem. Eur. J.*, 19 (2013) 7214-7220.
57. Hayashi, F., Iwamoto, M., *ACS Catal.*, 3 (2013) 14-17.
58. Iwamoto, M., *Catal. Surv. Asia*, 12 (2008) 28-37.
59. Iwamoto, M., Kosugi, Y., *J. Phys. Chem. C*, 111 (2007) 13-15.
60. Kato, Y., Nishioka, Y., Wada, T., Nakagawa, K., Sotowa, K.-I., Sugiyama, S., *Int. J. Mod Phys B*, 24 (2010) 3253-3256.
61. Tanaka, M., Itadani, A., Kuroda, Y., Iwamoto, M., *J. Phys. Chem. C*, 116 (2012) 5664-5672.
62. Lehmann, T., Wolff, T., Zahn, V.M., Veit, P., Hamel, C., Seidel-Morgenstern, A., *Catal. Commun.*, 12 (2011) 368-374.
63. Lehmann, T., Wolff, T., Hamel, C., Veit, P., Garke, B., Seidel-Morgenstern, A., *Microporous Mesoporous Mater.*, 151 (2012) 113-125.
64. Alvarado Perea, L., Wolff, T., Veit, P., Hilfert, L., Edelmann, F.T., Hamel, C., Seidel-Morgenstern, A., *J. Catal.*, 305 (2013) 154-168.
65. Andrei, R.D., Popa, M.I., Fajula, F., Cammarano, C., Khudhair, A.A., Bouchmella, K., Mutin, P.H., Hulea, V., *ACS Catal.*, 5 (2015) 2774-2777.
66. Sugiyama, S., Kato, Y., Wada, T., Ogawa, S., Nakagawa, K., Sotowa, K.-I., *Top. Catal.*, 53 (2010) 550-554.
67. Iwamoto, M., *Molecules*, 16 (2011) 7844-7863.

68. Iwase, Y., Motokura, K., Koyama, T.-r., Miyaji, A., Baba, T., *Phys. Chem. Chem. Phys.*, 11 (2009) 9268-9277.
69. Zhou, H., Wang, Y., Wei, F., Wang, D., Wang, Z., *Appl. Catal. A- Gen*, 348 (2008) 135-141.
70. Lin, B., Zhang, Q., Wang, Y., *Ind. Eng. Chem. Res.*, 48 (2009) 10788-10795.
71. Oikawa, H., Shibata, Y., Inazu, K., Iwase, Y., Murai, K., Hyodo, S., Kobayashi, G., Baba, T., *Appl. Catal. A- Gen*, 312 (2006) 181-185.
72. Duan, C., Zhang, X., Zhou, R., Hua, Y., Chen, J., Zhang, L., *Catal. Lett.*, 141 (2011) 1821-1827.
73. Inoue, K., Okabe, K., Inaba, M., Takahara, I., Murata, K., *React. Kinet, Mech. Catal.*, 101 (2010) 477-489.
74. Inoue, K., Inaba, M., Takahara, I., Murata, K., *Catal. Lett.*, 136 (2010) 14-19.
75. Song, Z., Takahashi, A., Mimura, N., Fujitani, T., *Catal. Lett.*, 131 (2009) 364-369.
76. Song, Z., Liu, W., Chen, C., Takahashi, A., Fujitani, T., *React. Kinet, Mech. Catal.*, 109 (2013) 221-231.
77. Inoue, K., Okabe, K., Inaba, M., Takahara, I., Murata, K., *React. Kinet, Mech. Catal.*, 101 (2010) 227-235.
78. K.Morikawa, *Kogyo Kagaku Zasshi*, 41 (1938) 694.
79. Reid, G.C.B.a.J.A., 1952, US 2581228 and US 2606940.
80. T. Shiba, A.O., *Nippon Kagaku Zasshi*, 74 (1953) 295.
81. Uchida, H., Imai, H., *Bull. Chem. Soc. Jpn.*, 35 (1962) 989-995.
82. Uchida, H., Imai, H., *Bull. Chem. Soc. Jpn.*, 35 (1962) 995-1000.
83. Imai, H., Uchida, H., *Bull. Chem. Soc. Jpn.*, 38 (1965) 925-930.
84. Sohn, J., Han, J., *Appl. Catal. A- Gen*, 298 (2006) 168-176.
85. Sohn, J.R., Lee, S.H., *Appl. Catal. A- Gen*, 321 (2007) 27-34.
86. Sohn, J.R., Kim, H.W., Park, M.Y., Park, E.H., Kim, J.T., Park, S.E., *Appl. Catal. A-Gen*, 128 (1995) 127-141.
87. Sohn, J.R., Lee, S.Y., *Appl. Catal. A- Gen*, 164 (1997) 127-140.
88. Sohn, J.R., Lim, J.S., *Catal. Today*, 111 (2006) 403-411.
89. Sohn, J.R., Kwon, S.H., Shin, D.C., *Appl. Catal. A- Gen*, 317 (2007) 216-225.
90. Sohn, J.R., Park, W.C., *Appl. Catal., A*, 239 (2003) 269-278.
91. Sohn, J.R., *Catal. Surv. Asia*, 8 (2004) 249-263.
92. Sohn, J.R., Park, W.C., Park, S.-E., *Catal. Lett.*, 81 (2002) 259-264.
93. Sohn, J.R., Lee, M.H., Shin, D.C., *J. Ind. Eng. Chem. (Seoul, Repub. Korea)*, 12 (2006) 710-719.
94. Sohn, J.R., Park, W.C., Shin, D.C., *J. Mol. Catal. A: Chem.*, 256 (2006) 156-163.
95. Wendt, G., Fritsch, E., Deininger, D., Schoellner, R., *React. Kinet. Catal. Lett.*, 16 (1981) 137-141.
96. Wendt, G., Jusek, M., Hagenau, K., Kiessling, D., Schoellner, R., *Geterog. Katal.*, 5th, Pt. 1 (1983) 249-254.
97. Finiels, A., Fajula, F., Hulea, V., *Catal. Sci. Technol.*, 4 (2014) 2412-2426.
98. Hulea, V., Fajula, F., *J. Catal.*, 225 (2004) 213-222.
99. Martínez, A., Arribas, M.A., Concepción, P., Moussa, S., *Appl. Catal. A- Gen*, 467 (2013) 509-518.
100. Heydenrych, M.D., Nicolaides, C.P., Scurrell, M.S., *J. Catal.*, 197 (2001) 49-57.
101. Heveling, J., van der Beek, A., de Pender, M., *Appl. Catal.*, 42 (1988) 325-336.
102. Espinoza, R.L., Korf, C.J., Nicolaides, C.P., Snel, R., *Appl. Catal.*, 29 (1987) 175-184.
103. Nkosi, B., Ng, F.T.T., Rempel, G.L., *Appl. Catal. A- Gen*, 158 (1997) 225-241.
104. Hogan, J.P., Banks, R.L., Lanning, W.C., Clark, A., *Ind. Eng. Chem.*, 47 (1955) 752-757.

105. Matsuda, T., Miura, H., Sugiyama, K., Ohno, N., Keino, S., Kaise, A., *J. Chem. Soc., Faraday Tran. 1*, 75 (1979) 1513-1520.
106. Wendt, G., Finster, J., Schöllner, R., Siegel, H., *Structural and Catalytic Properties of NiO-Al2O3/SiO2 Catalysts for the Dimerization and Isomerization of Olefins*, Stud. Surf. Sci. Catal., Elsevier, 1981, 978-992.
107. Cai, T., Cao, D., Song, Z., Li, L., *Appl. Catal. A- Gen*, 95 (1993) L1-L7.
108. Sohn, J.R., Ozaki, A., *J. Catal.*, 59 (1979) 303-310.
109. Sohn, J.R., Ozaki, A., *J. Catal.*, 61 (1980) 29-38.
110. Sohn, J.R., Han, J.S., *Appl. Catal. A- Gen*, 298 (2006) 168-176.
111. Wendt, G., Hentschel, D., Finster, J., Schollner, R., Hanafi, S., Mikhail, R.S., *J. Chem. Soc., Faraday Tran. 1*, 79 (1983) 2013-2025.
112. Sarkar, A., Seth, D., Jiang, M., Ng, F.T.T., Rempel, G.L., *Top. Catal.*, 57 (2014) 730-740.
113. Yashima, T., Ushida, Y., Ebisawa, M., Hara, N., *J. Catal.*, 36 (1975) 320-326.
114. Ghosh, A.K., Kevan, L., *J. Phys. Chem.*, 94 (1990) 3117-3121.
115. Ng, F.T.T., Creaser, D.C., *Appl. Catal. A- Gen*, 119 (1994) 327-339.
116. Ng, F.T.T., Creaser, D.C., *Ethylene Dimerization: Kinetics and Selectivity for 1-Butene*, Stud. Surf. Sci. Catal., Elsevier, 1992, 123-131.
117. Zheng, L., Wang, G., Bad, X., *Interaction of Nickel Ions with Ethylene Molecules in Ethylene Dimerization over Ni-X Zeolites*, Stud. Surf. Sci. Catal., Elsevier, 1986, 965-972.
118. Bonneviot, L., Olivier, D., Che, M., *J. Mol. Catal.*, 21 (1983) 415-430.
119. Lallemand, M., Finiels, A., Fajula, F., Hulea, V., *Appl. Catal. A- Gen*, 301 (2006) 196-201.
120. Hartmann, M., Pöppl, A., Kevan, L., *J. Phys. Chem.*, 100 (1996) 9906-9910.
121. Lallemand, M., Rusu, O.A., Dumitriu, E., Finiels, A., Fajula, F., Hulea, V., *Appl. Catal. A- Gen*, 338 (2008) 37-43.
122. Lallemand, M., Finiels, A., Fajula, F., Hulea, V., *J. Phys. Chem. C*, 113 (2009) 20360-20364.
123. Sohn, J.R., Park, J.H., *Appl. Catal. A- Gen*, 218 (2001) 229-234.
124. Sohn, J.R., Park, J.H., *J. Ind. Eng. Chem.*, 4 (1998) 308-313.
125. Andreev, A., Edreva-Kardzhieva, R., Neshev, N., *Recl. Trav. Chim. Pays-Bas*, 96 (1977) 23-26.
126. Spinicci, R., Tofanari, A., *Appl. Catal.*, 14 (1985) 261-276.
127. McCoy, J.R., Farona, M.F., *J. Mol. Catal.*, 66 (1991) 51-58.
128. Xu, Y., Huang, J., Lin, Z., Guo, X., *J. Mol. Catal.*, 65 (1991) 275-285.
129. Mahmood, C.S., Yarmo, M.A., Hamid, S.B.D.A., *J. Mol. Catal. A: Chem.*, 161 (2000) 11-16.
130. Chauvin, Y., Commereuc, D., *J. Chem. Soc., Chem. Commun.*, (1992) 462-464.
131. Iwasawa, Y., Hamamura, H., *J. Chem. Soc., Chem. Commun.*, (1983) 130-132.
132. Iwasawa, Y., Kubo, H., Hamamura, H., *J. Mol. Catal.*, 28 (1985) 191-208.
133. Farona, M.F., Tucker, R.L., *J. Mol. Catal.*, 8 (1980) 85-90.
134. Laverty, D.T., Rooney, J.J., Stewart, A., *J. Catal.*, 45 (1976) 110-113.
135. Amakawa, K., Wrabetz, S., Kröhnert, J., Tzolova-Müller, G., Schlögl, R., Trunschke, A., *J. Am. Chem. Soc.*, 134 (2012) 11462-11473.
136. Olsthoorn, A.A., Boelhouwer, C., *J. Catal.*, 44 (1976) 197-206.
137. Okal, J., Kpiński, L., Krajczyk, L., Drozd, M., *J. Catal.*, 188 (1999) 140-153.
138. Sibeijn, M., Spronk, R., Veen, J.A.R., Mol, J.C., *Catal. Lett.*, 8 201-208.
139. Vuurman, M.A., Stufkens, D.J., Oskam, A., Wachs, I.E., *J. Mol. Catal.*, 76 (1992) 263-285.
140. Wang, L., Hall, W.K., *J. Catal.*, 82 (1983) 177-184.

141. Vuurman, M.A., Wachs, I.E., *J. Phys. Chem.*, 96 (1992) 5008-5016.
142. Salameh, A., Copéret, C., Basset, J.-M., Böhm, V.P.W., Röper, M., *Adv. Synth. Catal.*, 349 (2007) 238-242.

Chapter 3

3 Catalyst Synthesis and Testing

A series of catalysts, with H-ZSM-5, MCM-41, γ-Al_2O_3 and Al_2O_3-SiO_2 as support materials, were prepared by three synthesis methods. It was the goal of this project to investigate and test catalysts supported on metal oxides in a continuous flow reactor. These kind of catalysts are seldom reported in the literature for the ETP reaction. Moreover, Ni-H-ZSM-5 and Ni-MCM-41 catalysts were also tested in the same reactor for comparing with those catalysts based on metal oxides. Pulse reactor tests were carried out in order to study the activation period of our main catalysts in the last part of this chapter.

3.1 Catalyst Synthesis

Catalysts were prepared according to three synthesis methods: Incipient wetness impregnation, precipitation impregnation and ion exchange. All prepared catalysts are listed in Table 3.1. Three kinds of support materials were used: a) H-ZSM-5 is a microporous aluminosilicate zeolite with a channel structure of 10-membered rings, b) MCM-41 is composed of silicate or aluminosilicate having a one-dimension structure with a regularly mesoporsous arrangement, c) Metal oxides such as alumina and aluminosilicate are also a useful support material for many industrial catalysts but they do not have such special channel or regular structure like H-ZSM-5 and MCM-41.

Ni-H-ZSM-5 (Si/Al: 30) and Ni-MCM-41 (Si/Al: 34) catalysts were made by an ion exchange method. A mixture of a nickel nitrate aqueous solution (0.02 M, 40 ml) and zeolite (5.0 g), kept in a polyethylene (P.E.) bottle, was stirred vigorously for 1 hour at room temperature followed by treating at 353 K for 20 hours without stirring. The residual in the bottle was filtered out by vacuum filtration and washed with distilled water 3 times before drying at 353 K overnight and calcinating at 823 K for 6 hours.

Table 3.1: List of catalysts and synthesis methods.

Catalyst	Chemicals	Method	Color (in the atmosphere)
Ni/H-ZSM-5	$Ni(NO_3)_2 \cdot 6H_2O$ H-ZSM-5	Ion exchange	Light Green
Ni/MCM-41	$Ni(NO_3)_2 \cdot 6H_2O$ MCM-41	Ion exchange	Light Green
NiO-ZrO_2/SO_4^{2-}	$Ni(NO_3)_2 \cdot 6H_2O$ $ZrOCl_2 \cdot 8H_2O$ H_2SO_4 $NH_4 \cdot OH$	Co-precipitation impregnation	Brown
NiO-ZrO_2/WO_3	$Ni(NO_3)_2 \cdot 6H_2O$ $ZrOCl_2 \cdot 8H_2O$ $(NH_4)_6H_2W_{12}O_{40} \cdot XH_2O$ $NH_4 \cdot OH$	Co-precipitation impregnation	Light Green
$NiSO_4$/γ-Al_2O_3	$NiSO_4 \cdot 7H_2O$ γ-Al_2O_3	Incipient wetness impregnation	Light Green
Re_2O_7/γ-Al_2O_3	NH_4ReO_4 γ-Al_2O_3	Incipient wetness impregnation	White
NiO/γ-Al_2O_3	$Ni(NO_3)_2 \cdot 6H_2O$ γ-Al_2O_3	Incipient wetness impregnation	Black
$NiSO_4$/Al_2O_3-SiO_2	$NiSO_4 \cdot 7H_2O$ Al_2O_3-SiO_2	Incipient wetness impregnation	Light Green
$NiSO_4$-ReO_x/γ-Al_2O_3	$NiSO_4 \cdot 7H_2O$ NH_4ReO_4 γ-Al_2O_3	Incipient wetness impregnation	Light Green

The catalysts supported with metal oxides were synthesized in terms of two independent functions (dimerization and metathesis) respectively. Our focus was first on dimerization catalysts since only a few catalysts have been studied for ethylene dimerization. Two methods, a precipitation impregnation and an incipient wetness impregnation, were used to synthesize catalysts for the dimerization reaction. In the former method, $Zr(OH)_2$-$Ni(OH)_2$ was prepared by co-precipitation of a mixed aqueous

solution of zicrominum oxychloride and nickel nitrate at room temperature. In order to obtain a maximum precipitation, the pH value of the solution was adjusted to approximately eight by adding ammonia solution. In the meantime, the solution was evenly stirred. The nominal molar ratio of ZrO_2 to NiO is about three in the catalyst synthesis. The co-precipitate was filtered out, washed with distilled water and dried at room temperature. $Zr(OH)_2$-$Ni(OH)_2$ co-precipitate promoted with H_2SO_4 and WO_3 was prepared by wet impregnation of H_2SO_4 (30 ml, 0.5 M) solution and an aqueous solution of ammonium metatungstate (30 ml, 1.3 g), respectively, onto two grams of the dry powders. Catalyst precursors obtained by filtration, namely $Zr(OH)_2$-$Ni(OH)_2$/SO_4^{2-} and $Zr(OH)_2$-$Ni(OH)_2$/WO_3, were dried at 373 K and calcinated at 673 K for 2 hours. Furthermore, catalysts based on γ-Al_2O_3 and SiO_2-Al_2O_3 with different loadings of nickel salts were prepared by an incipient wetness impregnation method. All metal oxide supports were pre-treated at 673 K for 4 hours in order to remove the water and impurities before use. γ-Al_2O_3 and SiO_2-Al_2O_3 were impregnated with an aqueous solution of nickel sulfate or nickel nitrate followed by drying over night at 378 K and calcination in air at 673 K for 2 hours.

Table 3.2: Catalyst naming and abbreviation.

Catalyst	Abbreviation
8wt%-$NiSO_4$/1wt%-ReO_x/γ-Al_2O_3	8-Ni-1-Re
8wt%-$NiSO_4$/3wt%-ReO_x/γ-Al_2O_3	8-Ni-3-Re
8wt%-$NiSO_4$/5wt%-ReO_x/γ-Al_2O_3	8-Ni-5-Re
8wt%-$NiSO_4$/8wt%-ReO_x/γ-Al_2O_3	8-Ni-8-Re
8wt%-$NiSO_4$/11wt%-ReO_x/γ-Al_2O_3	8-Ni-11-Re
8wt%-ReO_x/8wt%-$NiSO_4$/γ-Al_2O_3	8-Re-8-Ni
3wt%-ReO_x/8wt%-$NiSO_4$/γ-Al_2O_3	3-Re-8-Ni
5wt%-$NiSO_4$/γ-Al_2O_3	5-NiS
8wt%-$NiSO_4$/γ-Al_2O_3	8-NiS
11wt%-$NiSO_4$/γ-Al_2O_3	11-NiS
8wt%-$NiSO_4$/Al_2O_3-SiO_2	8-NiS (A)
8wt%-$(NH_4)_2SO_4$/γ-Al_2O_3	8-S
10wt%-Re_2O_7/γ-Al_2O_3	10-Re
8wt%-NiO/γ-Al_2O_3	8-NiO

Catalytic performances of these prepared dimerization catalysts were determined in a continuous flow reactor and were compared with one another under their optimum

experimental conditions. Among these catalysts, the $NiSO_4/Al_2O_3$ catalyst could achieve a high yield of propylene. Thus this catalyst was considered in the subsequent catalyst synthesis for the ETP reaction. However, $NiO\text{-}ZrO_2/SO_4^{2-}$, $NiO\text{-}ZrO_2/WO_3$ and $NiSO_4/SiO_2\text{-}Al_2O_3$ were abandoned due to their inactivity or low activity during ethylene dimerization.

On the other hand, Re_2O_7/γ-Al_2O_3 is a well-known metathesis catalyst[1-6]. The Re_2O_7/γ-Al_2O_3 catalyst was prepared by impregnation of an aqueous solution of ammonia perrhenate onto γ-Al_2O_3 followed by drying over night at 378K and calcination in air at 673K for 2 hours.

Since both the dimerization and metathesis catalysts were obtained, a dual functional catalyst was prepared by co-impregnation of nickel sulfate and rhenium oxide on the same support material. γ-Al_2O_3 was impregnated with aqueous solutions of $NiSO_4 \bullet 7H_2O$ and $[NH_4][ReO_4]$ in different impregnation order, each impregnation following the same treatment procedures of the incipient wetness method. In addition, γ-Al_2O_3 modified with sulfate ions was also prepared by dry impregnation of γ-Al_2O_3 with an ammonium sulfate solution, in order to understand the role of the sulfate ion in the following characterization studies. Table 3.2 shows a series of prepared catalysts supported with metal oxides. The catalyst naming indicates the different impregnation order and weight percentage of active components contained in the catalyst. For instance, 8-Ni-8-Re means that the $NiSO_4 \bullet 7H_2O$ solution was impregnated first followed by $[NH_4][ReO_4]$ solution with 8wt% Ni corresponding to the $NiSO_4$/γ-Al_2O_3 part and 8wt% ReO_x corresponding to the whole catalyst, respectively and vice versa. The detailed information of the chemicals for the catalyst synthesis are given in Appendix A. All the chemicals were used as received. Catalyst synthesis procedures are given in Appendix B.

3.2 Catalytic Testing in a Continuous Flow Reactor

As shown in Figure 3.1, the test rig consists of two gas flow lines controlled by mass flow controllers, one fix-bed reactor vertically placed with a bypass to a ventilation hood and a gas chromatograph connected to an outlet of the gas line for online measurements. Three heating zones were designed by heating the gas lines and the reactor with heating bands wound around, two for preheating the gases before reaching

the reactor to 473 K and one for controlling the reactor temperature in the range from 293 K to 873 K. The length and inner diameter of the reactor was 60 cm and 1.27 cm, respectively. The reaction temperature was measured by a thermocouple positioned inside the catalyst bed. The catalyst bed was made up of 2 grams of catalyst located in the middle of the reactor and supported by silica-carbide particles and quartz wool. A three-way valve was used to switch the gas flow between the ventilation and the GC.

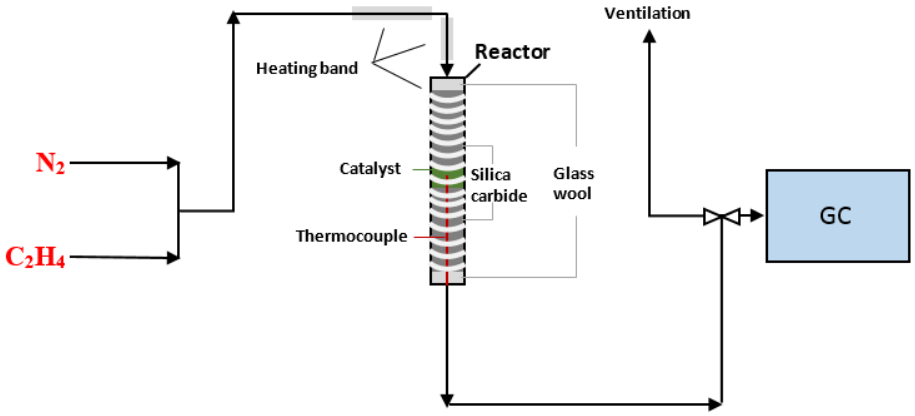

Figure 3.1 Sketch of the continuous reactor.

Catalyst testing in a continuous flow reactor was carried out at atmospheric pressure and at 323 K. The catalyst was heated to 773 K under nitrogen flow and kept at that temperature for 2 hours in order to remove water and impurities. Subsequently, the catalyst was cooled down with nitrogen to the reaction temperature. Nitrogen as a dilute gas then mixed with pure ethylene in a ratio of 3:2 for the reaction. Catalytic performance was determined at different reaction temperatures and gas hourly space velocities (GHSV) in order to optimize catalytic performance.

3.2.1 Gas Chromatography

Gas chromatography (GC) is a commonly used analytical technique for analyzing compounds that can be vaporized without decomposition[7]. Separating components is based on an interaction between a mobile phase and a stationary phase. The mobile phase is composed of an inert gas (He, N_2 or Ar) carrying a vaporized sample. With movements of the mobile phase, the components can be separated inside the column due to their specific affinities with the stationary phase resulting in different retention

times. The stationary phase is packed inside a large diameter column or coated in an inner wall of a capillary column.

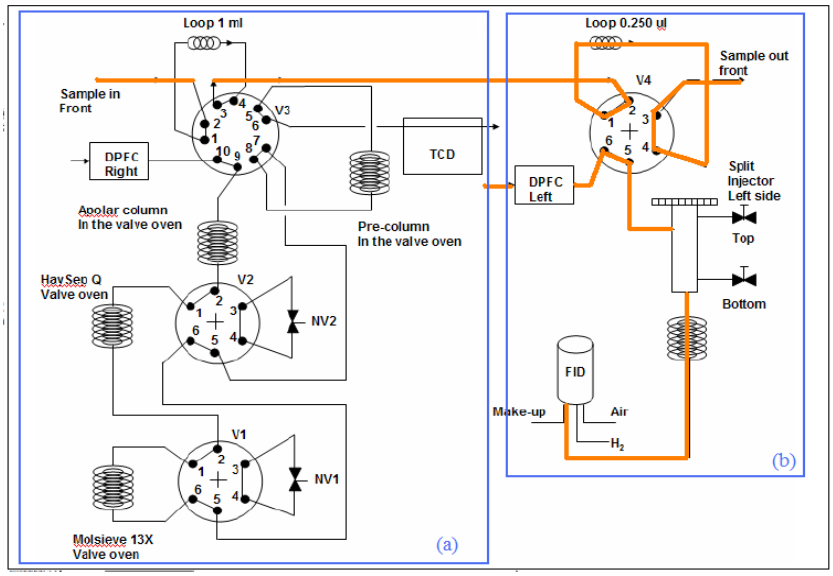

Figure 3.2: Configuration of the Trace GC Ultra. (a) inter gases and hydrocarbons channel, (b) extended hydrocarbons channel.

Trace GC Ultra was the instrument used to analyze the effluent gas online, which includes two channels equipped with one thermal conductivity detector (TCD) and one flame ionization detector (FID) detector, respectively (illustrated in Figure 3.2). Two channels enable detection of various organic and inorganic compounds at the same time by a single injection. However, only channel (b), marked by an orange line in Figure 3.2, was selected to be used in the catalytic test since this channel was able to analyze all the components in our catalyst testing. FID is very sensitive to hydrocarbons. Moreover, more intensive measurements could be provided in this channel due to a short over run-time in comparison of that in the channel (a). An Agilent Technologies J&W HP-PLOT-Al/KCl (50m × 0.32mm × 8.00µm) column was used in this GC, and has an excellent performance for separating light hydrocarbons. GC operating conditions are listed below:

- Temperature program: start at 373 K for 0 min; temperature ramp: 10K/min to 453 K; final hold time at 453 K for 0 min;
- Carrier gas (N_2): 1.5ml/min;
- Spit ratio: 200;
- Over run-time: 8 minutes.

3.2.2 Analysis Method

Channel (b) was equipped with a gas sampling valve to ensure a constant amount of gas (0.250µl) injected to the GC each time. An external standard method was applied for gas calibrations of the GC. Different ratios of pure ethylene gas and nitrogen were achieved by changing flow rates of ethylene and nitrogen while keeping the total flow rate unchanged. The mixing gas was measured three times at each ratio. Two calibration curves of ethylene gas were obtained at low and medial concentrations with respect to average peak areas over three parallel measurements, shown in Figure 3.3. Calibration of other desired gas products in the ETP reaction were determined by the same method but with a calibration gas. The calibration gas, purchased from Yara Praxair, consisted of ethylene (30%), propylene (30%), Trans-2-butene (13%), 1-butene (13%) and Cis-2-butene (13%). In this thesis, Trans-2-butene and Cis-2-butene will be abbreviated to T-2-butene and C-2-butene, respectively. The ethylene gas line was used as a calibration gas line and the whole gas line was heated by heating tapes to 313K during the calibration, in order to avoid gas condensation during gas feeding. The assumption was made that the composition of the calibration gas was steady in the gas line without any influence of the temperature and pressure. The calibration gas was also mixed with nitrogen at different ratios and the concentration of ethylene gas in the mixture was calculated based on the calibration curves of ethylene. Consequently, as the concentration of ethylene was known, the concentrations of other gases were easily calculated according to their composition in the calibration gas. Linear calibration curves of propylene, T-2-butene, 1-butene and C-2-butene were obtained and shown in Figure 3.4. All raw data of obtained peak areas of the gases from the GC are given in Appendix C. The conversion of ethylene and selectivity of products were calculated as:

$$\text{ethylene conversion} = \frac{\text{ethylene in} - \text{ethylene out}}{\text{ethylene in}} \cdot 100\% \tag{3.1}$$

$$\text{Selectivity} = \frac{\text{desired products (propylene, 1-butene and 2-butene)}}{\text{total gas products}} \cdot 100\% \tag{3.2}$$

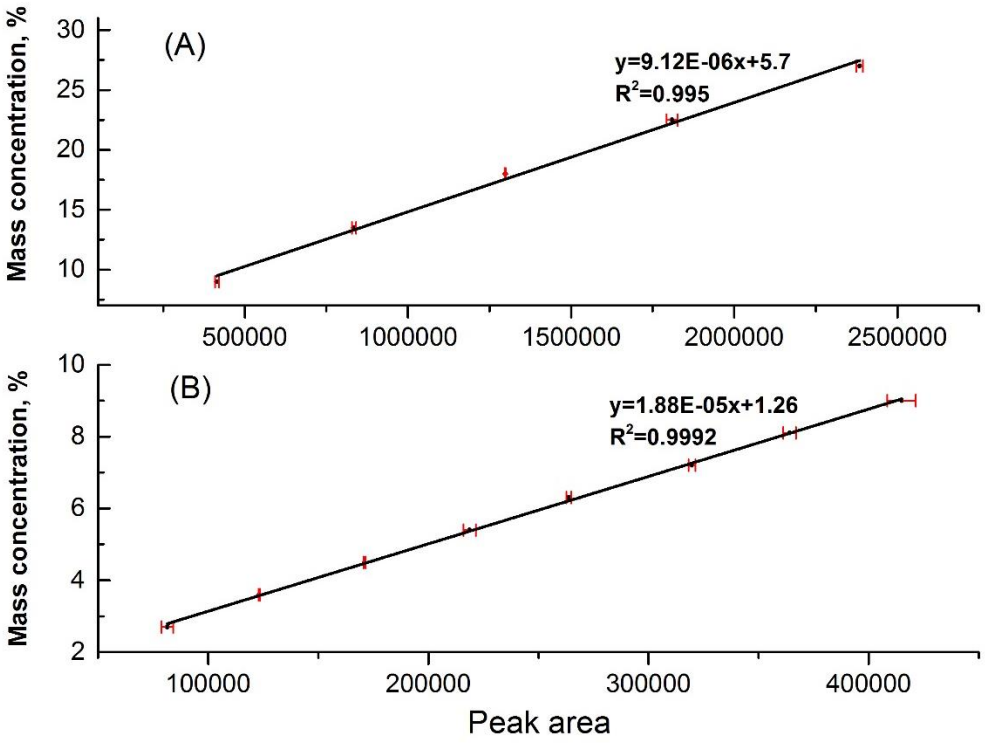

Figure 3.3: Calibration curve of ethylene gas at low and medial concentrations.

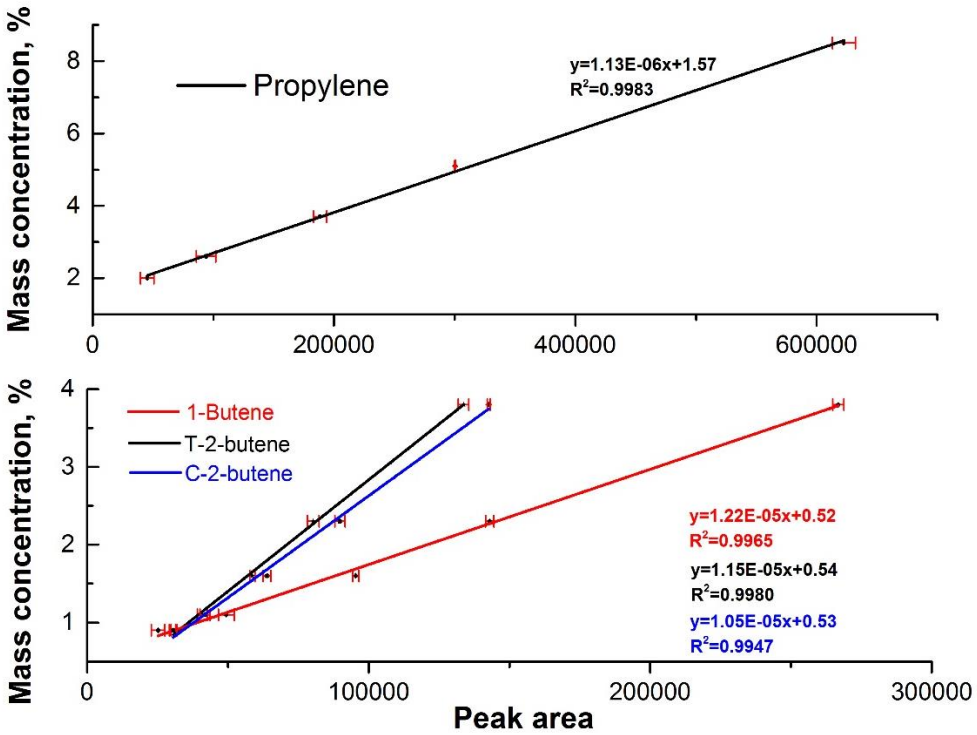

Figure 3.4: Calibration curves of propylene, 1-butene, T-2-butene and C-2-butene.

3.3 Catalytic Testing in a Pulse Reactor

The pulse reactor test rig consisted of twelve mass flow controllers installed on two separated panels, which was designed for multi-gas feed. An automated setup equipped with 4-way and 6-way VICI VALCO valves was used. The 4-way valve was connected to the loop in the 6-way valve. The 6-way valve was equipped with a loop (0.25 ml) and used to send discrete pulses of gas, with a continuous stream of He (10 ml/min), to the reactor. As shown in Figure 3.5, by switching the 6-way valve to an injection mode, the inert gas (He) carried ethylene from the loop to the reactor. By this process, one pulse was sent to the reactor. Interval time of pulses could be set by a computer program and then a known number of pulses could be automatically sent to the reactor with the same interval time. In our case, tests in the pulse reactor were only performed on the 8-Ni-8-Re and 8-Re-8-Ni due to their top performances on the yield of propylene in the previous continuous reactor tests. The catalytic test was conducted in a tubular quartz reactor (i.d. 8 mm) at 323 K and atmospheric pressure. The catalyst (0.4 g) was diluted with γ-Al_2O_3 (0.1 g) and activated under inert gas (He) at 773 K for 2 hours before use. γ-Al_2O_3 has been tested in the continuous flow reactor and showed no activity for both ethylene dimerization and ETP reaction. After the catalyst was cooled down to the reaction temperature (323 K), ethylene pulses were sent to the reactor every 2 minutes.

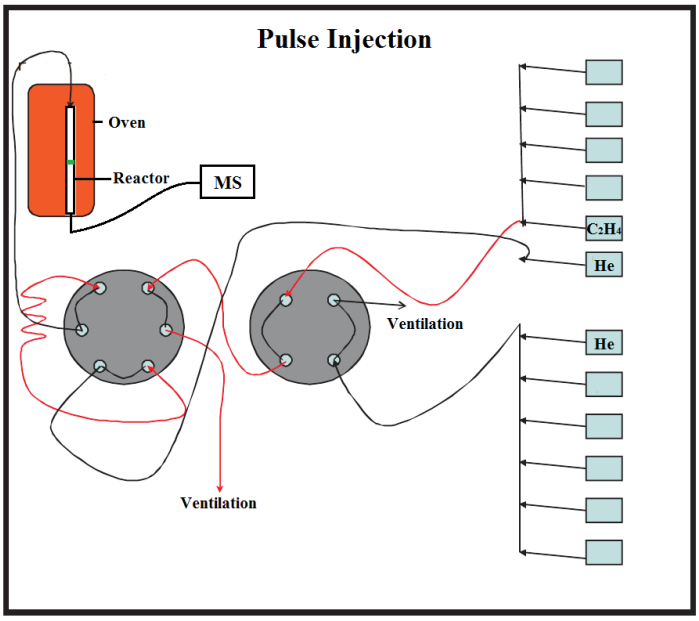

Figure 3.5: Sketch of the pulse reactor in an injection mode.

3.3.1 Online Mass Spectrometer and Analysis Method

Mass spectrometry is one of the most popular analysis techniques. Substances of a sample can be recognized according to their different mass-to-charge ratios. Atoms or molecules in the sample are bombarded with a stream of electrons generating some positive ions, and some of the collisions are energetic enough to break large molecules into small-ionized fragments. Ionized substances are accelerated in the acceleration chamber in order to obtain the same kinetic energy. Subsequently, the ions are deflected in a magnetic field, dependent on their mass and charge, and pass through a detector to be amplified and recorded.

Product was monitored continuously by an online mass spectrometer (Pfeiffer Omnistar) equipped with a quadruple mass spectrometer. The online MS (Pfeiffer Omnistar) analysis system includes inlet system, PrismaPlus mass spectrometer, a dry diaphragm vacuum pump and Hipace turbopump. Calibration values for quantification of C_2H_4, C_3H_6 and C_4H_8 were found by sending known pulses of ethylene, propylene and butene to an empty reactor preheated to 323 K and integrating the area under the peaks of m/z 28, 42 and 56, respectively. The conversion and selectivity were calculated:

$$\text{ethylene conversion} = \frac{\text{ethylene in} - \text{ethylene out}}{\text{ethylene in}} \cdot 100\% \qquad (3.3)$$

$$\text{Selectivity of propylene} = \frac{\text{propylene out}}{\text{ethylene in} - \text{ethylene out}} \cdot \frac{3}{2} \cdot 100\% \qquad (3.4)$$

3.4 Results and Discussion

Initial experiments were run to establish the dimerization function of the Ni based metal oxide (Al_2O_3 and Al_2O_3-SiO_2) catalysts. It has been reported that Ni based metal oxide catalysts favor a low reaction temperature and a low pressure for the ethylene dimerization reaction. These catalysts could exhibit a high activity at room temperature under atmospheric pressure[8-10]. In the continuous flow reactor test, experiments were carried out under atmospheric pressure. However, considering the design of the reactor, the tests at room temperature would be inappropriate due to a possible condensation of desired products (1-butene and 2-butene) in the reactor and thus the reaction

temperature was set to 323 K. The flow rate ratio of ethylene to nitrogen was kept at 2:3 and GHSV was set to 2682 h^{-1} at first. Abbreviations (see Table 3.2) of the catalysts are used in the thesis. The two NiO-ZrO_2 catalysts with different promoters and the 8-NiO catalyst exhibited no ethylene dimerization activity. The ethylene concentration was unchanged and no product was detected in the effluent by GC analysis during the duration of the catalytic test. Fortunately, $NiSO_4$ based metal oxide catalysts showed ethylene dimerization activity and their performances are demonstrated in Figure 3.6. Of the four catalysts, 8-NiS is the most efficient in the conversion of ethylene, although all catalysts deactivated quite fast as the reaction progressed. As shown in Figure 3.6, the catalyst with a higher $NiSO_4$ loading performs a higher conversion of ethylene. This indicates the amount of $NiSO_4$ on γ-Al_2O_3 relates to the number of active sites for the dimerization reaction. Figure 3.6 (B) shows the concentration ratio of 2-butene (T-2-butene and C-2-butene) to 1-butene in the products during the reaction. In fact, only butene was observed as product in the GC analysis. Long chain oligomers such as hexene and octene were condensed as by-products in the reactor due to the low reaction temperature. It was suggested by Sohn that the active site of the $NiSO_4$/γ-Al_2O_3 catalyst, for the ethylene dimerization reaction, consisted of the low valent Ni and a surface acidity [11]. Catalyst deactivation may result in a decrease of acidity on the active sites, which influences isomerization of 1-butene to 2-butene leading to a decrease of the 2-butene/1-butene ratio with the reaction as shown in Figure 3.6 (B).

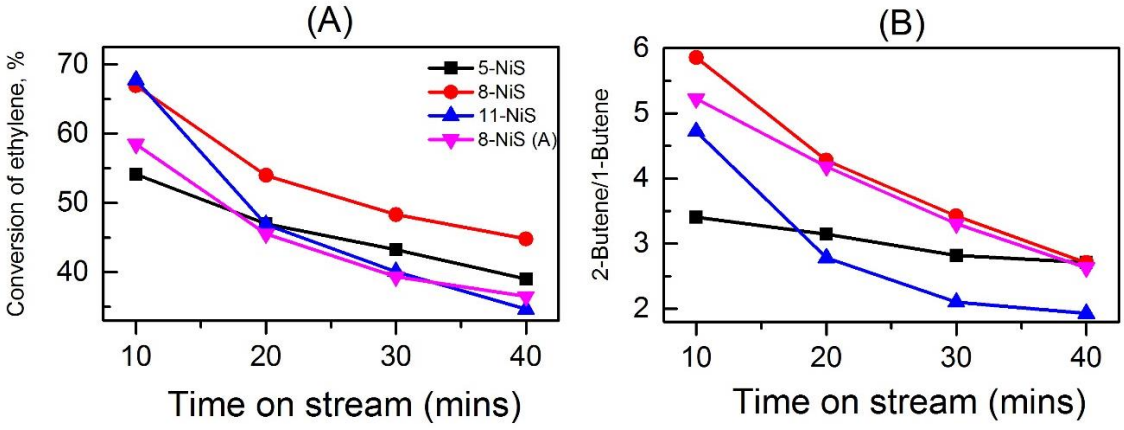

Figure 3.6: Catalytic performance in a continuous flow test on a series of $NiSO_4$ based catalysts (323K, C_2H_4:N_2 2:3, GHSV: 2682h^{-1}).

In the following experiments, the 8-NiS catalysts were tested under different GHSV (2104 and 3000 h^{-1}) while the reaction temperature and the flow rate ratio of ethylene to nitrogen were kept as before. Adjusting GHSV was expected to change the 2-butene/1-butene ratio. A high 2-butene/1-butene ratio is important for propylene yield since only 2-butene participates in the metathesis reaction in the second step of the ETP reaction. However, the ratio did not show evident change in the test of the 8-NiS catalyst under different GHSV. Therefore, GHSV was kept at 2682 h^{-1} in the subsequent tests.

Based on recommendations in the literature, the 10-Re catalyst was prepared for the metathesis reaction[1, 12-14]. This catalyst was then mixed with 8-NiS in both physical and chemical (co-impregnation) ways for further ETP tests. In Table 3.3, the prepared 10-Re catalyst shows no ethylene dimerization activity in the continuous flow reactor test. Compared with the physical mixture, the chemical mixture method (co-impregnation) demonstrates higher activity and selectivity. The Ni-H-ZSM-5 catalyst has a rather high conversion of ethylene. However, the selectivity of propylene is quite low and many by-products were detected by GC analysis. The propylene yield on this catalyst is much lower than that on the Ni-Re catalysts in the catalytic tests under the same dilution ratio, pressure and GHSV. Moreover, Ni-MCM-41 shows a competitive propylene yield in comparison to the yield of the Ni-Re catalysts whereas the reaction on this catalyst occurs at a high temperature.

Table 3.3: Catalytic performance in a continuous flow reactor[a].

Catalyst	Reactant	Reaction temperature	Conversion of ethylene	Selectivity of propylene
10-Re	C_2H_4	323K	-	-
Physical mixture[b]	C_2H_4	323K	48%	30%
8-Ni-10-Re	C_2H_4	323K	60%	43%
Ni-H-ZSM-5	C_2H_4	723K	80%	Low[c]
Ni-MCM-41	C_2H_4	723K	73%	17%

[a]All results were collected after 10mins on-stream (atmospheric pressure, C_2H_4:N_2 3:2, GHSV: 2682h^{-1}).

[b]Two catalyst 8-NiS and 10-Re mixed 1:1 physically.

[c]Selectivity of propylene could not be calculated since the peak areas of propylene from the GC analysis were rather low and out of the applicable range of the propylene calibration curve.

Figure 3.7 shows the catalytic performance of a series of catalysts with different loadings of ReO_x and different impregnation orders in the continuous flow reactor tests.

The catalysts with the same loading of $NiSO_4$ (8wt%) exhibit similar ethylene conversions (Figure 3.7(A)) except the one with the highest loading of ReO_x. This implies a high loading of ReO_x on the catalysts may cover or block some active sites of $NiSO_4$ leading to a decrease in ethylene conversion. As shown in Figure 3.7(B), propylene selectivity jumps from 26% to 45% with increasing ReO_x on the catalyst. Moreover, it can be seen in Figure 3.7(C and D) that the selectivity of 2-butene drops while the selectivity of 1-butene rises with the reaction on the Ni-Re catalysts. In addition, the conversion of ethylene and the selectivity of butene on Ni-Re catalysts demonstrates similar trends to that on $NiSO_4$/γ-Al_2O_3 catalysts. All these phenomena suggest that the ethylene dimerization reaction is mainly attributed to metallic active sites of $NiSO_4$ and the metathesis reaction is most likely due to ReO_x. The reaction mechanism may consist of two steps, dimerization of ethylene as the first step followed by metathesis of the produced 2-butene and ethylene as the second step.

The results show that the 8-Ni-8-Re and 8-Re-8-Ni catalysts perform better in the production of propylene than other catalysts. It seems the catalyst with the low ReO_x loading could not provide enough active sites for the metathesis reaction, but high loading may limit the number of active sites for the dimerization reaction. Catalyst deactivation causes the change of selectivity of 1-butene and 2-butene, whereas the selectivity of propylene keeps almost constant during the reaction time. This reveals that the two metal components ($NiSO_4$ and ReO_x) seem to work to a large extent independent of each other and deactivation of the catalyst is mainly due to the dimerization step.

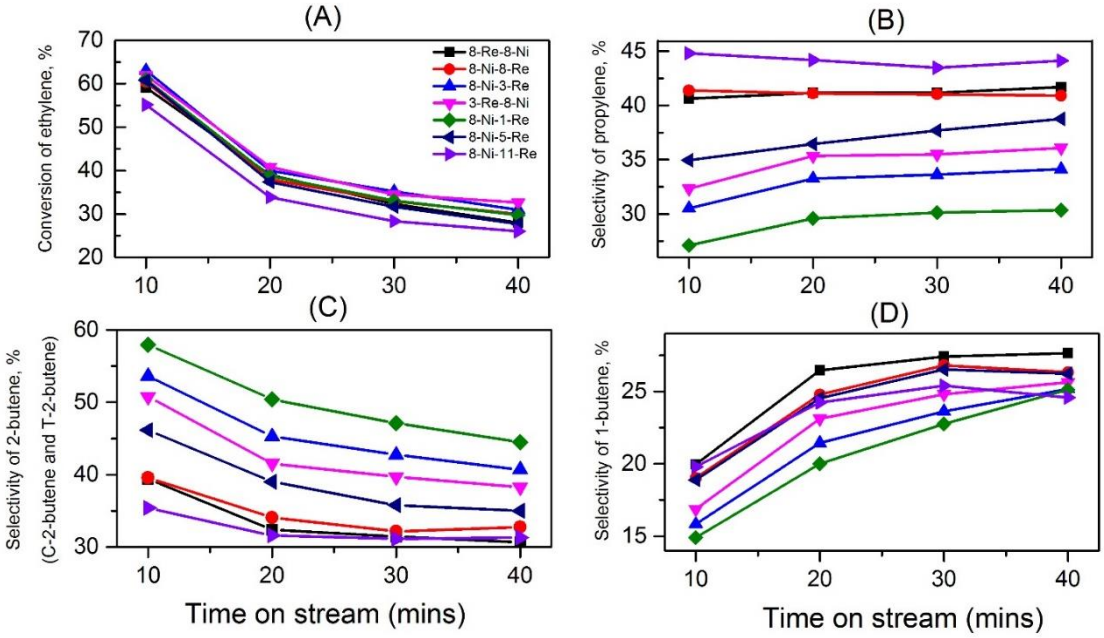

Figure 3.7: Catalytic performance in a continuous flow test on a series of Ni-Re catalysts (323K, C_2H_4:N_2 2:3, GHSV: 2682h^{-1}).

Pulse reactor tests were carried out in order to study the activation period of the catalysts. As shown in Figure 3.8, the conversion of the catalysts drops fast from 60% to 30% within 30 pulses of ethylene followed by leveling out to a constant value. This could be interpreted in analogy to the proposed mechanism[9, 10] for ethylene dimerization on the $NiSO_4$/γ-Al_2O_3 catalyst. It could be speculated that ethylene adsorption and product desorption reach an equilibrium on the surface of the catalyst after a certain time. Furthermore, a special feature of the catalyst is high product selectivity at mild reaction conditions (323 K, 1 atm). Uneven speed of desorption could be a reason for the selectivity curve fluctuation. The differences between the pulse number at maximum conversion and selectivity indicate that the rate of desorption is much slower than the rate of adsorption. Alternatively, the two consecutive reactions (dimerization and metathesis) may work independently. It could take time for the intermediate to find the right catalytic sites for continuous reaction. Comparing two catalysts in different order, 8-Ni-8-Re demonstrates a slightly higher conversion and lower selectivity than the 8-Re-8-Ni catalyst, which could be due to the impregnation order influencing the interaction of the impregnated components with the surface of the catalyst.

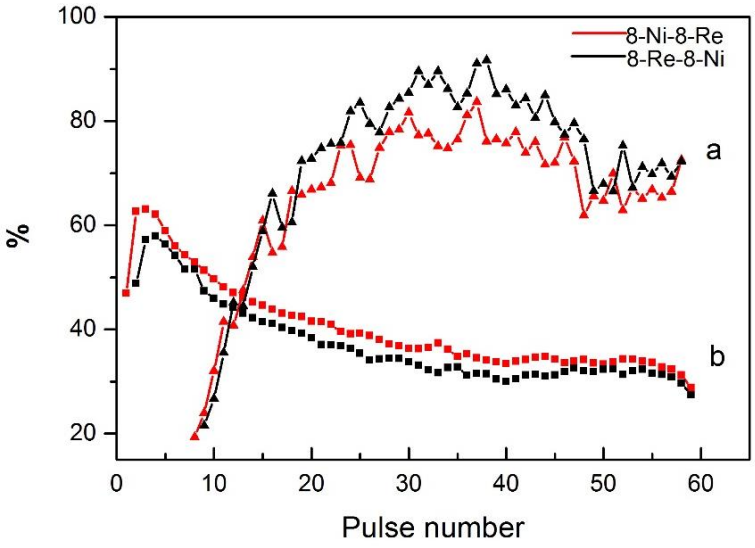

Figure 3.8: Catalytic performance in a pulse reactor test on 8-Ni-8-Re and 8-Re-8-Ni catalysts. (a) Selectivity of propylene, (b) Conversion of ethylene.

3.5 Conclusion

The bimetallic catalyst, $NiSO_4/Re_2O_7/\gamma\text{-}Al_2O_3$, catalyzes the direct conversion of ethylene to propylene at mild reaction conditions (323 K, 1 atm). It seems that the two catalyst functions work independently for dimerization and metathesis and deactivation of the catalyst is mainly due to the $NiSO_4$ driven dimerization step. The yield of the catalyst for propylene is approximately 29%, which is superior to other metal based catalysts[15, 16]. However, the present catalyst deactivates fast even under mild reaction conditions.

Reference

1. Mol, J.C., *Catal. Today*, 51 (1999) 289-299.
2. Mol, J.C., *J. Mol. Catal. A: Chem.*, 213 (2004) 39-45.
3. Sheu, F.C., Hong, C.T., Hwang, W.L., Shih, C.J., Wu, J.C., Yeh, C.T., *Catal. Lett.*, 14 (1992) 297-304.
4. Spinicci, R., Tofanari, A., *Appl. Catal.*, 14 (1985) 261-276.
5. McCoy, J.R., Farona, M.F., *J. Mol. Catal.*, 66 (1991) 51-58.
6. Xu, Y., Huang, J., Lin, Z., Guo, X., *J. Mol. Catal.*, 65 (1991) 275-285.
7. Mcnair, H.M., Miller, J. M. , *Basic Gas chromatograph, Second Edition.* John Wiley & Sons, 2009.
8. Finiels, A., Fajula, F., Hulea, V., *Catal. Sci. Technol.*, 4 (2014) 2412-2426.
9. Cai, T., Cao, D., Song, Z., Li, L., *Appl. Catal. A- Gen*, 95 (1993) L1-L7.
10. Sohn, J.R., Park, W.C., Park, S.-E., *Catal. Lett.*, 81 (2002) 259-264.
11. Sohn, J.R., Park, W.C., *Appl. Catal., A*, 239 (2003) 269-278.
12. Andreev, A., Edreva-Kardzhieva, R., Neshev, N., *Recl. Trav. Chim. Pays-Bas*, 96 (1977) 23-26.
13. El-Sawi, M., Iannibello, A., Morelli, F., Catalano, G., Intrieri, F., Giordano, G., *J. Chem. Technol. Biotechnol.*, 31 (1981) 388-394.
14. El-Sawi, M., Iannibello, A., Giordano, G., Fedele, U., Ricca, G., *J. Chem. Technol. Biotechnol.*, 32 (1982) 1049-1054.
15. Yamaguchi, T., Tanaka, Y., Tanabe, K., *J. Catal.*, 65 (1980) 442-447.
16. Taoufik, M., Le Roux, E., Thivolle-Cazat, J., Basset, J.-M., *Angew. Chem. Int. Ed.*, 46 (2007) 7202-7205.

Chapter 4

4 Characterization of Ni-Re Catalysts

A series of Ni-Re catalysts have been characterized by BET method, elemental analysis, thermogravimetric analysis, scanning electron microscopy and transmission electron microscopy. In this chapter, basic theories of these characterization methods as well as the corresponding instruments are described. Moreover, experimental results of the characteristics and surface structures of the catalysts are given and discussed.

4.1 BET Surface Area and Element Analysis

The BET method was proposed by Brunauer, Emmett and Taylor in 1938. The theory is an extension of the Langmuir theory and is applicable for physical multilayer adsorption of non-corrosive gases on a solid surface. The BET equation is

$$\frac{1}{V_a\left(\frac{P_0}{P}-1\right)} = \frac{C-1}{V_m C}\times\frac{P}{P_0}+\frac{1}{V_m C} \tag{4.1}$$

Where V_a is the amount of gas that is adsorbed at a standard temperature and pressure (273.15 K and the atmospheric pressure). P and P_0 are the equilibrium pressure and saturation pressure respectively of adsorbed gas. C is a dimensionless constant related to heat of gas adsorption on the sample. According to the BET equation, the gas quantity of monolayer adsorption (V_m) on the sample can be obtained when the gas quantity and the ratio of equilibrium pressure to saturation pressure of the adsorbed gas are measured at a constant temperature. Knowing monolayer adsorbed gas quantity allows calculation of the total surface area (external and internal) and specific surface area according to the equations below:

$$S_{total} = \frac{V_m N_s}{V} \tag{4.2}$$

$$S_{BET} = \frac{S_{total}}{a} \tag{4.3}$$

Where N_S is an Avogadro constant ($6.022 \cdot 10^{23}$ mol^{-1}), V is the molar volume of the gas and α is the mass of solid sample.

In the experiment, BET surface area of catalysts was determined by multipoint measurement under atmospheric pressure and at liquid nitrogen temperature (77 K) on a FlowsorbⅢ-2310 instrument. The catalysts were outgassed at 573 K before the test.

The elemental analysis was performed by Mikroanalytische Labor Pascher, An der Pulvermühle 1, 53424 Remagen, Germany.

4.2 Thermogravimetric Analysis (TGA)

TGA is a significant method of thermal analysis and has various applications in material characterizations such as thermal stability and oxidative stability. In a common catalyst test, TGA monitors the mass of a sample continuously as a function of temperature or time when the sample is heated/cooled with a controlled temperature program in a controlled atmosphere. Weight changes in a sample can be used to determine the composition of a material or its thermal stability. Weight loss of a sample may be due to decomposition, dehydration, reduction or desorption while weight gain is probably attributed to oxidation or adsorption.

Figure 4.1 shows a schematic diagram of a TGA. The core part of the TGA is the precision balance, which is used for weighing the mass of a sample loaded on a sample pan. When a furnace is lifted up, the sample pan precisely fits inside the furnace so that the sample can be heated or cooled. A sample purge gas protects and controls the sample environment.

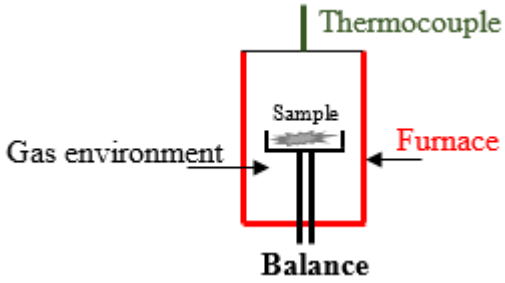

Figure 4.1: Schematic drawing of thermogravimetric analysis.

A Thermal gravimetric analysis of fresh catalysts was carried out in a Rheometric Scientific STA 1500 instrument. Around 20 mg of each sample was used and heated to 1173 K with a heating rate of 5 K/min in nitrogen flow.

4.3 Scanning Electron Microscope (SEM)

Scanning electron microscope (SEM) is widely used in studying morphology and examining compositions of a sample. SEM is a type of electron microscope. A focused beam of electrons penetrates a specimen and it interacts with atoms generating various kinds of signals as shown in Figure 4.2. Secondary electrons and backscattered electrons are the two most common signals used for producing SEM images[1]. Scattered electrons that are ejected from the outer-shell of the specimen atoms by inelastic collisions are known as secondary electrons. The secondary electrons can only escape from 5-10 nm depth of the specimen surface, since their energy is lower than 50 eV. Due to this, secondary electrons are very sensitive to the surface characteristics. Compared with secondary electrons, backscattered electrons have a higher energy and originate in the electron beam. The high-energy electrons from the primary beam interacting with specimen atoms is scattered back from the specimen, back in the same direction as they came with little energy loss. Chemical elements having a high atomic number generate more backscattered electrons than those with a low atomic number. Therefore, the heavy elements in the specimen look brighter in the image.

Figure 4.3 shows a configuration of a typical SEM. The SEM works under a vacuum, and is composed of an electron gun, two condenser lenses, an objective lens, an electron detection system and a set of deflector. The electrons from the electron gun pass through three-stage electron lenses where the primary electron beam is generated. The primary electrons scan the sample and various signals are collected in the detector.

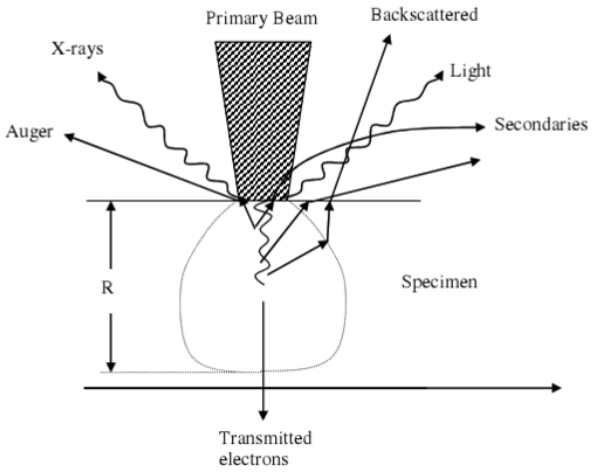

Figure 4.2: interaction volume and emitted signals from an interaction between an electron beam and a specimen[2].

Energy dispersive spectroscopy (EDS) is typically integrated in a SEM instrument for elemental analysis of the sample. X-rays, produced from the interaction between the primary beam and the specimen, can provide characteristic information of various elements. Therefore, EDS is a very effective tool for determining elements and analyzing chemical compositions of a sample.

In the SEM experiment, the SEM measurements were run using a FEI Nova^{TM} NanoSEM. Fresh catalysts, which were exposed to air after catalyst preparation, were directly used for testing without any treatment.

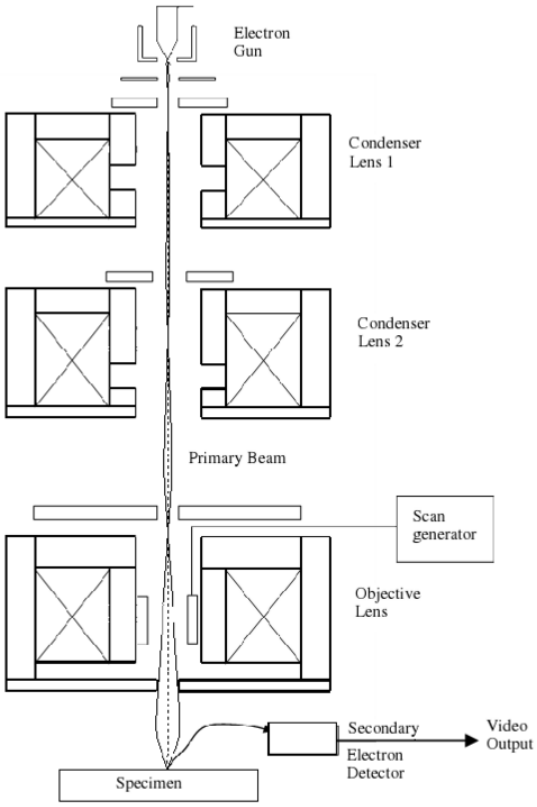

Figure 4.3: Schematic drawing of SEM[3].

4.4 Transmission Electron Microscope (TEM)

The transmission electron microscope (TEM) is another useful instrument to analyze microstructure of a sample and provide information of surface morphology. Like the optical microscope, the source of illumination is a beam of electrons with very short wavelengths, which passes through and illuminates a very thin specimen so as to create an image of it. However, TEM has more advantages. The maximum resolution of an optical microscope has been limited by the wavelength of the light whereas the short wavelength of electrons can enhance the resolution largely[2]. Moreover, contrast is caused not only by the attenuation of the electrons due to different densities and thicknesses on the specimen, but also by diffraction and interference. This allows the analysis of crystal structures and lattice imperfection on an atomic scale. As shown in Figure 4.4, the TEM consists of three main systems. a) The illumination system is above the sample aperture, where a high-voltage electron beam produced from the electron gun transfers to the specimen. b) Objective lens is responsible for magnifying the

images, which is the heart of the TEM. c) The TEM imaging system includes the intermediate lens and projector lens that are below the objective lens.

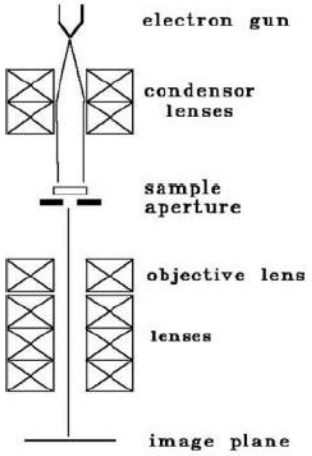

Figure 4.4: Schematic drawing of a TEM[3].

High resolution electron microscopy (HRTEM) was carried out by a Jeol 3010-UHR electron microscope operating at 300 kV equipped with a LaB6 filament and with an Oxford Inca Energy TEM 300 EDS X-rays analyzer by Oxford Link. The powder samples were grinded in an agate mortar and deposited on a copper grid covered with a lacey carbon film. The activated samples were obtained by heating the fresh samples at 673 K for 2 hour under vacuum.

4.5 Results and Discussion

The TGA analysis of the fresh catalysts is shown in Figure 4.5. The catalysts were stored in small vials and exposed to air after preparation, so the $NiSO_4$ and ReO_x on the catalysts were in a hydrated state. The weight loss of γ-Al_2O_3 (see Figure 4.5a) at 373-473 K is attributed to the loss of physisorbed water and surface hydroxyl groups. The TG curve of 8-NiS (see Figure 4.5b) shows two clear areas of weight loss, one below 673 K and the other one above 1003 K. M. Maneva et al. reported that thermal dehydration of $NiSO_4 \cdot 7H_2O$ to monohydrate $NiSO_4 \cdot H_2O$ occurs stepwise at a wide temperature range from 353 to 753 K[4]. The last coordinated water molecule is evolved at around 623 K and the anhydrous nickel sulfate is stable within a broad temperature range[4]. From the TG-curve of $NiSO_4 \cdot 7H_2O$, they also found a distinct weight loss at the temperature range of 1013-1173 K caused by decomposition of anhydrous nickel sulfate to nickel oxide[4].

Considering our case, the weight loss of the catalyst in the first region (below 673 K) is mainly due to the evolution of water molecules from the hydrated nickel sulfate beside the water loss from γ-Al_2O_3. The weight loss at above 1003 K could result from decomposition of anhydrous nickel sulfate. The 8-Ni-8-Re curve shows a similar trend as the curve of 8-NiS. Beside the reasons mentioned above, dehydration of the hydrated rhenium oxide contributes to the weight loss of 8-Ni-8-Re at around 473 K as well[5]. Analysis information indicates that the catalyst is stable up approximately 950 K and the thermal stability of the 8-Ni-8-Re catalyst is dominated by the decomposition temperature of anhydrous nickel sulfate.

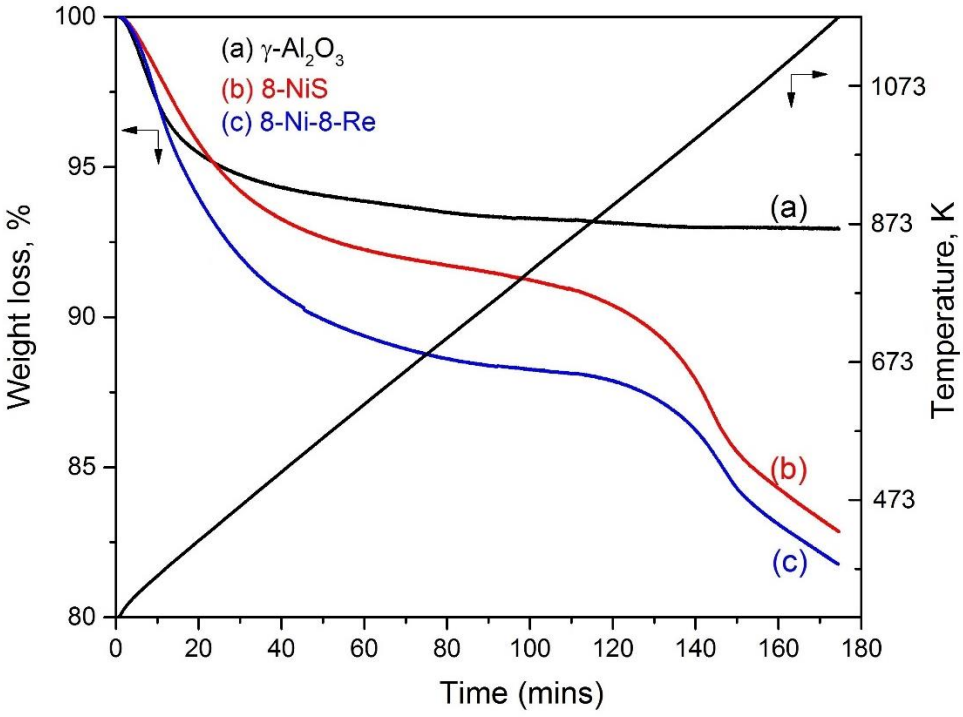

Figure 4.5: TGA analysis of fresh catalysts.

The specific surface area of the catalysts and γ-Al_2O_3 (see Table 4.1) indicates that pore blockage or sintering may have occurred during the catalyst preparation procedure. Moreover, elemental analysis results (see Table 4.1) were re-calculated to mole percentages of Ni, Re and S to γ-Al_2O_3, in order to see if material loss occurred during the synthesis procedures. The roughly equal mole amount of Ni and S on the catalyst reveals that loss of material due to decomposition of $NiSO_4$ is slight in the calcination at 773 K. When preparing catalysts, operating error is existent because the weighing weight and the analysis weight of Ni and Re in the catalysts differ slightly.

Table 4.1: BET surface area and elemental analysis for a series of Ni-Re catalysts.*

Catalyst	Surface area [m^2/g]	Ni/γ-Al_2O_3 (mol %)	Re/γ-Al_2O_3 (mol %)	S/γ-Al_2O_3 (mol %)	Ni/SO_4^{2-} (mol %)	Coke/Catalyst (Weight %)
γ-Al_2O_3	178	-	-	-	-	-
8-NiS	130	13	-	-	-	-
10-Re	132	-	4.2	-	-	-
8-Ni-1-Re	121	15	0.5	17	0.88	-
8-Ni-3-Re	121	14	1.4	14	1	-
8-Ni-5-Re	125	13	2.5	14	0.93	-
8-Ni-8-Re	127	13	3.8	12	1.08	-
8-Ni-11-Re	114	12	5.5	13	0.92	-
3-Re-8-Ni	123	16	1.7	17	0.94	-
8-Re-8-Ni	128	12	4.2	14	0.85	-
Deactivated 8-Ni-8-Re	-	-	-	-	-	2.43
Deactivated 8-Re-8-Ni	-	-	-	-	-	2.39

* The mole percentage of Ni, Re and S was calculated based on the mole number for each of components in the catalysts.

Coke formation is a common reason of deactivation of ethylene oligomerization catalysts. In our case, deactivation of the Ni-Re catalysts might have been similarly caused despite the low experiment temperature. The catalyst deactivates rather quickly, possibly through olefin adsorption on the catalyst surface leading to subsequent coke formation blocking the active sites. To further verify our speculation, the amount of coke deposited on the used catalysts was determined by elemental analysis. As shown in Table 4.1, the weight percentage of coke in the used 8-Ni-8-Re and 8-Re-8-Ni catalysts were 2.43 wt% and 2.39 wt% respectively. Therefore, the large amount of coke may be the reason of the fast deactivation of the catalysts. One should also take into account possible catalyst surface acidity due to the presence of sulfate anions.

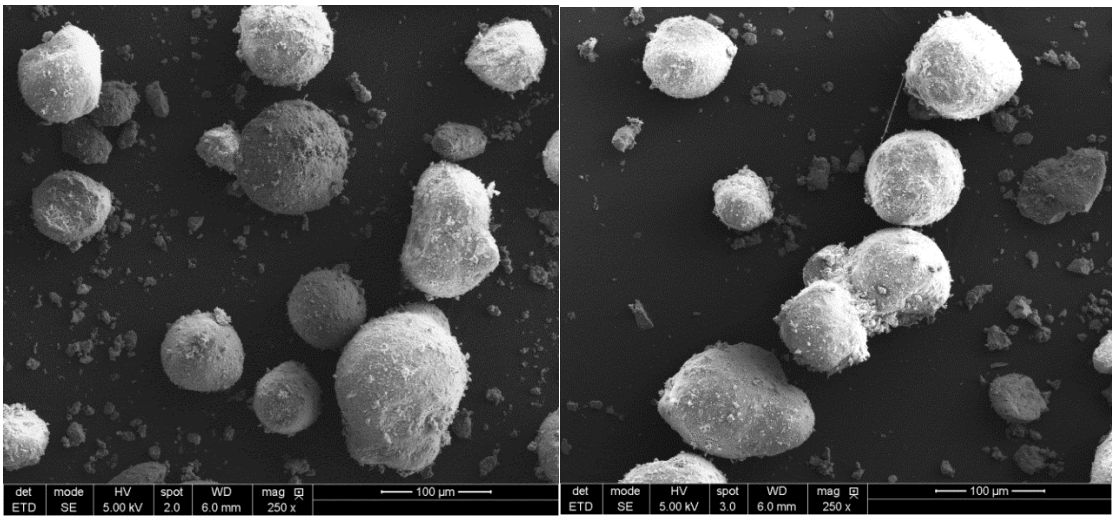

Figure 4.6: Scanning electron micrographs for different catalysts by SEM. 8-Ni-8-Re (left), 8-Re-8-Ni (right).

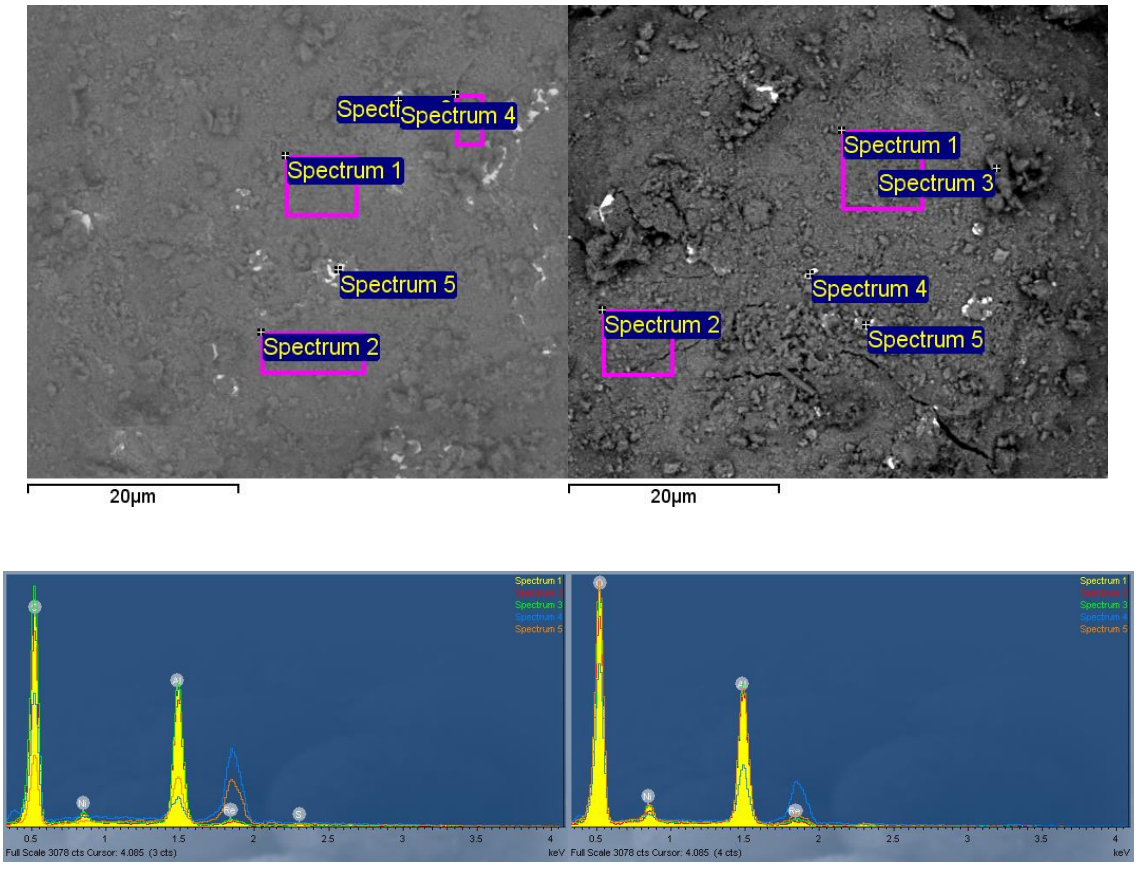

Figure 4.7: SEM backscattered images and element distributions of different catalysts. 8-Ni-8-Re (left), 8-Re-8-Ni (right).

From the SEM micrographs in Figure 4.6 it can be clearly seen that the shape of the catalyst particles are round or oval and catalyst particle sizes are approximately 50-150

μm. Particle size distribution of 8-Ni-8-Re observed by SEM micrographs seems to be more homogeneous than 8-Re-8-Ni.

In Figure 4.7, the bright spots of the backscattered images indicate Re rich particles. Five spots were randomly selected from each of the catalysts and used for EDS analysis. As expected, the brighter spots were Re enriched catalyst particles. Both catalyst particles reveal heterogeneous Ni and Re distributions on their surface, but the Ni distribution seems more homogeneous than the Re distribution. Low solubility of the aqueous solution of ammonium perrhenate may be a possible reason for the heterogeneous distribution of Re. Comparing the element distribution of two catalyst particles, the first impregnated component always seems to have a more even distribution than the last one.

In order to obtain detailed morphological information for $NiSO_4$ and ReO_x on the catalyst, HRTEM was performed. A series of catalysts under ambient conditions were measured by HRTEM. The TEM image of 8-NiS (see Figure 4.8 (b)) demonstrates a good dispersion of $NiSO_4$ on the γ-Al_2O_3 since there is no observation of agglomerates and clusters on 8-Ni. In Figure 4.8 (c), most of the ReO_4^- is isolated and well dispersed on the alumina, but a small number of clusters (<1nm) are observed on 10-Re. In fact, many publications have concluded that due to its low melting temperature ReO_x is molecularly dispersed on alumina after calcinating the catalyst at a high temperature (673-837K)as[5-7]. The material loss is little during calcination because of an interaction between ReO_x and surface hydroxyl groups on alumina. Okal and co-workers have studied the formation of small clusters on oxidized Re/γ-Al_2O_3 by HRTEM[8, 9]. They proposed that the small clusters could be ReO_4^- aggregates interacting with special sites on γ-Al_2O_3 or Re clusters formed inside the electron microscopy due to an influence of the electron beam. In analogy to our case, the latter can be excluded since the samples are quite stable under the electron beam without any formation of new agglomerates. It is no surprise that the small clusters are also observed on Ni-Re catalysts and are increased with a higher loading of ReO_x (see Figure 4.8(e)). The dispersion of $NiSO_4$ and ReO_x seems generally not to be impacted by a different impregnation order in the catalyst synthesis, although the image of 8-Ni-8-Re (see Figure 4.8 (f)) shows somewhat less clusters than

that of 8-Re-8-Ni (Figure 4.8 (d)). Most of the isolated $NiSO_4$ and ReO_x co-exist on γ-Al_2O_3 without modification of each other.

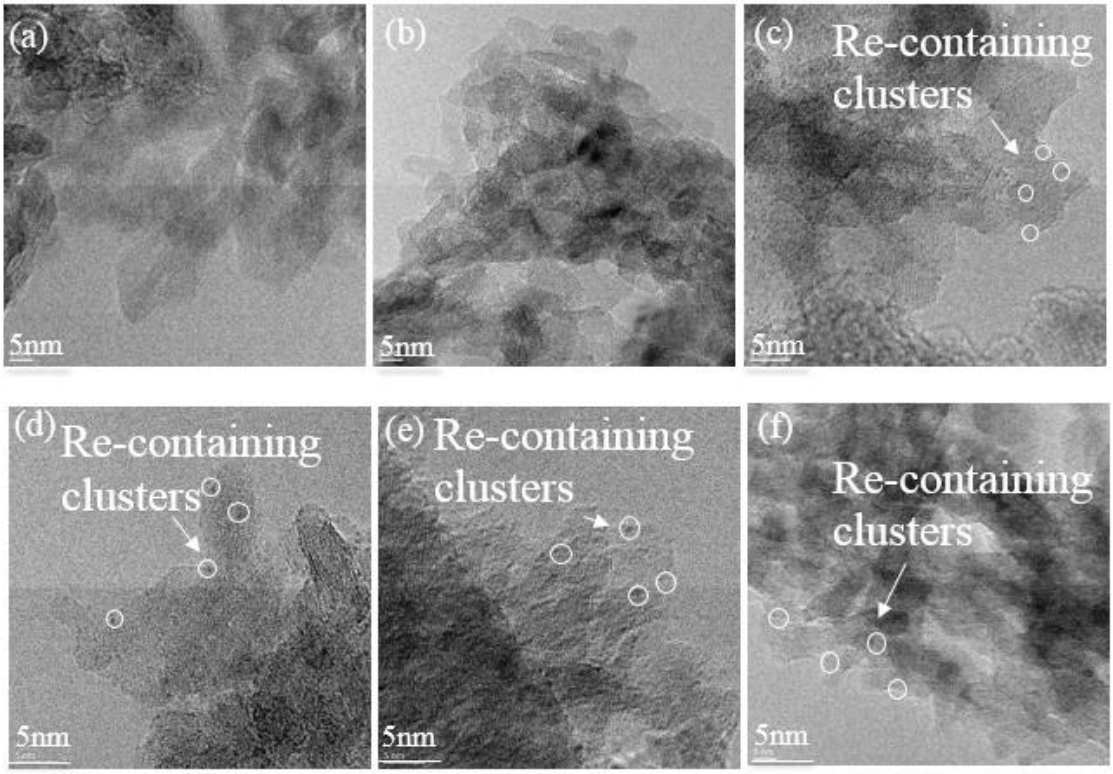

Figure 4.8: HRTEM images of (a) pure γ-Al_2O_3, (b) 8-NiS, (c) 10-Re, (d) 8-Re-8-Ni, (e) 8-Ni-11-Re and (f) 8-Ni-8-Re under ambient conditions.

The activated samples were also examined by HRTEM. The catalysts were treated at 673K under vacuum for 2 hours and were cooled down to room temperature avoiding air contact before test. The catalysts exhibited similar morphology to the catalysts under ambient conditions, but the size of the Re containing clusters varied slightly. As shown in Figure 4.9, small agglomerations of the particles with sizes around 0.5-0.75 nm are formed during the catalyst activation, possibly due to changes in the surface hydroxyl groups and water evaporation.

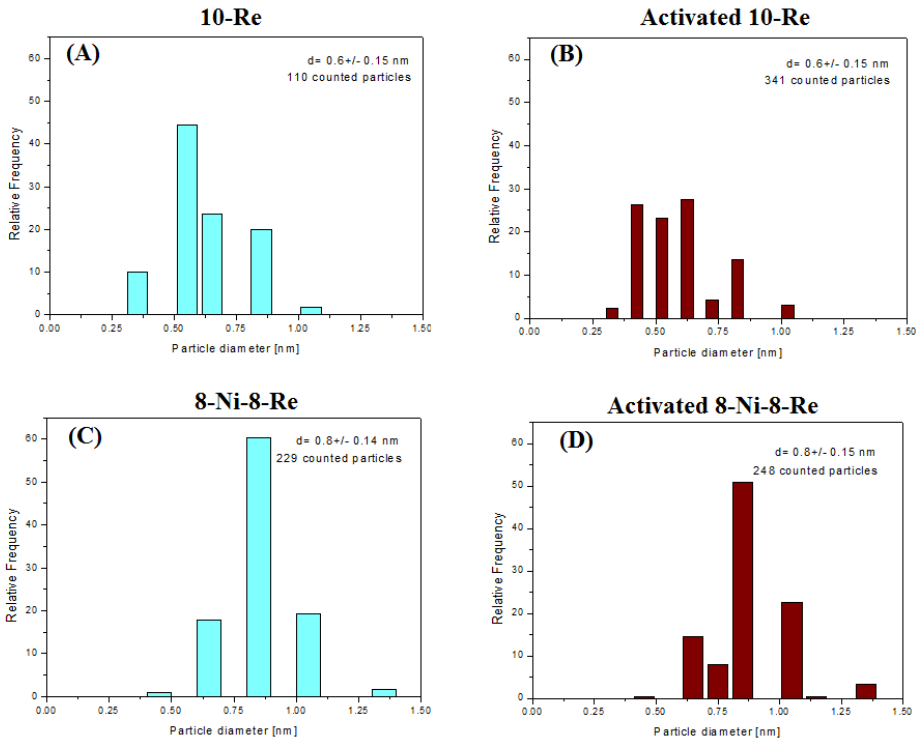

Figure 4.9: Particle size distributions of the clusters in HRTEM.

4.6 Conclusions

Ni-Re catalysts show a good thermal stability up to 950 K. Decomposition of $NiSO_4$ may take place at above 1003K. Material loss is minor during the catalyst preparation. Coke formation could be the reason for catalyst deactivation. $NiSO_4$ and ReO_x have good dispersion on γ-Al_2O_3, but their element distributions are heterogeneous.

References

1. Khursheed, A., *Scanning Electron Microscope Optics and spectrometers.* World Scientific Publishing Co., 2010.
2. Brydson, R., *RMS-Royal Microscopical Society: Aberration-Corrected Analytical Electron Microscopy.* John Wiley & Sons, 2011.
3. Browning, N.D., Pennycook, S. J., *Characterization of High Tc materials ad Devices by Electron Microscopy.* Cambridge University Press, 2000.
4. Maneva, M., Rizova, D., Genov, L., Liptay, G., *J. Therm. Anal.*, 36 (1990) 915-922.
5. Mol, J.C., *Catal. Today*, 51 (1999) 289-299.
6. Lwin, S., Wachs, I.E., *ACS Catal.*, 4 (2014) 2505-2520.
7. Lwin, S., Li, Y., Frenkel, A.I., Wachs, I.E., *ACS Catal.*, 5 (2015) 6807-6814.
8. Okal, J., Kpiński, L., Krajczyk, L., Drozd, M., *J. Catal.*, 188 (1999) 140-153.
9. Okal, J., Kępiński, L., Krajczyk, L., Tylus, W., *J. Catal.*, 219 (2003) 362-371.

Chapter 5

5 Investigation of the Nature of the Active Sites

5.1 Introduction

The reaction mechanism of this dual-function catalyst was suggested to consist of two steps, dimerization of ethylene ($NiSO_4$ responsible) as the first step followed by metathesis (ReO_x responsible) of the products, 2-butene and ethylene, as the second step. As mentioned in Chapter 2, Cai[1] and Sohn[2-4] reported that $NiSO_4$/γ-Al_2O_3 could exhibit a high activity for ethylene dimerization. They concluded that the catalytic active sites responsible for the dimerization reaction consist of a low valent Ni site and surface acidity. Ni^+ has been identified by FT-IR, XPS and EPR techniques on the activated $NiSO_4$/γ-Al_2O_3 catalyst, which was pretreated at 773K for 1 hour in vacuum. An acid strength of $H_0 \leq 3$ was needed for the ethylene dimerization reaction to proceed and both Brønsted and Lewis acid sites were identified on the support surface by an ammonia adsorption FT-IR study. Furthermore, G. Wendt and co-workers studied the mechanism and deactivation of a NiO-Al_2O_3/SiO_2 dimerization catalyst[5, 6]. They reported that catalytically active sites are formed from the combination of acid sites with coordinatively unsaturated nickel ions (Ni^{2+}). They also reported that catalyst deactivation is caused by coke formation.

In Chapter 3, the results of the catalytic tests in the continuous flow reactor and pulse reactor showed that the two metallic sites of the $NiSO_4$-ReO_x/γ-$A_{l2}O_3$ catalyst seem to work independently of each other. However, the catalyst deactivates quite fast by coking which was driven by ethylene dimerization. In order to understand this phenomenon, investigation of the $NiSO_4$ based ethylene dimerization step is necessary.

In a nickel-based homogeneous alkene dimerization/oligomerization system, it is well known that the reactivity of lower alkenes decreases in the order ethylene > propylene > butylene[7]. Similar findings were also found for $NiSO_4$/γ-Al_2O_3 catalyst[8] and the author concluded that the mechanism of alkene oligomerization changes from coordination catalysis to acid catalysis with the increasing carbon number of alkenes.

Many researchers have devoted their attentions to the role of the acid sites and the oxidation state of active Ni on Ni-based oligomerization catalysts such as NiO-SiO_2[9], NiO/SiO_2-Al_2O_3[10-12], Ni-MCM-41[13] and Ni^{2+}/zeolite[14-16]. However, for ethylene dimerization derived from the $NiSO_4$/γ-Al_2O_3 catalyst, the nature of active sites at a molecular level and in particular the role of $[SO_4]^{2-}$ is still not very well understood.

Therefore, in this chapter, focus has been on the ethylene dimerization function, $NiSO_4$ supported on alumina, which is believed to be a key step affecting the reaction and catalyst deactivation rate of the $NiSO_4$/ReO_x/γ-Al_2O_3 ETP catalyst. The oxidation state of active Ni ions on Ni modified catalysts for ethylene oligomerization is always a controversial topic, since this factor significantly affects the catalyst performance[17]. Therefore, FT-IR, XPS and EPR experiments were carried out in order to figure out the oxidation state of Ni in our catalyst. The adsorption and investigation of probe molecules on Ni-containing catalysts has been widely studied by in-situ FT-IR[18-23] and UV-Vis[22-27] spectroscopies. To understand the nature of the active sites, an investigation was carried out by means of in-situ FT-IR and UV-Vis-NIR spectroscopies following the course of thermal activation of the catalysts followed by subsequent CO or C_2H_4 adsorption. This approach allows monitoring of changes during catalyst activation in the coordination structure of the transition metal Ni, the surface hydroxyl groups on γ-Al_2O_3 as well as the symmetry of surface $[SO_4]^{2-}$ anions. Moreover, IR spectra of CO adsorption on a series of activated catalysts at a low temperature could reveal information about the oxidation state of Ni and acid strength (Brønsted and Lewis) of the acid sites. Furthermore, experiments of time-resolved C_2H_4 adsorption on the catalysts provide the possibility to understand the initiation reaction and find out a reason for catalyst deactivation.

5.2 Experimental Instruments and Methods

In this section, a brief theory of each instrument is introduced and the experimental methods are described as well. One gas distribution panel and one vacuum line are depicted in detail, since all in-situ experiments need at least one of them to be completed. Several cells were specially designed for different instruments.

5.2.1 Fourier Transform Infrared Spectroscopy (FT-IR)

FT-IR is one of the most important techniques for materials analysis in the laboratory[28]. The basic principle of infrared spectroscopy is an interaction between an infrared radiation and electrical dipolar motions within molecules[29]. To be infrared active, a change in an electric dipolar motion of a molecule must occur during the vibration or rotation. A molecule absorbing an infrared radiation may induce a transition of the molecule from one rotational or vibrational energy state to another state. Since energy levels of a molecule are quantized, the energy of the radiation needed for the transition must exactly fit the energy gap between the two states. Consequently, the frequency of adsorption or emission of radiation associated with a particular atomic or molecular process is characteristic. Compared with a traditional dispersive instrument, Fourier-transform infrared spectrometer improves the acquisition of infrared spectra dramatically due to the application of a mathematical method of Fourier-transformation. FT-IR can be applied for samples in solid or gaseous or liquid states.

In-situ FT-IR experiments have been performed at both room temperature and at liquid nitrogen temperature in transmission mode. For the room temperature experiment, spectra were collected by a Perkin Elmer Spectrum One FT-IR spectrometer equipped with a Harrick in-situ FT-IR cell. Figure 5.1 shows an overall block diagram. A gas distribution panel, specially designed for introduction and evacuation of gases, was placed in a fume hood. This panel was connected to a gas cylinder, a hydraulic pump and the in-situ cell. To ensure safety, a CO detector was installed outside the fume hood and the outlet of the pump was directed to the fume hood. The main body of the in-situ cell resembles a horizontal cylinder, which has two layers, a thick outer layer and a hollow inner chamber. The outer layer was made of chemically-resistant stainless steel. Two K-type thermocouples were capable of monitoring and controlling the temperature of a sample. A display panel in the temperature controller kit showed a real temperature and a setting temperature. CaF_2 windows were mounted on the sides of the cell and cooling water was needed to protect the windows at a high temperature. The upper temperature limit of the cell is 673K. In order to keep the consistency, the catalyst was also pre-treated at 673K in the following characterization experiments (FTIR, UV-Vis-NIR, XPS and ESR). In the continuous flow reactor test, it has been confirmed that the 8-

NiS and 8-Ni-8-Re catalysts still exhibit high activity when calcinated at 673K with nitrogen. A sample holder was located in the middle of the inner chamber which could be completely sealed for in-situ experiments. PerkinElmer Spectrum software was used to control the IR instrument and process data.

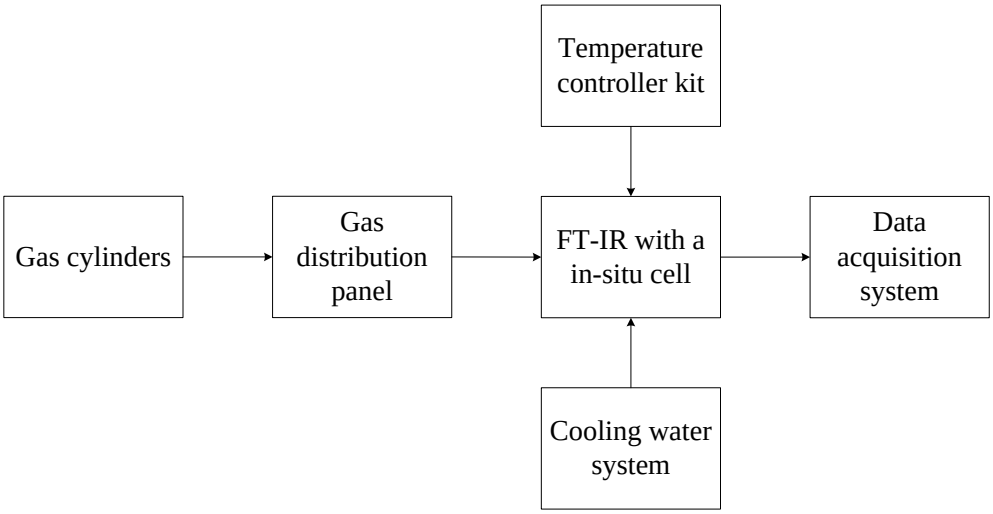

Figure 5.1 Experimental flow diagram of FT-IR system for CO adsorption at room temperature.

Figure 5.2 shows schematic drawings of the gas distribution system and the in-situ cell. 15mg of a sample was ground and compressed into a thin wafer of 13 mm diameter by a hydraulic press manufactured by Specac. The wafer supported by the sample holder was carefully delivered to the cell. After all these preparations, the hydraulic pump was turned on. The temperature was increased to 673 K and the pellet was pretreated under vacuum at 673 K for 1 hour in order to remove water and other impurities. Subsequently, when the cell was cooled down to room temperature, CO (400-500 mbar) was introduced to the cell. The amount of CO was adjusted by a needle valve (V-8) and the pressure was viewed in the pressure gauge. A set of IR spectra was obtained followed by a stepwise outgassing of CO. Desorption of CO was achieved by slowly pumping CO out of the cell. The detailed procedures are given in Appendix D.

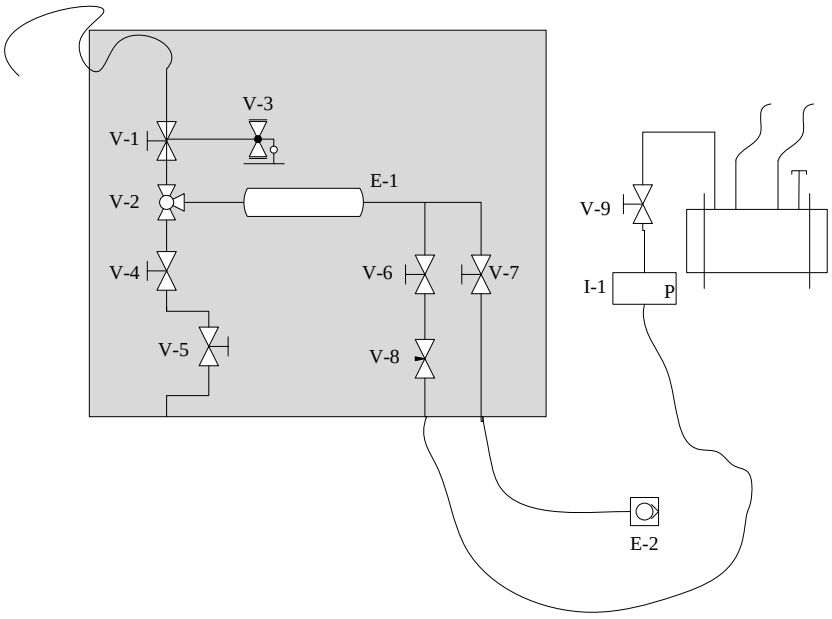

Figure 5.2: Schematic drawing of a gas distribution system and an in-situ cell.

The low temperature FT-IR experiment was carried out in inGAP center of the University of Oslo. IR spectra were recorded by a BRUKER Vertex 70 spectrometer equipped with a mercury cadmium telluride cryo-detector at a resolution of 4 cm^{-1}. A thin, self-supporting wafer was made under the same condition as the one used for the room temperature experiment, but it was necessary to cut the wafer into a rectangle in order to fit the shape of the self-designed cell as shown in Figure 5.3. To protect the pellet, its edges were covered by a gold foil paper. The pellet was moveable between two positions in the cell. One was the lowest part of the cell (see Figure 5.3A). This part is able to resist a high temperature, so the sample could be treated by inserting this part into an oven. The other part is where the infrared radiation could well pass through the sample (see Figure 5.3B) between two CaF_2 windows (see Figure 5.3D). A metal sample holder is shown in Figure 5.3B and its' round holes precisely allow the radiation through when the cell is assembled. It is worth mentioning that liquid N_2 can fill the inner tube (see Figure 5.3C) so as to cool down the metal sample holder as well as the pellet to a low temperature. The self-designed cell allows gas dosage of CO and ethylene.

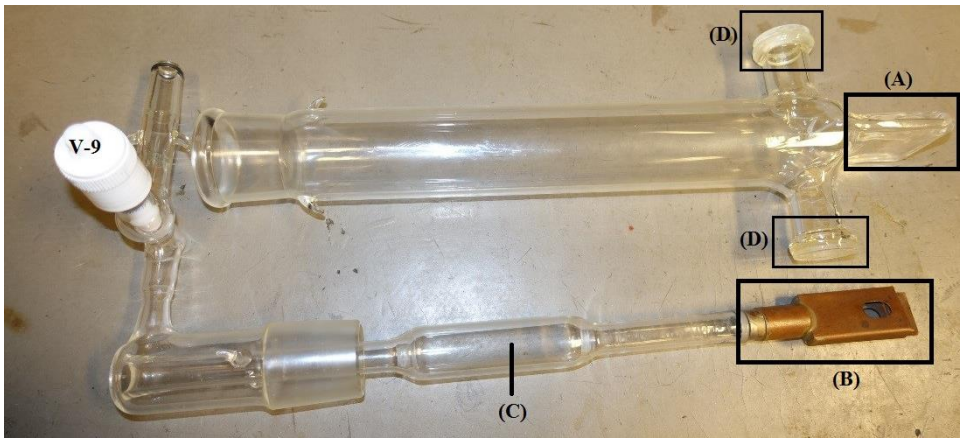

Figure 5.3: Photo of the self-designed cell for a low temperature experiment.

The cell could connect to a vacuum line whose schematic drawing is demonstrated in Figure 5.4. The vacuum line consisted of a pressure gauge ranging from 1 mbar to 1000 mbar and another pressure gauge working below 10 mbar. The turbo pump can reach a lower pressure (10^{-3} mbar) than the hydraulic pump (1 mbar). A dry ice trap was mounted before the in-situ cell in order to remove trace amounts of water in the CO and C_2H_4 gases. This is not shown in Figure 5.4. CO and C_2H_4 adsorption on the activated catalysts were performed at a low temperature:

a) CO adsorption and desorption on the activated catalysts.

Prepared pellet was slowly transported to part A of the cell (Figure 5.3A) for a temperature treatment. The cell was connected to the vacuum line and the pellet was treated at the same condition (673 K, 1 hour) as the previous one in the room temperature experiment. After the treatment, the cell was cooled down to room temperature and was moved to the sample compartment of the IR instrument for measurements. To avoid big influences of air during the measurement, the sample compartment was covered by self-made plastic door. The cell was then cooled down to liquid N_2 temperature by filling liquid N_2 into the inner tube of the cell (Figure 5.3C). Before sending CO to the vacuum line, a CO flask was connected to the line and the air carried by the flask was pumped out of the line. CO of around 50mbar was introduced to the cell at a low temperature followed by warming up the cell and outgassing of CO. Outgassing of CO occurred by the typical process of gas expansion. Spectra were recorded by following a stepwise desorption of CO.

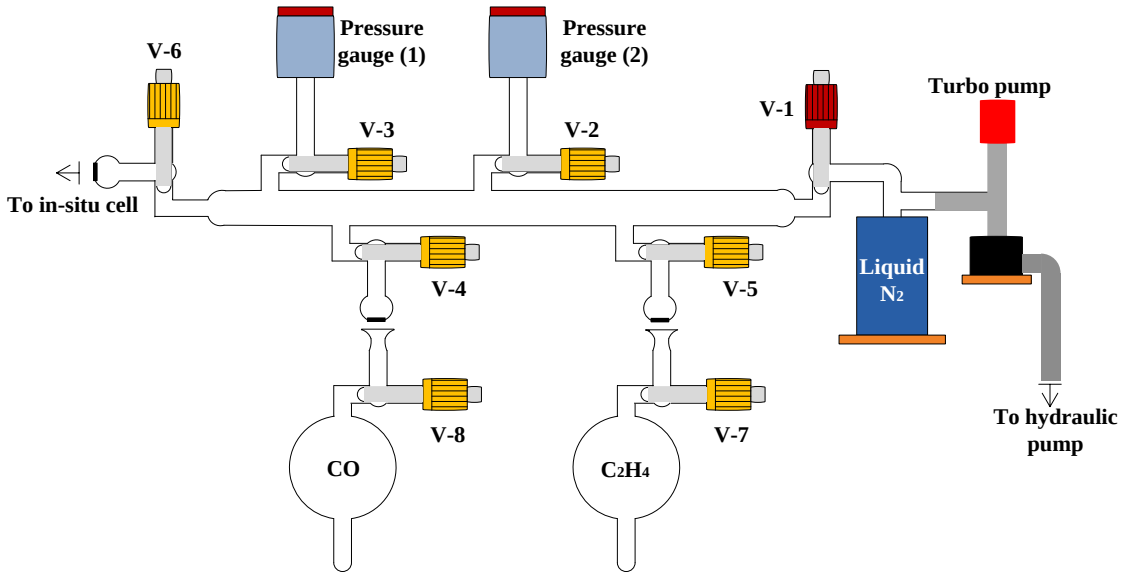

Figure 5.4: Schematic drawing of a vacuum line for a low temperature experiment.

b) C_2H_4 adsorption and desorption on the activated catalysts.

Procedures of catalyst activation in a) was repeated in this experiment. After the cell was cooled down to the low temperature, ethylene of 10 mbar was introduced into the cell. At such low temperature, ethylene was totally frozen in the cell since the starting temperature is lower than the freezing point of ethylene. As the temperature slowly rose, the pressure of ethylene increased suddenly at the boiling point due to the state change. Ethylene (10mbar) was fully in contact with the catalyst at room temperature for 2 hours. Subsequently, more ethylene (30mbar) was sent to the cell again in order to deactivate the catalysts. After that, ethylene was kept in the cell overnight. During the next day, ethylene was totally pumped off from the vacuum line and the cell. Spectra were recorded every 2 minutes during the reaction.

The detailed procedures are shown in Appendix D

5.2.2 Ultraviolet-Visible-Near Infrared Spectroscopy (UV-Vis-NIR)

Besides IR, UV-Vis spectroscopy is another widely used instrument in analytical chemistry. UV radiation (200-400 nm) and visible light (400-700 nm) have higher energy than IR radiation (700 nm-1 mm), so they are able to excite valence electrons of atoms

and molecules[30]. Electron excitation is a process whereby electrons can move from a ground state to a higher energy state by absorbing photon energy. This absorbed energy from radiation exactly matches the energy required to excite an electronic transition. Organic molecules contain three types of electrons, sigma (σ) and pi (π) electrons involved in σ and π bonds, and non-bonding n electrons. n→ π*, n→σ* and π→π* transition can be observed in the UV-Vis region. Moreover, many inorganic compounds can have charge-transfer transitions expressing an internal oxidation-reduction process by absorbing the UV photons. Transition metals may show electronic transitions occurring in d and f orbitals.

UV-Vis-NIR experiments were performed in the NIS Centre and INSTM, University of Torino. Diffuse reflectance (DR) UV-Vis-NIR spectra were collected on a Varian Cary 5000 instrument at a spectral resolution of 2 nm. Approximately 1 g of sample was introduced into a quartz cell (shown in Figure 5.5), which was capable of connecting to the vacuum line for catalyst activation and gas dosage. The vacuum line was similar to the one shown in Figure 5.4. The design of the arc-shaped bottom exactly matched the sample holder. The quartz cell could be heated at a high temperature by inserting it into an oven. The sample was outgassed in-situ overnight and then was activated under 673 K for 2 hours in the vacuum line before cooling down to room temperature again. The following procedures of ethylene adsorption (100 mbar) on the activated sample were repeated according to the procedures of the in-situ FT-IR experiment.

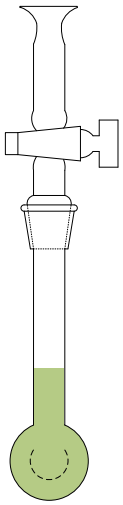

Figure 5.5: schematic drawing of the self-designed cell for UV-Vis-NIR experiments.

5.2.3 X-ray Photoelectron Spectrometer (XPS)

X-ray photoelectron Spectroscopy (XPS), also referred to as electron spectroscopy for chemical analysis (ESCA), is an advanced technique for analyzing the surface chemistry of a material ranging from metals, oxides, semiconductors, glasses, ceramics, polymers, composites to biomaterials[31]. XPS employs a beam of soft X-ray to irradiate a solid surface (1-10nm) where emitted electrons are characterized simultaneously according to their kinetic energy. Figure 5.6(A) illustrates the process of X-ray core-level photoemission. An X-ray photon interacts with a core level electron transferring its kinetic energy and causing emission of the electron. The kinetic energy (E_k) of the emitted photoelectron is calculated as follows:

$$E_K = h\nu - E_B + \phi \qquad (5.1)$$

Where *hν* is the X-ray photon energy (*h* is the Plank's constant and *ν* is the X-ray frequency). E_B is the binding energy of the core-level electron. ϕ is the instruments spectrometer work function. The binding energy of an electron in a particular cell of an atom is unique for each element so the elements on a material surface can be identified.

Figure 5.6 (B-C) illustrates the process of photoemission called emission of Auger electrons. A core level vacancy after emission of a photoelectron can be occupied by relaxation of an electron from a higher level. This causes emission of an Auger electron in order to conserve the energy difference, ΔE, from the previous step.

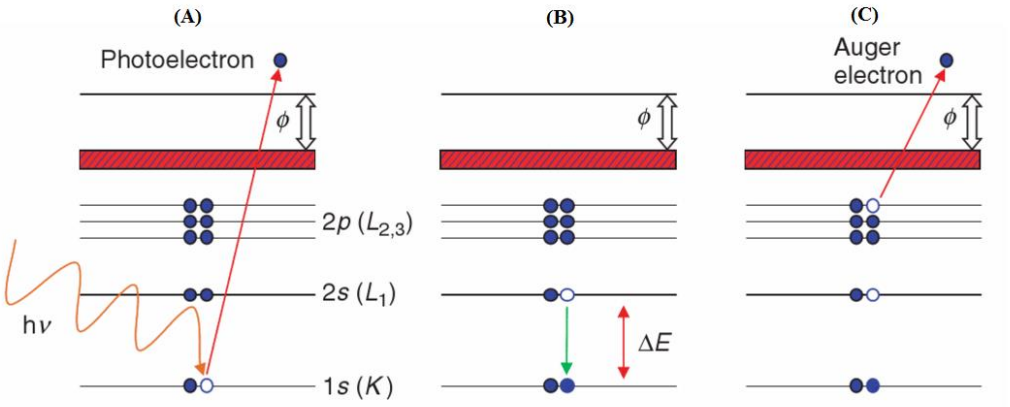

Figure 5.6: The process of X-ray core-level photoemission and X-ray-stimulated Auger electron emission[32].

A common XPS consists of an excitation source, an electron energy analyzer, an Ultra-High Vacuum (UHV) system, a data processing system and ancillary processing features[33]. X-ray is generated from accelerated electrons colliding with a target anode. Mg and Al K_α anodes with linewidths of 0.75 and 0.85 eV are often used in laboratory instruments. The electron energy analyzer is used to scan the electrons located in the entire target region to obtain an entire spectrum. The UHV system ensures the safety of the emitted electrons without the influence of the residual gas molecules on the material surface. The acquired data is processed in the data processing system. Ancillary processing features are to adjust the position of the sample holder in order to modify electron emission.

The photoelectron binding energy of an element depends not only on the photoemission level of an atom but also on the oxidation state or local electron density of the atom. Therefore, valence of an element can be determined according to their chemical shift by measuring the photoelectron binding energy. The binding energy increases when an atom losses an electron and vice versa. In a typical XPS spectrum, six features can be seen[34]:

- Sharp peaks appear when the photoelectrons are generated in an elastic scattering process.
- Multiplet splitting occurs when there are unfilled shells with unpaired electrons.
- A broad peak is probable due to electrons from an inelastic process generated in a comparatively deeper position of a material.
- Satellites normally contain shake-up peaks and shake-off peaks. Shake-up peaks are caused by an outgoing photoelectron exciting a valence electron to a higher level. Consequently, the kinetic energy of the emitted photoelectron is reduced and this leads to a shake-up peak at a higher binding energy in a spectrum. Shake-off peaks are attributed to a valence electron ejected after the photoemission.
- Plasmons are created by collective excitations of the valence band.
- Auger peaks are due to the production of Auger electrons by X-ray, which has been described before in this section.

The catalysts were analyzed by an Axis Ultra^{DLD} XP spectrometer (Kratos Analytical). The XPS spectra were taken by using a monochromatic Al Kα radiation, along with pressures in the analysis chamber of $6*10^{-8}$ Torr - $6*10^{-9}$ Torr. The instrument resolution was determined as the full width at half the maximum (FWHM) of the Ag $3d_{5/2}$ peak. The fresh samples were outgassed in the analysis chamber. One of the catalysts was activated under nitrogen flow at 673K for 1 hour followed by cooling down to room temperature before testing. The spent catalyst was collected from the continuous flow reactor test without contacting air. This XPS experiment was operated by Martin F. Sunding in the University of Oslo.

5.2.4 Electron Paramagnetic Resonance (EPR)

Electron paramagnetic resonance (EPR) or electron spin resonance (EPR) provides the possibility of detecting unpaired electrons [35]. Electrons behave like a spinning sphere, thus they have an intrinsic mechanical angular momentum. According to the Pauli Exclusion Principle, two paired electrons occupy the same orbital having the same orbital quantum numbers but differing in the spin quantum numbers. That means that the magnetic moment of the paired electrons counteract each other and they express diamagnetic property in a magnetic field. On the contrary, an unpaired electron has a paramagnetic property in a magnetic field.

The Energy of a magnetic moment of an electron in a magnetic field is written as:

$$E = g\mu_B B_o S \qquad (5.2)$$

Where g is Landé factor (g factor). μ_B is called the Bohr magneton. B_o is the magnetic field intensity. If one considers that the electron spin can be in two states, α or β, the spin vector S can be either 1/2 or -1/2. As shown in Figure 5.7, the two spin states, α and β, have the same energy at a zero field (B_o=0). However, when a static magnetic field (B_o≠0) applies, the α state shifts to a higher energy level and the β is at a lower energy level (Zeeman effect). The energy difference between two states is expressed as:

$$\Delta E = g\mu_B B_o \qquad (5.3)$$

This energy difference is proportional to the magnetic field intensity and relates to the *g* value as well. An electron at the low energy state can absorb electromagnetic radiation energy so it can transit to the high energy state.

$$h\nu = g\mu_B B_o \qquad (5.4)$$

Where *v* is the frequency of the radiation. In EPR, radiation with a microwave frequency is applied, which can be classified into several types in terms of the frequency such as X-band (8-12 GHz), Q-band (around 34 GHz) and W-band (around 95 GHz). The most commonly used band is the X-band with a frequency around 9.6 GHz in EPR. In the experiment, a sample is measured at a fixed microwave frequency but a swept magnetic field. A typical EPR consists of:

- Microwave Bridge, which is where the X-band microwaves are produced.
- Magnet system which generates a magnetic field.
- Microwave resonator which is used to provide a sufficient microwave magnetic field at the sample position and convert the sample response to a detectable microwave signal.
- Data system

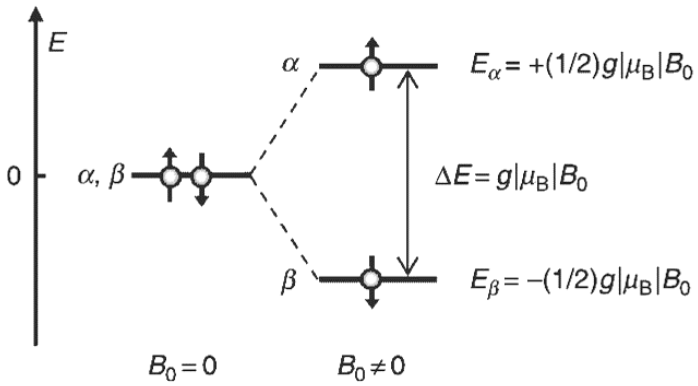

Figure 5.7: the electron spin Zeeman effect [36].

EPR measurements were performed at both room temperature and liquid nitrogen temperature using an X-band Bruker EleXsySES60 spectrometer. A special quartz cell was designed for an in-situ evacuation and heat treatment (shown in Figure 5.8). As with the UV-Vis-NIR cell, this one could also connect to the vacuum line (see Figure 5.4). A

sample of 500 mg was transferred into the high temperature resistant tube. The diameter of the tube perfectly fitted the EPR cavity. The sample was activated under 673 K for 2 hours in the vacuum line before cooling down to room temperature for measurements. The EPR experiment was operated by Einar Sagstuen, in the University of Oslo.

Figure 5.8: Photo of an EPR cell.

5.2.5 GC-MS Analysis of Spent Catalyst

Powder samples of spent catalysts were obtained from a static reactor after 24 hours ethylene reaction at 323 K. The photo of the static reactor is shown in Figure 5.9. In the experiment, the reactor was surrounded by heating tapes for temperature control and it was possible to connect the gas distribution panel (see Figure 5.2) for catalyst activation and subsequent ethylene reaction. After reaction, the reactor was cooled down in an ice-water bath and CH_2Cl_2 was injected into the reactor to dissolve the soluble products in a glove bag by purging with nitrogen. The extraction was analyzed by GC-MS. The GC-MS instrument was an Agilent 7890A gas chromatograph coupled with a 5975C mass spectrometer. 1 µL of solution was injected each time by an automatic liquid sampler and analyzed by a HP-PLOT Al_2O_3/KCl column

Figure 5.9: photo of a static reactor.

5.3 Results and Discussion

5.3.1 Effects of Thermal Activation on the Vibrational and Electronic Properties of the Investigated Catalysts

All the catalysts have been subjected to a complete spectroscopic characterization both before and after thermal activation at 673 K. The FT-IR spectra of all the samples are dominated by the vibrational manifestation of physisorbed water (broad absorption band in the 3700 – 2500 cm^{-1} region due to the ν(OH) vibrational mode, and band at 1635 cm^{-1} due to the δ(HOH) vibrational mode). Activation at 673 K causes substantial changes in the FT-IR spectra of all the catalysts. Figure 5.10a shows the evolution of the FT-IR spectra during thermal activation for the 8-NiS catalyst as an example, while Figure 5.10b and Figure 5.10c show the FT-IR spectra of all the activated samples in the 3900 – 3000 cm^{-1} and 1600 – 1200 cm^{-1} regions, respectively. During the activation, the physically adsorbed water is removed, as affirmed by the disappearance of the δ(HOH) absorption band at 1635 cm^{-1} and by the gradual decrease of the ν(OH) absorption band (Figure 5.10a). In the ν(OH) region, five absorption bands were clearly observed in the spectrum of the activated alumina, which reveals the presence of both bridged (more acidic) and terminal (less acidic) hydroxyl species. This is in agreement with previous studies[37]. In contrast, for all the other activated samples, only a weak and broad absorption band is observed in the ν(OH) region around 3500 cm^{-1}, indicating that the remaining hydroxyl groups at the alumina surface are still H-bonded.

Interestingly, for all the Ni-containing catalysts and for the 8-S sample, the disappearance of the absorption bands assigned to physically adsorbed water is accompanied by the appearance of a well-defined band just below 1400 cm^{-1} (Figure 5.10c). The connection between the two phenomena is demonstrated by a clear isosbestic point around 1400 cm^{-1} (Figure 5.10a). This band is assigned to a stretching vibration of the $[SO_4]^{2-}$ anion, whose symmetry decreases upon water removal. Indeed, an $[SO_4]^{2-}$ anion in perfect tetrahedral environment gives a single ν(SO_4) vibration around 1100 cm^{-1}[138]. However, this band splits into multiple bands upon decreasing the symmetry on all the Ni-containing samples (i.e. by going from an ionic to a covalently bonded sulfate). The $\nu_{asym}(SO_4)$ band appears near 1400 cm^{-1} (see Figure 5.10c) and a

$\nu_{sym}(SO_4)$ band is expected to be around 1200 cm^{-1} (covered by the out-of-scale absorption of bulk alumina)[39]. The FT-IR spectrum of the activated 8-S sample shows well-defined bands in this spectral region, which indicate the presence of two kinds of SO_4 species, namely monodentate species (accounting for the bands at 1403 and 1426 cm^{-1}) and bidentate species (accounting for the bands at 1381, 1284 and 1244 cm^{-1}). Hence, it is concluded that dehydration at 673 K causes a change in the symmetry of the sulfate anions in all the sulfated samples. Small differences are observed in the width and position of the corresponding absorption bands among the different samples, indicating that the surroundings of the $[SO_4]^{2-}$ anions is not exactly the same and is likely influenced by the presence of the metal phases.

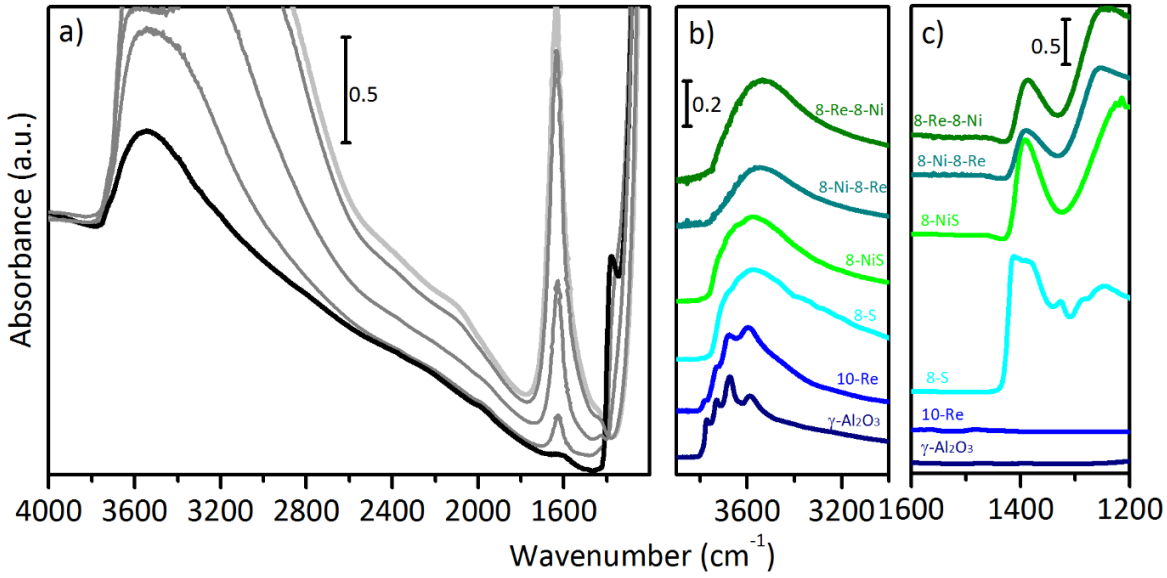

Figure 5.10: a): FT-IR spectra of the 8-NiS catalyst collected during the thermal activation from room temperature to 673 K. b) and c): FT-IR spectra of all the investigated samples after thermal activation at 673 K, in the 3900-3000 cm^{-1} and 1600-1200 cm^{-1} regions, respectively.

Complementary information was obtained by means of DR UV-Vis-NIR experiments, which provides information on the electronic properties of the samples. Figure 5.11a shows the DR UV-Vis-NIR spectra of all the samples before activation. Generally speaking, the very intense (often out-of-scale) absorptions above 26000 cm^{-1} are due to charge-transfer transitions. The bands observed in the 26000 – 8000 cm^{-1} region are assigned to d-d transitions. Finally, the narrow and weak absorptions in the NIR region (8000 – 4000 cm^{-1}) are due to the combination and/or overtones of vibrational modes involving mainly OH groups. The UV-Vis-NIR spectra of bare alumina and 8-S do not show any absorption band in the UV and Vis region, but only weak bands around 7000 and

5100 cm^{-1}, which are assigned to the ν(OH)+δ(HOH) and 2ν(OH) vibrational modes related to physisorbed water. The spectrum of 10-Re shows a very intense absorption in the UV-region (above 30000 cm^{-1}), easily ascribed to the charge-transfer transition of rhenium oxide[40]. In contrast, the spectra of all the samples containing nickel display three well defined bands in the region of d-d transitions, centered around 8650 cm^{-1} (band O1, $^3A_{2g}(F) \rightarrow {}^3T_{2g}(F)$), 13700 – 15050 cm^{-1} (band O2, $^3A_{2g}(F) \rightarrow {}^3T_{1g}(F)$ and $^3A_{2g}(F) \rightarrow {}^1E_g(D)$), and 25260 cm^{-1} (band O3, $^3A_{2g}(F) \rightarrow {}^3T_{1g}(P)$)[27, 41, 42]. The same three bands are observed in the spectrum of $NiSO_4 \cdot 6H_2O$ reference sample at 8500, 14100 – 15300 and 25800 cm^{-1}. Hence, DR UV-Vis-NIR spectroscopy provides evidence that the Ni^{2+} cations in the Ni-containing samples display a 6-fold coordination and all the coordination vacancies are filled by water molecules. Finally, the spectra of 8-Ni-8-Re and 8-Re-8-Ni also show the intense charge-transfer band characteristic of Re oxide.

As with the FT-IR spectra discussed above, the DR UV-Vis spectra also greatly change upon thermal activation, and in particular those of the samples containing the nickel phase. Figure 5.11b, c, d show the evolution of the DR UV-Vis spectra for a series of Ni-containing catalysts. After outgassing the samples overnight at room temperature, a small fraction of physically adsorbed water is removed, resulting in a blue shift of all the d-d bands and in the decrease of the bands in the NIR region due to OH vibrations. After activation at 673 K, most of the water is removed. Simultaneously, the d-d bands greatly change, both in position and in intensity. The new spectrum is indicative of the presence of Ni^{2+} sites with a symmetry lower than in the hydrated sample, in analogy to the what has been reported by D. Cornet et al. [43] for a similar NiO/Al_2O_3 sample activated at 723 K.

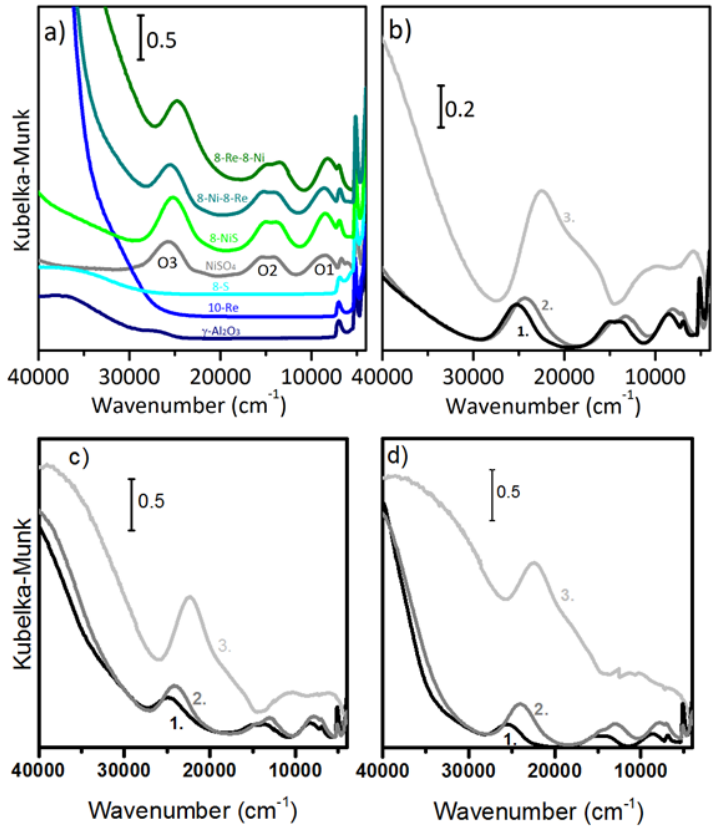

Figure 5.11: a): DR UV-Vis spectra of all the investigated samples in the hydrated form. b): DR UV-Vis spectra of the 8-NiS catalyst; c) 8-Ni-8-Re; d) 8-Re-8-Ni in (1) the hydrated form, (2) after degassing overnight at room temperature, and (3) after thermal activation at 673 K.

When considered together the in-situ FT-IR and DR UV-Vis data discussed above indicate that the Ni^{2+} sites in hydrated samples display a 6-fold coordination with all the coordination vacancies filled by water molecules. The $[SO_4]^{2-}$ counter-anions are in turn solvated by water molecules and are not directly coordinated neither to the Ni^{2+} nor to the Al^{3+} cations. Upon thermal activation, coordinated water is gradually lost, implying the creation of some coordination vacancies around the Ni^{2+} sites. Simultaneously, it is expected that a small fraction of the Al^{3+} sites at the alumina surface are dehydroxylated and behave as strong Lewis sites. As a consequence, at least a fraction of the adjacent $[SO_4]^{2-}$ ions are covalently bonded either to the Ni^{2+} or to the surface Al^{3+} cations, with a consequent decrease of symmetry and an enhancement of the covalent character. In analogy to what has been proposed by Saur et al.[39] , a schematic representation of the hypothesized structures on sulfated alumina and sulfated Ni/Al_2O_3 is proposed in Figure 5.12. M stands for the Ni^{2+} or Al^{3+} surface sites. In addition, the covalently bonded sulfate groups might be partially protonated by the surface OH groups, as suggested in the literature, and in agreement with our observation of an enhanced Brønsted acidity for

sulfated catalysts (vide infra). As suggested by Davydov et. al.[44], the Brønsted proton might be delocalized over the oxygen atoms of the covalent sulfate groups, as shown in Figure 5.12.

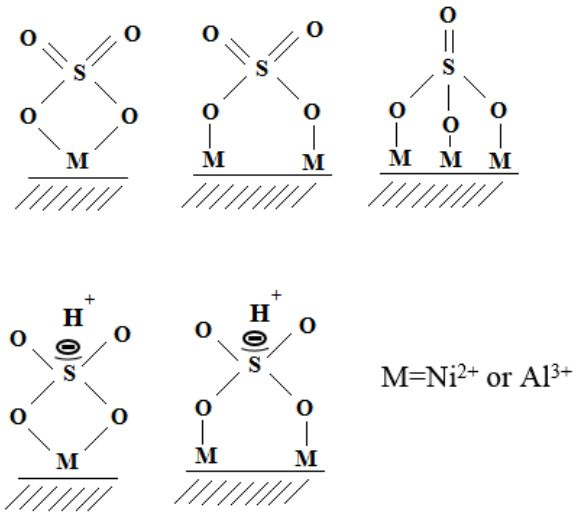

Figure 5.12: Schematic representation of hypothesized structures present on sulfated alumina and sulfated Ni/Al_2O_3, where M stands for the Ni^{2+} or Al^{3+} surface sites. In addition, the covalently bonded sulfate groups might be partially protonated by the surface OH groups.

5.3.2 Probing the Surface Properties of the Activated Catalysts by Means of FT-IR Spectroscopy of CO Adsorbed at 100 K

In the next step, the surface properties of the catalysts were investigated by means of in-situ FT-IR spectroscopy of CO adsorbed at 100 K. This method has been widely applied to investigate Ni-containing catalysts[18-21, 24, 44-48]. This is because it allows to determination of the Ni oxidation state in different conditions, according to the ν(CO) modes of the carbonyl complexes. Furthermore, the strengths of both Lewis and Brønsted acid sites can be simultaneously probed, since CO is also able to interact at 100 K with both the non-coordinated Al^{3+} (Lewis acid) surface sites and hydroxyl groups (Brønsted acid) at the surface of acid catalysts, forming $\equiv Al^{3+}\cdots CO$ adducts and ≡Al-OH···CO adducts, respectively. The sequence of the FT-IR spectra of CO adsorbed at 100 K on all the investigated samples as a function of the CO coverage (θ) is shown in Figure 5.13. In all the cases, the insets report the evolution of the FT-IR spectra in the ν(OH) region.

The FT-IR spectra of CO adsorbed on bare alumina (Figure 5.13a) displays two main ν(CO) absorption bands, which are completely reversible upon degassing at 100 K. The first one, centered at 2154 cm^{-1} at θ_{max}, is attributed to CO adsorbed on the surface hydroxyl groups [49]. Correspondingly, a perturbation of the ν(OH) bands is observed (inset in Figure 5.13a). This band slightly shifts up to 2160 cm^{-1} upon decreasing θ and disappears fast. The second band, centered at 2186 cm^{-1} at θ_{max}, is assigned to the CO adsorbed on the coordinatively unsaturated Al^{3+} ions. This band shifts upwards to 2202 cm^{-1} upon decreasing of the CO coverage and it is more resistant at low temperature. The shift with decreasing θ is due to the vanishing of the lateral interaction between adjacent CO molecules as widely documented in the literature[50, 51].

Similarly, FT-IR spectra were obtained for CO adsorbed on the 8-S sample (Figure 5.13b), except that the two main ν(CO) absorption bands shifted to higher values compared to bare alumina and display a different relative intensity. In particular, the band attributed to ≡Al-OH···CO adducts is observed at 2168 cm^{-1} at θ_{max} and shifts to 2177 cm^{-1} at θ_{min}. Correspondingly, the broad ν(OH) band downward shifts by approximately 70 cm^{-1}. This behavior witnesses an enhanced Brønsted acidity for sulfated alumina, as widely reported in literature [39]. It is worth noticing that, although low temperature CO adsorption measures a medium-weak Brønsted acid strength, other methods indicate a much larger acidity[52-54]. The absorption band assigned to ≡Al^{3+}···CO adducts goes from 2203 cm^{-1} at θ_{max} to 2212 cm^{-1} at θ_{min}, indicating a slightly stronger Lewis acid sites than in bare alumina. This is in agreement with earlier reports[52, 55].

The effect of rhenium phase on the surface properties of the catalysts is much less pronounced than that of sulfates. The FT-IR spectra of CO adsorbed on 10-Re (Figure 5.13c) almost exhibit the same behavior as for pure alumina, except that the band assigned to ≡Al^{3+}···CO adducts is less intense relative to that due to ≡Al-OH···CO adducts. This indicates that the ReO_x phase partially covers the alumina surface.

In contrast, the FT-IR spectra of CO adsorbed on 8-NiS (Figure 5.13d), 8-Ni-8-Re (Figure 5.13e) and 8-Re-8-Ni (Figure 5.13f) catalysts are substantially different from those discussed above. Three main absorption bands are observed in all the three cases:

1) The most intense absorption band is centered at 2202 cm^{-1} at θ_{max} and undergoes a pronounced shift upon decreasing θ down to 2214 cm^{-1} at θ_{min}. This band, which is also the most resistant to a decrease in θ, is assigned to CO adsorbed on coordinatively unsaturated Ni^{2+} sites[44, 47, 56], and overlaps with the band ascribed to $\equiv Al^{3+}\cdots CO$ adducts.
2) The band centered at 2162 cm^{-1} at θ_{max}, which shifts to 2170 cm^{-1} at θ_{min}, is assigned to $\equiv Al\text{-}OH\cdots CO$ adducts. The Brønsted acidity of the surface hydroxyl groups is very weak, suggesting that the effect of sulfate anions on the properties of alumina is weaker in presence of the nickel phase than on sulfated alumina.
3) In addition, a broad band centered around 2143 cm^{-1} is observed in all the three cases, which is easily removable upon decreasing θ. This band is attributed to physisorbed CO, and affirms that an increase in the complexity of catalyst formulation creates new opportunities for CO adsorption.

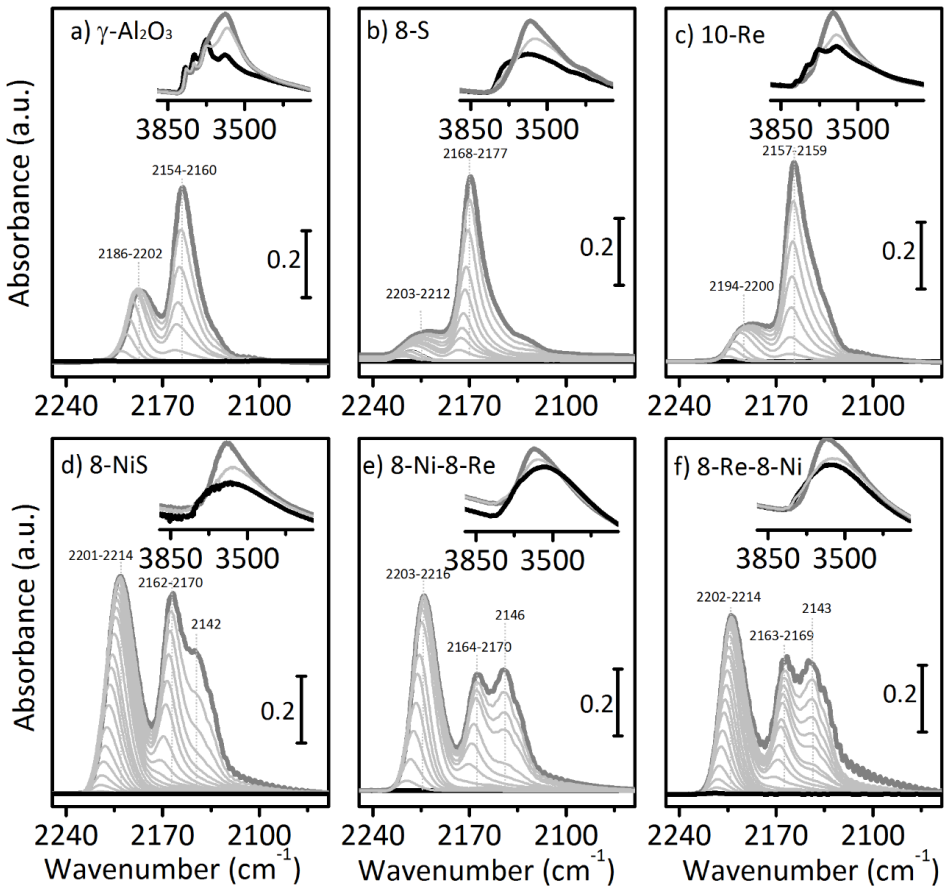

Figure 5.13: Evolution of the FT-IR spectra of CO adsorbed at 100 K over different samples as a function of CO coverage, from θ_{CO} = 30 mbar (dark grey) to θ_{CO} = 10^{-3} mbar (black). All the spectra are reported after subtracting the spectrum of the activated sample prior CO dosing. The insets show the evolution of the spectra in the ν(OH) region. Activated catalyst (black), after CO adsorption (dark grey) and stepwise outgassing (light grey).

It is important to point out that in all the three cases no absorption bands are observed in the 2100 – 2080 cm^{-1} and 2140 – 2130 cm^{-1} regions, where $Ni^{+}(CO)_2$ complexes are expected to contribute[56, 57]. Hence, Ni^{+} is not formed during the catalysts' activation in our experimental conditions. Similarly, no absorption bands attributable to CO adsorbed on Re cations (2500 – 1800 cm^{-1}) are observed in the spectra of 8-Ni-8-Re and 8-Re-8-Ni. The intensity of the bands attributed to ≡Al-OH···CO adducts and to physisorbed CO relative to that of CO adsorbed on the Ni^{2+} cations is lower for 8-Re-8-Ni and 8-Ni-8-Re compared to 8-NiS, which suggests that the rhenium phase deactivates or replaces some Brønsted sites.

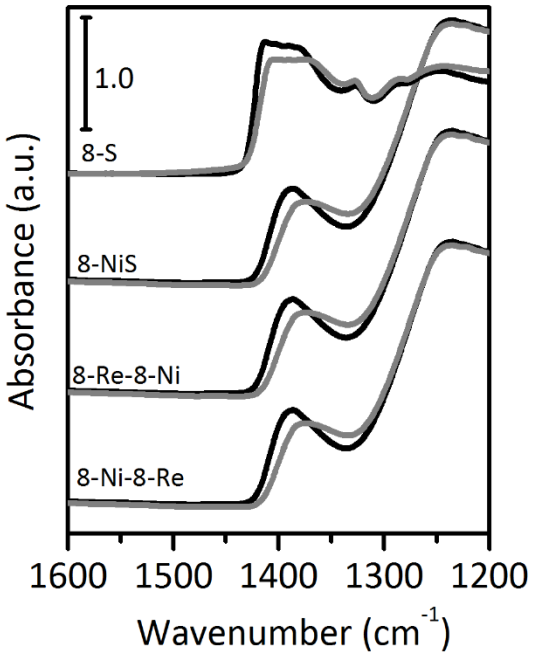

Figure 5.14. FT-IR spectra of 8-S, 8-NiS, 8-Re-8-Ni and 8-Ni-8-Re samples before (black) and after (grey) adsorption of CO at 100 K in the 1600-1200 cm^{-1} region, where the $\nu_{asym}(SO_4)$ vibrational mode of covalently bonded sulfate groups is observed.

Finally, it is interesting to observe that adsorption of CO causes a perturbation of the absorption band at around 1400 cm^{-1} on 8-S and Ni containing catalysts, previously ascribed to the $\nu_{asym}(SO_4)$ vibrational mode of covalently bonded sulfate groups (Figure 5.14). This band downward shifts by around 10 cm^{-1} at θ_{max}, but the shift is reversible upon CO removal. This observation suggests that the sulfate groups play an active role in defining the ligand sphere of both Ni^{2+} and Al^{3+} Lewis sites, and are flexible enough to allow the entrance of additional molecules such as CO.

5.3.3 Reactivity towards C_2H_4 Followed by Spectroscopic Methods

Successively, the reactivity of all the catalysts towards ethylene at room temperature was investigated by means of in-situ FT-IR and DR UV-Vis spectroscopies, aimed to understand the initiation step and the deactivation mechanism. FT-IR spectra were recorded in the presence of ethylene at room temperature at a time resolution of 2 minutes and the reactivity was followed for 12 hours. For bare γ-Al_2O_3, 8-NiO and 10-Re samples no changes were observed in the FT-IR spectra before and after introduction of ethylene, indicating that these samples were not active in ethylene conversion, in agreement with previous work[58]. In contrast, FT-IR spectroscopy revealed that the 8-S,

8-NiS, 8-Ni-8-Re and 8-Re-8-Ni catalysts were active towards ethylene. Hence, the presence of sulfate anions seems fundamental to the development of activity towards ethylene at room temperature. Figure 5.15 shows the time-resolved FT-IR spectra collected within the first 4 hours of the reaction of 8-S, 8-Ni, and 8-Ni-8-Re with ethylene (equilibrium pressure P_{C2H4} = 10 mbar within the first 2 hours, increased to 40 mbar in the successive 2 hours). It is evident that the three systems behave in different ways, 8-S being the most diverse one.

Starting the discussion with 8-S (Figure 5.15ab), a complex series of absorption bands gradually grow up in the presence of ethylene, indicating the presence of saturated alkyl groups, and certainly of methyl groups. The spectra are characterized by three resolved absorption bands in the $\nu(CH_x)$ region at 2960 cm^{-1} ($\nu_{asym}(CH_3)$), 2928 cm^{-1} ($\nu_{asym}(CH_2)$) and 2871 cm^{-1} ($\nu_{sym}(CH_3)$), along with a broad band due to the $\delta_{asym}(CH_2)$ vibrational mode (a doublet at 1477 and 1468 cm^{-l}). Moreover, two bands at 1383 and 1367 cm^{-l} overlap into the intense bands due to the vibrations of the sulfate anion. These bands are assigned to the $\delta_{sym}(CH_3)$ vibrational mode of $>C(CH_3)_2$ species and are indicative of branching[59, 60]. In addition to these absorption bands, two weak bands are observed around 1671 cm^{-1} and 1618 cm^{-1}, which are likely due to ν(C=C) vibrational modes. All the above-mentioned absorption bands grow at the same rate along the whole investigated time interval, except for the band at 1618 cm^{-1}, which appears immediately after contact with ethylene and then remains almost constant during the reaction. As a whole, the time-resolved FT-IR spectra indicate the formation of branched oligomers.[61, 62] As a final observation, the very intense $\nu_{asym}(SO_4)$ absorption band originally centered around 1400 cm^{-1} gradually downward shifts during the reaction of ethylene, indicating that the $[SO_4]^{2-}$ anions are perturbed by the reaction products. In contrast, no great changes are observed in the ν(OH) region (not shown), where only the shoulder around 3710 cm^{-1} is eroded in favor of a band centered around 3650 cm^{-1}, indicating that reactivity has to be ascribed mainly to Lewis and not Bronsted acidity.

It is well known that sulfated alumina displays acidic properties and in general the presence of sulfate anions enhances the catalytic activity of alumina in acid-catalyzed reactions, such as olefin oligomerization and skeletal isomerization[63-65]. The accepted mechanism involves the formation of carbocationic species[64, 66]. Carbocations may be

generated in a number of ways, involving both Brønsted acid sites and Lewis acid sites. The products formed in the initiation stage are the thermodynamically more stable secondary or tertiary carbocations, and this explains why branched species are observed in our experiments. Propagation involves the repeated additions of ethylene to the carbocationic center, which in principle, may migrate well away from the site of initial attack. Carbocations are very reactive species and, in absence of super-acids, they terminate quickly. The principal mechanism for termination is a chain-transfer process involving deprotonation of the carbocationic end-group by an incoming monomer, aided by the anion ($[SO_4]^{2-}$ in our case). Sulfated alumina is not sufficiently acidic to stabilize the carbocationic species and this justifies the observation of vinyl terminations (ν(C=C) bands around 1650 cm^{-1}). Moreover, it is also clear that sulfate anions play a vital role, not only in enhancing the acidity of alumina, but also in guiding the termination process. The involvement of the $[SO_4]^{2-}$ anions in the reaction is affirmed by the perturbation of the corresponding absorption bands.

A different spectra evolution is observed for both 8-NiS and 8-Ni-8-Re catalysts. At a short contact time, the FT-IR spectra are very similar to those observed for the 8-S catalyst, although less intense, indicating the acid-catalyzed formation of branched oligomers. However, after about 30-40 minutes the absorption bands associated with vibrational modes involving CH_2 groups start to grow faster (and slightly shift to lower wavenumber values) than those related to CH_3 groups. The phenomenon is more evident for 8-NiS than for 8-Ni-8-Re. As a consequence, the spectra collected after 40 minutes of reaction resemble those of aliphatic hydrocarbons with linear chain-like structure and a few branches. Simultaneously, in the ν(C=C) region the band at 1671 cm^{-1} grows at a higher rate than that at 1618 cm^{-1}. The intense absorption band around 1400 cm^{-1} ascribed to $\nu_{asym}(SO_4)$ vibration downward shifts even more than for 8-S sample.

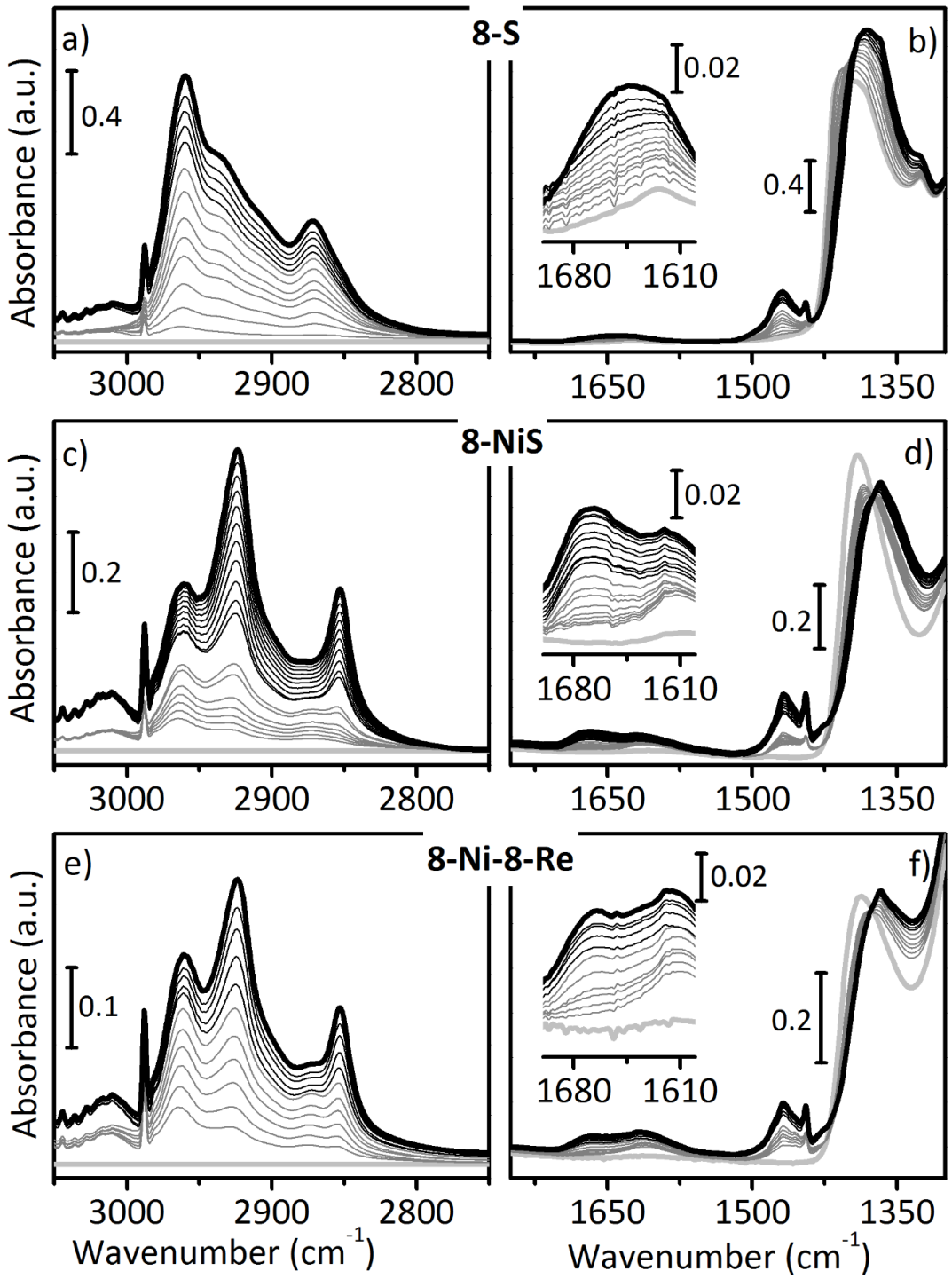

Figure 5.15. Time-resolved FT-IR spectra collected during reaction of ethylene at room temperature with 8-S, 8-NiS, and 8-Ni-8-Re catalysts. Parts a), c) and e) display the 3100 – 2700 cm^{-1} region, where ν(CH_x) absorption bands are observed. Parts b), d) and f) show the 2000 – 1300 cm^{-1} region, where ν(C=C), δ(CH_x) and ν(SO_4) bands contribute to the spectra. The insets zoom in the 1700 – 1600 cm^{-1} region, where the bands are attributed to ν(C=C).

The CH_2/CH_3 intensity ratio may give a rough estimation of the structure of the oligomeric products[59, 67]. With this aim, the FT-IR spectra collected during ethylene reaction on the three catalysts were analyzed by curve-fitting in the 3000 – 2700 cm^{-1}

region, by using five gaussian curves centered at 2960 cm^{-1} ($\nu_{asym}(CH_3)$), 2930 cm^{-1} ($\nu_{asym}(CH_2)$), 2900 cm^{-1} ($\nu(CH)$), 2871 cm^{-1} ($\nu_{sym}(CH_3)$), and 2853 cm^{-1} ($\nu_{sym}(CH_2)$). A CH_2/CH_3 ratio was calculated based on the $\upsilon_{asym}(CH_2)$ and $\upsilon_{asym}(CH_3)$ bands at 2960 and 2930 cm^{-1} and the extinction coefficient of $\epsilon(CH_3)/\epsilon(CH_2)$ was chosen as approximately 2.2, obtained from a reference measurement of n-heptane in CCl_4[61]. It is important to notice that the only reflects an average value for a complex distribution of all products and not a single product. An increase in the CH_2/CH_3 intensity ratio indicates that the aliphatic chains are becoming longer or less branched. In contrast, if the aliphatic chains are short or more branched, the CH_2/CH_3 ratio is low. The evolution of the CH_2/CH_3 ratio as a function of the reaction time is shown in Figure 5.16. For 8-S, the CH_2/CH_3 ratio maintains at approximately one during the whole reaction time, indicating that the nature of the branched oligomers remains constant. Attempts to extract the products of reactions failed, in that only ethylene was detected in the extraction solution. Hence, the acid catalyzed oligomerization products are difficult to extract, possibly because of cationic interaction with the catalyst surface.

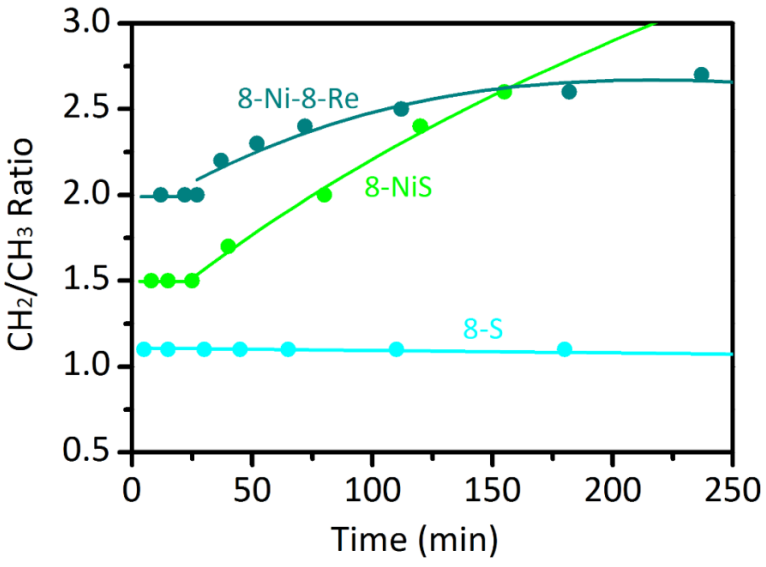

Figure 5.16. Evolution of the CH_2/CH_3 ratio versus reaction time as determined by the analysis of the FT-IR spectra collected during reaction of ethylene (10 mbar) at room temperature over 8-S, 8-NiS and 8-Ni-8-Re catalysts.

In contrast, for 8-NiS and 8-Ni-8-Re the CH_2/CH_3 ratio stays constant only during the first 40 minutes of reaction, followed by an increase. The increase was more pronounced for 8-NiS than for 8-Ni-8-Re. The different starting CH_2/CH_3 ratios of 8-NiS and 8-Ni-8-Re reflect that the reaction products are dependent on the functional metal sites, which well supports the previous catalytic tests in a continuous flow reactor[58]. This data also

indicates that after 40 minutes of reaction long-chain aliphatic hydrocarbons start to be formed and stick to the surface of both catalysts. These long hydrocarbon chains may be responsible for the fast deactivation previously observed in catalytic tests[58]. Formation of long-chain oligomers with a few branches on 8-NiS has been confirmed by GC-MS analysis of spent catalyst extracted in CH_2Cl_2 solution (273 K) after two hours reaction in contact with ethylene at room temperature. The long chain aliphatic products could be formed by an ethylene oligomerization reaction and a side dimerization/oligomerization reaction of olefinic products. Since Ni sites are responsible for the formation of linear olefin products, it is believed that the long chain products are mainly attributed to the $NiSO_4$ sites. Slow increase of the CH_2/CH_3 ratio for 8-Ni-8-Re shows the formation of shorter chain length or more branched by-products, which illustrates the function of the Re sites for metathesis.

The same experiment was followed by means of DR UV-Vis-NIR spectroscopy, which reveals only very small changes during ethylene reaction. Figure 5.17 shows the most relevant DR UV-Vis-NIR spectra for the 8-NiS sample as an example. Upon ethylene dosage in the reaction cell, very few changes are observed in the UV-Vis-NIR spectrum: the d-d bands centered around 7000 and 17000 cm^{-1} slightly decrease in intensity, while the charge transfer band around 35000 cm^{-1} increases. Accordingly, the coordination environment of the Ni sites changes only slightly in the presence of ethylene. This observation that seems in contrast with the expected increase in the ligand field around the Ni sites upon ethylene adsorption might actually be explained in terms of ligand displacement, i.e. ethylene displays other ligands (the sulfate anions) originally present around the Ni sites, in agreement with the FT-IR results. After prolonged reaction time, a weak band appears around 25000 cm^{-1}, which may be assigned to the carbocationic conjugated olefinic double-bond [68, 69].

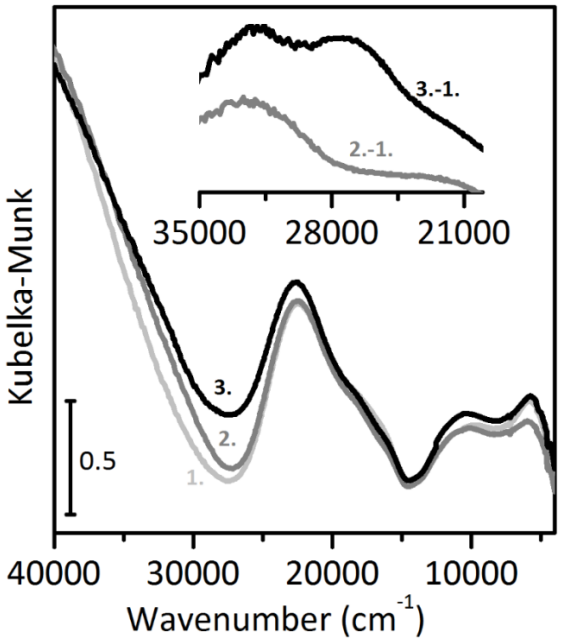

Figure 5.17. DR UV-Vis-NIR spectra of (1) 8-NiS after activation, (2) immediately after dosage of ethylene, (3) after an overnight reaction in presence of ethylene at room temperature. The inset shows spectra after subtraction of spectrum (1).

5.3.4 Investigation of the Oxidation State of the Active Ni Sites

In our previous FT-IR study at low temperature, Ni^+ was not observed on 8-NiS after thermal activation. As mentioned in Chapter 2, T. X. Cai[1] and J. R. Sohn[3] confirmed the reduction of Ni^{2+} to Ni^+ on the activated $NiSO_4$/γ-Al_2O_3 catalyst by means of FT-IR, EPR and XPS. Similar experiments have been conducted by us, in order to better clarify the oxidation state of the Ni sites after catalyst activation.

T. X. Cai[1] and J. R. Sohn[3] reported the observation of $Ni^+(CO)_2$ species based on the IR spectra of CO adsorbed on activated $NiSO_4$/ γ-Al_2O_3. The authors concluded that bands at 2170 and 2122 cm^{-1} represented a $Ni^+(CO)_2$ species. FT-IR experiment at room temperature have also been carried out by us and the spectra are presented in Figure 5.18. All the samples were pretreated at 673 K for 1 hour under vacuum before CO adsorption and spectra were collected during stepwise desorption of CO at room temperature. Spectra of Al_2O_3 and 8-S (see Figure 5.18a and b) demonstrate similar features. Two bands obtained at 2171cm-1 and 2117cm-1 disappear by outgassing, which are the typical bands of P and Q rotation branches of gaseous CO. In the spectra of 8-NiS (see Figure 5.18c), a band appears at 2200 cm^{-1} shifting to 2213 cm^{-1} upon CO

outgassing. This band is assigned to the stretching vibration of CO adsorbed on the Ni^{2+} ions. However, the other two bands (2170 and 2115 cm^{-1}) are clearly due to the gas phase of CO and that is in good agreement with the observation in Al_2O_3 and 8-S. In this FT-IR study, we do not observe Ni^{+} after catalyst activation at 673 K.

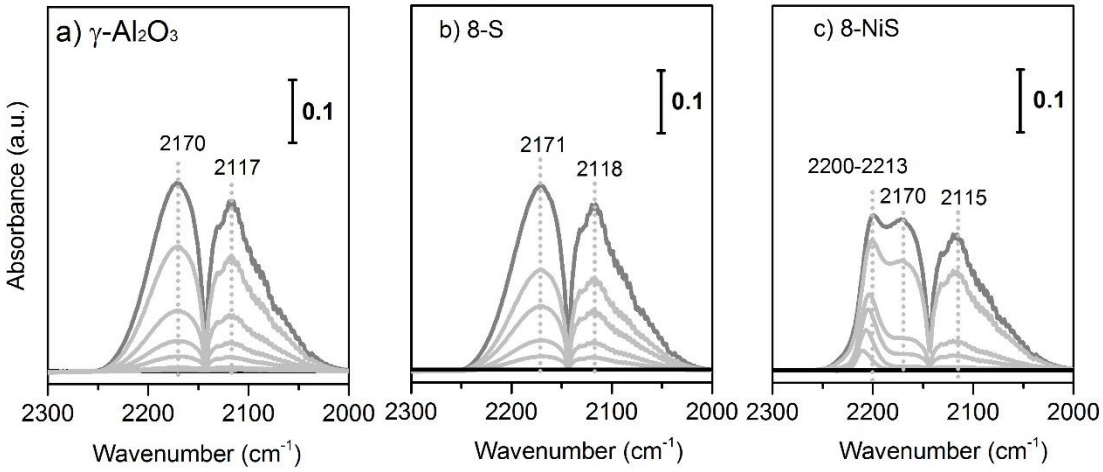

Figure 5.18: IR spectra of CO adsorbed over a series of catalysts pretreated at 673 K for 1 hour under vacuum, in the presence of CO (400-500 mbar) at room temperature.

The Ni 2p XPS spectra of fresh and activated 8-NiS catalyst are shown in Figure 5.19(a). The spectrum of the fresh catalyst (Figure 5.19a, spectrum 1) shows the Ni $2p_{3/2}$ and Ni $2p_{1/2}$ core level lines at 856.8 and 875 eV and the shake-up satellites at the typical 6eV binding energy difference relative to the corresponding main lines[70]. This line pattern is attributed to the presence of Ni^{2+} ions on γ-Al_2O_3, and is in good agreement with the results reported by P. Dufresne[71] and D. Nikolova[72]. The spectrum of 8-NiS does no change after calcination for 1 hour at 473 K (Figure 5.19a, spectrum 2). A slight peaks shift to lower binding energy of about 0.4 eV is observed after thermal activation at 673 K (Figure 5.19a, spectrum 3). This shift indicates a small change in the electronic structure of the Ni ions, likely as a consequence of the changes occurring to the adjacent sulfate ions or surface hydroxyl groups, but is not compatible with the reduction of Ni^{2+} to Ni^{+} sites. Indeed, the energy difference of Ni $2p_{3/2}$ lines for reference Ni^{0} vs Ni^{2+} species is approximately 2.3 eV, as reported for Ni/Al_2O_3 or Ni/SiO_2 systems.[73, 74] Hence, in the adopted experimental conditions, the Ni^{2+} sites preserve their oxidation state also after catalyst activation. . In the following test, the spent catalyst from the continuous flow reactor test was directly transferred into the analysis chamber of XPS in a glove box without contacting air. The spectrum of the spent catalyst (Figure 5.19, spectrum 4) still

keeps the same line patterns as that of the fresh catalyst. Therefore, it is evident that Ni^{2+} is not reduced to Ni^{+} or metallic Ni on the 8-NiS catalyst after the reaction.

This is further confirmed by the EPR measurements. Indeed, the EPR spectrum of activated 8-NiS catalyst (Figure 5.19b, spectra 2 and 3) is the same as for the fresh catalyst, despite a higher resolution obtained by measurement at liquid nitrogen temperature. This indicates that Ni^{+} is not produced during catalyst activation at 673 K.

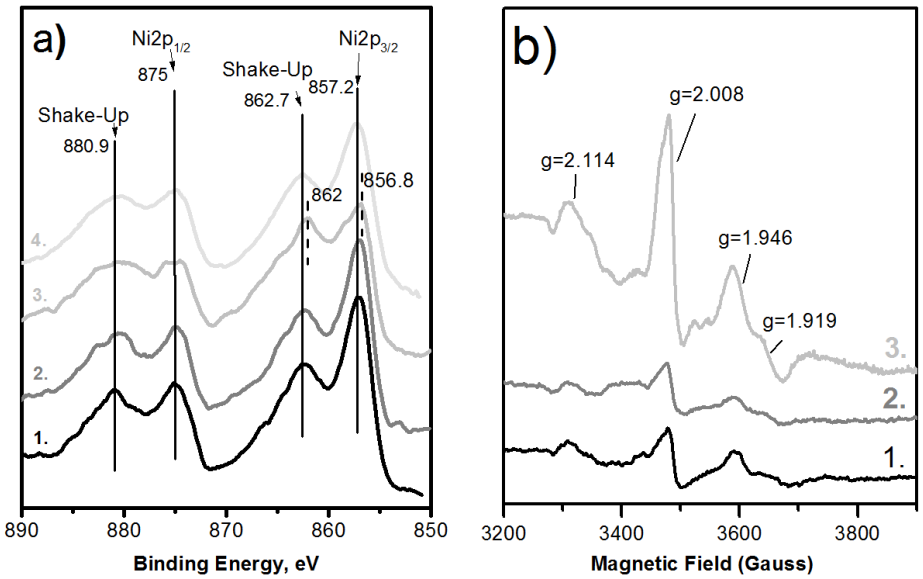

Figure 5.19: Part a) Ni 2p XPS spectra of 8-NiS (1) as made; (2) thermally activated at 473K; (3) thermally activated at 673K; (4) spent catalyst. Part b) EPR spectra of 8-NiS (a) as made; (b) thermally activated at 673K and measured at room temperature; (c) thermally activated at 673K and measured at liquid nitrogen temperature.

5.4 Conclusions

It was found that the sulfate ions play an essential role in increasing the acidity of the Al_2O_3 surface (as demonstrated by FT-IR spectroscopy of CO adsorbed at 100 K), and also in influencing the electronic structure of the Ni cations. During thermal catalyst activation the sulfate ions are covalently bonded either to Ni^{2+} or/and Al^{3+} cations. Unexpected and in contrast to earlier reports[1, 3], the Ni cations retain the +2 oxidation state also after the catalyst activation step, as shown directly by EPR and XPS analysis, and indirectly by FT-IR spectroscopy of CO adsorbed at 100 K and room temperature.

FT-IR experiments performed in presence of ethylene at room temperature and low pressure (40 mbar) allowed to monitor the initial steps of the reaction on the different

catalysts. It was proved that sulfated alumina promotes the slow formation of branched oligomers through a carbocationic mechanism. The sulfate ions covalently bonded to the Ni^{2+} (or Al^{3+}) sites are partially displaced during the reaction, as testified by the perturbation of the corresponding IR absorption bands. In presence of the Ni^{2+} function, formation of long chain hydrocarbons is observed at longer reaction times. It is concluded that deactivation of the $NiSO_4$-ReO_x/Al_2O_3 catalysts is mainly the consequence of absorption of higher linear ethylene oligomers or due to Ni^{2+} sites not being anymore in interaction with the sulfate ions. Improvements in the catalyst lifetime could be achieved by limiting the mobility of the sulfate anions or utilizing another reactor technology, such as e.g. a slurry reactor[75].

Reference

1. Cai, T., Cao, D., Song, Z., Li, L., *Appl. Catal. A- Gen*, 95 (1993) L1-L7.
2. Sohn, J.R., Park, W.C., Park, S.-E., *Catal. Lett.*, 81 (2002) 259-264.
3. Sohn, J.R., Park, W.C., *Appl. Catal., A*, 239 (2003) 269-278.
4. Sohn, J.R., *Catal. Surv. Asia*, 8 (2004) 249-263.
5. Wendt, G., Fritsch, E., Deininger, D., Schoellner, R., *React. Kinet. Catal. Lett.*, 16 (1981) 137-141.
6. Wendt, G., Jusek, M., Hagenau, K., Kiessling, D., Schoellner, R., *Geterog. Katal.*, 5th, Pt. 1 (1983) 249-254.
7. Beller, M., *A Personal View on Important Developments in Homogeneous Catalysis*, Basic Principles in Applied Catalysis, Springer Berlin Heidelberg, Berlin, Heidelberg, 2004, 363-401.
8. Cai, T., *Catal. Today*, 51 (1999) 153-160.
9. Sohn, J.R., Ozaki, A., *J. Catal.*, 59 (1979) 303-310.
10. Wendt, G., Fritsch, E., Deininger, D., Schöllner, R., *React. Kinet. Catal. Lett.*, 16 137-141.
11. Hogan, J.P., Banks, R.L., Lanning, W.C., Clark, A., *Ind. Eng. Chem.*, 47 (1955) 752-757.
12. Uchida, H., Imai, H., *Bull. Chem. Soc. Jpn.*, 35 (1962) 989-995.
13. Lallemand, M., Finiels, A., Fajula, F., Hulea, V., *J. Phys. Chem. C*, 113 (2009) 20360-20364.
14. Ng, F.T.T., Creaser, D.C., *Appl. Catal. A- Gen*, 119 (1994) 327-339.
15. Ghosh, A.K., Kevan, L., *J. Phys. Chem.*, 94 (1990) 3117-3121.
16. Heveling, J., van der Beek, A., de Pender, M., *Appl. Catal.*, 42 (1988) 325-336.
17. Finiels, A., Fajula, F., Hulea, V., *Catal. Sci. Technol.*, 4 (2014) 2412-2426.
18. Knozinger, H., Huber, S., *J. Chem. Soc., Faraday Trans.*, 94 (1998) 2047-2059.
19. Coluccia, S., Marchese, L., Martra, G., *Microporous Mesoporous Mater.*, 30 (1999) 43-56.
20. Coluccia, S., Marchese, L., Martra, G., *Res. Chem. Intermed.*, 26 (2000) 1-5.
21. Lamberti, C., Zecchina, A., Groppo, E., Bordiga, S., *Chem. Soc. Rev.*, 39 (2010) 4951-5001.
22. Priecel, P., Kubička, D., Čapek, L., Bastl, Z., Ryšánek, P., *Appl. Catal. A- Gen*, 397 (2011) 127-137.
23. Pazè, C., Sazak, B., Zecchina, A., Dwyer, J., *J. Phys. Chem. B*, 103 (1999) 9978-9986.
24. Garbarino, G., Sanchez Escribano, V., Finocchio, E., Busca, G., *Appl. Catal., B*, 113-114 (2012) 281-289.
25. Kiricsi, I., Förster, H., Tasi, G., Nagy, J.B., *Chem. Rev.*, 99 (1999) 2085-2114.
26. Yang, S., Kondo, J.N., Domen, K., *Catal. Today*, 73 (2002) 113-125.
27. Lepetit, C., Che, M., *J. Phys. Chem.*, 100 (1996) 3137-3143.
28. Stuart, B.H., *Infrared Spectroscopy: Fundamentals and Applications.* Wiley, 2004.
29. George, W.O., Mcintyre, P.S., *Infrared Spectroscopy.* John Wiley & Sons, London, 1987.
30. Robinson, J.W., *Undergraduate Instrumental Analysis.* Marcel Dekker, Inc., New York, 1994.
31. Wagner, J.M., *Chemical Engineering Methods and Technology: X-Ray Photoelectro Spectroscopy.* Nova Science Publishers, 2010.
32. Bruce, D.W., O'Hare, D., Walton, R.I., *Inorganic Materials Series: Local Structual Characterisation.* John Wiley & Sons, New York, 2013.

33. Wolf, R.A., *Atmospheric Pressure Plasma for Surface Modification.* John Wiley & Sons, 2012.
34. Van der Heide, P., *X-Ray Photoelectro Spectroscopy: An Introduction to Principles and Practices.* Jonh Wiley & Sons, 2011.
35. Brustolon, M.R., *Electron Paramagnetic Resonance: A Practitioner's Toolkit.* Wiley, 2009.
36. Schäfer, R., Schmidt, P.C., *Methods in Physical Chemistry.* 2nd ed., John Wiley & Sons, 2012.
37. Morterra, C., Magnacca, G., *Catal. Today*, 27 (1996) 497-532.
38. Peak, D., Ford, R.G., Sparks, D.L., *J. Colloid Interface Sci.*, 218 (1999) 289-299.
39. Saur, O., Bensitel, M., Saad, A.B.M., Lavalley, J.C., Tripp, C.P., Morrow, B.A., *J. Catal.*, 99 (1986) 104-110.
40. Edreva-Kardjieva, R.M., Vuurman, M.A., Mol, J.C., *J. Mol. Catal.*, 76 (1992) 297-305.
41. Sendoda, Y., Ono, Y., Keii, T., *J. Catal.*, 39 (1975) 357-362.
42. Lever, A.B.P., *Inorganic Electronic Spectroscopy.* 2nd ed., Elsevier: Amsterdam, 1984.
43. Cornet, C.H., J.F.; Mariette, C., *Nouv. J. Chim.*, 8 (1984) 159-164.
44. Davydov, A., Kantcheva, M., Chepotko, M., *Catal. Lett.*, 83 (2002) 97-108.
45. Berthomieu, C., Hienerwadel, R., *Photosynth. Res.*, 101 (2009) 157-170.
46. Vimont, A., Thibault-Starzyk, F., Daturi, M., *Chem. Soc. Rev.*, 39 (2010) 4928-4950.
47. Garbarino, G., Romero Perez, A., Finocchio, E., Busca, G., *Catal. Commun.*, 38 (2013) 67-73.
48. Jensen, M.B., Morandi, S., Prinetto, F., Sjaastad, A.O., Olsbye, U., Ghiotti, G., *Catal. Today*, 197 (2012) 38-49.
49. Montanari, T., Castoldi, L., Lietti, L., Busca, G., *Appl. Catal. A- Gen*, 400 (2011) 61-69.
50. Tsyganenko, A.A., Zverev, S.M., *React. Kinet. Catal. Lett.*, 36 (1988) 269-274.
51. Eischens, R.P., Francis, S.A., Pliskin, W.A., *J. Phys. Chem.*, 60 (1956) 194-201.
52. Mekhemer, G.A.H., Khalaf, H.A., Mansour, S.A.A., Nohman, A.K.H., *Monatshefte für Chemie / Chemical Monthly*, 136 (2005) 2007-2016.
53. Arata, K., Hino, M., *Appl. Catal.*, 59 (1990) 197-204.
54. Yang, T.-s., Chang, T.-h., Yeh, C.-t., *J. Mol. Catal. A: Chem.*, 123 (1997) 163-169.
55. Jin, T., Yamaguchi, T., Tanabe, K., *J. Phys. Chem.*, 90 (1986) 4794-4796.
56. Hadjiivanov, K., Knözinger, H., Mihaylov, M., *J. Phys. Chem. B*, 106 (2002) 2618-2624.
57. Hadjiivanov, K.I., Vayssilov, G.N., *Adv. Catal.*, 47 (2002) 307-511.
58. Li, L., Palcheva, R., Jens, K.-J., *Top. Catal.*, 56 (2013) 783-788.
59. Bauer, F., Karge, H.G., *Characterization of Coke on Zeolites.* Springer Berlin Heidelberg, Heidelberg, 2007.
60. Karge, H., Geidel, E., *Vibrational Spectroscopy.* Springer Berlin Heidelberg, Heidelberg, 2004.
61. Bjørgen, M., Lillerud, K.-P., Olsbye, U., Bordiga, S., Zecchina, A., *J. Phys. Chem. B*, 108 (2004) 7862-7870.
62. Spoto, G., Bordiga, S., Ricchiardi, G., Scarano, D., Zecchina, A., Borello, E., *J. Chem. Soc., Faraday Trans.*, 90 (1994) 2827-2835.
63. Smirnova, M.Y., Toktarev, A.V., Ayupov, A.B., Echevsky, G.V., *Catal. Today*, 152 (2010) 17-23.
64. Ferreira, M.a.L., Rueda, E.H., *J. Mol. Catal. A: Chem.*, 178 (2002) 147-160.
65. Wang, J.-H., Mou, C.-Y., *Appl. Catal. A- Gen*, 286 (2005) 128-136.
66. Hwang, C.-C., Mou, C.-Y., *J. Phys. Chem. C*, 113 (2009) 5212-5221.

67. Igisu, M., Ueno, Y., Shimojima, M., Nakashima, S., Awramik, S.M., Ohta, H., Maruyama, S., *Precambrian Res.*, 173 (2009) 19-26.
68. Forster, H., Seebode, J., Fejes, P., Kiricsi, I., *J. Chem. Soc., Faraday Tran. 1*, 83 (1987) 1109-1117.
69. Kiricsi, I., Förster, H., Tasi, G., *Stud. Surf. Sci. Catal.*, Volume 46 (1989) 355-364.
70. de Jesús, J.C., Pereira, P., Carrazza, J., Zaera, F., *Surf. Sci.*, 369 (1996) 217-230.
71. Dufresne, P., Payen, E., Grimblot, J., Bonnelle, J.P., *J. Phys. Chem.*, 85 (1981) 2344-2351.
72. Nikolova, D., Krstić, J., Spasov, L., Simeonov, D., Lončarević, D., Stefanov, P., Jovanović, D., *Russ. J. Phys. Chem.*, 85 (2011) 2380-2385.
73. van Looij, F., Geus, J.W., *J. Catal.*, 168 (1997) 154-163.
74. Manukyan, K.V., Cross, A.J., Yeghishyan, A.V., Rouvimov, S., Miller, J.J., Mukasyan, A.S., Wolf, E.E., *Appl. Catal. A- Gen*, 508 (2015) 37-44.
75. Zhang, Q., Kantcheva, M., Dalla Lana, I.G., *Ind. Eng. Chem. Res.*, 36 (1997) 3433-3438.

Chapter 6

6 A Feasibility study of Regeneration of the Coke Deactivated catalysts

6.1 Introduction

Catalyst deactivation is inevitable and costly for most industrial processes, despite significant efforts to postpone, alleviate or avoid the issue[1]. Catalyst change out requires process shutdown leading to potential product revenue loss in combination with personnel and material costs. Consequently, catalyst deactivation and regeneration is a topic of great interest.

Coke deactivated catalysts are usually regenerated by burning of coke in the presence of oxidative reactants (e.g. O_2 , H_2O, etc.)[2]. Although removal of carbon with oxygen is generally very rapid, air/N_2 regeneration is typically employed in industrial processes (e.g. catalytic cracking, hydro-treating process and catalytic reforming), in order to avoid hot spots or over heating temperatures that could modify surface structures or destroy the catalyst[3]. Coke combustion temperatures are closely related to its C/H ratio[4]. For example, metal-catalyzed hydrogen-rich residue can be removed with steam at temperatures below 673 K. In contrast, carbonaceous deposits having a more graphic structure or less reactive properties may require temperatures above 973 K. Such high regeneration temperature may be accompanied by sintering or destruction of the catalyst surface[1].

In the previous Chapter, the causes of catalyst deactivation was investigated by means of FT-IR and UV-Vis-NIR spectroscopies. We found that deactivation of the Ni-Re catalyst was accompanied by formation of long aliphatic hydrocarbon chains depositing on the catalyst surface and this was driven by $NiSO_4$ responsible dimerization reaction. Therefore, regeneration of the deactivated catalyst focuses on the 8-NiS catalysts at first. For $NiSO_4$/γ-Al_2O_3 catalysts, little is known about the deactivation mechanism, although this catalyst class has been reported several times for giving high ethylene

dimerization activity[5, 6]. Generally, for reactions involving hydrocarbons and especially olefinic hydrocarbons, the rate and extent of coke formation on metal oxide catalysts increases with increasing acid strength and concentration[1]. However, Ni-modified metal oxides without sufficient acid strength exhibit no activity for ethylene dimerization[7], as also observed in our study.

Deposition of hydrogen-rich residues can be easily reversed by gasification with air at around 600 K[1, 8]. Therefore, we investigated regeneration of spent catalysts by purging a deactivated catalyst with a mixture of nitrogen (79%) and oxygen (21%) at 673 K. The long chain hydrocarbons, being hydrogen rich, were expected to be burned off in synthetic air at a temperature of around 600 K. TG-MS analysis and FT-IR were used to monitor the process of catalyst regeneration. Lastly, a HRTEM study was conducted to analyze elemental distribution and surface morphology of the regenerated catalyst.

6.2 Experimental Section

6.2.1 Thermogravimetric-Mass Spectrometer (TG-MS)

A combination of TGA with MS is an advanced technique to investigate thermal behavior of materials and analyze their interactions with probe molecules. TG-MS allows the gaseous products to be detected simultaneously.

A Thermal gravimetric analysis of deactivated catalysts was carried out in a Rheometric Scientific STA 1500 instrument. As described in Chapter 5, powder samples of deactivated catalysts were obtained from a static reactor after 24 hours ethylene reaction at 323 K. The TGA was equipped with an online mass spectrometer (Pfeiffer Omnistar) and effluent gas was analyzed by mass scanning from 1 to 100 m/z. The MS started to analyze the gas from the TGA at the same time when the TGA began to work and the scanning frequency was set to one minute. Around 20 mg of each sample was used and heated to 1273 K with a heating rate of 5K/min in a mixture flow of oxygen (21%) and nitrogen (79%). Besides, a blank TG-MS experiment was also conducted for the fresh catalyst under the same conditions. TG-MS experiments were performed in inGAP center, University of Oslo.

6.2.2 Fourier Transmission Infrared Spectrometry (FT-IR)

Unlike the IR experiments described in the previous chapter, this in-situ FT-IR experiment was carried out in a continuous gas flow. Spectra were recorded by a Bruker Vertex 70 spectrometer equipped with a mercury cadmium telluride cryo-detector equipped with a Harrick in-situ FT-IR cell. As mentioned, this cell enabled work at a high temperature. Two thermocouples were inserted into the center of the cell where the sample holder is and a thermal controller controlled cell temperatures from 293 K to 723 K. Cell windows (CaF_2) were protected by cooling water. The sample was compressed into a thin wafer and placed in the cell connected to a gas distribution panel consisting of three gas flow lines (nitrogen, air and ethylene) shown in Figure 6.1. This gas distribution panel was designed for pyridine and toluene adsorption experiments before this experiment, so a modification was needed to remove all the contaminated piping and add some bypasses avoiding a possible gas contamination. Figure 6.1 only demonstrates the lines employed for this FT-IR experiment. A cooling trap was mounted before the cell and placed in a box of dry ice in order to remove trace amounts of water in all the experimental gases. The flow rates of the three gases were controlled by the regular flow meters that were pre-calibrated for each gas by a digital flow calibrator. Spectra were collected in transmission mode. This experiment consisting of four stages was performed in the University of Oslo.

a) Activate the catalyst

One of the challenges in this experiment was to remove all moisture or water in the gas flow. This was necessary as FT-IR is very sensitive to water. Even small amounts of water can give rise to intense water related bands that perhaps overlap or hide other characteristic bands from the catalyst itself. Moreover, the cell can accommodate 80 ml of gas and it needs more time to be purged. Therefore, the cell was purged by nitrogen (5 ml/min) overnight at room temperature after transferring the pellet into it. The next day, the catalyst activation could be started by increasing the temperature by 50 K every half an hour until the temperature reached to 673 K. The catalyst was kept at that temperature for 2 hours.

b) Deactivate the catalyst

Ethylene (5 ml/min) was sent to the cell for 2 hours after the temperature of the cell was cooled down to 323 K. As a consequence the catalyst was expected to be completely deactivated. After that, nitrogen (10 ml/mins) was introduced to the cell to remove the residual ethylene from the pipe line as well as in the cell. In the meantime, the temperature of the cell was cooled down to the room temperature again.

c) Re-activate the catalyst

In the final stage, a mixture of oxygen (21%) and nitrogen (79%) was applied by a temperature program from 293 K to 673 K. The temperature was kept at 323 K, 373 K, 473 K, 573 K and 673 K for half an hour at each temperature. The entire course of the re-activation was recorded by FT-IR.

d) Test the re-activated catalyst

Ethylene (5 ml/min) was sent to the cell for 2 hours after the temperature of the cell was cooled down to 323 K, in order to test the activity of the re-activated catalyst.

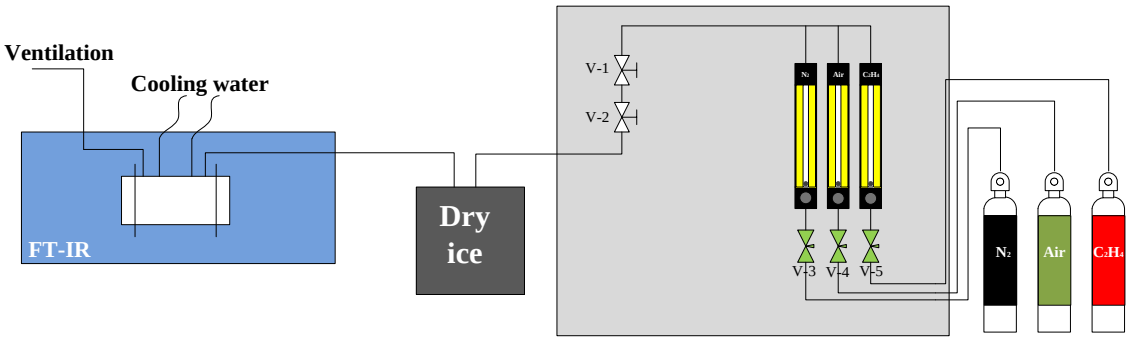

Figure 6.1: Experimental flow diagram of FT-IR system for a continuous gas flow test.

6.2.3 High Resolution Electron Microscopy (HRTEM)

High resolution electron microscopy (HRTEM) was carried out using a Jeol 3010-UHR electron microscope operating at 300 kV equipped with a LaB6 filament and with an Oxford Inca Energy TEM 300 EDS X-rays analyzer by Oxford Link. The powder samples were ground in an agate mortar and deposited on a copper grid covered with a lacey carbon film. The re-activated catalyst was obtained from the in-situ FT-IR experiment

described in this chapter. This experiment was operated by Maela Manzoli in the University of Torino.

6.3 Results and Discussion

It was concluded in chapter 5 that the catalyst deactivation is mainly caused by the $NiSO_4$ responsible dimerization reaction forming long chain hydrocarbons. Therefore, the effort was concentrated on the re-activation of the 8-NiS catalyst. A common way to remove these hydrocarbons is to burn them under O_2 or air at 623 K-873 K[1]. As this burn-off process is an exothermal reaction, burning under pure oxygen easily leads to a sudden temperature increase in some spots on the catalyst that may result in decomposition of $NiSO_4$. Thus, a mixture of oxygen and nitrogen in terms of their compositions in the air was applied. To start with, TGA analysis coupling with MS was performed on the deactivated 8-NiS catalysts. Moreover, a blank experiment was performed under the same conditions as well.

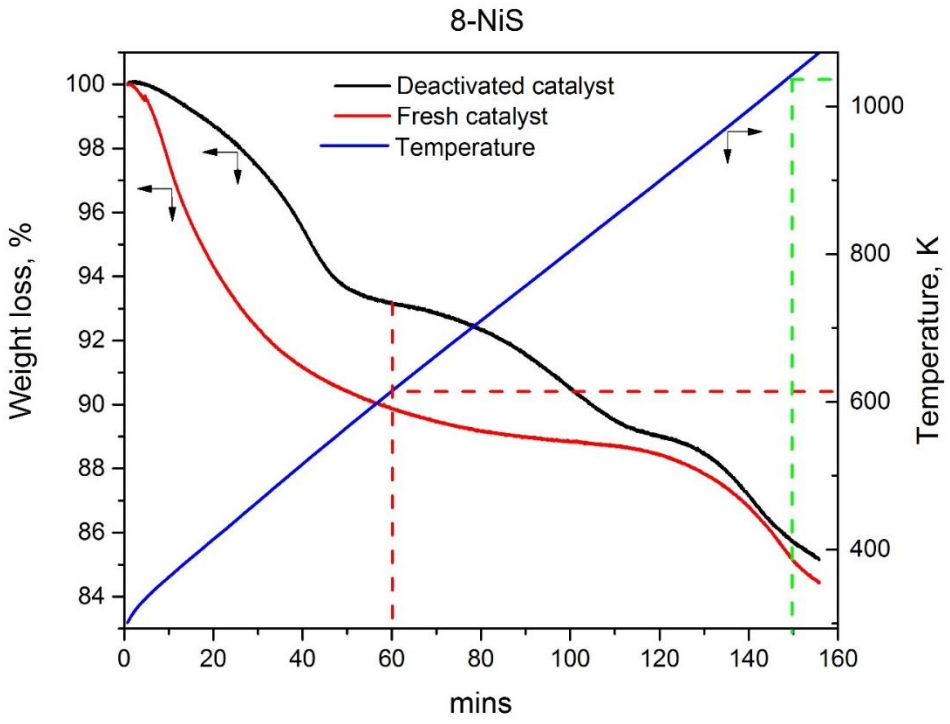

Figure 6.2: TGA analysis of re-activation process of deactivated 8-NiS catalyst and fresh catalyst (blank test) under mixing flows of nitrogen (79%) and oxygen (21%).

The trend of fresh 8-NiS TG-curve obtained in an atmosphere of synthetic air in Figure 6.2 is very similar to the 8-NiS curve collected under pure nitrogen flow in Figure

4.5. As mentioned in Chapter 4, thermal dehydration of $NiSO_4 \cdot 7H_2O$ to monohydrate $NiSO_4 \cdot H_2O$ occurs stepwise with increasing temperature and the last coordinated water molecule is evolved at quite a high temperature above 623 K[9]. Consequently, it can be seen in Figure 6.2 that the loss of coordinated water from hydrated nickel sulfate and hydroxyl groups from the Al_2O_3 surface proceeds at a wide temperature range. Moreover, weight loss at above 1003 K could be attributed to decomposition of anhydrous nickel sulfate, since the decomposition temperature is known to be around 1013-1173 K[9].

Furthermore, the MS signals of fresh 8-NiS, showed several high-intensity mass-to-charge lines which could be attributed to nitrogen, oxygen and impurities of these gases below 44 m/z; their intensities kept constant during the entire process. Moreover, it is necessary to point out that a weak signal presented at 44m/z was due to trace amounts of CO_2 in the mixing gas (O_2 and N_2). This signal remained at a steady level during the experiment. Furthermore, no signal of SO_3 and SO_2 was detected from 1013 K to 1073 K in the test. In the TG-curve, the decomposition process may have corresponded to a wide temperature range since a high heating rate (5 K/min) was applied in this experiment. Decomposition of anhydrous nickel sulfate was not complete at the temperature ranging from 1013 K to 1073 K and maybe only a very small amount of anhydrous nickel sulfate decomposed. Therefore, the produced SO_2 and SO_3 was probably below the detection limit of the MS detector.

The TG-curve of deactivated catalyst in Figure 6.2 can be divided into three regions according to the rate of the weight loss. During the first 60 minutes, the temperature increases from room temperature to around 623K and the weight loss is mainly associated with the evaporation of water molecules. During this period, considerably weak signals were observed in the range of 45-100 m/z and the signal at 44 m/z stayed at the same level as that of fresh 8-NiS in the blank test. This indicates that desorption or burning of the deposited hydrocarbons does not occur during this period. The mass scans of the effluent gas from the re-activation of deactivated 8-NiS in 80-150 minutes are plotted in Figure 6.3. In the middle period (80-120 minutes) there are several groups of signal mainly present at 54, 56, 70 and 84m/z. These signals could be assigned to fragments of the hydrocarbons, e.g. C_4H_8, C_5H_{10}, and C_6H_{12}, revealing that the weight

loss is largely due to desorption and evaporation of the deposited carbon species. In the third period (120-150 minutes), the CO_2 signal (44m/z) increases from 80 to 150 minutes and rises sharply from 130-150 minutes. In fact, this observation is unexpected, because hydrogen-rich hydrocarbons are expected to burn at temperatures around 600K under air[4]. The combustion temperature of coke depends on its location (external vs. internal deposits) and composition (i.e., H/C ratio). Hydrogen-poor coke species need a higher combustion temperature than the hydrogen-rich components.[4] The TG-MS analysis indicates that long-chain oligomers may convert further to highly condensed carbon species with low C/H ratios during the re-activation process, since oxidation of hydrocarbons start at quite a high temperature above 723 K. However, it seems such high temperatures would damage or destroy surface texture of the catalysts and might even cause decomposition of the nickel sulfate.

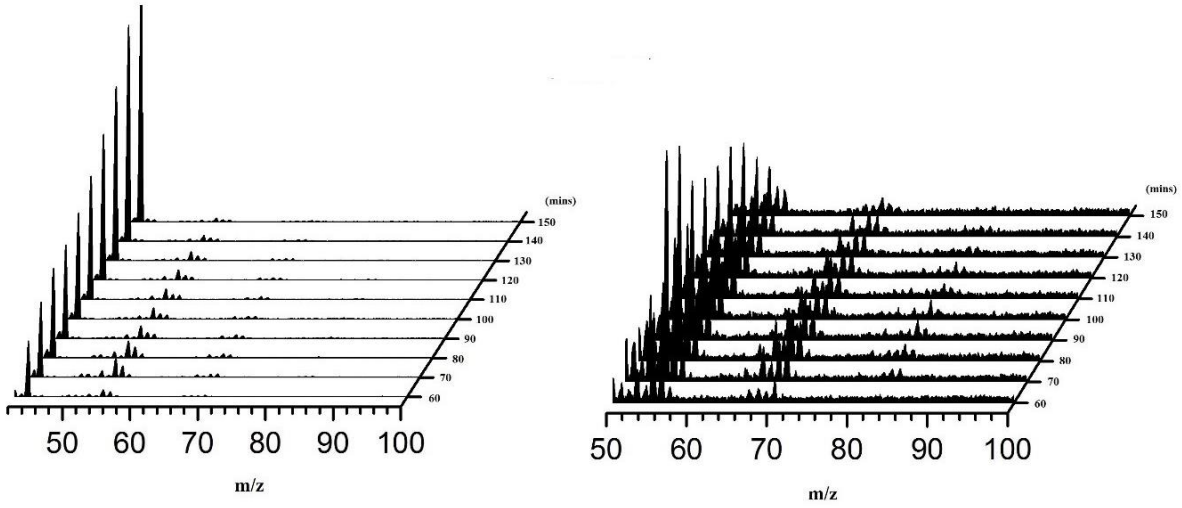

Figure 6.3: MS scanning (44-100m/z) of the effluent gas from the reactivation of deactivated 8-NiS catalyst in 80-150 minutes.

In order to determine the structural change of the hydrocarbons during the re-activation, a FT-IR experiment was carried out. Figure 6.4 shows spectra of deactivated catalyst in the re-activation process. The pellet of the 8-NiS catalyst was first thermally activated at 673 K for 2 hour under vacuum followed by deactivation by a two-hour exposure to a pure ethylene flow through the in-situ cell at 323 K. After that, the deactivated catalyst was heated from 323 K to 673 K under a flow of synthetic air. As

mentioned, burning of hydrocarbons is an exothermic reaction and $NiSO_4$ becomes unstable above 950 K. Thus, in order to avoid destruction of the surface structure on the catalyst during the re-activation process, the maximum re-activation temperature was only set up to 673 K. After the regeneration process, the pellet was removed from the cell and directly sent for a HRTEM measurement. The spectra are shown in Figure 6.4a, bands in the υ(C-H) vibrational region (2800-3000 cm^{-1}) are assigned to the asymmetric vibration of -CH_3 and -CH_2- (2960 and 2871cm^{-1}) groups, the symmetric vibration of -CH_3 and -CH_2- (2930 and 2853cm^{-1}) groups. These CH_X groups are indicative of long chain aliphatic hydrocarbons deposited on the catalyst during catalyst deactivation. These bands decrease and finally disappear with increasing regeneration temperature. However, these deposited hydrocarbons are not desorbed from the catalyst surface. They evolve and convert to coke, namely, carbonaceous species deficient in hydrogen[4]. A set of bands at low frequency from 1300 to1700cm^{-1} (Figure 6.4b) rise dramatically accompanying the disappearance of the bands in the υ(C-H) vibrational region. At low temperature (323 K-473 K), two bands at 1672 and 1465 cm^{-1}, originating from the υ(C=C) and δ(-CH_2-) bands increase gradually. At high temperature (473 K-673 K), a band at 1590cm^{-1} increases remarkably. This band reflects the complex nature of coke, which is assigned to highly unsaturated carbonaceous species[10-15] or to graphite deposits.[16] It can be speculated that side reactions (e.g. cracking) occur at high temperature generating highly condensed coke on the catalyst surface. Therefore, high temperature is necessary to remove this coke. In addition, the $\nu_{asym}(SO_4)$ band at around 1400 cm^{-1} is shifted downward by 20 cm^{-1} with increasing regeneration temperature, probably due to perturbation by the accumulated coke. In the previous FT-IR and DR UV-Vis-NIR studies, it was concluded that deactivation of the $NiSO_4$/γ-Al_2O_3 catalysts is due to the formed hydrocarbons not only blocking the active sites but also hindering the interaction between Ni^{2+} and [SO_4^{2-}]. In this case, the shift of $\nu_{asym}(SO_4)$ band indicates clearly that the bonding of Ni^{2+} and [SO_4^{2-}] becomes very weak in this re-activation process.

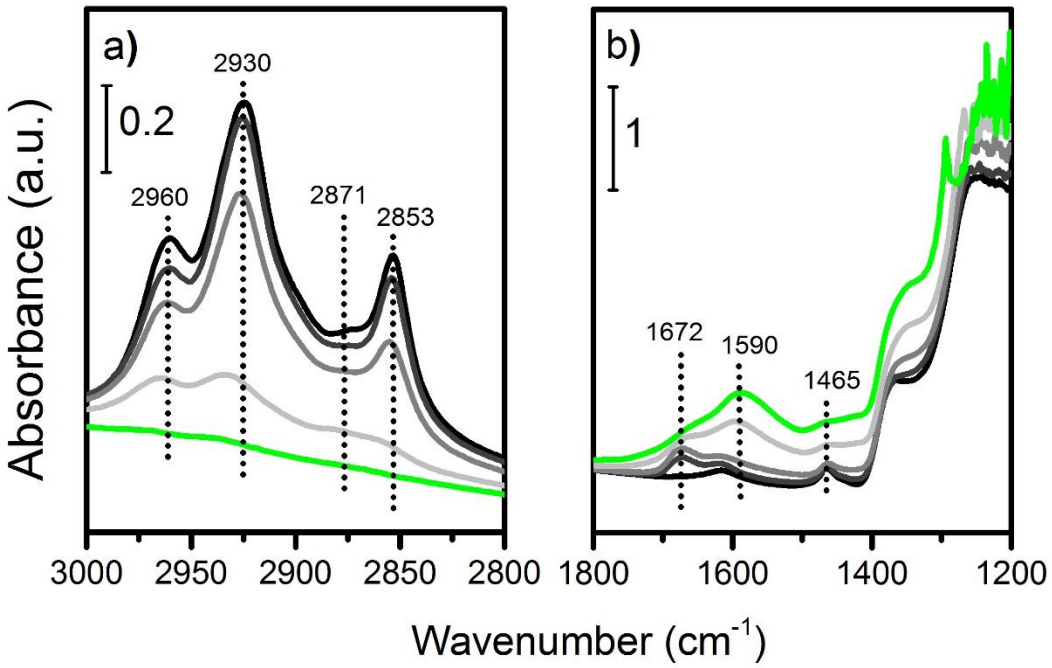

Figure 6.4: FT-IR spectra of activation of the deactivated catalyst under synthetic air with increasing temperature from 323K to 673K (323K (black), 373K (dark grey), 473K (grey), 573K (light grey) and 673K (green)). a) display the 3000 – 2800 region, where ν(CH_x) absorption bands are observed. b) show the 1800 – 1200 cm^{-1} region, where ν(C=C), δ(CH_x) and ν(SO_4) bands contribute to the spectra.

In order to verify the unsuccessful re-activation of the deactivated 8-NiS catalyst, the regeneration process was repeated and followed by sending an ethylene flow (5ml/min) to the re-activated catalyst. The spectra of the fresh and the re-activated 8-NiS after two-hour ethylene reaction is shown in Figure 6.5. From the figure, it is evident that the fresh 8-NiS exhibits a high activity, since the four intense CHx bands reveal the adsorption of abundant products on the catalyst surface. On the contrary, the four bands show rather low intensities for the re-activated 8-NiS catalyst, which indicates that the re-activated catalyst performs a quite low activity. Therefore, it is concluded that the deactivated 8-NiS catalyst could not be regenerated by purging synthetic air at 673K. It is speculated that the regeneration failure could be due to further evolution of the hydrogen-rich hydrocarbons to highly condensed coke and the weak interaction between Ni^{2+} and [SO_4^{2-}] perturbed by coke formed in the re-activation process.

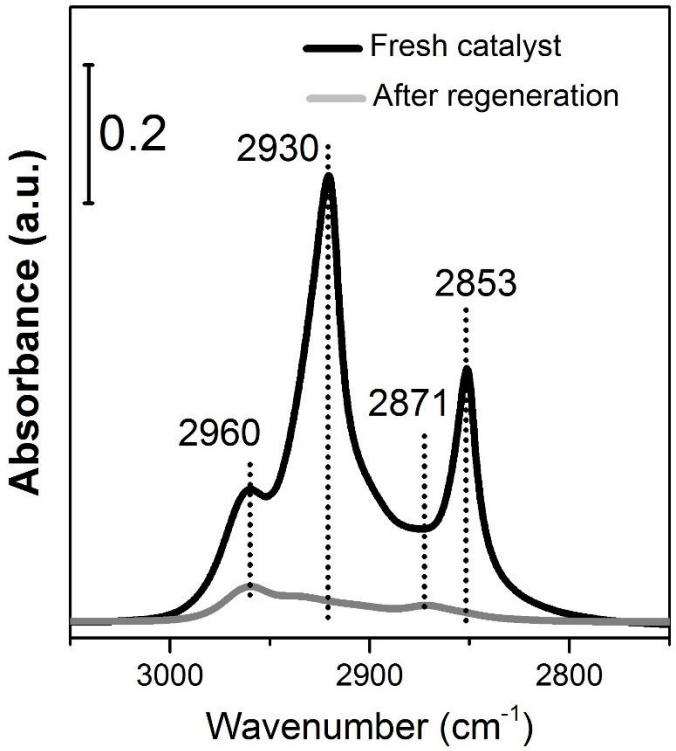

Figure 6.5: FT-IR spectra of 8-NiS after two-hour reaction under an ethylene flow (5ml/min). a) The fresh catalyst (black); b) The re-activated catalyst (grey).

The pellet was collected and sent for a HRTEM measurement after the re-activation process in FT-IR. HRTEM images of deactivated 8-NiS after the re-activation as well as the mapping of C, Ni and S are shown in Figure 6.6. By comparing with the HRTEM images of the fresh catalyst in Figure 4.8, the dark spots in the HRTEM images in Figure 6.6 are assigned to coke formation during catalyst regeneration with synthetic air at 673 K. This observation is consistent with the IR spectra of 673 K regenerated catalyst (Figure 6.4).

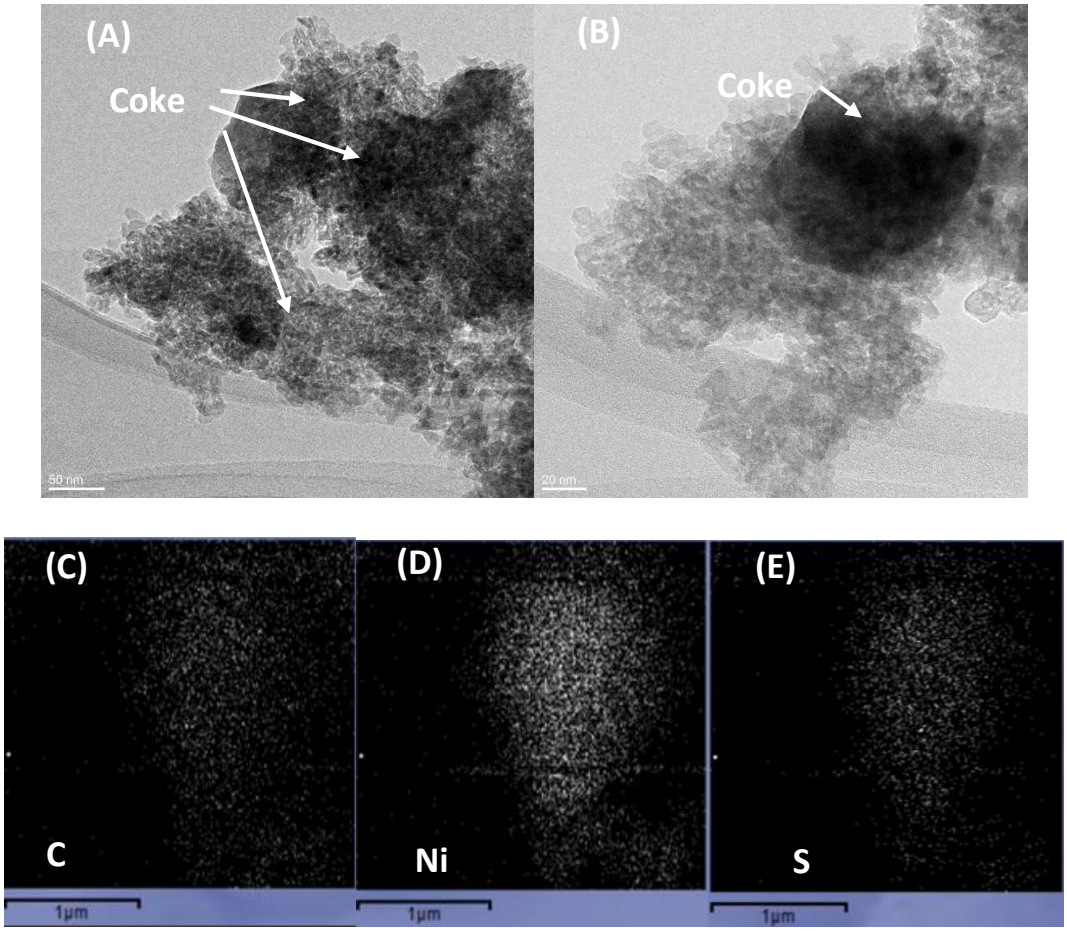

Figure 6.6: HRTEM images (A-B) of deactivated 8-NiS after reactivation at 673K under a mixture of oxygen (21%) and nitrogen (79%); mappings of C (C), Ni (D) and S (E) elements.

6.4 Conclusion

During catalyst regeneration using synthetic air, the long-chain hydrocarbons adsorbed on the catalyst surface evolve to highly unsaturated species or graphite-like residues with the increasing re-activation temperatures. The highly condensed species or graphite-like residues require a high combustion temperature. TG-MS data shows that the evolved coke on the deactivated catalyst starts to burn above 723 K and the burning rate increases with temperature. It seems that the coke deposited on the 8-NiS catalyst needs to be burned at higher temperature, e.g. >673 K, which may either damage the surface texture of the catalyst or cause decomposition of nickel sulfate. It appears that the failure of catalyst regeneration could also be due to the destruction of the active nickel dimerization site.

Reference

1. Argyle, M., Bartholomew, C., *Catalysts*, 5 (2015) 145-269.
2. Royo, C., Ibarra, J.V., Monzon, A., Santamaria, J., *Ind. Eng. Chem. Res.*, 33 (1994) 2563-2570.
3. Figueiredo, J.L., *Carbon Formation and Gasification on Nickel*, Progress in Catalyst Deactivation: Proceedings of the NATO Advanced Study Institute on Catalyst Deactivation, Springer Netherlands, Dordrecht, 1982, p45.
4. Bauer, F., Karge, H.G., *Characterization of Coke on Zeolites.* Springer Berlin Heidelberg, Heidelberg, 2007.
5. Cai, T., Cao, D., Song, Z., Li, L., *Appl. Catal. A- Gen*, 95 (1993) L1-L7.
6. Sohn, J.R., Park, W.C., *Appl. Catal., A*, 239 (2003) 269-278.
7. Andrei, R.D., Popa, M.I., Fajula, F., Hulea, V., *J. Catal.*, 323 (2015) 76-84.
8. Klusáček, K., Davidová, H., Fott, P., Schneider, P., *Chem. Eng. Sci.*, 40 (1985) 1717-1721.
9. Maneva, M., Rizova, D., Genov, L., Liptay, G., *J. Therm. Anal.*, 36 (1990) 915-922.
10. Chang, C.C., Conner, W.C., Kokes, R.J., *J. Phys. Chem.*, 77 (1973) 1957-1964.
11. Kokes, R.J., Dent, A.L., *J. Phys. Chem.*, 75 (1971) 487-491.
12. Trombetta, M., Busca, G., Rossini, S., Piccoli, V., Cornaro, U., Guercio, A., Catani, R., Willey, R.J., *J. Catal.*, 179 (1998) 581-596.
13. Meunier, F.C., Domokos, L., Seshan, K., Lercher, J.A., *J. Catal.*, 211 (2002) 366-378.
14. Rozwadowski, M., Lezanska, M., Wloch, J., Erdmann, K., Golembiewski, R., Kornatowski, J., *Chem. Mater.*, 13 (2001) 1609-1616.
15. Eberly, P.E., *J. Phys. Chem.*, 71 (1967) 1717-1722.
16. Eisenbach, D., Gallei, E., *J. Catal.*, 56 (1979) 377-389.

Chapter 7

7 Summary and Suggestions for Future Work

7.1 Summary

1. This project aimed to discover a catalyst for the direct conversion of ethylene to propylene. A series of catalysts were synthesized and tested in a fixed-bed continuous flow reactor, among which the bimetallic catalyst, $NiSO_4$/ReO_x/γ-Al_2O_3, exhibited high ethylene conversion and propylene gas phase selectivity at mild reaction conditions (323 K, 1 atm). By comparing the trends of the catalytic performances of $NiSO_4$/γ-Al_2O_3 and $NiSO_4$/ReO_x/γ-Al_2O_3 catalysts, it seems the two metallic sites, $NiSO_4$ and ReO_x work independently for dimerization and metathesis, respectively. Moreover, catalyst deactivation may accompany a decrease of acidity, which influences the production ratio of 1-butene to 2 butene. Furthermore, 8-Ni-8-Re and 8-Re-8-Ni with a different impregnation sequence show different ethylene conversion and propylene selectivity in the continuous flow test and the pulse reactor test, although the yields of propylene on the two catalysts are quite similar. This indicates that the different impregnation order of the catalysts influences the interaction of the impregnated components on the catalyst surface and affects their performances.
2. Pulse reactor tests indicate that an induction period is necessary for the ETP reaction on the Ni-Re catalysts. Adsorption of ethylene is fast whereas desorption of products takes some time. The fluctuation of the propylene selectivity curve reflects an uneven speed of desorption.
3. In the TGA analysis experiment, Ni-Re catalysts showed a good thermal stability below 1003K. Weight loss of the catalysts below 673K is mainly contributed to the removal of water molecules. Moreover, decomposition of $NiSO_4$ may take place at above 1003K. Elemental analysis shows that material loss is minor

during the catalyst preparation. Coke analysis of the deactivated catalysts implies coke formation could be the reason for catalyst deactivation.

4. Based on analysis of the SEM micrographs, particle sizes of the 8-Ni-8-Re and 8-Re-8-Ni catalysts were approximately 50-150 μm and both catalysts showed an uneven particle size distribution. EDS analysis revealed heterogeneous Ni and Re elemental distribution on the surface of the catalysts, although Ni and Re seemed to be more homogeneous on 8-Ni-8-Re than on 8-Re-8-Ni. More detailed morphological information was obtained by HRTEM measurements. TEM imaging of 8-NiS demonstrated a good dispersion of $NiSO_4$ since there was no observation of agglomerates and clusters on 8-Ni. Moreover, from TEM images of 10-Re, most of the hydrated ReO_4^- was well dispersed on the alumina, although small clusters (less than 1nm) were observed. Therefore, TEM images of the Ni-Re catalysts showed a good dispersion of $NiSO_4$ and ReO_x, in spite of some small clusters related to rhenium oxide.
5. Spectra of CO adsorption at 100 K and C_2H_4 reaction at room temperature on the activated catalysts, which were pretreated at 473 K for 1 hour, were recorded by means of in-situ FT-IR and UV-Vis-NIR spectroscopies. During the thermal activation, symmetry of the $[SO_4]^{2-}$ anions decrease and eventually they are expected to be covalently bonded either to the Ni^{2+} or to the surface Al^{3+} cations. Both Brønsted and Lewis acid sites revealed stronger acidities in the presence of sulfate modified alumni than in bare alumina, but the strength of the acidity is not sufficient to stabilize carbocationic species leading to a termination of the linear oligomerization reaction. Chain structures of the products with reaction time were roughly estimated according to CH_2/CH_3 ratio calculated based on the $\upsilon_{asym}(CH_2)$ and $\upsilon_{asym}(CH_3)$ bands in the FT-IR spectra. This indicates that $NiSO_4$ sites act the role of dimerization and Re sites behave the function of metathesis. In addition, $[SO_4]^{2-}$ anions modify the acidity needed for a dimerization reaction and they may also influence the electronic structure of the Ni cation. Catalyst deactivation could be due to formation and absorption of long-chain hydrocarbons, or slow displacement of sulfate anions from their initial position connected to the Ni ions.

6. Deactivated catalysts seem not to be re-generated after our re-activation process under air at 673 K. The FT-IR experiment was conducted to monitor the change in the spectra during the re-activation process. Disappearance of the bands at around 2800-3000 cm^{-1} and the rise of the bands at 1590 cm^{-1} indicate that long-chain hydrocarbons deposited on the catalyst surface convert to high unsaturated species or graphite-like components, which request a high combustion temperature to be burned. However, TG-MS analysis reveals that decomposition of nickel sulfate may occur and surface texture may be destroyed at such high temperature.

7.2 Suggestions for the Future Work

Suggestions are given in terms of four aspects, 1) further investigation of oxidation state of Ni during the ethylene dimerization reaction, 2) improving the catalytic performance of the studied catalyst, 3) developing second regeneration catalysts and 4) investigating methods for re-activation of the deactivated catalysts.

1. In this project, no reduction of Ni^{2+} ions on the activated 8-NiS catalyst was observed by means of FT-IR, XPS or EPR. According to our proposed catalytic cycle, the reduction may be induced in-situ by feeding with ethylene. Hence, to affirm our hypothesis, it is suggested that the oxidation state of Ni ions on the activated catalyst after dosing ethylene be measured in-situ by means of EPR.
2. Catalyst deactivation is mainly attributed to $NiSO_4$ responsible dimerization reaction. Moreover, from literature data, it is known that the product distribution of the ethylene oligomerization reaction is affected by the reaction temperature, pressure and GHSV[1-7]. Therefore, careful design of experiment (DOE) is recommended for the next stage, which can provide a systematical method to determine the relationship between experimental conditions (factors) and yield of desired products (outputs of the process). By this, optimizing experimental conditions could be easily achieved by using a suitable software. However, it is necessary to point out that our continuous flow test rig must be modified or renovated in order to meet the requirements of various temperatures and pressures. For example, in our test rig, the reaction

temperature must be higher than 323 K, otherwise the desired products (e.g. butene) would condense in the reactor causing inaccuracy of the measurement. The reason for catalyst deactivation is the long chain hydrocarbons blocking or deactivating the active sites. Catalysts working in a slurry reactor with a proper organic solvent may alleviate the catalyst deactivation, since formed oligomers would quickly dissolve in the solvent. Zhang et al. reported a Ni(II)/sulfated alumina catalyst, prepared by an ion-exchange method, gave good 1-butene (around 85%) and 1-hexene (about 10%) yield without any apparent deactivation in the slurry reactor at temperature at or below 298 K and at near-atmospheric pressure[8]. Moreover, they also found isomers of 1-butene and 1-hexene generated with longer contact time of the dissolved oligomers with the catalyst. According to the literature research, the Ni-Re catalyst has never been tested in a slurry reactor system. Therefore, it is recommended that the Ni-catalyst be further tested in a slurry reactor system, which may provide an effective way of avoiding fast deactivation of the catalyst.

3. Generally, in reactions involving hydrocarbons and especially olefinic hydrocarbons, the rate and extent of coke formation on metal oxide catalysts increases with increasing acid strength and concentration[9]. However, Ni-modified metal oxides without sufficient strength of acidity exhibit no activity for ethylene dimerization in our case. Hence, it is essential to discover an appropriate acid strength of the Ni-based catalysts for the ethylene dimerization reaction. This means that the acidity of the catalyst is sufficient for the reaction, but not so strong so as to accelerate catalyst deactivation. Acidity of the Ni-based dimerization catalyst can be adjusted by modifications with acid solutions (e.g. H_2SO_4, H_3PO_4, H_3BO_3 and H_2SeO_4) or by varying the acidities of support materials (e.g. Si/Al ratio of SiO_2-Al_2O_3). J. R. Sohn et al. concluded that catalyst activities of NiO-TiO_2 catalysts, modified with a series of acid solutions for the ethylene dimerization and 1-butene isomerization reactions, were dependent on their acid strengths[10]. Moreover, they found Al_2O_3-promoted $NiSO_4/SiO_2$ catalyst showed a remarkably higher catalyst activity than non-promoted $NiSO_4/SiO_2$ catalyst[11, 12]. However, all the catalysts reported by J. R. Sohn et al. were tested in a conventional static system and the conversion of

ethylene was determined only by following pressure changes. The deactivation rate and the lifetime of the catalyst were not well studied by them. Therefore, a systemical experimental plan, following up on the above studies from the literature, could be established to investigate how acid strengths of the catalysts affect the catalytic performances and deactivation rates.

4. During the re-activation process of the deactivated catalysts, long-chain hydrocarbons depositing on the catalyst convert to highly condensed coke or graphite-like species, which require a high combustion temperature. In fact, those long-chain hydrocarbons were supposed to be gasified at a temperature as low as 673 K under air as a gasify agent. The goal of removal of deposits at low temperatures may be achieved, if the further conversion of the hydrocarbons could be largely prevented during the re-activation process or alternatively, the hydrocarbons could be quickly burned-off before they further evolve. Therefore, adjusting heating rate or changing the gasify agent are suggested in the next step of catalyst regeneration. Gasification rates are known to occur in the following order O_2>H_2O>H_2[13]. Therefore, choosing an appropriate gasify agent and a proper dilution ratio are very important issues in this case, since decomposition of nickel sulfate occurs at above 1013 K.

Reference

1. Hulea, V., Fajula, F., *J. Catal.*, 225 (2004) 213-222.
2. Martínez, A., Arribas, M.A., Concepción, P., Moussa, S., *Appl. Catal. A- Gen*, 467 (2013) 509-518.
3. Heydenrych, M.D., Nicolaides, C.P., Scurrell, M.S., *J. Catal.*, 197 (2001) 49-57.
4. Finiels, A., Fajula, F., Hulea, V., *Catal. Sci. Technol.*, 4 (2014) 2412-2426.
5. Heveling, J., van der Beek, A., de Pender, M., *Appl. Catal.*, 42 (1988) 325-336.
6. Espinoza, R.L., Korf, C.J., Nicolaides, C.P., Snel, R., *Appl. Catal.*, 29 (1987) 175-184.
7. Nkosi, B., Ng, F.T.T., Rempel, G.L., *Appl. Catal. A- Gen*, 158 (1997) 225-241.
8. Zhang, Q., Kantcheva, M., Dalla Lana, I.G., *Ind. Eng. Chem. Res.*, 36 (1997) 3433-3438.
9. Argyle, M., Bartholomew, C., *Catalysts*, 5 (2015) 145-269.
10. Sohn, J.R., *Catal. Today*, 73 (2002) 197-209.
11. Sohn, J.R., Lee, M.H., Shin, D.C., *J. Ind. Eng. Chem. (Seoul, Repub. Korea)*, 12 (2006) 710-719.
12. Sohn, J.R., Park, W.C., Shin, D.C., *J. Mol. Catal. A: Chem.*, 256 (2006) 156-163.
13. Figueiredo, J.L., *Carbon Formation and Gasification on Nickel*, Progress in Catalyst Deactivation: Proceedings of the NATO Advanced Study Institute on Catalyst Deactivation, Springer Netherlands, Dordrecht, 1982, p45.

Appendix A: List of Chemicals

All chemicals used for experimentation or analytical techniques were laboratory grade. All chemicals were used as received. Details of the chemicals are listed in Table A1.

Table A1: Details of All Chemical Used

*synonym

Chemical Regent	Chemical formula	CAS#	M.W. (g/mol)	Purity (%)	Supplier
Gamma-alumina	γ-Al_2O_3		101.96		SASOL
Nickel (II)sulfate heptahydrate	$NiSO_4 \cdot 7H_2O$	10101-98-1	280.86	≥99.0	SIGMA-ALDRICH
Nickel nitrate hexahydrate	$Ni(NO_3)_2 \cdot 6H_2O$	13478-00-7	290.79	≥98.5	SIGMA-ALDRICH
Ammonia solution in water	$NH_3 \cdot H_2O$			25	Merck
Ammonium perrhenate	NH_4ReO_4	13598-65-7	268.24	≥99.0	SIGMA-ALDRICH
H-MFI-90 *ZSM-5 zeolite	SiO_2/Al_2O_3				Süd-Chemie
Silica-alumina catalyst support, grade 135	SiO_2/Al_2O_3	1335-30-4			SIGMA-ALDRICH
Ammonium metatungstate hydrate	$(NH_4)_6H_2W_{12}O_{40} \cdot xH_2O$	12333-11-8	2956.30	≥99.0	SIGMA-ALDRICH
Zirconium oxychloride octahydrate	$ZrOCl_2 \cdot 8H_2O$	13520-92-8	322.25	≥99.5	SIGMA-ALDRICH
Sulfuric acid	H_2SO_4	7664-93-9	98.08	95-97	Merck
Aluminosilicate mesostructured MCM-41 (hexagonal)	$(SiO_2)_{0.9875}(Al_2O_3)_{0.0125} \cdot xH_2O$	1218-02-1			SIGMA-ALDRICH
Nitrogen	N_2		28	99.999	AGA

Hydrogen	H_2		2	99.999	AGA

Table A1: Details of All Chemical Used (continued)

Chemical Regent	Chemical formula	CAS#	M.W. (g/mol)	Purity (%)	Supplier
Air					AGA
Ethylene	C_2H_4			99.9	AGA
Calibration gas				99.9	Yara Praxair

Appendix B: Procedures for the Catalyst Synthesis

B1: Procedures for Ni-ZSM-5 synthesis

a) Measure H-ZSM-5 (5.0g) and nickel nitrate hexahydrate (0.48g)
b) Make a solution of $Ni(NO_3)_2$ [0.02M] in de-ionized water (80g)
c) Mix the $Ni(NO_3)_2$ solution (40g) with H-ZSM-5 (5.0g) in a P.E. bottle
d) Stir the mixture in the P.E. bottle for 1 hour at room temperature
e) Place the bottle into water bath and keep it at 353K for 20hours
f) Filter out the residual, and wash it with enough demineralised water
g) Dry the precursors at 353K over the night
h) Calcinate the precursors at 823K for 6 hours

B2: Procedures for Ni-MCM-41 synthesis

a) Measure MCM-41 (2.0g) and nickel nitrate hexahydrate (0.48g)
b) Make a solution of $Ni(NO_3)_2$ [0.02M] in de-ionized water (80g)
c) Mix the $Ni(NO_3)_2$ solution (40g) with H-ZSM-5 (5.0g) in a P.E. bottle
d) Stir the mixture in the P.E. bottle for 1 hour at room temperature
e) Place the bottle into water bath and keep it at 353K for 20hours
f) Filter out the residual, and wash it with enough demineralised water
g) Dry the precursors at 353K over the night
h) Calcinate the precursors at 823K for 6 hours

B3: Procedures for NiO-ZrO_2/SO_4^{2-} synthesis

a) Measure $ZrOCl_2 \cdot 8H_2O$ (19.3g) and $Ni(NO_3)_2 \cdot 6H_2O$ (5.8g)
b) Put $ZrOCl_2 \cdot 8H_2O$ and $Ni(NO_3)_2 \cdot 6H_2O$ into a flask with a magnetic stirrer and add de-ionized water to 0.5L
c) When the solution is well mixed, use a burette to add ammonia solution droplet by droplet. Meanwhile, use an acidity meter to measure the pH of the solution and try to keep the pH value (pH=8) constant
d) Stir the mixture solution for 2 hours at room temperature
e) Filter out the residual by vacuum filter and wash it several times with de-ionized water until no chloride ion is detected
f) Dry the powder at room temperature
g) Pour 30 ml of 0.5M H_2SO_4 onto powder sample (2g)
h) Filter out the precipitate again by vacuum filter and wash it several times
i) Dry the precursors at 373K overnight
j) Calcinate the precursors at 673K for 2 hours

B4: Procedures for NiO-ZrO_2/WO_3 synthesis

a) Measure $ZrOCl_2 \cdot 8H_2O$ (12.5g) and $Ni(NO_3)_2 \cdot 6H_2O$ (7.8g)
b) Put $ZrOCl_2 \cdot 8H_2O$ and $Ni(NO_3)_2 \cdot 6H_2O$ into a flask with a magnetic stirrer and add de-ionized water to 0.5L
c) When the solution is well mixed, use a burette to add ammonia solution droplet by droplet. Meanwhile, use an acidity meter to measure the pH of the solution and try to keep the pH value (pH=8) constant
d) Stir the mixture solution for 2 hours at room temperature
e) Filter out the precipitate by vacuum filter and wash it several times with de-ionized water until no chloride ion is detected.
f) Dry the powder at room temperature
g) Impregnate the powder with an aqueous solution of $(NH_4)_6H_2W_{12}O_{40} \cdot XH_2O$ (1.3g)
h) Dry the precursors at 373K overnight
i) Calcinate the precursors at 673K for 2 hours

B5: Procedures for $NiSO_4$/γ-Al_2O_3 synthesis

a) Calcinate around 10g of γ-Al_2O_3 at 673K for 4 hours
b) Measure γ-Al_2O_3 (10g) and $NiSO_4 \cdot 7H_2O$*
c) Make an aqueous solution of $NiSO_4 \cdot 7H_2O$
d) Put γ-Al_2O_3 into an Erlenmeyer flask with a stirring bar
e) Impregnate γ-Al_2O_3 with the solution while keep the mixture well stirred
f) Stir the mixture for 24 hours at room temperature
g) Dry the precursors at 373K overnight
h) Calcinate the precursors at 673K for 2 hours

*the amount of $NiSO_4 \cdot 7H_2O$ depends on the weight percentage of Ni needed for the catalysts

B6: Procedures for Re_2O_7/γ-Al_2O_3 synthesis

a) Calcinate around 7g of γ-Al_2O_3 at 673K for 4 hours
b) Measure γ-Al_2O_3 (4.5g) and NH_4ReO_4 (0.5537g)
c) Make an aqueous solution of NH_4ReO_4
d) Put γ-Al_2O_3 into an Erlenmeyer flask with a stirring bar
e) Impregnate γ-Al_2O_3 with the solution of NH_4ReO_4 while keep the mixture well stirred
f) Stir the mixture for 24 hours at room temperature
g) Dry the precursors at 373K overnight
h) Calcinate the precursors at 673K for 2 hours

B7: Procedures for $NiSO_4/SiO_2$-Al_2O_3 synthesis

a) Calcinate around 5g of γ-Al_2O_3 at 673K for 4 hours
b) Measure SiO_2-Al_2O_3 (4g) and $NiSO_4 \cdot 7H_2O$ (1.91g)
c) Make an aqueous solution of $NiSO_4 \cdot 7H_2O$
d) Put SiO_2-Al_2O_3 into an Erlenmeyer flask with a stirring bar
e) Impregnate SiO_2-Al_2O_3 with the solution while keeping the mixture well stirred
f) Stir the mixture for 24 hours at room temperature
g) Dry the precursors at 373K overnight
h) Calcinate the precursors at 673K for 2 hours

B8: Procedures for $NiSO_4$-ReO_x/γ-Al_2O_3† synthesis

a) Calcinate around 7g of γ-Al_2O_3 at 673K for 4 hours
b) Measure γ-Al_2O_3 (4g), $NiSO_4 \cdot 7H_2O$(1.91g) and NH_4ReO_4*
c) Make an aqueous solution of $NiSO_4 \cdot 7H_2O$
d) Put γ-Al_2O_3 into an Erlenmeyer flask with a stirring bar
e) Impregnate γ-Al_2O_3 with the solution while keep the mixture well stirred
f) Stir the mixture for 24 hours at room temperature
g) Dry the precursors at 373K overnight
h) Calcinate the precursors at 673K for 2 hours
i) Impregnate $NiSO_4$/γ-Al_2O_3 of 4.6g with an aqueous solution of NH_4ReO_4 while keeping the mixture well stirred
j) Stir the mixture for 24 hours at room temperature
k) Dry the precursors at 373K overnight
l) Calcinate the precursors at 673K for 2 hours

†catalysts with different impregnation order were prepared by the same methods as mentioned above, but an aqueous solution of NH_4ReO_4 was impregnated to γ-Al_2O_3 first followed by impregnation with an aqueous solution of $NiSO_4 \cdot 7H_2O$.

*the amount of NH_4ReO_4 depends on the weight percentage of ReO_x needed for the catalysts

Appendix C: Raw Data of Calibration on GC

Table C1: Raw experimental data of ethylene calibration on GC

Mass concentration of C_2H_4	Peak area (Three parallel measurements)	Mean	Standard deviation
2.7	78785.0 81606.0 84132.0	81507.7	2674.9
3.6	123625.0 123299.0 122952.0	123292.0	336.6
4.5	171058.0 171595.0 170680.0	171111.0	459.8
5.4	214091.0 217468.0 219736.0	217098.3	2840.6
6.3	264476.0 262518.0 264327.0	263773.7	1090.0
7.2	320832.0 320314.0 317965.0	319703.7	1527.8

Table C1: Raw experimental data of ethylene calibration on GC (continued)

Mass concentration of C_2H_4	Peak area (Three parallel measurements)	Mean	Standard deviation
8.1	366303.0 360858.0 365103.0	364088.0	2860.9
9.0	410346.0 411966.0 422208.0	414840.0	6432.1
13.5	839114.0 831695.0 843475.0	838094.7	5955.8
18.0	1297003.0 1299837.0 1297573.0	1298137.7	1499.0
22.5	1790173.0 1819678.0 1819392.0	1809747.7	16952.8
27.0	2389036.0 2391270.0 2372902.0	2384402.7	10022.3

Table C2: Raw experimental data of peak areas of components in the calibration gas

Concentration of C_2H_4	Ethylene	Concentration of C_3H_6 and C_4H_8	Propylene	T-2-butene	1-butene	C-2-butene
	Peak area		Peak area			
	2691030.0		4441805.0	1995732.0	1763404.0	1801186.0
30.1	2732125.0	13.4	4514497.0	2031768.0	1779228.0	1824169.0
	2710772.0		4460966.0	2018100.0	1765803.0	1801152.0
	1628138.0		2679628.0	1156402.0	1019990.0	1053835.0
20.3	1622607.0	9.0	2755530.0	1179034.0	1043278.0	1078364.0
	1614829.0		2739033.0	1172902.0	1041653.0	1074551.0
	948979.0		1650022.0	708061.0	645006.0	675952.0
14.3	958015.0	6.3	1662742.0	713795.0	647474.0	679454.0
	959858.0		1665899.0	714784.0	647131.0	684766.0
	366097.0		625466.0	289396.0	267381.0	307811.0
8.5	363576.0	3.8	630078.0	283265.0	268383.0	306821.0
	350575.0		611946.0	280207.0	264565.0	305322.0
	195051.0		300692.0	145104.0	141525.0	171594.0
5.1	189059.0	2.3	300782.0	154934.0	144510.0	172098.0
	191636.0		299980.0	152317.0	142931.0	179810.0
	114482.0		192723.0	97218.0	95381.0	107738.0
3.7	115496.0	1.6	190436.0	98851.0	96492.0	118060.0
	129228.0		182322.0	94275.0	94282.0	103730.0

Table C2: Raw experimental data of peak areas of components in the calibration gas (continued)

Concentration of C_2H_4	Ethylene	Concentration of	Propylene	T-2-butene	1-butene	C-2-butene
	Peak area	C_3H_6 and C_4H_8	Peak area			
2.6	70252.0	1.1	103100.0	57558.0	52535.0	59147.0
	64119.0		91314.0	51083.0	48674.0	55199.0
	59997.0		87712.0	48751.0	47148.0	50245.0
1.9	29050.0	0.9	39245.0	25021.0	22877.0	24252.0
	37299.0		46358.0	25915.0	25147.0	24974.0
	37061.0		50303.0	28861.0	27700.0	30180.0

Appendix D: Detailed Procedures for the FT-IR Experiments

D1: Procedures for CO adsorption over the Ni-containing catalysts at room temperature

1) Make sure that there is no leakage in the line. Place sample holder into cell and seal the windows.
2) Switch off V-4, V-5 and open the rest of valves and switch V-2 in a downward position. Turn on the hydraulic pump.
3) Open cooling water system.
4) Wait until the pressure goes down to 1mbar.
5) Switch on the temperature controller and increase the temperature to 673K.
6) Wait for one hour until the temperature reaches 673K.
7) Decrease the temperature of the cell to room temperature.
8) Run one measurement to collect spectra of an activated sample.
9) Switch off V-7 and V8.
10) Open main valve of CO gas cylinder and adjust the regulator to 1 bar (if the pressure is above 3bars, relief valve (V-3) will release excessive gas).
11) Wait for a couple of seconds until the buffer bottle (E-3) is filled by CO and close the main valve of gas cylinder.
12) Slowly open the need valve (V-8). Close V-8 when the pressure goes up to 500 mbar. (spectra are collected followed by a desorption of CO)
13) Keep V-8 close, but open V-7 to pump the remaining CO gas.
14) Slowly open V-8. Close the V-8 when the pressure decreases by 10 mbar.
15) Repeat procedure 14) until the pressure in the cell is 1 mbar.
16) Switch off temperature controller and cooling water.

D2: Procedures for CO and C_2H_4 adsorption over the Ni-containing catalysts at low temperature

1. CO adsorption on the activated catalysts

1) Place a pellet into part A (see Figure 5.3) of the in-situ cell. Seal the cell with vacuum grease. Fill the liquid N_2 container.
2) Close V-1, V-2, V-3, V-4, V-5, V-6 (see Figure 5.4) and switch on the hydraulic pump and the turbo pump.
3) Slowly open V-1 and V-3.
4) Open V-2 until the pressure is below 5 mbar.
5) Close V-9 (see Figure 5.3) and connect the cell to the vacuum line.
6) Slowly open V-6 when the pressure is down to 0.1mbar.
7) Slowly open V-9 when the pressure is down to 0.1mbar.
8) Stick a thermocouple on the part A of the cell and insert them into an oven. Cover the oven with glass wool.
9) Wait until the pressure is below 0.01mbar.
10) Turn on the oven and increase the temperature by 50K every 15 minutes until the temperature reaches 673K.
11) Wait for one hour at 673K.
12) Remove the oven and the thermocouple. Cool down the cell to room temperature.
13) Fill the mercury cadmium telluride cryo-detector of IR with liquid N_2.
14) Close V-9 and V-6.
15) Transport and mount the cell to the IR. Meanwhile, cover the sample compartment with a self-made glass door.
16) Adjust the cell in a best position and check the quality of the spectrum.
17) Collect one spectrum of the activated sample.
18) Connect a flask filled with CO to the vacuum line.
19) Open V-4, V-6 and pump off the gas carried by the CO flask.
20) Fill the inner tube of the cell (see Figure 5.3C) with liquid nitrogen.
21) Close V-1 and slowly open V-8. Close V-8 until the pressure is around 50 mbar in the line.

22) Open V-9 and spectra are recorded followed by desorption of CO.
23) Close V-9 and open V-1 to pump off all CO in the line.
24) Close V-1 and open V-9. (procedures 21) and 22) are the typical gas expansion in order to reduce the pressure of CO in the cell)
25) Repeat procedures 21) and 22) and stop filling the liquid N_2 when the spectra show no change.
26) Repeat procedure 21) and 22) as the temperature increases to room temperature until the pressure goes down to the vacuum level (0.01mbar).

2. C_2H_4 adsorption and desorption on the activated catalysts

1) Repeat procedure of catalyst activation in D2 from 1) to 17)
2) Connect a flask filled with C_2H_4 to the vacuum line.
3) Open V-4, V-6 and pump off the gas carried by the C_2H_4 flask.
4) Fill the inner tube of the cell with liquid nitrogen.
5) Close V-1 and slowly open V-8. Close V-8 until the pressure is around 15 mbar in the line.
6) Open V-9 and warm up the cell to room temperature (spectra are collected every 2 minutes for 2 hours).
7) Close V-1, V-9 and slowly open V-8. Close V-8 until the pressure is around 50 mbar in the line.
8) Open V-9 and collect spectra every 2 minutes for 4 hours.
9) Keep ethylene in the line overnight and then pump off all ethylene in the cell and line.

Appendix E: List of Publications

Articles

1. L. Li, R. D. Palcheva, K. J. Jens, 2013. Conversion of ethylene to propylene by a dual function $NiSO_4/Re_2O_7$/γ-Al_2O_3 catalyst. Top. Catal. 56(2013), 783.
2. L.Li, S. Chavan, E. Groppo, S. Borgida, U. Olsbye, K. J. Jens, Characterization of the $NiSO_4$ site on a $NiSO_4$-ReO_x/γ-Al_2O_3 catalyst for tandem conversion of ethylene to propylene. *(has been submitted to ACS Catalysis)*
3. L. Li, S. Chavan, M. Manzoli, K. J. Jens, A feasibility study of regeneration of coke deactivated $NiSO_4$/γ-Al_2O_3 catalyst. (*going to be submitted)*

Conference presentations

4. Li L. and Jens K.-J., 2013. Characterization of $NiSO_4/Re_2O_7$/γ-Al_2O_3 catalyst for conversion of ethylene to propylene.10th Natural Gas Conversion Syposium, poster presentation, Doha, 2-7 March, Qatar.
5. Li L. and Jens K.-J., 2013. Conversion of ethylene to propylene by a dual function NiSO4/Re2O7/γ-Al2O3 catalyst, 14th Norwegian Catalysis Symposium 2013, oral presentation, Trondheim, December 1-2, Norway.
6. Li L., Chavan S. M., Olsbye U. and Jens K.-J, 2015. Deactivation of $NiSO_4$/ReO_x/γ-Al_2O_3 catalyst for conversion of ethylene to propylene, 17th international symposium on relations between homogeneous and heterogeneous catalysis, poster presentation, utrech, July 12-15, the Netherlands.

Top Catal (2013) 56:783–788
DOI 10.1007/s11244-013-0036-z

ORIGINAL PAPER

Conversion of Ethene to Propene by a Dual Function $NiSO_4/Re_2O_7/\gamma\text{-}Al_2O_3$ Catalyst

Lu Li · Radostina Dimitrova Palcheva · Klaus-Joachim Jens

Published online: 18 April 2013

Abstract A $NiSO_4/Re_2O_7/\gamma\text{-}Al_2O_3$ catalyst was prepared by co-impregnation using an aqueous solution of $NiSO_4$ and $[NH_4][ReO_4]$, which catalyzes direct conversion of ethene to propene at mild reaction condition (323 K, 1 atm). Catalyst deactivation may be caused by coke formation. The two catalytic components appear to work independently of each other.

Keywords Ethene · Propene · Co-impregnation · Nickel sulfate · Rhenium oxide · γ-Aluminum oxide

1 Introduction

Polyethylene (PE) and polypropylene (PP) are the backbone of the international petrochemical industry. The major source of ethylene and propylene raw material is the steam cracking process. However, the recent growth rate of PE versus PP (3 vs 5 %) is not matching the ethylene to propylene production ratio (2:1) [1].

The need for 'on-purpose' propylene technology has brought about development of processes utilizing steam cracker by-products as raw material. Examples are the Lummus OCT process or the UOP/Total Petrochemical OCP process [1]. However, if shale gas ethane is going to be a future steam cracker raw material source, steam cracker by-products can be expected to be very much less available for propylene production. Thus in certain situations interest for direct conversion of ethylene to propylene may arise. Furthermore, conversion of 'bio-ethene' in one step to 'bio-propene' (the former derived from bioethanol) could also be a future option for sustainable chemical technology.

Recently, a bimetallic catalyst, $Re_2O_7/NiO/B_2O_3/Al_2O_3$ was reported in the patent literature for synthesis of propene from ethene claiming high propene selectivity [2]. In a previous report, Ni-MCM-41 showed activity for conversion of ethene to propene [3, 4]. For Ni-MCM-41, the reaction mechanism was suggested to consist of two steps, dimerization of ethene as the first step followed by metathesis of the products, 2-butene and ethene as the second step. Considering each step of above propene synthesis, many studies have been devoted to dimerization and metathesis, respectively. Ni supported on oxides as catalyst for dimerization and oligomerization of olefins has been studied widely [5–7]. Sohn and Park [8, 9] reported a series of catalysts consisting of $NiSO_4$ on $\gamma\text{-}Al_2O_3$ exhibiting high ethene dimerization activity as compared to other Ni based oxide catalysts. The authors concluded low valent Ni combined with acidity to be responsible for the active catalyst site. Furthermore, Wendt et al. [10, 11] studied the mechanism and deactivation of a $NiO–Al_2O_3/SiO_2$ dimerization catalyst. They concluded that catalytically active sites are formed from acid sites in conjunction with coordinatively unsaturated nickel ions and that catalyst deactivation is caused by coke formation. On the other hand, $Re_2O_7/\gamma\text{-}Al_2O_3$ is a well-known metathesis catalyst, which is a low temperature (293–373 K) active and selective metathesis catalyst [12, 13]. On this background, we wish to report a dual site bimetallic catalyst, $NiSO_4/Re_2O_7/\gamma\text{-}Al_2O_3$, for the direct conversion of ethene to propene.

L. Li · K.-J. Jens (✉)
Faculty of Technology, Telemark University College,
P.O. Box 203, Porsgrunn 3901, Norway
e-mail: klaus.j.jens@hit.no

R. D. Palcheva
Department of Chemistry, InGAP centre, Oslo University,
Blindern, P.O. Box 1072, Oslo 0316, Norway

2 Experimental Setup

2.1 Catalyst Preparation

A series of catalysts based on γ-Al_2O_3 support containing nickel sulfate and rhenium oxide were prepared by co-impregnation. The precursors of nickel sulfate and rhenium oxide were nickel(II) sulfate heptahydrate (Sigma-Aldrich, purity: ≥99.999 %) and ammonium perrhenate (Sigma-Aldrich, purity: ≥99 %), respectively and used as received. γ-Al_2O_3 was impregnated by the incipient wetness method with aqueous solutions of $NiSO_4 \cdot 7H_2O$ and $[NH_4][ReO_4]$ in different order, each impregnation being followed by drying over night at 378 K and calcination in air at 773 K for 2 h. A summary of the prepared catalysts is given in Table 1. Table 4 shows the elemental analysis of these catalysts. The elemental analysis shows some deviation from the catalyst synthesis stoichiometry, this could be due to uneven impregnation of the catalyst particles (see Fig. 3). We propose the composition of the fresh catalyst to be $NiSO_4/Re_2O_7/\gamma$-Al_2O_3 based on the analysis stochiometry (Table 4) and the synthesis procedure [13] of the Rhenium function of the catalyst. The catalysts were activated in situ under nitrogen flow at 773 K for 2 h before use. Table 1 summarizes the prepared catalysts; the catalyst naming indicates the impregnation order and weight percentage of active components contained by the catalyst, for instance, 8 wt%-$NiSO_4$/11 wt%-Re_2O_7/γ-Al_2O_3 meaning the $NiSO_4 \cdot 7H_2O$ (1.91 g) solution to be impregnated first followed by $[NH_4][ReO_4]$ (0.68 g) solution as the second one—with 8 wt% Ni corresponding to the $NiSO_4/\gamma$-Al_2O_3 part and 11 wt% Re_2O_7 corresponding to the whole catalyst, respectively.

2.2 Catalyst Characterization

BET surface area of catalysts was determined by single-point measurement under atmospheric pressure and at liquid nitrogen temperature (77 K) on a Flowsorb III-2310 apparatus. Furthermore, the SEM measurements were run using a FEI Nova™ NanoSEM. The elemental analysis was performed by Mikroanalytisches Labor Pascher, An der Pulvermühle 1, 53424 Remagen, Germany.

Table 1 Summary of prepared catalysts

Catalyst	Abbreviation
8 wt%-$NiSO_4/\gamma$-Al_2O_3	8-Ni
10 wt%-Re_2O_7/γ-Al_2O_3	10-Re
8 wt%-$NiSO_4$/1 wt%-Re_2O_7/γ-Al_2O_3	8-Ni-1-Re
8 wt%-$NiSO_4$/3 wt%-Re_2O_7/γ-Al_2O_3	8-Ni-3-Re
8 wt%-$NiSO_4$/5 wt%-Re_2O_7/γ-Al_2O_3	8-Ni-5-Re
8 wt%-$NiSO_4$/8 wt%-Re_2O_7/γ-Al_2O_3	8-Ni-8-Re
8 wt%-$NiSO_4$/10 wt%-Re_2O_7/γ-Al_2O_3	8-Ni-10-Re
8 wt%-$NiSO_4$/11 wt%-Re_2O_7/γ-Al_2O_3	8-Ni-11-Re
3 wt%-Re_2O_7/8 wt%-$NiSO_4/\gamma$-Al_2O_3	3-Re-8-Ni
8 wt%-Re_2O_7/8 wt%-$NiSO_4/\gamma$-Al_2O_3	8-Re-8-Ni

2.3 Catalytic Testing

Catalyst testing was determined at the range from 333 to 373 K in a fixed-bed reactor at atmospheric pressure. The length and inner diameter of the fix-bed reactor was 60 and 1.27 cm respectively. The reactor was heated by heating tapes wound around it; the reaction temperature is measured by a thermocouple positioned inside the catalyst bed. The catalyst bed was made up of 2 g catalyst located in the middle of the reactor and supported by silica–carbide particles and quartz wool. The catalyst was heated from room temperature to 873 K under nitrogen flow at 20 ml/min and kept at that temperature for 2 h in order to activate it. Subsequently the catalyst was allowed to cool down under nitrogen to the reaction temperature, 323 K. Nitrogen as the dilute gas was mixed with pure ethene in a ratio of 3:2 to a total GHSV of 2,682/h. The reaction product was analyzed on a Trace GC Ultra equipped with HP-Al/KCl column (temperature program: start 373 K for 0 min; temperature ramp: 10 °C/min to 453 K; final hold time at 453 K for 0 min). The conversion of ethene and selectivity of products were calculated as:

$$\text{Ethene conversion} = \frac{\text{ethene in} - \text{ethene out}}{\text{ethene in}} \times 100\,\%$$

$$\text{Selectivity} = \frac{\text{desiredproduct}}{\text{total products in gas phase}\ (\text{propene, 1 - butene and 2 - butene})} \times 100\%$$

Pulse reactor testing was performed in a tubular quartz reactor (i.d. 8 mm) at 323 K and 1 atm pressure. The catalyst (0.4 g) was diluted by γ-Al_2O_3 (0.1 g). An automated setup equipped with 4-way and 6-way VICI VALCO valves was used. The 4-way valve was connected to the loop in the 6-way valve. The 6-way valve was equipped with a loop (0.25 ml) and used to send discrete pulses of gas, with a continuous stream of He (10 ml/min), to the reactor. In the experiment, the catalyst was activated under inert gas (He) at 773 K for 2 h before use. After activation, ethene pulses were sent to the reactor every 2 min, while the catalyst was cooled to 323 K. The test was performed on the $NiSO_4/Re_2O_7/\gamma$-Al_2O_3 and $Re_2O_7/NiSO_4/\gamma$-Al_2O_3. Product was analyzed by an online mass spectrometer (Pfeiffer Omnistar). Calibration values for quantification of C_2H_4, C_3H_6 and C_4H_8 were found by sending known pulse of these gases to an empty reactor

preheated to 323 K and integrating the area under the peaks of m/z 28, 42 and 56, respectively. The conversion and selectivity was calculated:

$$\text{Ethene conversion} = \frac{\text{ethene in} - \text{ethene out}}{\text{ethene in}} \times 100\,\%$$

$$\text{Selectivity} = \frac{\text{propene out}}{(\text{ethene in} - \text{ethene out})} \times \frac{3}{2} \times 100\,\%$$

3 Results and Discussion

3.1 Catalytic Performance

In this study, a series of catalysts with different loading of active components and different impregnation order were tested in a continuous flow catalyst test rig. A large number of reports show ethane dimerization over $NiSO_4/\gamma\text{-}Al_2O_3$ and olefin metathesis over $Re_2O_7/\gamma\text{-}Al_2O_3$ [8, 12]. As shown in Table 2, initial tests were run to establish the function of the single catalyst components, i.e. $NiSO_4/\gamma\text{-}Al_2O_3$ (8-Ni; Table 1) and $Re_2O_7/\gamma\text{-}Al_2O_3$ (10-Re; Table 1). Both physical and chemical mixture (co-impregnation) of two single component catalysts was used for further tests to explore the components of the dual-function catalysts, $NiSO_4\text{-}Re_2O_7/\gamma\text{-}Al_2O_3$. Compared with the physical mixture, the chemical mixture method (co-impregnation) demonstrates higher activity and similar selectivity. Thus the two metal components seem to work to a large extent independent of each other.

Table 3 shows catalytic performance of different co-impregnated catalysts. The specific surface area of the catalysts and $\gamma\text{-}Al_2O_3$ (see Table 3) indicates that sintering or pore blockage may have occurred during the catalyst preparation procedure. Since the maximum reaction temperature of the catalyst was 323 K, we do not expect the catalyst to sinter during the catalyst reaction, pore blockage by carbon formation can, however, not be excluded. Furthermore, maximum yield of propene is achieved with 8-Ni-8-Re and 8-Re-8-Ni catalysts. This result is in analogy to previous research [8, 9], since we selected a nickel loading which was reported to give maximum activity for ethene dimerization. With increasing Re_2O_7 loading, propene selectivity jumps from 19 to 49 %. It seems that Re_2O_7 loading relates to the capacity of the metathesis step; the low Re_2O_7 loading could not provide enough sites for metathesis reaction, while the high loading may cause a limitation of dimerization step. Moreover, the small changes in 1-butene selectivity could be an evidence that only 2-butene as an intermediate affects the yield of propene.

Pulse reactor tests were carried out in order to study the activation period of the catalysts. As shown in Fig. 1, the conversion of the catalysts drops fast from 60 to 30 % within 30 pulses of ethene followed by a leveling out to a constant value. This could be interpreted in analogy to the proposed mechanism [7, 8] for ethene dimerization on $NiSO_4/Al_2O_3$ catalyst; it could be speculated that ethene

Table 2 Initial tests of single component catalysts and dual-function catalysts

Catalyst	Reactant	Main products	Conversion of ethene (%)
8-Ni	C_2H_4	Butene[b]	62
10-Re	C_2H_4	–	–
Physical mixture[a]	C_2H_4	Propene, butene[b]	48
8-Ni-10Re	C_2H_4	Propene, butene[b]	60

All results were collected after 10 min on-stream (atmospheric pressure, 323 K, C_2H_4:N_2 3:2, GHSV: 3,682 h^{-1})

[a] Two catalysts 8-Ni and 10-Re mixed 1:1 physically

[b] Butene includes 1-butene, T-2-butene and C-2-butene

Table 3 Catalytic performance of different catalysts

Catalyst	Surface area (m^2/g)	Conversion of ethene (%)	Selectivity		
			Propene (%)	1-Butene (%)	2-Butene (%)
$\gamma\text{-}Al_2O_3$	178	–	–	–	–
8-Ni-1-Re	121	61	19	16	64
8-Ni-3-Re	121	63	27	17	57
8-Ni-8-Re	127	60	48	17	35
8-Ni-11-Re	114	55	49	18	32
3-Re-8-Ni	123	62	30	17	52
8-Re-8-Ni	128	59	49	18	35

All results were collected after 10 min on-stream (atmospheric pressure, 323 K, C_2H_4:N_2 3:2, GHSV: 3,682 h^{-1})

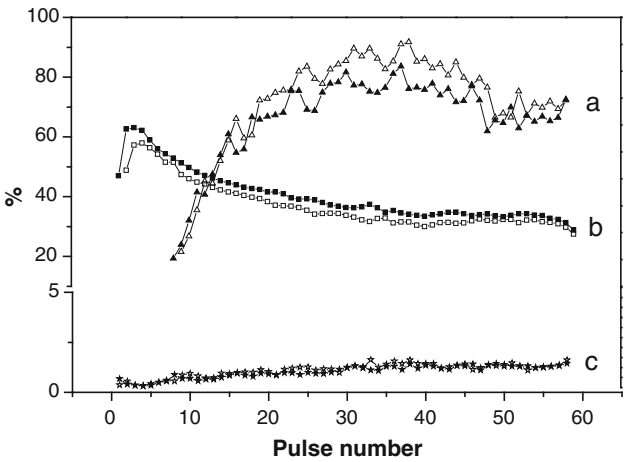

Fig. 1 Catalytic performance in a pulse reactor test. (*filled square*, *filled triangle*, *filled star*) 8 wt%-$NiSO_4$/8 wt%-$Re_2O_7/\gamma\text{-}Al_2O_3$; (*open square*, *open triangle*, *open star*) 8 wt%-Re_2O_7/8 wt%-$NiSO_4/\gamma\text{-}Al_2O_3$. (*a*) Selectivity of propene. (*b*) Conversion of ethylene. (*c*) Selectivity of hydrogen

Table 4 Elemental analysis for a series of Ni–Re catalysts

Catalyst	Ni/γ-Al_2O_3 (mol %)	Re/γ-Al_2O_3 (mol %)	S/γ-Al_2O_3 (mol %)	Ni/SO_4^{2-} (−)[a]	Coke/ catalyst (wt%)
8-Ni	13	–	–	–	–
10-Re	–	4.2	–	–	–
8-Ni-1-Re	15	0.5	17	0.88	–
8-Ni-3-Re	14	1.4	14	1	–
8-Ni-5-Re	13	2.5	14	0.93	–
8-Ni-8-Re	13	3.8	12	1.08	–
8-Ni-11-Re	12	5.5	13	0.92	–
3-Re-8-Ni	16	1.7	17	0.94	–
8-Re-8-Ni	12	4.2	14	0.85	–
Used 8-Ni-8-Re	–	–	–	–	2.43
Used 8-Re-8-Ni	–	–	–	–	2.39

The mole percentage of Ni, Re, S was calculated based on the weight percentage determined by elemental analysis

[a] Ratio of mole Ni to mole SO_4^{2-}

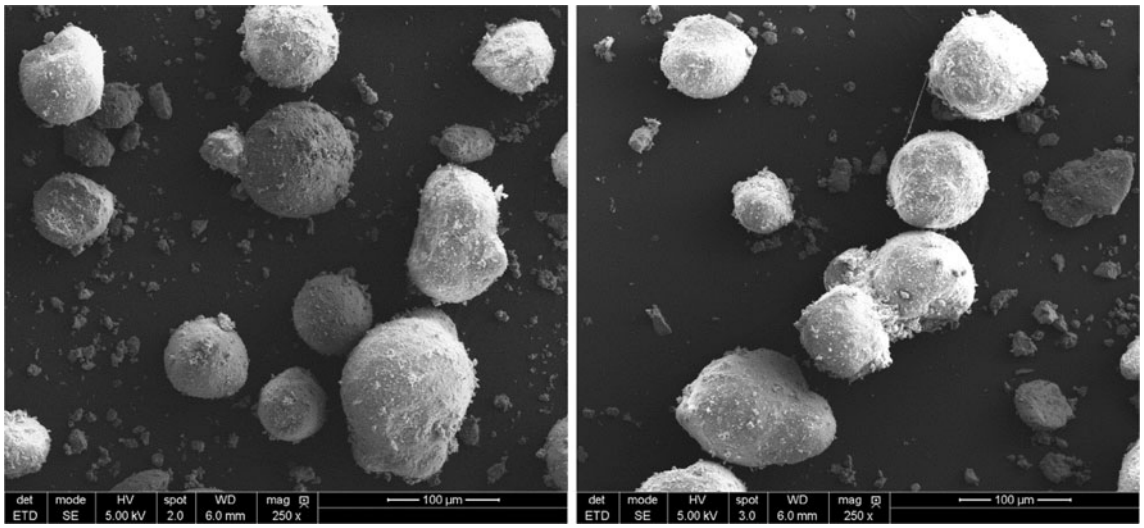

Fig. 2 Scanning electron micrographs for different catalysts by SEM. 8-Ni-8-Re (*left*); 8-Re-8Ni (*right*)

adsorption and product desorption reach an equilibrium on the surface of the catalyst after a certain time, which is also related to the desorption of the intermediates from the first reaction step. Furthermore, a special feature of the catalysts is high selectivity to product formation at mild reaction conditions (323 K, 1 atm). Uneven speed of desorption could be a reason for the selectivity curve fluctuation. The differences between the pulse number of maximum conversion and selectivity indicate that the rate of desorption is much slower than the rate of adsorption. Alternatively, the two consecutive reactions (dimerization and metathesis) may work independently; it could take time for the intermediate to find the right catalytic sites for continuous reaction. Comparing two catalysts in different order, 8-Ni-8-Re demonstrates a slight higher conversion and lower selectivity than the 8-Re-8Ni catalyst, which could be caused by the impregnation order influencing the interaction of the impregnated components with the surface of the catalyst.

The catalyst deactivates rather quickly, possibly through olefin adsorption on the catalyst surface leading to subsequent coke formation. The coke formation is indirectly shown through the hydrogen selectivity in this experiment; since hydrogen production can be closely related to coke formation. For further follow-up on coke formation, the amounts of coke deposited on the used catalysts were determined by elemental analysis. As shown in Table 4, the weight percentage of coke in the used 8-Ni-8-Re and 8-Re-8-Ni catalysts are 2.43 and 2.39, respectively. The large amounts of coke may be the reason of the fast deactivation of the catalysts last-not-least taking into account possible catalyst surface acidity due to the

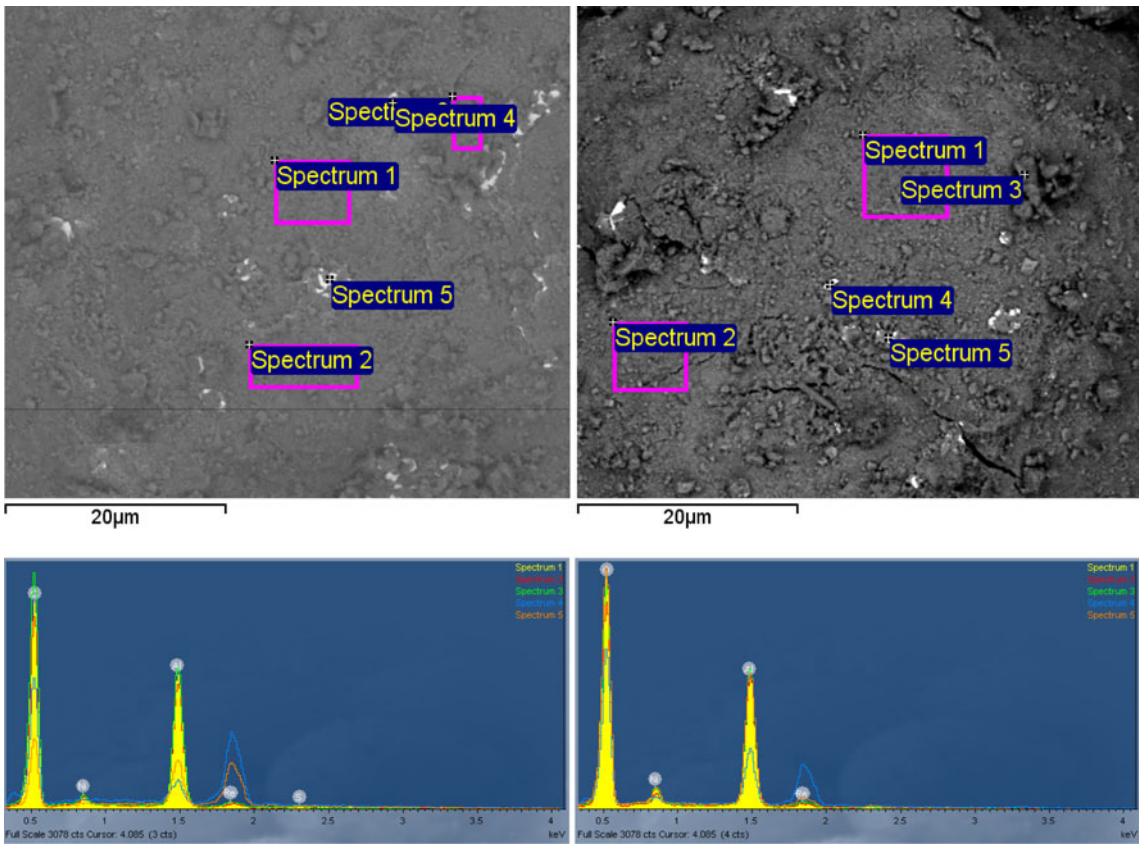

Fig. 3 SEM backscattered images and element distributions of different catalysts. 8-Ni-8-Re (*left*); 8-Re-8Ni (*right*)

presence of sulfate anions. From elemental analysis, the roughly equal amount of Ni and S on the catalyst indicates that loss of material is slight when synthesizing the catalysts, although such decomposition could be assumed due to decomposition of $NiSO_4$ to NiO and SO_3 at high temperature.

3.2 Catalyst Characterization

As mentioned above, both 8-Ni-8-Re and 8-Re-8-Ni exhibit a maximum yield of propene, however, a slight difference between conversion and selectivity aroused our interest in the surface properties of these two catalysts. From SEM micrographs in Fig. 2, it can be clearly seen that the shape of the catalyst particles are round or oval and catalyst particle sizes are approximate 50–150 μm. Particle size distribution of 8-Ni-8-Re observed by SEM micrographs seems to be more homogeneous than 8-Re-8-Ni, although both catalyst particles reveal heterogeneous Ni and Re distributions on the surface of the catalysts.

From Fig. 3, the bright spots of the backscattered images indicate Re rich particles. Five spots were randomly selected from each of the catalysts and used for EDS analysis. As expected, the brighter spots are Re enriched catalyst particles but still show a heterogeneous distribution on the surface of the catalysts. However, the Ni distribution seems better than the Re distribution. Low solubility of the aqueous solution of ammonium perrhenate may be a possible reason for the heterogeneous distribution of Re. Comparing the element distribution of two catalyst particles, the first impregnated component always seems to have a more even distribution than the last one.

4 Conclusion

The dual component bimetallic catalyst, $NiSO_4/Re_2O_7/\gamma\text{-}Al_2O_3$, catalyzes the direct conversion of ethene to propene at mild reaction conditions (323 K, 1 atm). It may be concluded that the two catalyst functions work independently for dimerization and metathesis. The yield of the catalyst for propene is approximate 29 %, which is superior to other metal based catalysts [3, 4]; however the present catalyst deactivates fast under our reaction conditions. The reason for catalyst deactivation may be coke formation on the surface of the catalyst.

Acknowledgments We thank Dr. M. Fleissner Sunding for the SEM analysis and Prof. Dr. U. Olsbye for her supporting interest in this work.

References

1. Plotkin JS (2005) Catal Today 106:10
2. Lavrenov AV, Mikhailova MS, Buluchevskii EA (2011) RU 2427421, C1 20110827
3. Lehmann T, Wolff T, Zahn VM, Veit P, Hamel C, Seidel-Morgenstern A (2011) Catal Commun 12:368
4. Ikeda K, Kawamura Y, Yamamoto T, Iwamoto M (2008) Catal Commun 9:106
5. Bernardi F, Bottoni A, Rossi I (1998) J Am Chem Soc 120:7770
6. K. Urabe, M. Koga, Y. Izumi (1989) J Chem Soc Chem Commun 807
7. Sohn JR, Ozaki A (1979) J Catal 59:303
8. Sohn JR, Park WC (1998) J Mol Catal A 133:297
9. Sohn JR, Park WC, Kim HW (2002) J Catal 209:69
10. Wendt G, Hentschel D, Finster J, Schollner R, Hanafi S, Mikhail RS (1983) J Chem Soc 79:2013
11. Kiessling D, Wendt G, Hagenau K, Schoellner R (1991) Appl Catal 71:69
12. Stoyanova M, Rodemerck U, Bentrup U, Dingerdissen U, Linke D, Mayer RW, LansinkRotgerink HGJ, Tacke T (2008) Appl Catal A 340:242
13. Mol JC (1999) Catal Today 51:289

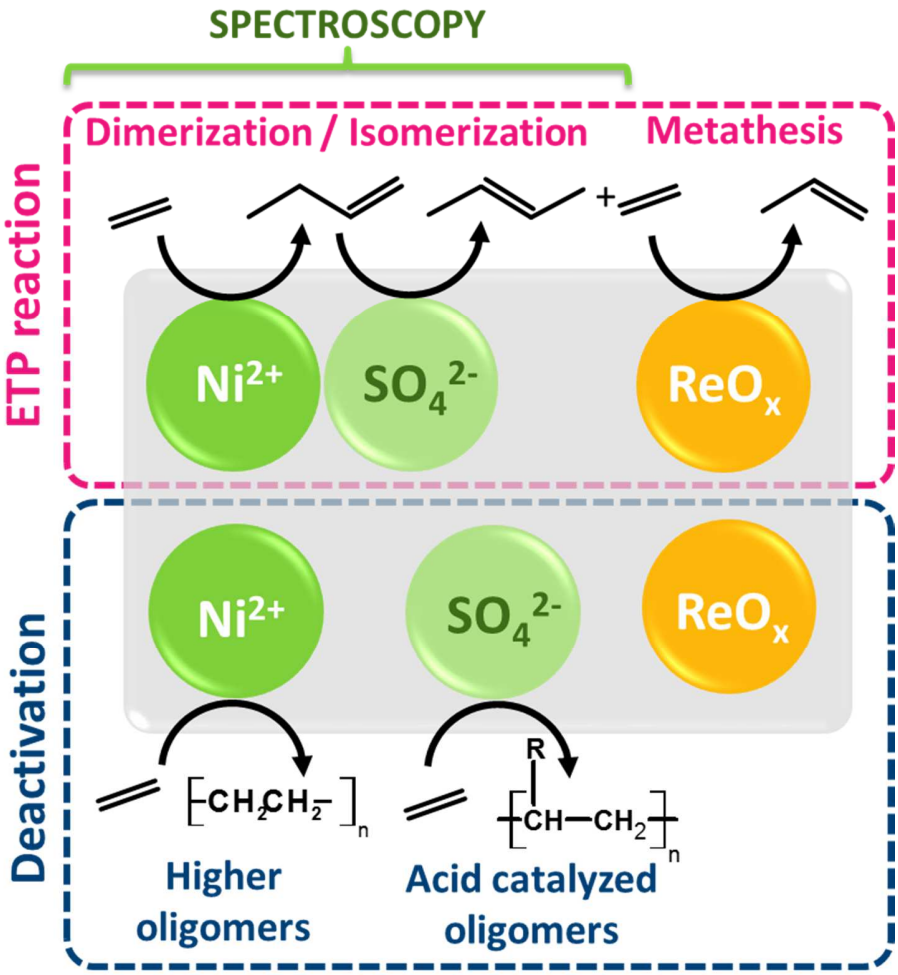

(This paper has been submitted to ACS Catalysis)

Characterization of the $NiSO_4$ site on a $NiSO_4$-ReO_x/γ-Al_2O_3 catalyst for tandem conversion of ethylene to propylene

Lu Li[†], Sachin Chavan[‡], Elena Groppo[*,§], Silvia Bordiga[§], Unni Olsbye[‡], Klaus-J. Jens*[*,†]*

[†]Faculty of Technology, University College of Southeast Norway, P.O.Box 203, Porsgrunn 3901, Norway

[‡]Centre for material science and nanotechnology, Department of chemistry, University of Oslo, P.O.box 1033, N-0315 Oslo Norway

[§]Department of Chemistry, NIS and INSTM Reference Centre, University of Turin, Via G. Quarello 15 A, 1-10135 Torino, Italy

Abstract

A series of $NiSO_4$-ReO_x/Al_2O_3 catalysts were synthesized by a co-impregnation method, tested in the conversion of ethylene to propylene at mild conditions, and thoroughly characterized by FT-IR, DR UV-Vis-NIR, XPS and ESR spectroscopies. In particular, the attention was focused on the $NiSO_4$ function, which is directly involved in ethylene dimerization/isomerization to 2-butylene, but also drives the catalyst deactivation. It was found that the sulfate anions increase the surface acidity of alumina, and simultaneously influence the electronic properties of the Ni sites. Indeed, thermal activation of the catalyst promotes the formation of covalent bonds between the sulfate anions and the Ni^{2+} or Al^{3+} cations, while keeping constant the +2 oxidation state of the Ni sites. The initial steps of the ETP reaction were investigated by FT-IR spectroscopy in the presence of ethylene, which revealed the initial acid-catalyzed formation of branched oligomers. The sulfate anions are involved in the reaction. Catalyst deactivation could be due to formation and absorption of long-chain oligomers, or slow displacement of sulfate anions from their initial position connected to the Ni ions.

Keywords

Ethylene dimerization, ethylene-butylene metathesis, propylene, Nickel sulfate, Rhenium oxide, Brønsted acidity, Lewis acidity.

1. Introduction

Ethylene and propylene are key petrochemical building blocks produced by steam cracking of hydrocarbons; propylene being a by-product of ethylene production.[1] Recently, the average global growth rate of polypropylene has overtaken that of polyethylene creating a supply/demand gap for propylene.[2] Furthermore, as oil and gas is substituted by shale gas derived ethane, the propylene gap is expected to widen. Hence there is a need for direct conversion of ethylene to propylene (ETP). Several technologies based on different catalysts have been developed for this purpose. In all the cases, two consecutive reactions have to take place, dimerization/isomerization of ethylene to 2-butene, and successive metathesis of the rest of ethylene with the produced 2-butene to give propylene. The two cascade reactions can be performed by the sequential use of two different catalysts. For example, the Lummus OCT process,[3] the reverse of the Phillips Triolefin process, can combined with a dimerization step to convert ethylene to propylene by a dual reactor dimerization – metathesis reaction system, the latter based on MgO and supported W catalysts.[4] However, it would be highly desirable to reduce this complex process to a single reactor technology, using a single catalyst with a dual function. Such a process would also open a sustainable and 'compact' route to bio-ethanol derived propylene. Early studies have shown molybdenum and tungsten supported metal oxides to convert ethylene to propylene at low yield.[5-7] Ni exchanged zeolites,[8-10] metal oxide catalysts, $NiO\text{-}Re_2O_7/B_2O_3\text{-}Al_2O_3$[11, 12] and a Ni-AlSBA-15/$MoO_3{-}SiO_2{-}Al_2O_3$ catalyst mix[13] are also active in the ETP reaction.

Recently, we reported a highly selective $NiSO_4/ReO_x/\gamma\text{-}Al_2O_3$ catalyzed tandem reaction of ethylene dimerization/metathesis to propylene at mild conditions.[14] Our system contains in the same catalytic body two components well known for their respective functions. As a matter of fact, nickel-based solid ethylene dimerization catalysts have been known for a long time.[4] The highly

active cocatalyst free low temperature $NiSO_4/\gamma\text{-}Al_2O_3$ dimerization catalyst was first reported by Cai[15] and Sohn[16-18] twenty years ago, although the nature of the active sites at a molecular level and in particular the role of $[SO_4]^{2-}$ is still little understood. On the other hand, the $Re_2O_7/\gamma\text{-}Al_2O_3$ function represents a typical olefin metathesis catalyst operating at low temperature in the range of 293K to 393K.[19-23] Although highly selective in the ETP reaction, our $NiSO_4/ReO_x/\gamma\text{-}Al_2O_3$ catalyst suffers from fast deactivation, which is driven by the ethylene dimerization step. Hence, insight into the $NiSO_4$ based ethylene dimerization step is needed.

We now report for the first time a systematic experimental study on the $NiSO_4/ReO_x/\gamma\text{-}Al_2O_3$ catalyst and concentrate especially on the $NiSO_4$ site. The investigation on the molecular nature of the active dimerization site is carried out by means of in-situ FT-IR and UV-Vis-NIR spectroscopies, following the course of thermal catalyst activation and includes subsequent CO adsorption and reactivity in presence of C_2H_4. The DR UV-Vis-NIR data are complemented with XPS and ESR measurements. This approach allows monitoring the changes occurring in the coordination structure of the transition metal Ni sites, in the population of the surface hydroxyl groups on $\gamma\text{-}Al_2O_3$, as well as in the symmetry of surface $[SO_4]^{2-}$ anions during the catalyst activation. Furthermore, IR spectra of CO adsorbed at 100 K on a series of activated catalysts reveal indirect information about the oxidation state of the Ni sites and the strength of the acid sites (Brønsted and Lewis). Finally, the time-resolved experiments during reaction with C_2H_4 provide a possibility to understand the dimerization initiation reaction and gain insight into the catalyst deactivation.

2. Experimental

2.1 Catalysts' preparation

Catalysts based on γ-Al_2O_3 containing nickel sulfate and rhenium oxide were prepared by the co-impregnation method. The detailed synthetic procedures have been described in the previous paper.[14] The precursors of nickel sulfate and rhenium oxide were nickel (II) sulfate hexahydrate (Sigma-Aldrich, purity: ≥99.99%) and ammonium perrhenate (Sigma-Aldrich, purity: ≥ 99%) and used as received. The catalysts with separately active components were prepared in the same way and impregnated with an aqueous solution of $NiSO_4 \cdot 6H_2O$, $(NH_4)_2SO_4$ (Sigma-Aldrich, purity: ≥ 99%), $[NH_4][ReO_4]$ and $Ni(NO_3)_2 \cdot 7H_2O$ (Sigma-Aldrich, purity ≥99%), respectively. Table 1 shows the prepared catalysts and the corresponding abbreviations, which indicate the different impregnation order and the nominal weight percentage of active components contained in the catalysts. For instance, 8-Ni-8-Re means that the $NiSO_4 \bullet 7H_2O$ solution was impregnated first, followed by $[NH_4][ReO_4]$ solution, with 8 wt% Ni corresponding to the $NiSO_4/\gamma$-Al_2O_3 part and 8 wt% ReOx corresponding to the whole catalyst, respectively.

Table 1. Summary of the catalysts synthetized and investigated in this work.

Catalyst	Abbreviation
8wt%-$NiSO_4$/8wt%-ReO_x/γ-Al_2O_3	8-Ni-8-Re
8wt%-ReO_x/8wt%-$NiSO_4/\gamma$-Al_2O_3	8-Re-8-Ni
8wt%-$NiSO_4/\gamma$-Al_2O_3	8-NiS
8wt%-$(NH_4)_2SO_4/\gamma$-Al_2O_3	8-S
10wt%-ReO_x/γ-Al_2O_3	10-Re
8wt%-NiO/γ-Al_2O_3	8-NiO

2.2 Methods

2.2.1 FT-IR spectroscopy

In situ FT-IR experiments have been performed with the dual aim to characterize the catalysts and to follow the reaction with ethylene. FT-IR spectra were recorded in transmission mode on a Bruker Vertex 70 spectrometer equipped with a mercury cadmium telluride cryo-detector, at a resolution of 4 cm^{-1}. The general procedure was as follows. A thin, self-supporting wafer of the catalyst, placed in an infrared cell designed to allow in-situ temperature treatment and gas dosage, was activated under vacuum at 673 K for 1 hour. FT-IR spectra were collected during the thermal treatment at regular temperature interval. The FT-IR spectrum of the activated catalyst was then collected at room temperature. In order to characterize the surface properties of the catalysts, CO adsorption experiments were performed at 100 K. To this aim, CO was sent into the cell at room temperature, followed by cooling to 100 K. FT-IR spectra were collected at the maximum CO coverage and for successive controlled gas evacuation steps, up to the complete desorption of CO. The reactivity of the catalysts towards ethylene at room temperature was investigated by dosing ethylene at an initial equilibrium pressure of P_{C2H4} = 10 mbar and collecting FT-IR spectra at regular time intervals for 2 hours. The equilibrium pressure was then increased to P_{C2H4} = 40 mbar and the reaction was monitored for another 2 hours.

2.2.2 Diffuse Reflectance (DR) UV-Vis-NIR spectroscopy

DR UV-Vis-NIR spectra were collected on a Varian Cary 5000 instrument, at spectral resolution of 2 nm. Approximately 1 g of sample was introduced into a cell equipped with a suprasil quartz window specially designed for in-situ gas dosage. The samples were outgassed in-situ overnight and successively degassed at 673 K for 2 hours. DR UV-Vis-NIR spectra of the activated catalysts

were collected at room temperature before and after reaction with ethylene at room temperature overnight.

2.2.3 X-ray photoelectron spectroscopy (XPS)

XPS analysis of the catalyst sample was conducted on an Axis Ultra^{DLD} XP spectrometer (Kratos Analytical). The XPS spectra were taken by using monochromatic Al Kα radiation, at pressures of $6*10^{-8}$ Torr - $6*10^{-9}$ Torr in the analysis chamber. The instrument resolution was determined as the full width at half maximum (FWHM) of the Ag $3d_{5/2}$ peak. The fresh catalyst sample was outgassed in the analysis chamber followed by in-situ activation under nitrogen flow at 473 K and 673 K for 1 hour.

2.2.4 Electron spin resonance (ESR)

ESR measurements were performed at both room temperature and liquid nitrogen temperature using aX-band Bruker EleXsySES60 spectrometer and a special designed cell for in-situ evacuation and heat treatment. The sample was activated under vacuum at 673K for 2 hours before being cooled to room temperature for measurements.

2.2.4 Analysis of deactivated catalysts

Powder samples of deactivated catalysts were obtained from a self-designed static reactor after 24 hours ethylene reaction at 323 K. After reaction, the reactor was cooled down in an ice-water bath and CH_2Cl_2 was injected into the reactor to dissolve the soluble products. The extraction was analyzed by GC-MS. The GC-MS instrument was an Agilent 7890A gas chromatograph coupled with a 5975C mass spectrometer. 1 μL of solution was injected each time by an automatic liquid sampler and analyzed by a HP-PLOT Al_2O_3/KCl column.

2.3 Catalyst testing

Catalyst testing was performed in the range of 333 K to 373 K in a fixed-bed reactor at atmospheric pressure. The length and inner diameter of the fixed-bed reactor was 60 cm and 1.27 cm respectively. The reactor was heated by heating tapes wound around it; the reaction temperature was measured by a thermocouple positioned inside the catalyst bed. The catalyst bed was made up of 2 grams catalyst located in the middle of the reactor and supported by silica-carbide particles and quartz wool. The catalyst was heated from room temperature to 873 K under nitrogen flow at 20ml/min and kept at that temperature for 2 hours in order to activate it. Subsequently the catalyst was allowed to cool down under nitrogen to the reaction temperature, 323 K. Nitrogen as dilute gas was mixed with pure ethylene in a ratio of 3:2 to a total GHSV of 2682 h^{-1}. The reaction product was analyzed on a Trace GC Ultra equipped with a HP-PLOT Al_2O_3/KCl column (temperature program: start 373 K for 0 min; temperature ramp: 10℃/min to 453 K; final hold time at 453 K for 0 minute). The conversion of ethylene and the selectivity to products were calculated as:

$$\text{ethylene conversion} = \frac{\text{ethylene in-ethylene out}}{\text{ethylene in}} \cdot 100\%$$

$$\text{selectivity} = \frac{\text{desired product}}{\text{total products in gas phase (propylene, 1-butylene and 2-butylene)}} \cdot 100\%$$

3. Results and Discussion

3.1 Catalytic performance

A series of catalysts were tested in a continuous flow reactor and their performances are shown in Table 2. 8-Ni-8-Re and 8-Re-8-Ni catalysts exhibit similar performance. Interestingly, the 8-NiS catalyst demonstrates a strong activity for ethylene dimerization, while 8-NiO shows no

activity without modification with $[SO_4]^{2-}$. Besides, it is no surprise that 10-Re as a typical olefin metathesis catalyst has no product to be detected when exposed to ethylene feed. This observation supports our earlier finding[14] about the roles of the active metal sites, where the Ni function is responsible for the dimerization reaction and the Re function catalyzes the metathesis reaction. Moreover, $[SO_4]^{2-}$ plays an essential role in the ETP reaction where probably three active sites; ReOx, a Ni cation as well as a $[SO_4]^{2-}$ promoted acid site are involved.

Table 2. Catalytic performance of different catalysts*.

Catalyst	Ethylene Conversion (%)	Selectivity (%)		
		Propene	1-butylene	2-butylene
8-Ni-8-Re	60	48	17	35
8-Re-8-Ni	59	49	16	35
8-NiS	62	-	14	86

*All results were collected after 10 minutes on-stream (atmospheric pressure, 323 K, C_2H_4:N_2 3:2, GHSV: 3682 h^{-1})

3.2 Effects of thermal activation on vibrational and electronic properties of the catalysts

All catalysts have been subjected to a complete spectroscopic characterization both before and after thermal activation at 673 K. The FT-IR spectra of all the samples are dominated by physisorbed water (broad absorption band in the 3700 – 2500 cm^{-1} region due to the ν(OH) vibrational mode, and a band at 1635 cm^{-1} due to the δ(HOH) vibrational mode). Activation at 673 K causes substantial changes in the FT-IR spectra of all the catalysts. Figure 1a shows the evolution of the FT-IR spectra during thermal activation for the 8-NiS catalyst as an example, while Figure 1b and Figure 1c show the FT-IR spectra of all the activated samples in the 3900 – 3000 cm^{-1} and 1600 – 1200 cm^{-1} regions, respectively. During the activation, the physically adsorbed water is

removed, as testified by the disappearance of the δ(HOH) absorption band at 1635 cm^{-1} and by the gradual decrease of the ν(OH) absorption band (Figure 1a). In the ν(OH) region, five absorption bands are clearly observed in the spectrum of activated alumina, which reveal the presence of both bridged (more acidic) and terminal (less acidic) hydroxyl species, in agreement with previous studies.[24, 25] In contrast, for all the other activated samples, only a weak and broad absorption band is observed in the ν(OH) region around 3500 cm^{-1}, indicating that the remaining hydroxyl groups at the alumina surface are still H-bonded.

Interestingly, for all the Ni-containing catalysts and for the 8-S sample, the disappearance of the absorption bands assigned to physically adsorbed water is accompanied by the appearance of a well-defined band just below 1400 cm^{-1} (Figure 1c). The connection between the two phenomena is demonstrated by a clear isosbestic point around 1400 cm^{-1} (Figure 1a). This band is assigned to the asymmetric stretching vibration of the $[SO_4]^{2-}$ anion, whose symmetry decreases upon water removal. Indeed, an $[SO_4]^{2-}$ anion in perfect tetrahedral environment gives a single $\nu(SO_4)$ asymmetric vibration band around 1100 cm^{-1}.[26] However, this band splits into multiple bands upon decreasing the symmetry on all the Ni-containing samples (i.e. by going from an ionic to a covalently bonded sulfate), the $\nu_{asym}(SO_4)$ mode being expected near 1400 cm^{-1} and the $\nu_{sym}(SO_4)$ mode around 1200 cm^{-1} (and hence covered by the out-of-scale absorption of bulk alumina).[27] The FT-IR spectrum of activated 8-S sample shows well-defined bands in this spectral region, which indicate the presence of two kinds of SO_4 species, namely monodentate species (accounting for the bands at 1403 and 1426 cm^{-1}) and bidentate species (accounting for the bands at 1381, 1284 and 1244 cm^{-1}).[27] Hence, we can conclude that dehydration at 673 K causes a change in the symmetry of the sulfate anions in all the sulfated samples. Small differences are observed in the width and position of the corresponding absorption bands among the different samples, indicating

that the surroundings of the $[SO_4]^{2-}$ anions is not exactly the same and it is likely influenced by the presence of the metal phases.

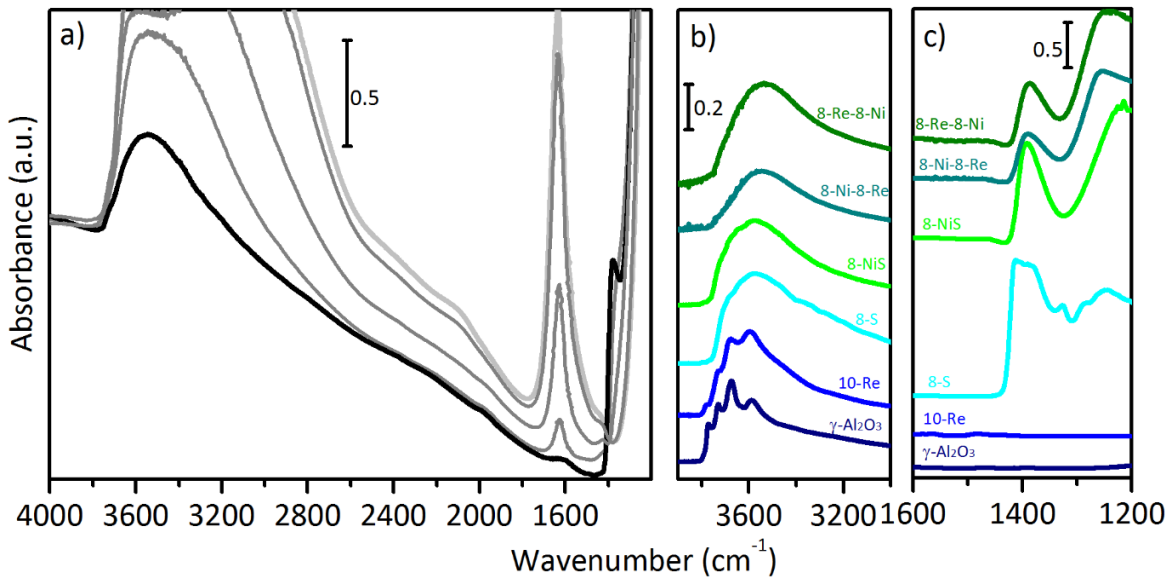

Figure 1. Part a) FT-IR spectra of the 8-NiS catalyst collected during the thermal activation from room temperature to 673 K. Parts b) and c): FT-IR spectra of all the investigated samples after thermal activation at 673 K, in the 3900-3000 cm^{-1} and 1600-1200 cm^{-1} regions, respectively.

Complementary information was obtained by means of DR UV-Vis-NIR, XPS and ESR experiments. Figure 2a shows the DR UV-Vis-NIR spectra of all the samples before activation. Generally speaking, the very intense (often out-of-scale) absorptions above 26000 cm^{-1} are due to charge-transfer transitions. The bands observed in the 26000 – 8000 cm^{-1} region are assigned to d-d transitions. Finally, the narrow and weak absorptions in the NIR region (8000 – 4000 cm^{-1}) are due to the combination and/or overtones of vibrational modes involving mainly OH groups. The UV-Vis-NIR spectra of bare alumina and 8-S do not absorb in the UV and Vis region, but only weak bands are observed around 7000 and 5100 cm^{-1}, which are assigned respectively to the $\nu(OH)+\delta(HOH)$ and $2\nu(OH)$ vibrational modes related to physisorbed water. The spectrum of 10-Re shows a very intense absorption in the UV-region (above 30000 cm^{-1}), easily ascribed to the

charge-transfer transition of rhenium oxide.[28] In contrast, the spectra of all the samples containing nickel display three well defined bands in the region of d-d transitions, centered around 8650 cm^{-1} (band O1, $^3A_{2g}(F) \rightarrow {}^3T_{2g}(F)$), 13700 – 15050 cm^{-1} (band O2, $^3A_{2g}(F) \rightarrow {}^3T_{1g}(F)$ and $^3A_{2g}(F) \rightarrow {}^1E_g(D)$), and 25260 cm^{-1} (band O3, $^3A_{2g}(F) \rightarrow {}^3T_{1g}(P)$).[29-31] The same three bands are observed in the spectrum of a $NiSO_4 \cdot 6H_2O$ reference sample at 8500, 14100 – 15300 and 25800 cm^{-1}. Hence, DR UV-Vis-NIR spectroscopy provides evidence that the Ni^{2+} cations in the Ni-containing samples display a 6-fold coordination and that all the coordination vacancies are filled by water molecules. [32]

As for the FT-IR spectra described above, also the DR UV-Vis spectra greatly change upon thermal activation, and in particular those of the samples containing the nickel phase. Figure 2b shows the evolution of the DR UV-Vis spectra for 8-NiS as an example, whereas the spectra of the other activated samples are reported in Figure S1. After outgassing 8-NiS overnight at room temperature, a small fraction of physically adsorbed water is removed, resulting in a blue shift of all the d-d bands and in the decrease of the bands in the NIR region due to OH vibrations. After activation at 673 K, most of the water is removed. Simultaneously, the d-d bands greatly change, both in position and in intensity. The new spectrum is indicative of the presence of Ni^{2+} sites with a symmetry lower than in the hydrated sample, in analogy to what is reported by Cornet et al.[33] for a similar NiO/Al_2O_3 sample activated at 723 K, but at difference with the works of both Cai et al.[15] and Sohn et al.,[17] who reported reduction of Ni^{2+} to Ni^{+} by calcination of a $NiSO_4/\gamma\text{-}Al_2O_3$ catalyst at 873 K.

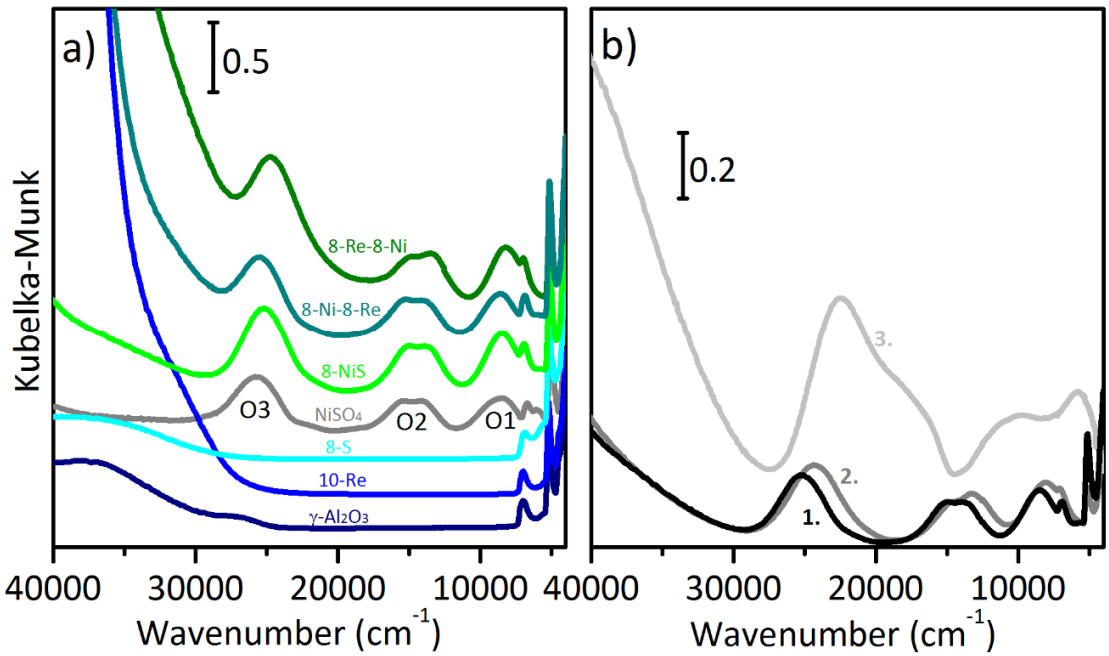

Figure 2. Part a): DR UV-Vis spectra of all the investigated samples in the hydrated form. Part b): DR UV-Vis spectra of the 8-NiS catalyst in (1) the hydrated form, (2) after degassing overnight at room temperature, and (3) after thermal activation at 673 K.

In order to better clarify the oxidation state of the Ni sites after catalyst activation, we analyzed the 8-NiS catalyst also by XPS and ESR spectroscopy. The Ni 2p XPS spectra of fresh and activated 8-NiS catalyst are shown in Figure 3a. The spectrum of the fresh catalyst (Figure 3a, spectrum 1) shows the Ni $2p_{3/2}$ and Ni $2p_{1/2}$ core level lines at 856.8 and 875.0 eV, and the shake-up satellites at the typical 6 eV binding energy difference relative to the corresponding main lines.[34] This line pattern is attributed to the presence of Ni^{2+} ions on γ-Al_2O_3, and is in good agreement with the results reported by Dufresne et al.[35] and Nikolova et al.[36] The spectrum of 8-NiS does not change after calcination for 1 hour at 473 K (Figure 3a, spectrum 2). A slight peaks shift to lower binding energy of about 0.4 eV is observed after thermal activation at 673 K (Figure 3a, spectrum 3). This shift indicates a small change in the electronic structure of the Ni ions, likely as a consequence of the changes occurring to the adjacent sulfate ions or surface hydroxyl groups, but is not compatible with the reduction of Ni^{2+} to Ni^{+} sites. Indeed, the energy difference of Ni $2p_{3/2}$

lines for reference Ni^0 vs Ni^{2+} species is approximately 2.3 eV, as reported for Ni/Al_2O_3 or Ni/SiO_2 systems.[37, 38] Hence, in the adopted experimental conditions, the Ni^{2+} sites preserve their oxidation state also after catalyst activation. This is further confirmed by the ESR measurements. Indeed, the ESR spectrum of activated 8-NiS catalyst (Figure 3b, spectra 2 and 3) is the same as for the fresh catalyst, despite a higher resolution obtained by measurement at liquid nitrogen temperature. This indicates that Ni^+ is not produced during catalyst activation at 673 K.

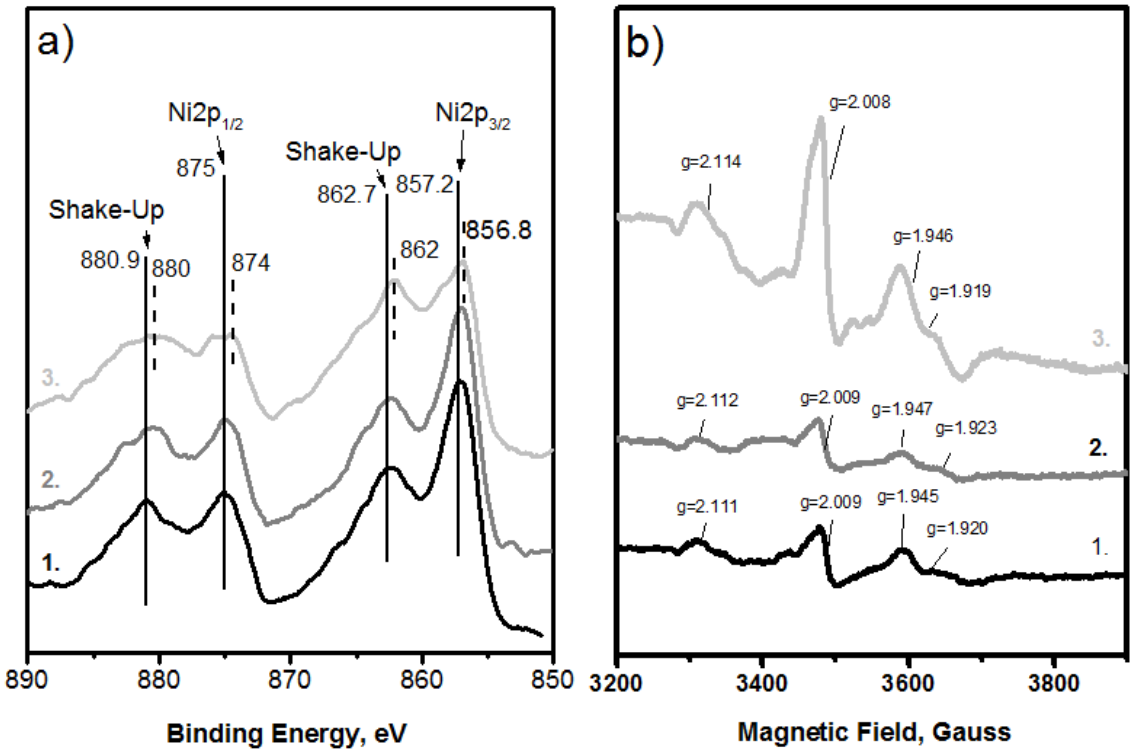

Figure 3. Part a): Ni 2p XPS spectra of 8-NiS (1) as made, (2) thermally activated at 473 K, and (3) thermally activated at 673 K. Part b): ESR spectra of 8-NiS (1) as made, (2) thermally activated at 673 K and measured at room temperature and (3) thermally activated at 673 K and measured at liquid nitrogen temperature.

Taken together, the in situ FT-IR and DR UV-Vis data discussed above indicate that the Ni^{2+} sites in hydrated samples display a 6-fold coordination with all the coordination vacancies filled by water molecules. The $[SO_4]^{2-}$ counter-anions are in turn solvated by water molecules and not

directly coordinated neither to the Ni^{2+} nor to the Al^{3+} cations. Upon thermal activation, coordinated water is gradually lost, implying the creation of some coordination vacancies around the Ni^{2+} sites, which however retain their oxidation state, as confirmed by both XPS and ESR spectroscopy. Simultaneously, it is expected that a small fraction of the Al^{3+} sites at the alumina surface are dehydroxylated and behave as strong Lewis sites. As a consequence, at least a fraction of the adjacent $[SO_4]^{2-}$ ions are covalently bonded either to the Ni^{2+} or to the surface Al^{3+} cations, with a resulting decrease of symmetry and an enhancement of the covalent character. A schematic representation of hypothetical structures present on the surface of SO_4/Al_2O_3 and $NiSO_4/Al_2O_3$ is proposed in Chart 1, in analogy to what was proposed by Saur et al.,[27] where M represents the Ni^{2+} or Al^{3+} surface sites. In addition, the covalently bonded sulfate groups might be partially protonated by the surface OH groups, as suggested in the literature, and in agreement with our observation of an enhanced Brønsted acidity for sulfated catalysts (vide infra). As suggested by Davydov et al.,[39] the Brønsted proton might be delocalized over the oxygen atoms of the covalent sulfate groups, as shown in Chart 1.

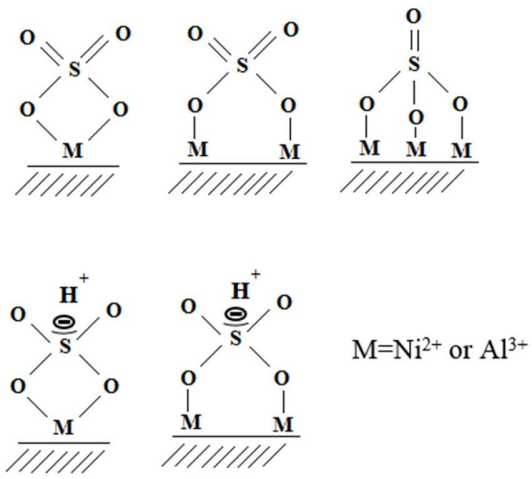

Chart 1. Schematic representation of hypothetical structures present on surface of SO_4/Al_2O_3 and $NiSO_4/Al_2O_3$ after dehydration at 673 K, where M represents the Ni^{2+} or Al^{3+} surface sites. In addition, the covalently bonded sulfate groups might be partially protonated by the surface OH groups.

3.3 Probing the surface properties of the activated catalysts by means of FT-IR spectroscopy of CO adsorbed at 100 K

In the next step, we investigated the surface properties of our catalysts by means of in-situ FT-IR spectroscopy of CO adsorbed at 100 K. This method has been widely applied to investigate Ni-containing catalysts,[39-48] since it allows determination of the Ni oxidation state in different conditions, according to the ν(CO) modes of the carbonyl complexes. Furthermore, the strengths of both Lewis and Brønsted acid sites can be simultaneously probed, since CO is also able to interact at 100 K with both the non-coordinated Al^{3+} (Lewis acid) surface sites and hydroxyl groups (Brønsted acid) at the surface of acid catalysts, forming $\equiv Al^{3+}\cdots CO$ adducts and $\equiv Al\text{-}OH\cdots CO$ adducts, respectively. The sequence of FT-**I**R spectra of CO adsorbed at 100 K on all the investigated samples as a function of the CO coverage (θ) is shown in Figure 4. In all the cases, the insets report the evolution of the FT-IR spectra in the ν(OH) region.

The FT-IR spectra of CO adsorbed on bare alumina (Figure 4a) display two main ν(CO) absorption bands, which are completely reversible upon degassing at 100 K. The first one, centered at 2154 cm^{-1} at θ_{max}, is attributed to CO adsorbed on the surface hydroxyl groups.[49] Correspondingly, a perturbation of the ν(OH) bands is observed (inset in Figure 4a). This band slightly shifts up to 2160 cm^{-1} upon decreasing θ and disappears fast. The second band, centered at 2186 cm^{-1} at θ_{max}, is assigned to the CO adsorbed on the coordinatively unsaturated Al^{3+} ions. This band blue shifts up to 2202 cm^{-1} upon decreasing the CO coverage and it is more resistant at low temperature, witnessing a higher strength of interaction. The shift with decreasing θ is due to the vanishing of the lateral interaction between adjacent CO molecules, as widely documented in the literature.[50, 51]

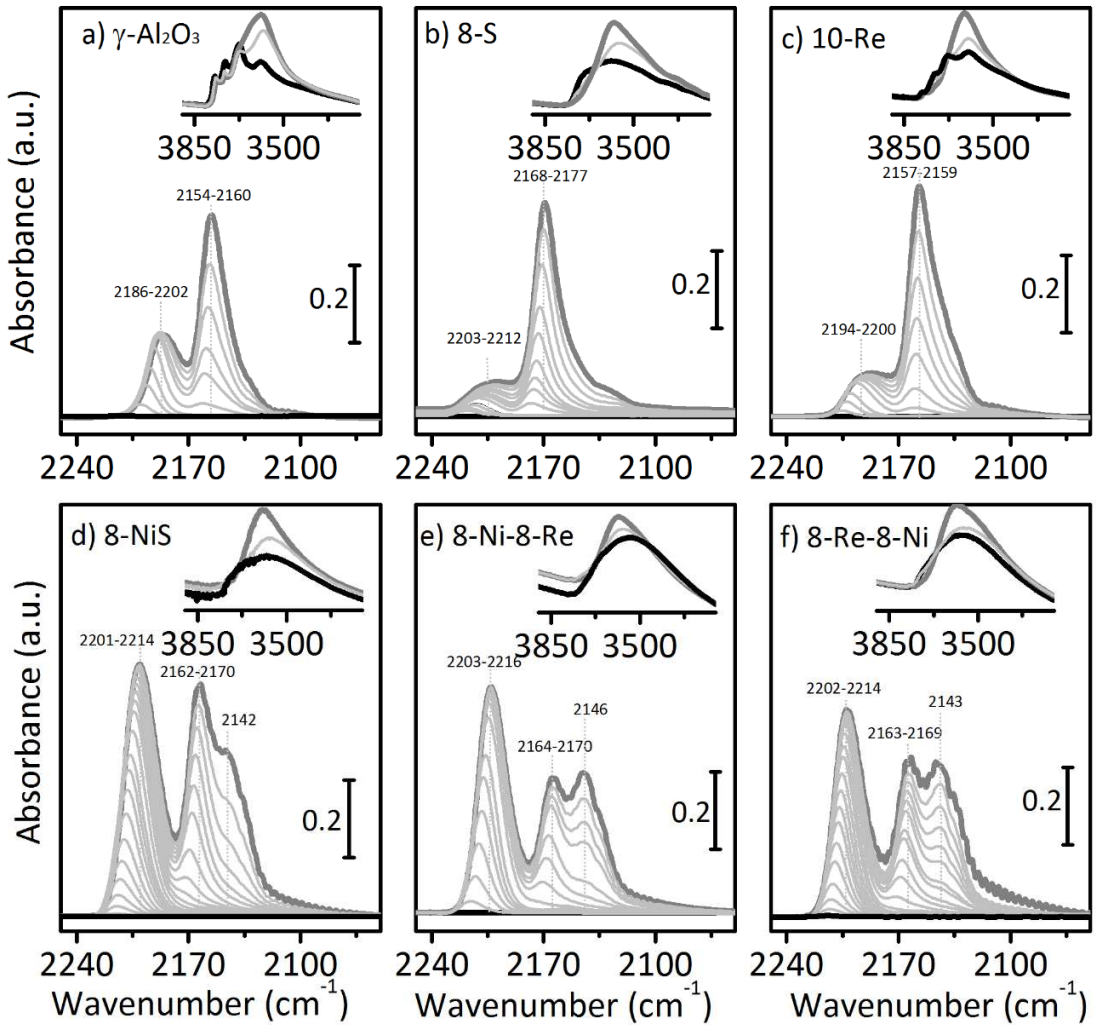

Figure 4. Evolution of the FT-IR spectra of CO adsorbed at 100 K over different samples as a function of CO coverage, from θ_{CO} = 30 mbar (dark grey) to θ_{CO} = 10^{-3} mbar (black). All the spectra are reported after subtracting the spectrum of the sample prior CO dosing. The insets show the evolution of the spectra in the ν(OH) region: activated catalyst (black), after CO adsorption (dark grey) and stepwise outgassing (light grey).

Similar FT-IR spectra were obtained for CO adsorbed on the 8-S sample (Figure 4b), except that the two main ν(CO) absorption bands are shifted at higher values compared to bare alumina and display a different relative intensity. In particular, the band attributed to ≡Al-OH···CO adducts is observed at 2168 cm^{-1} at θ_{max} and shifts to 2177 cm^{-1} at θ_{min}. Correspondingly, the broad ν(OH) band downward shifts by approximate 70 cm^{-1}. This behavior witnesses an enhanced Brønsted

acidity for sulfated alumina, as widely reported in literature.[27] It is worth noticing that, although low temperature CO adsorption measures a medium-weak Brønsted acid strength, other methods indicate a much larger acidity.[52-54] The absorption band assigned to $\equiv Al^{3+}\cdots CO$ adducts goes from 2203 cm^{-1} at θ_{max} to 2212 cm^{-1} at θ_{min}, indicating that the Al^{3+} sites are stronger Lewis acid sites than in bare alumina. This is in agreement with earlier reports.[52, 55]

The effect of the rhenium phase on the surface properties of the catalysts is much less pronounced than that of sulfates. The FT-IR spectra of CO adsorbed on 10-Re (Figure 4c) almost exhibit the same behavior as pure alumina, except that the band assigned to $\equiv Al^{3+}\cdots CO$ adducts is less intense relative to that due to $\equiv$Al-OH$\cdots$CO adducts. This indicates that the ReO_x phase partially covers the alumina surface.

In contrast, the FT-IR spectra of CO adsorbed on 8-NiS (Figure 4d), 8-Ni-8-Re (Figure 4e) and 8-Re-8-Ni (Figure 4f) catalysts are substantially different from those discussed above. Three main absorption bands are observed in all the three cases:

1) The most intense absorption band is centered around 2202 cm^{-1} at θ_{max} and undergoes a pronounced shift upon decreasing θ down to about 2214 cm^{-1} at θ_{min}. This band, which is also the most resistant to a decrease in θ, is assigned to CO adsorbed on coordinatively unsaturated Ni^{2+} sites,[39, 46, 56] and overlaps with the band ascribed to $\equiv Al^{3+}\cdots CO$ adducts.

2) The band centered around 2162 cm^{-1} at θ_{max}, which shifts to about 2170 cm^{-1} at θ_{min}, is assigned to $\equiv$Al-OH$\cdots$CO adducts. The Brønsted acidity of the surface hydroxyl groups is very weak, suggesting that the effect of sulfate anions on the properties of alumina is weaker in presence of the nickel phase than on sulfated alumina.

3) In addition, a broad band centered around 2143 cm^{-1} is observed in all the three cases, which is easily removable upon decreasing θ. This band is attributed to physisorbed CO, and testifies that

an increase in the complexity of catalyst formulation creates new opportunities for CO physisorption.

It is important to point out that in all the three cases no absorption bands are observed in the 2100 – 2080 cm^{-1} and 2140 – 2130 cm^{-1} regions, where $Ni^{+}(CO)_2$ complexes are expected to contribute,[56, 57] in well agreement with DR UV-Vis-NIR, XPS and ESR data. Hence, we can conclude that Ni^{+} is not formed during the catalysts' activation in our experimental conditions. Similarly, no absorption bands attributable to CO adsorbed on Re cations (2500 – 1800 cm^{-1}) are observed in the spectra of 8-Ni-8-Re and 8-Re-8-Ni. The intensity of the bands attributed to ≡Al-OH···CO adducts and to physisorbed CO relative to that of CO adsorbed on the Ni^{2+} cations is lower for 8-Re-8-Ni and 8-Ni-8-Re compared to 8-NiS, which suggests that the rhenium phase deactivates or replaces some Brønsted sites.

Finally, it is interesting to observe that on 8-S and Ni containing catalysts adsorption of CO causes a perturbation of the absorption band at around 1400 cm^{-1}, previously ascribed to the $\nu_{asym}(SO_4)$ vibrational mode of covalently bonded sulfate groups (Figure 5). This band downward shifts by around 10 cm^{-1} at θ_{max}, but the shift is reversible upon CO removal. This observation suggests that the sulfate groups play an active role in defining the ligand sphere of both Ni^{2+} and Al^{3+} Lewis sites, and are flexible enough to allow the entrance of an additional molecule such as CO.

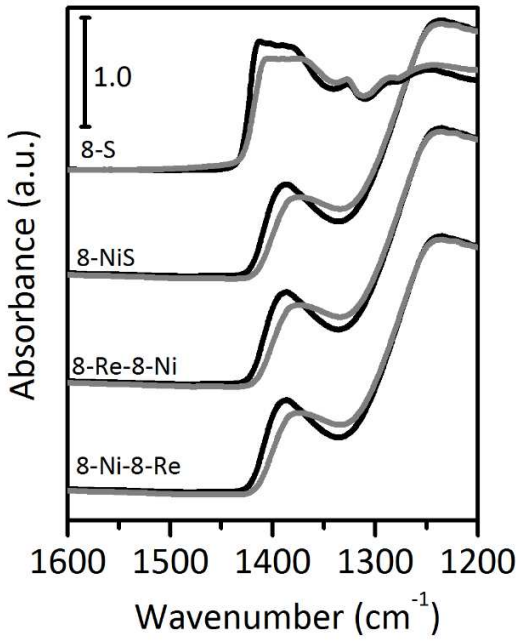

Figure 5. FT-IR spectra of 8-S, 8-NiS, 8-Re-8-Ni and 8-Ni-8-Re samples before (black) and after (grey) adsorption of CO at 100 K in the 1600-1200 cm^{-1} region, where the $\nu_{asym}(SO_4)$ vibrational mode of covalently bonded sulfate groups is observed.

3.4 Reactivity towards C_2H_4 followed by spectroscopic methods

Successively, the reactivity of all the catalysts towards ethylene at room temperature was investigated by means of in situ FT-IR and DR UV-Vis spectroscopies, aimed to understand the initiation step and the deactivation mechanism. FT-IR spectra were recorded in the presence of ethylene at room temperature at a time resolution of 2 minutes and the reactivity was followed for 12 hours. For bare γ-Al_2O_3, 8-NiO and 10-Re samples no changes were observed in the FT-IR spectra before and after introduction of ethylene, indicating that these samples are not active in ethylene conversion, in agreement with previous results.[14] In contrast, FT-IR spectroscopy revealed that the 8-S, 8-Ni, 8-Ni-8-Re and 8-Re-8-Ni catalysts are active towards ethylene. Hence, the presence of sulfate anions seems fundamental to develop activity towards ethylene at room temperature. Figure 6 shows the time-resolved FT-IR spectra collected within the first 4 hours of

reaction of 8-S, 8-Ni, and 8-Ni-8-Re with ethylene (equilibrium pressure P_{C2H4} = 10 mbar within the first 2 hours, increased to 40 mbar in the successive 2 hours). It is evident that the three catalysts behave in a different way, the 8-S being the most diverse one.

Starting the discussion from 8-S (Figure 6a and 5b), a complex series of absorption bands gradually grow up in the presence of ethylene, indicating the formation of saturated alkyl groups, and certainly of methyl groups. The spectra are characterized by three resolved absorption bands in the $\nu(CH_x)$ region at 2960 cm^{-1} ($\nu_{asym}(CH_3)$), 2928 cm^{-1} ($\nu_{asym}(CH_2)$) and 2871 cm^{-1} ($\nu_{sym}(CH_3)$), along with a broad band due to the $\delta_{asym}(CH_2)$ vibrational mode (a doublet at 1477 and 1468 cm^{-1}). Moreover, two bands are grasped at 1383 and 1367 cm^{-1} overlapped to the intense bands due to the vibrations of the sulfate anion, which are assigned to the $\delta_{sym}(CH_3)$ vibrational mode of $>C(CH_3)_2$ species, and therefore are indicative of branching[32]. In addition to these absorption bands, two weak bands are observed around 1671 cm^{-1} and 1618 cm^{-1}, which are likely due to $\nu(C=C)$ vibrational modes[32, 58]. All the above-mentioned absorption bands grow at the same rate along the whole investigated time interval, except for the band at 1618 cm^{-1}, which appears immediately after contact with ethylene and then remains almost constant during the reaction. As a whole, the time-resolved FT-IR spectra indicate the formation of branched oligomers.[59, 60] As a final observation, the very intense $\nu_{asym}(SO_4)$ absorption band originally centered around 1400 cm^{-1} gradually downward shifts during the reaction of ethylene, indicating that the $[SO_4]^{2-}$ anions are perturbed by the reaction products. In contrast, no great changes are observed in the $\nu(OH)$ region (not shown), where only the shoulder around 3710 cm^{-1} is eroded in favor of a band centered around 3650 cm^{-1}, indicating that reactivity has to be ascribed mainly to Lewis and not Bronsted acidity.

It is well known that sulfated alumina displays acidic properties and in general the presence of sulfate anions enhances the catalytic activity of alumina in acid-catalyzed reactions, such as olefin oligomerization and skeletal isomerization.[61-63] The accepted mechanism involves the formation of carbocationic species.[62, 64] Carbocations may be generated in a number of ways, involving both Brønsted acid sites and Lewis acid sites. The products formed in the initiation stage are the thermodynamically more stable secondary or tertiary carbocations, and this explains why branched species are observed in our experiments. Propagation involves the repeated additions of ethylene to the carbocationic center, which in principle may migrate well away from the site of initial attack. Carbocations are very reactive species and, in absence of super-acids, they terminate fast. The principal mechanism for termination is a chain-transfer process involving deprotonation of the carbocationic end-group by an incoming monomer, aided by the anion ($[SO_4]^{2-}$ in our case). Sulfated alumina is not sufficiently acid to stabilize the carbocationic species and this justifies the observation of vinyl terminations (ν(C=C) bands around 1650cm^{-1}). Moreover, it is also clear that sulfate anions play a vital role not only in enhancing the acidity of alumina, but also in guiding the termination process. The involvement of the $[SO_4]^{2-}$ anions in the reaction is testified by the perturbation of the corresponding absorption bands.

A different spectra evolution is observed for both 8-NiS and 8-Ni-8-Re catalysts. At short contact time, the FT-IR spectra are very similar to those observed for 8-S catalyst, although less intense, witnessing the acid-catalyzed formation of branched oligomers. However, after about 30-40 minutes the absorption bands associated to vibrational modes involving CH_2 groups start to grow faster (and slightly shift to lower wavenumber values) than those related to CH_3 groups. The phenomenon is more evident for 8-NiS than for 8-Ni-8-Re. As a consequence, the spectra collected after 40 minutes of reaction resemble those of aliphatic hydrocarbons with linear chain-like

structure and a few branches. Simultaneously, in the ν(C=C) region the band at 1671 cm^{-1} grows at a higher rate than that at 1618 cm^{-1}. The intense absorption band around 1400 cm^{-1} ascribed to $\nu_{asym}(SO_4)$ vibration downward shifts even more than for the 8-S sample.

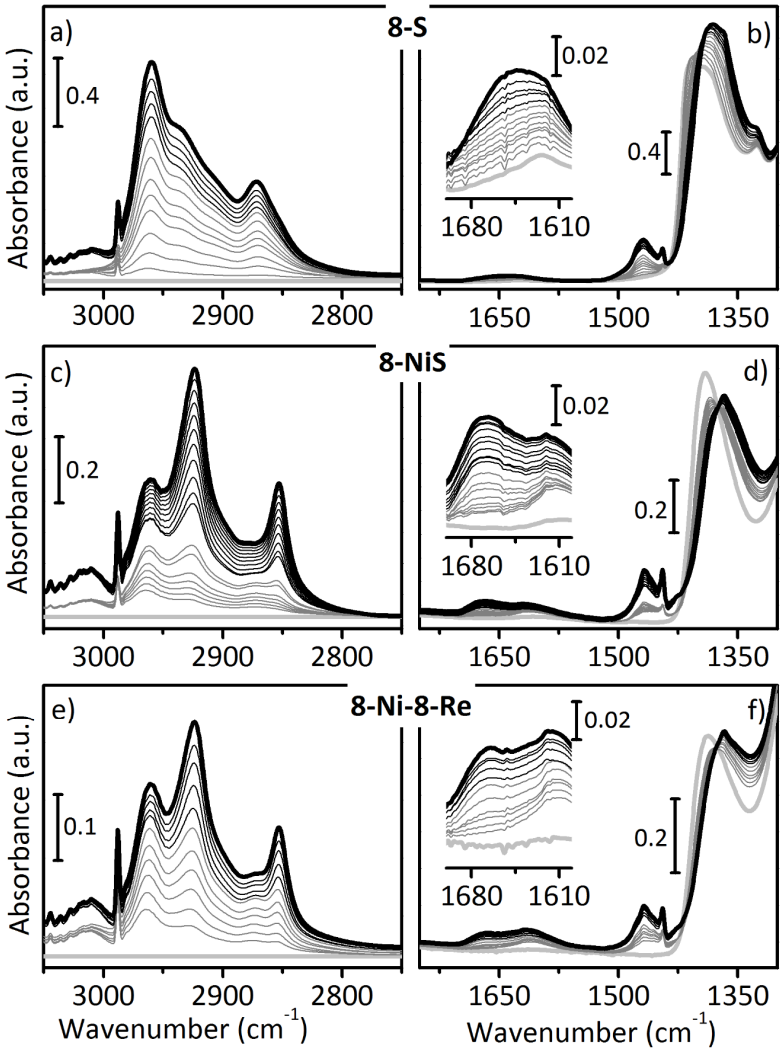

Figure 6. Time-resolved FT-IR spectra collected during reaction of ethylene at room temperature with 8-S, 8-NiS, and 8-Ni-8-Re catalysts. a), c) and e) display the 3100 – 2700 cm^{-1} region, where $\nu(CH_x)$ absorption bands are observed. b), d) and f) show the 2000 – 1300 cm^{-1} region, where ν(C=C), $\delta(CH_x)$ and $\nu(SO_4)$ bands contribute to the spectra. The insets zoom in the 1700 – 1600 cm^{-1} region, where the bands are attributed to υ(C=C).

The CH_2/CH_3 intensity ratio may give a rough estimation of the structure of the oligomeric products.[58, 65] To this aim, the FT-IR spectra collected during ethylene reaction on the three catalysts were analyzed by curve-fitting in the 3000 – 2700 cm^{-1} region, by using five gaussian curves centered at 2960 cm^{-1} ($\nu_{asym}(CH_3)$), 2930 cm^{-1} ($\nu_{asym}(CH_2)$), 2900 cm^{-1} ($\nu(CH)$), 2871 cm^{-1} ($\nu_{sym}(CH_3)$), and 2853 cm^{-1} ($\nu_{sym}(CH_2)$). A CH_2/CH_3 ratio was calculated based on the $\nu_{asym}(CH_2)$ and $\nu_{asym}(CH_3)$ bands at 2960 and 2930 cm^{-1} and the extinction coefficient of $\varepsilon(CH_3)/\varepsilon(CH_2)$ is chosen as approximately 2.2 obtained from a reference measurement of n-heptane in CCl_4.[59] It is important to notice that the CH_2/CH_3 ratio only reflects an average value for a complex distribution of all the products and not a single product. An increase in the CH_2/CH_3 intensity ratio indicates that the aliphatic chains are becoming longer or less branched. In contrast, if the aliphatic chains are short or more branched, the CH_2/CH_3 ratio is low. The evolution of the CH_2/CH_3 ratio as a function of the reaction time is shown in Figure 7. For 8-S, the CH_2/CH_3 ratio maintains at approximate one during the whole reaction time, indicating that the nature of the branched oligomers remains constant. Attempts to extract the products of reactions failed, in that only ethylene was detected in the extraction solution. Hence, the acid catalyzed oligomerization products are difficult to extract, possibly because of cationic interaction with the catalyst surface.

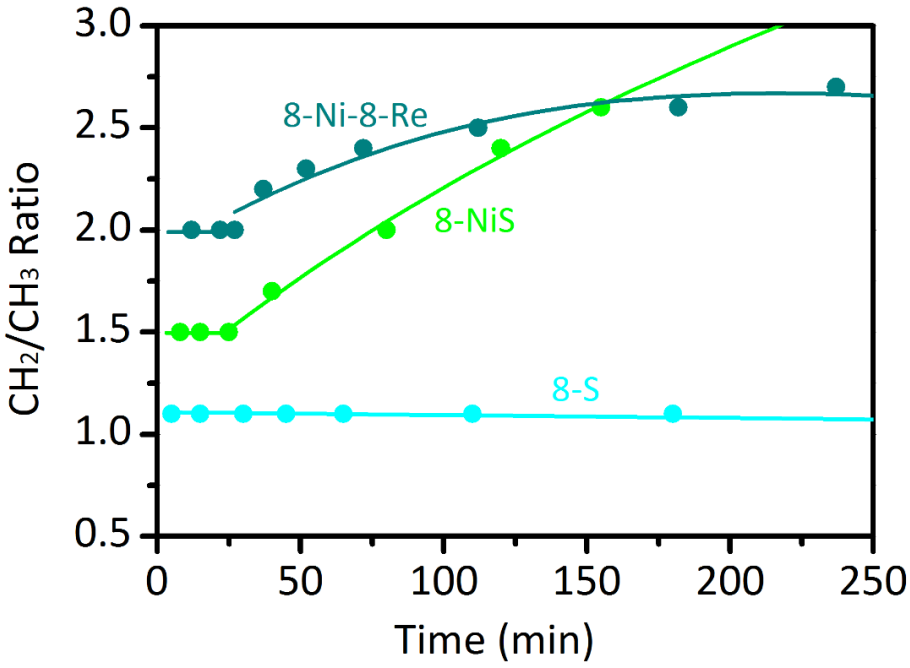

Figure 7. Evolution of the CH_2/CH_3 ratio versus reaction time as determined by the analysis of the FT-IR spectra collected during reaction of ethylene (10 mbar) at room temperature over 8-S, 8-NiS and 8-Ni-8-Re catalysts.

In contrast, for 8-NiS and 8-Ni-8-Re the CH_2/CH_3 ratio stays constant only during the first 40 minutes of reaction, followed by an increase, more pronounced for 8-NiS than for 8-Ni-8-Re. The different starting CH_2/CH_3 ratios of 8-NiS and 8-Ni-8-Re reflect the products of these acid-catalyzed reactions in dependence on the functional metal sites, which well supports the previous catalytic tests in a continuous flow reactor showing mainly butylene on 8-NiS and abundant propylene on 8-Ni-8-Re in the first 15 minutes. These data also indicate that after 40 minutes of reaction long-chain aliphatic hydrocarbons start to be formed and stick to the surface of both catalysts. These long hydrocarbon chains (which are stable also after prolonged degassing at room temperature) would be responsible for the fast deactivation previously observed in catalytic tests.[14] Formation of long-chain oligomers with a few branches on 8-NiS has been confirmed by GC-MS analysis of spent catalyst extracted in CH_2Cl_2 solution (273 K) after two hours reaction in contact

with ethylene at room temperature. The long chain aliphatic products could be formed by an ethylene oligomerization reaction and a side dimerization/oligomerization reaction of olefinic products. Since Ni sites are responsible for formation of linear olefin products, it is believed that the long chain products are mainly attributed to the Ni sites. The comparatively little-increased rate of the CH_2/CH_3 ratio for 8-Ni-8-Re shows the formation of shorter chain length or more branched by-products, which indicates well the function of the Re sites for metathesis.

The same experiment was followed by means of DR UV-Vis-NIR spectroscopy, which however reveals only very small changes during ethylene reaction at room temperature. Figure 8 shows the most relevant DR UV-Vis-NIR spectra for the 8-NiS sample as an example. Similar spectra were collected for the other catalysts as shown in Figure S2. Upon ethylene dosage in the reaction cell, very few changes are observed in the DR UV-Vis-NIR spectrum: the d-d bands centered around 7000 and 17000 cm^{-1} slightly decrease in intensity, while the charge transfer band around 35000 cm^{-1} increases. Accordingly, the coordination environment of the Ni sites changes only slightly in presence of ethylene. This observation which seems in contrast with the expected increase in the ligand field around the Ni sites upon ethylene adsorption might be explained in terms of ligand displacement, i.e. ethylene displays other ligands (the sulfate anions) originally present around the Ni sites, in agreement with the FT-IR results. After prolonged reaction time, a weak band appears around 25000 cm^{-1}, which may be assigned to a carbocationic conjugated olefinic double-bond.[66, 67]

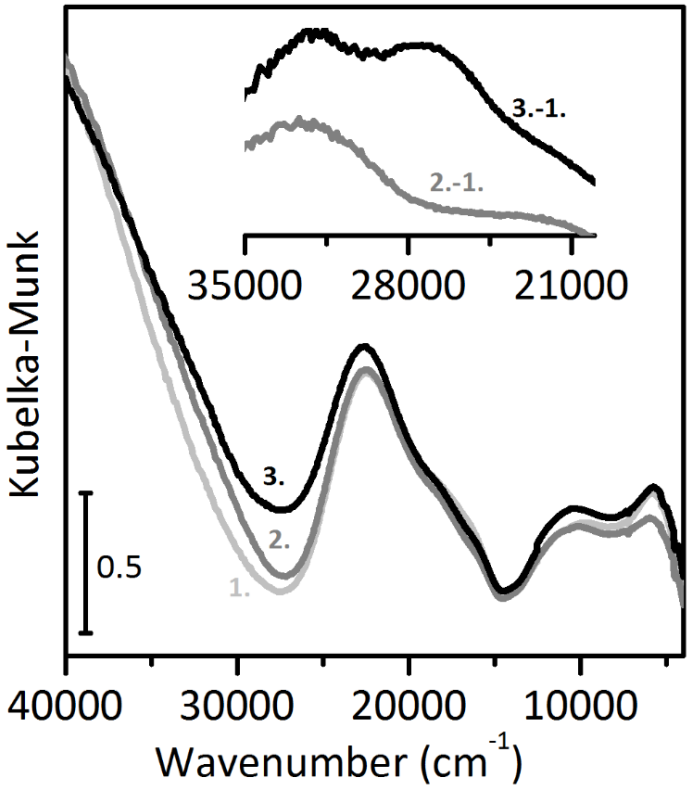

Figure 8. DR UV-Vis-NIR spectra of (1) 8-NiS after activation, (2) immediately after dosage of ethylene, (3) after an overnight reaction in presence of ethylene at room temperature. The insert shows spectra after subtraction of spectrum (1).

5. Conclusion

We have carried out a systematic spectroscopic investigation of the molecular structure and functions in a bimetallic $NiSO_4/ReO_x/\gamma\text{-}Al_2O_3$ catalyst which performs the direct conversion of ethylene to propylene at mild reaction conditions (323 K, 1 atm). Our own and literature results[14, 15, 17] conclude that ethylene is dimerized/isomerized to 2-butylene over a site requiring both Ni and sulfate ions, while the Re sites are responsible for the ethylene-butylene metathesis reaction, resulting in the tandem production of propylene. Albeit highly selective, the catalyst deactivates fast. Since deactivation is driven by the ethylene dimerization reaction, in this work we put focus

on the molecular investigation of the $NiSO_4$ site, with the aim to understand the changes occurring at the $NiSO_4$ sites during the catalyst activation, and in presence of ethylene.

A series of $NiSO_4$-ReO_x/Al_2O_3 catalysts differing in the relative amount of the two functions were synthetized, tested in the ETP reaction, and thoroughly characterized by means of FT-IR, DR UV-Vis-NIR, XPS and ESR spectroscopies, before and after thermal activation. It was found that the sulfate ions play an essential role in increasing the acidity of the Al_2O_3 surface (as demonstrated by FT-IR spectroscopy of CO adsorbed at 100 K), and also in influencing the electronic structure of the Ni cations. During thermal catalyst activation the sulfate ions are covalently bonded either to Ni^{2+} or/and Al^{3+} cations. Unexpected and in contrast to earlier reports[15, 17], the Ni cations retain the +2 oxidation state also after the catalyst activation step, as shown directly by DR UV-Vis-NIR, ESR and XPS analysis, and indirectly by FT-IR spectroscopy of CO adsorbed at 100 K.

FT-IR experiments performed in presence of ethylene at room temperature and low pressure (40 mbar) allowed to monitor the initial steps of the reaction on the different catalysts. It was proved that sulfated alumina promotes the slow formation of branched oligomers through a carbocationic mechanism. These are the only products detected by FT-IR spectroscopy during the first 30 minutes of reaction (i.e. when the catalysts work). The sulfate ions covalently bonded to the Ni^{2+} (or Al^{3+}) sites are partially displaced during the reaction, as testified by the perturbation of the corresponding IR absorption bands. In presence of the Ni^{2+} function, formation of long chain hydrocarbons is observed at longer reaction times. We conclude that deactivation of the $NiSO_4$-ReO_x/Al_2O_3 catalysts is mainly the consequence of absorption of higher linear ethylene oligomers or due to Ni^{2+} sites not being anymore in interaction with the sulfate ions. Improvements in the catalyst lifetime could be achieved by limiting the mobility of the sulfate anions or utilizing another reactor technology, such as e.g. a slurry reactor[68].

ASSOCIATED CONTENT

Supporting Information

DR UV-Vis-NIR spectra of the Ni-Re catalysts during the process of thermal activation (Figure S1); DR UV-Vis-NIR spectra of the Ni-Re catalysts in the course of ethylene reaction (Figure S2). The supporting information is available free of charge via the Internet at http://pubs.acs.org.

AUTHOR INFORMATION

Corresponding Author

*E-mail for K.-J. Jens: klaus.j.jens@hit.no

*E-mail for E. Groppo: elena.groppo@unito.it

Notes

The authors declare no competing financial interest.

ACKNOWLEDGMENT

The financial assistance provided by the Research Council of Norway (Program nr. 224980 (OLIGOM)) is gratefully acknowledged. We thank Dr. M. Fleissner Sunding for the XPS analysis and Prof. Dr. E. Sagstuen for ESR measurements.

REFERENCES

(1) Wittcoff, H.A., Reuben, B.G., Ploktin, J.S. In *Industrial Organic Chemicals.* 3rd ed.; John Wiley & Sons Ltd: Chicester, 2012, p 224.
(2) Plotkin, J.S., *Catal. Today* **2005**, 106, 10-14.
(3) Mol, J.C., *J. Mol. Catal. A: Chem.* **2004**, 213, 39-45.

(4) Mol, J.C., van Leenwen, P.W.N.M., In *Handbook of Heterogenenous Catalysis.* 2nd ed.; Ertl, G., Knozinger, H., Schuth, F., Weitkamp, J.; Wiley-VCH: Weinheim, 2008, Vol. 7, p 3240.
(5) Suzuki, T., Hirai, T., Hayashi, S., *Chem. Express* **1990**, 5, 877-880.
(6) O'Neill, P.P., Rooney, J.J., *J. Am. Chem. Soc.* **1972**, 94, 4383-4384.
(7) Yamaguchi, T., Tanaka, Y., Tanabe, K., *J. Catal.* **1980**, 65, 442-447.
(8) Lehmann, T., Wolff, T., Zahn, V.M., Veit, P., Hamel, C., Seidel-Morgenstern, A., *Catal. Commun.* **2011**, 12, 368-374.
(9) Oikawa, H., Shibata, Y., Inazu, K., Iwase, Y., Murai, K., Hyodo, S., Kobayashi, G., Baba, T., *Appl. Catal. A- Gen* **2006**, 312, 181-185.
(10) Zhou, H., Wang, Y., Wei, F., Wang, D., Wang, Z., *Appl. Catal. A- Gen* **2008**, 348, 135-141.
(11) Buluchevskii, E.A., Mikhailova, M.S., Lavrenov, A.V., *Khim. Interesakh Ustoich. Razvit.* **2013**, 21, 55-59.
(12) Buluchevskii, E.A., Lavrenov, A.V., Saifulina, L.F., *Khim. Interesakh Ustoich. Razvit.* **2014**, 22, 561-567.
(13) Andrei, R.D., Popa, M.I., Fajula, F., Hulea, V., *J. Catal.* **2015**, 323, 76-84.
(14) Li, L., Palcheva, R., Jens, K.-J., *Top. Catal.* **2013**, 56, 783-788.
(15) Cai, T., Cao, D., Song, Z., Li, L., *Appl. Catal. A- Gen* **1993**, 95, L1-L7.
(16) Sohn, J.R., Park, W.C., Park, S.-E., *Catal. Lett.* **2002**, 81, 259-264.
(17) Sohn, J.R., Park, W.C., *Appl. Catal., A* **2003**, 239, 269-278.
(18) Sohn, J.R., *Catal. Surv. Asia* **2004**, 8, 249-263.
(19) Andreev, A., Edreva-Kardzhieva, R., Neshev, N., *Recl. Trav. Chim. Pays-Bas* **1977**, 96, 23-26.
(20) Nakamura, R., Echigoya, E., *J. Mol. Catal.* **1982**, 15, 147-156.
(21) McCoy, J.R., Farona, M.F., *J. Mol. Catal.* **1991**, 66, 51-58.
(22) Xu, Y., Huang, J., Lin, Z., Guo, X., *J. Mol. Catal.* **1991**, 65, 275-285.
(23) Mol, J.C., *Catal. Today* **1999**, 51, 289-299.
(24) Morterra, C., Magnacca, G., *Catal. Today* **1996**, 27, 497-532.
(25) Busca, G., *Catal. Today* **2014**, 226, 2-13.
(26) Peak, D., Ford, R.G., Sparks, D.L., *J. Colloid Interface Sci.* **1999**, 218, 289-299.
(27) Saur, O., Bensitel, M., Saad, A.B.M., Lavalley, J.C., Tripp, C.P., Morrow, B.A., *J. Catal.* **1986**, 99, 104-110.
(28) Edreva-Kardjieva, R.M., Vuurman, M.A., Mol, J.C., *J. Mol. Catal.* **1992**, 76, 297-305.
(29) Lepetit, C., Che, M., *J. Phys. Chem.* **1996**, 100, 3137-3143.
(30) Sendoda, Y., Ono, Y., Keii, T., *J. Catal.* **1975**, 39, 357-362.
(31) Lever, A.B.P. In *Inorganic Electronic Spectroscopy.* 2nd ed.; Elsevier: Amsterdam: 1984, Vol.33, p 33.
(32) Karge, H., Geidel, E. In *Vibrational Spectroscopy.* Springer Berlin Heidelberg: Heidelberg, 2004, Vol. 4, p 1.
(33) Cornet, C.H., J.F.; Mariette, C., *Nouv. J. Chim.* **1984**, 8, 159-164.
(34) de Jesús, J.C., Pereira, P., Carrazza, J., Zaera, F., *Surf. Sci.* **1996**, 369, 217-230.
(35) Dufresne, P., Payen, E., Grimblot, J., Bonnelle, J.P., *J. Phys. Chem.* **1981**, 85, 2344-2351.
(36) Nikolova, D., Krstić, J., Spasov, L., Simeonov, D., Lončarević, D., Stefanov, P., Jovanović, D., *Russ. J. Phys. Chem.* **2011**, 85, 2380-2385.
(37) van Looij, F., Geus, J.W., *J. Catal.* **1997**, 168, 154-163.
(38) Manukyan, K.V., Cross, A.J., Yeghishyan, A.V., Rouvimov, S., Miller, J.J., Mukasyan, A.S., Wolf, E.E., *Appl. Catal. A- Gen* **2015**, 508, 37-44.

(39) Davydov, A., Kantcheva, M., Chepotko, M., *Catal. Lett.* **2002**, 83, 97-108.
(40) Knozinger, H., Huber, S., *J. Chem. Soc., Faraday Trans.* **1998**, 94, 2047-2059.
(41) Coluccia, S., Marchese, L., Martra, G., *Microporous Mesoporous Mater.* **1999**, 30, 43-56.
(42) Coluccia, S., Marchese, L., Martra, G., *Res. Chem. Intermed.* **2000**, 26, 1-5.
(43) Berthomieu, C., Hienerwadel, R., *Photosynth. Res.* **2009**, 101, 157-170.
(44) Lamberti, C., Zecchina, A., Groppo, E., Bordiga, S., *Chem. Soc. Rev.* **2010**, 39, 4951-5001.
(45) Vimont, A., Thibault-Starzyk, F., Daturi, M., *Chem. Soc. Rev.* **2010**, 39, 4928-4950.
(46) Garbarino, G., Romero Perez, A., Finocchio, E., Busca, G., *Catal. Commun.* **2013**, 38, 67-73.
(47) Garbarino, G., Sanchez Escribano, V., Finocchio, E., Busca, G., *Appl. Catal., B* **2012**, 113-114, 281-289.
(48) Jensen, M.B., Morandi, S., Prinetto, F., Sjaastad, A.O., Olsbye, U., Ghiotti, G., *Catal. Today* **2012**, 197, 38-49.
(49) Montanari, T., Castoldi, L., Lietti, L., Busca, G., *Appl. Catal. A- Gen* **2011**, 400, 61-69.
(50) Tsyganenko, A.A., Zverev, S.M., *React. Kinet. Catal. Lett.* **1988**, 36, 269-274.
(51) Eischens, R.P., Francis, S.A., Pliskin, W.A., *J. Phys. Chem.* **1956**, 60, 194-201.
(52) Mekhemer, G.A.H., Khalaf, H.A., Mansour, S.A.A., Nohman, A.K.H., *Monatshefte für Chemie / Chemical Monthly* **2005**, 136, 2007-2016.
(53) Arata, K., Hino, M., *Appl. Catal.* **1990**, 59, 197-204.
(54) Yang, T.-s., Chang, T.-h., Yeh, C.-t., *J. Mol. Catal. A: Chem.* **1997**, 123, 163-169.
(55) Jin, T., Yamaguchi, T., Tanabe, K., *J. Phys. Chem.* **1986**, 90, 4794-4796.
(56) Hadjiivanov, K., Knözinger, H., Mihaylov, M., *J. Phys. Chem. B* **2002**, 106, 2618-2624.
(57) Hadjiivanov, K.I., Vayssilov, G.N., *Adv. Catal.* **2002**, 47, 307-511.
(58) Bauer, F., Karge, H.G. In *Characterization of Coke on Zeolites.* Springer Berlin Heidelberg: Heidelberg, 2007, Vol. 5, p 249.
(59) Bjørgen, M., Lillerud, K.-P., Olsbye, U., Bordiga, S., Zecchina, A., *J. Phys. Chem. B* **2004**, 108, 7862-7870.
(60) Spoto, G., Bordiga, S., Ricchiardi, G., Scarano, D., Zecchina, A., Borello, E., *J. Chem. Soc., Faraday Trans.* **1994**, 90, 2827-2835.
(61) Smirnova, M.Y., Toktarev, A.V., Ayupov, A.B., Echevsky, G.V., *Catal. Today* **2010**, 152, 17-23.
(62) Ferreira, M.a.L., Rueda, E.H., *J. Mol. Catal. A: Chem.* **2002**, 178, 147-160.
(63) Wang, J.-H., Mou, C.-Y., *Appl. Catal. A- Gen* **2005**, 286, 128-136.
(64) Hwang, C.-C., Mou, C.-Y., *J. Phys. Chem. C* **2009**, 113, 5212-5221.
(65) Igisu, M., Ueno, Y., Shimojima, M., Nakashima, S., Awramik, S.M., Ohta, H., Maruyama, S., *Precambrian Res.* **2009**, 173, 19-26.
(66) Forster, H., Seebode, J., Fejes, P., Kiricsi, I., *J. Chem. Soc., Faraday Tran. 1* **1987**, 83, 1109-1117.
(67) Kiricsi, I., Förster, H., Tasi, G., *Stud. Surf. Sci. Catal.* **1989**, Volume 46, 355-364.
(68) Zhang, Q., Kantcheva, M., Dalla Lana, I.G., *Ind. Eng. Chem. Res.* **1997**, 36, 3433-3438.

A feasibility study of regeneration of coke deactivated $NiSO_4/\gamma\text{-}Al_2O_3$ catalyst

Lu Li[†], *Sachin Chavan*[‡], *Maela Manzoli*[§], *Klaus-J. Jens*[*,†]

[†]Faculty of Technology, University College of Southeast Norway, P.O.Box 203, Porsgrunn 3901, Norway

[‡]Centre for material science and nanotechnology, Department of chemistry, University of Oslo, P.O.box 1033, N-0315 Oslo Norway

[§]Department of Chemistry, University of Turin, Via Pietro Giuria 7, 10125, Torino, Italy

(This paper is going to be submitted)

Abstract

Catalyst deactivation is a well-known issue for most industrial catalyst technologies. We have recently reported a $NiSO_4$-ReO_x/γ-Al_2O_3 catalyst for tandem conversion of ethylene to propylene at mild conditions. However, the catalyst deactivated fast due to coking of the catalytic nickel function. We ascribed deactivation of the $NiSO_4$/γ-Al_2O_3 ethylene dimerization catalyst to adsorption of hydrocarbons on the catalyst surface. This work investigated oxidative regeneration of the $NiSO_4$/γ-Al_2O_3 part of the $NiSO_4$-ReO_x/γ-Al_2O_3 catalyst. An attempt was made to regenerate the deactivated catalyst by purging with synthetic air in the temperature range of 298 to 673 K. The entire regeneration process was monitored and recorded by FT-IR and TG-MS. Long chain hydrocarbons deposited on the catalyst evolve and convert to highly condensed coke species, which need temperature higher than 673 K to be burned. However, regeneration temperatures higher than 673 K may destroy catalyst surface texture and cause decomposition of nickel sulfate. Hence, the catalyst could not be regenerated by purging synthetic air. It appears that the failure of catalyst regeneration could also be due to the destruction of the active nickel dimerization site.

Keywords

Nickel sulfate, ethylene dimerization, deactivation, γ-alumina

1. Introduction

Catalyst deactivation is inevitable and costly for most industrial processes, despite significant efforts to postpone, alleviate or avoid the issue.[1] Catalyst change out requires process shutdown leading to potential product revenue loss in combination with personnel and material costs. Consequently, catalyst deactivation and regeneration is a topic of great interest.

The discovery of the olefin metathesis reaction provides flexibility for production of various important olefins.[2, 3] The first industrial olefin metathesis process (Phillips Triolefin Process) was operated 1966-1972 for conversion of propylene to ethylene and butylene.[4] As demand for propylene increased, the Lummus OCT process adapted this technology to produce propylene in the reverse direction.[5] The OCT technology is often combined with the steam cracking process, but it meets the problem of butylene shortage if employed in a light gas (ethane) steamcracker. However, additional butylene capacity can be added by using the ethylene dimerization reaction.[6]

Heterogeneous Ni-based ethylene dimerization/oligomerization catalysts have been known for a long time; NiO supported on silica was first reported active for the ethylene oligomerization reaction eighty years ago by K. Morikawa.[7] Several studies[8-10] have been devoted to the nature of the active Ni sites and the role of acid sites due to their significance for catalytic performance, while other reports[8, 11, 12] concluded that catalyst deactivation is mainly attributed to strong adsorption of products (hydrocarbons) on actives sites. However, regeneration studies of the deactivated Ni-containing catalysts are seldom reported.

Coke deactivated catalysts are usually regenerated by burning of coke in the presence of oxidative reactants (e.g. O_2 , H_2O, etc.).[13] Although removal of carbon with oxygen is generally very rapid, air/N_2 regeneration is typically employed in industrial processes (e.g. catalytic cracking, hydro-treating process and catalytic reforming), in order to avoid hot spots or over

heating temperatures that could modify surface structures or destroy the catalyst.[14] Coke combustion temperatures are closely related to its C/H ratio.[15] For example, metal-catalyzed hydrogen-rich residue can be removed with steam at temperatures below 673 K. In contrast, carbonaceous deposits having a more graphic structure or less reactive properties may require temperatures above 973 K. Such high regeneration temperature may be accompanied by sintering or destruction of the catalyst surface.[1]

For $NiSO_4/\gamma\text{-}Al_2O_3$ catalysts, little is known about the deactivation mechanism, although this catalyst class has been reported several times for giving high ethylene dimerization activity.[16, 17] In our FT-IR studies,[18] we found that deactivation of the $NiSO_4/\gamma\text{-}Al_2O_3$ catalyst was accompanied by formation of long aliphatic hydrocarbon chains depositing on the catalyst surface. Generally, for reactions involving hydrocarbons and especially olefinic hydrocarbons, the rate and extent of coke formation on metal oxide catalysts increases with increasing acid strength and concentration.[1] However, Ni-modified metal oxides without sufficient acid strength exhibit no activity for ethylene dimerization,[19] as also observed in our case.

Deposition of hydrogen-rich residues can be easily reversed by gasification with air at around 600 K.[1, 20] Therefore, we investigated regeneration of spent catalysts by purging a deactivated catalyst with a mixture of nitrogen (79%) and oxygen (21%) at 673 K. The long chain hydrocarbons, being hydrogen rich, were expected to be burned off in synthetic air at a temperature of around 600 K. TG-MS analysis and FT-IR were used to monitor the process of catalyst regeneration. Lastly, a HRTEM study was conducted to analyze elemental distribution and surface morphology of the regenerated catalyst.

2 Experimental setup

2.1 Catalyst preparation

$NiSO_4/\ \gamma\text{-}Al_2O_3$ catalysts were prepared[21] by an incipient wetness impregnation method. $\gamma\text{-}Al_2O_3$ was impregnated with an aqueous solution of $NiSO_4 \cdot 7H_2O$ (Sigma-Aldrich, purity:≥99.999%) followed by drying overnight at 378 K and calcination in air at 673 K for 2 hours. A system of catalyst naming introduced in this report; catalyst naming indicates the nominal weight percentage of nickel corresponding to the whole catalyst. For instance, 8-NiS means the catalyst containing 8wt% of Ni.

2.2 Catalyst characterization

Thermal gravimetric analysis (TGA) of fresh and deactivated catalysts have been carried out in a Rheometric Scientific STA 1500 instrument. This TGA was equipped with an online mass spectrometer (Pfeiffer Omnistar), which enables analysis of the effluent gas by scanning mass from 1 to 100 m/z. Around 20mg of each sample was used and heated to 1273 K with a heating rate of 5 K/min either in a pure nitrogen flow or in a flow of oxygen (21%) and nitrogen (71%) mixture (synthetic air).

In situ FT-IR experiments have been performed in the transmission mode. Spectra were recorded by a Bruker Vertex 70 spectrometer equipped with a mercury cadmium telluride cryo-detector equipped with a Harrick in-situ FT-IR cell. %) and nitrogen (79%) was introduced a temperature program executed from 323 K to 673 K. The catalyst was degassed overnight under nitrogen flow at room temperature followed by thermal activation at 673 K for 2 hours. The activated catalysts was cooled down to 323 K and then ethylene (5ml/mins) was sent to the cell for 2 hours in order to completely deactivate the catalyst. After that, nitrogen (10ml/mins) was sent to the cell to remove all residual ethylene and other physisorbed products. Next, a mixture of oxygen (21%) for

4 hours. Finally, ethylene (5ml/min) was fed to the cell again. To remove trace amounts of water in the experimental gases, a cooling trap of dry ice was added before the cell.

High resolution electron microscopy (HRTEM) was carried out on a Jeol 3010-UHR electron microscope operating at 300 kV equipped with a LaB6 filament and with an Oxford Inca Energy TEM 300 EDS X-rays analyzer by Oxford Link. The powder samples were ground in an agate mortar and deposited on a copper grid covered with a lacey carbon film. The analyzed regenerated catalyst sample constituted the regenerated pellet of the deactivated catalyst from the FT-IR experiment.

3 Results and discussion

3.1 TGA analysis of fresh and deactivated catalyst

The TGA analysis of the fresh catalysts is shown in Figure 1. The catalysts were stored in small vials and exposed to air after preparation, so that the $NiSO_4$ and ReO_x on the catalysts were in a hydrated state. Weight loss of γ-Al_2O_3 at 373-473 K is attributed to the loss of physisorbed water and surface hydroxyl groups. The thermogravimetric (TG) curve of 8-NiS shows two clear areas of weight loss; one below 673 K and the other one above 1003 K. M. Maneva et al. reported that thermal dehydration of $NiSO_4 \cdot 7H_2O$ to monohydrate $NiSO_4 \cdot H_2O$ occurs stepwise over a wide temperature range from 353 to 753K.[22] The last coordinated water molecule is evolved at around 623 K and the anhydrous nickel sulfate is stable within a broad temperature range[22]. From the $NiSO_4 \cdot 7H_2O$ TG-curve, they also found a distinct weight loss caused by decomposition of anhydrous nickel sulfate to nickel oxide at a temperature range of 1013-1173 K[22]. Considering our case, the weight loss of the catalyst in the first region (below 673K), is mainly due to the evolution of water molecules from the hydrated nickel sulfate beside water loss from γ-Al_2O_3. The weight loss above 1003K could result from decomposition of anhydrous nickel sulfate. Thermal analysis

indicates that the catalyst seems stable up approximately 950 K and that thermal stability is dominated by the decomposition temperature of anhydrous nickel sulfate.

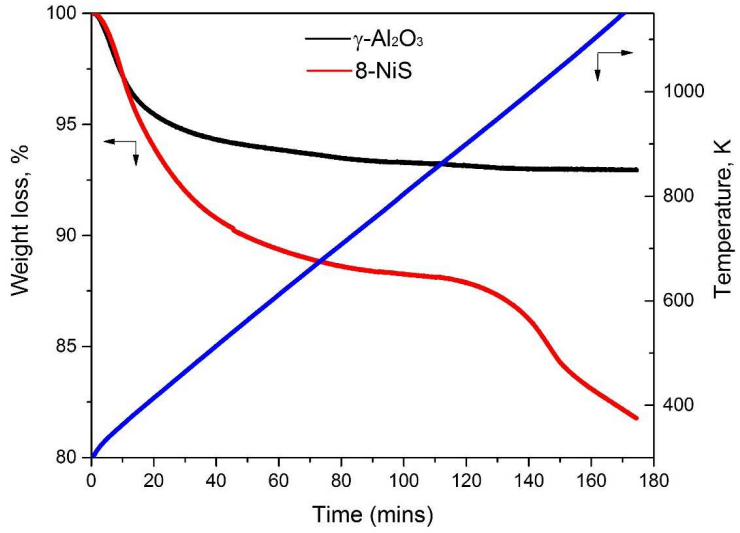

Figure 1: TGA analysis of activation process of γ-Al_2O_3 and 8-NiS under pure nitrogen flow.

It was concluded from previous FT-IR results[18] that catalyst deactivation is due to long chain hydrocarbons blocking the active sites. Therefore, in the following stage, effort was concentrated on the regeneration of the 8-NiS catalyst. A common way to remove hydrocarbons is to burn them under O_2 or air at 623 K-873 K.[1] As this burn-off process is an exothermic reaction, burning under pure oxygen easily leads to a sudden temperature increase in some part of the catalyst that may result in catalyst sintering or decomposition of $NiSO_4$. Hence, a mixture of oxygen and nitrogen in terms of their compositions in air was applied. Initially, TGA analysis coupling with the MS detector was performed on deactivated 8-NiS catalysts. Moreover, a blank experiment was performed under the same condition as well.

The TG-curve trend of fresh 8-NiS (Figure 2) obtained in an atmosphere of synthetic air is very similar to the 8-NiS curve collected under pure nitrogen flow (Figure 1). The loss of coordinated water from hydrated nickel sulfate and hydroxyl groups from the Al_2O_3 surface proceeds over a wide temperature range. Moreover, weight loss at above 1003 K could be attributed to

decomposition of anhydrous nickel sulfate, since the decomposition temperature is known to be around 1013-1173 K.[22]

Furthermore, the MS signals of fresh 8-NiS, showed several high-intensity mass-to-charge lines which could be attributed to nitrogen, oxygen and impurities of these gases below 44 m/z; their intensities kept constant during the entire process. Moreover, it is necessary to point out that a weak signal present at 44m/z was due to trace amounts of CO_2 in the mixing gas (O_2 and N_2). This signal remained at a steady level during the experiment. Furthermore, no signal of SO_3 and SO_2 was detected from 1013 K to 1073 K in the test. In the TG-curve, the decomposition process may have corresponded to a wide temperature range since a high heating rate (5 K/min) was applied in this experiment. Decomposition of anhydrous nickel sulfate was not complete at the temperature ranging from 1013 K to 1073 K and possibly only very small amounts of anhydrous nickel sulfate decomposed. Therefore, the resulting SO_2 and SO_3 gas mixture was probably below the detection limit of the MS detector.

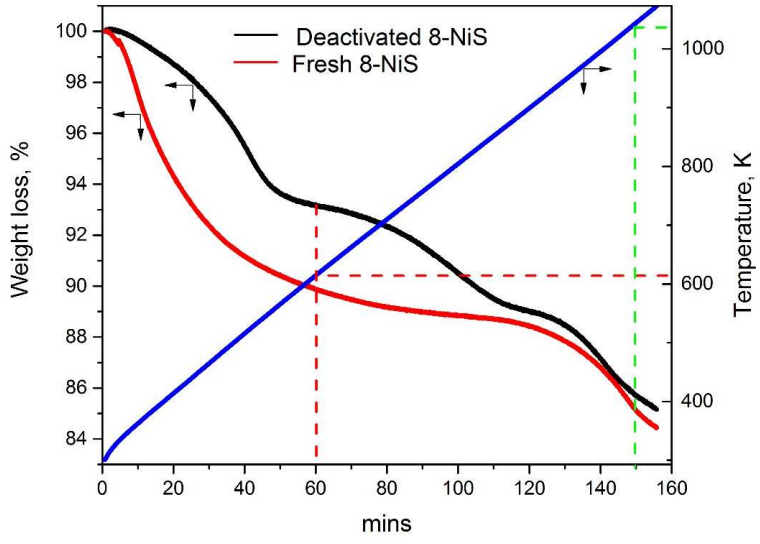

Figure 2: TGA analysis of re-activation process of the deactivated 8-NiS catalyst and fresh catalyst (blank test) under mixing flows of nitrogen (79%) and oxygen (21%).

The TG-curve of deactivated catalyst in Figure 2 can be divided into three regions according to the rate of the weight loss. During the first 60 minutes, the temperature increases from room temperature to around 633 K and the weight loss is mainly associated to loss of water molecules. During this period, considerably weaker signals were observed in the range of 45-100 m/z and the signal at 44m/z stays at the same level as that of fresh 8-NiS in the blank test. This indicates that desorption or burning of deposited hydrocarbons does not occur during this period. The mass scans of the effluent gas from the re-activation of deactivated 8-NiS in 80-150 minutes are plotted in Figure 3. In the middle period (80-120 minutes), several signal groups are mainly present at 54, 56, 70 and 84m/z. These signals could be assigned to fragments of hydrocarbons, e.g. C_4H_8, C_5H_{10}, and C_6H_{12}, revealing that the weight loss is largely due to desorption and of these carbon species. In the third period (120-150 minutes), the CO_2 signal (44m/z) increases from 80 to 150 minutes and rises sharply in the last 130-150 minute period. In fact, this observation is unexpected, because hydrogen-rich hydrocarbons are expected to burn under air at temperatures around 600 K.[15] The combustion temperature of coke depends on its location (external vs. internal deposits) and composition (i.e., H/C ratio). Hydrogen-poor coke species need a higher combustion temperature than the hydrogen-rich components.[15] The TG-MS analysis indicates that long-chain oligomers may convert further to highly condensed carbon species with low C/H ratios during the regeneration process, since oxidation of hydrocarbons only start at a quite high temperature above 723 K. However, it seems such high temperatures could damage or destroy surface texture of the catalysts and might even cause decomposition of nickel sulfate.

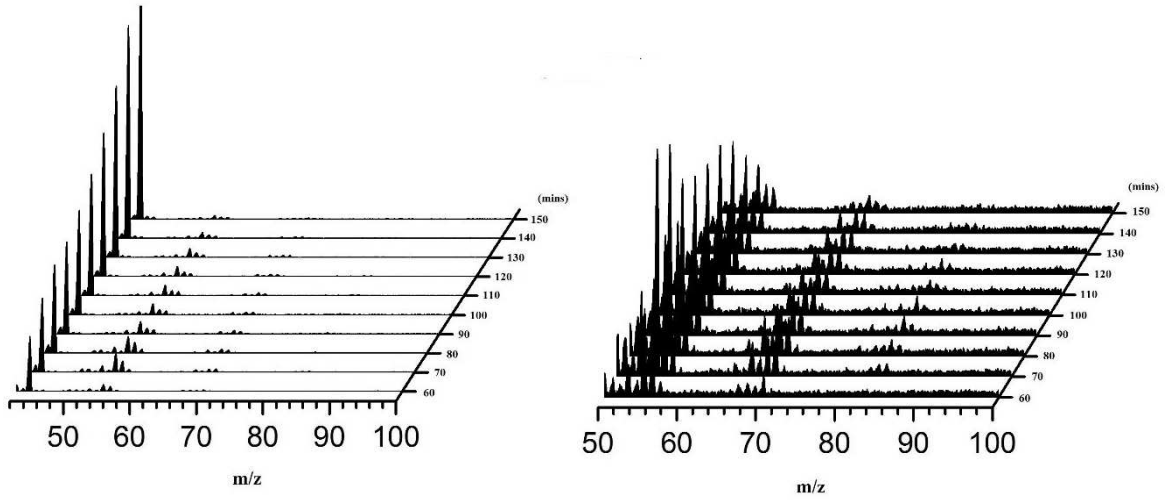

Figure 3: MS scanning (44-100m/z) of the effluent gas from the reactivation of deactivated 8-NiS catalyst in 80-150 minutes.

3.2 FT-IR study on the re-activation process of the deactivated catalyst

In order to determine the structural change of the hydrocarbons during catalyst re-activation, a FT-IR experiment was carried out. Figure 4 shows spectra of deactivated catalyst in the regeneration process. The pellet of the 8-NiS catalyst was first thermally activated at 673 K for 2 hour under vacuum followed by deactivation by a two-hour exposure to a pure ethylene flow through the in-situ cell at 323 K. After that, the deactivated catalyst was heated from 323 K to 673 K under a flow of synthetic air. As mentioned, burning of hydrocarbons is an exothermic reaction and $NiSO_4$ becomes unstable above 950 K. Thus, in order to avoid destruction of the surface structure on the catalyst during the re-activation process, the maximum re-activation temperature was only set up to 673 K. After the regeneration process, the pellet was removed from the cell and sent to HRTEM measurement. The spectra are shown in Figure 4a; bands in the υ(C-H) vibrational region (2800-3000 cm^{-1}) are assigned to the asymmetric vibration of $-CH_3$ and $-CH_2-$ (2960 and 2871cm^{-1}) groups, the symmetric vibration of $-CH_3$ and $-CH_2-$ (2930 and 2853cm^{-1}) groups. These

CH_X groups are indicative of long chain aliphatic hydrocarbons deposited on the catalyst during catalyst deactivation. These bands decrease and finally disappear with increasing regeneration temperature. However, these deposited hydrocarbons are not desorbed from the catalyst surface. They evolve and convert to coke, namely, carbonaceous species deficient in hydrogen.[15] A set of bands at low frequency from 1300 to1700 cm^{-1} rise dramatically accompanying the disappearance of the bands in the υ(C-H) vibrational region. At low temperature (323 K-473 K), two bands at 1672 and 1465 cm^{-1}, originating from the υ(C=C) and δ(-CH_2-) bands increase gradually. At high temperature (473 K-673 K), a band at 1590cm^{-1} increases remarkably. This band reflects the complex nature of coke, which is assigned to highly unsaturated carbonaceous species[23-28] or to graphite deposits.[29] It can be speculated that side reactions (e.g. cracking) occur at high temperature generating highly condensed coke on the catalyst surface. Therefore, high temperature is necessary to remove this coke. In addition, the $\nu_{asym}(SO_4)$ band at around 1400 cm^{-1} is shifted downward by 20 cm^{-1} with increasing regeneration temperature, probably due to perturbation by the accumulated coke. In the previous FT-IR and DR UV-Vis-NIR studies[18], it was concluded that deactivation of the $NiSO_4/\gamma$-Al_2O_3 catalysts is due to the formed hydrocarbons not only blocking the active sites but also hindering the interaction between Ni^{2+} and [SO_4^{2-}]. In this case, the shift of $\nu_{asym}(SO_4)$ band indicates clearly that the bonding of Ni^{2+} and [SO_4^{2-}] becomes very weak in this re-activation process.

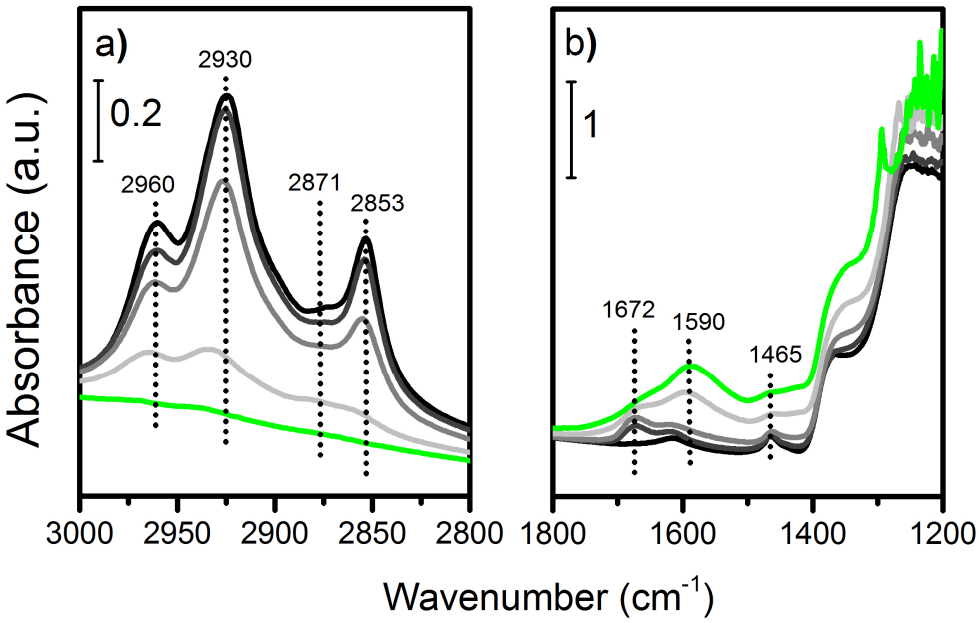

Figure 4: FT-IR spectra of activation of the deactivated catalyst under synthetic air with increasing temperature from 323K to 673K (323K (black), 373K (dark grey), 473K (grey), 573K (light grey) and 673K (green)). a) display the 3000 – 2800 region, where ν(CH_x) absorption bands are observed. b) show the 1800 – 1200 cm^{-1} region, where ν(C=C), δ(CH_x) and ν(SO_4) bands contribute to the spectra.

In order to verify the unsuccessful re-activation of the deactivated 8-NiS catalyst, the regeneration process was repeated and followed by sending an ethylene flow (5ml/min) to the re-activated catalyst. The spectra of the fresh and the re-activated 8-NiS after two-hour ethylene reaction is shown in Figure 5. From the figure, it is evident that the fresh 8-NiS exhibits a high activity, since the four intense CHx bands reveal the adsorption of abundant products on the catalyst surface. On the contrary, the four bands show rather low intensities for the re-activated 8-NiS catalyst, which indicates that the re-activated catalyst performs a quite low activity. Therefore, it is concluded that the deactivated 8-NiS catalyst could not be regenerated by purging synthetic

air at 673K. Considering that $NiSO_4$ was well distributed on the catalyst surface before deactivation/regeneration, it is speculated that the regeneration failure could be due to further evolution of the hydrogen-rich hydrocarbons to highly condensed coke and the weak interaction between Ni^{2+} and $[SO_4^{2-}]$ perturbed by coke formed in the re-activation process.

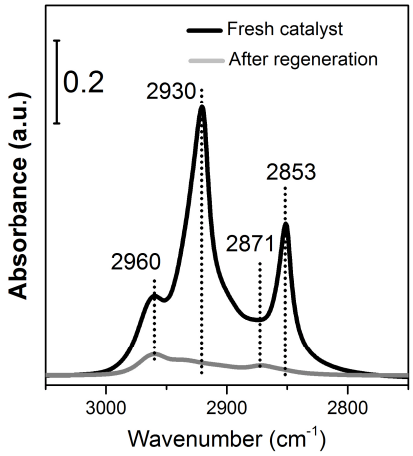

Figure 5: FT-IR spectra of 8-NiS after two-hour reaction under an ethylene flow (5ml/min). a) The fresh catalyst (black); b) The re-activated catalyst (grey).

3.3 Catalyst morphology

A series of catalysts were measured by HRTEM at ambient conditions. Figure 6(a) shows HRTEM images of support γ-Al_2O_3 material as reference. No observation of agglomerates and clusters were observed in the HRTEM image of fresh 8-NiS (Figure 6(b)) demonstrating good dispersion of $NiSO_4$ on γ-Al_2O_3. Figure 6(c-g) show HRTEM images of deactivated 8-NiS after regeneration as well as mapping of C, Ni and S elements. 8-NiS catalyst sample was directly collected from the FT-IR experiment of spent catalyst regeneration. By comparison with the HRTEM images of fresh catalyst, the dark spots in the HRTEM images in Figure 6 are assigned to coke formation during catalyst regeneration with synthetic air at 673 K. This observation is consistent with the IR spectra of 673 K regenerated catalyst (Figure 4).

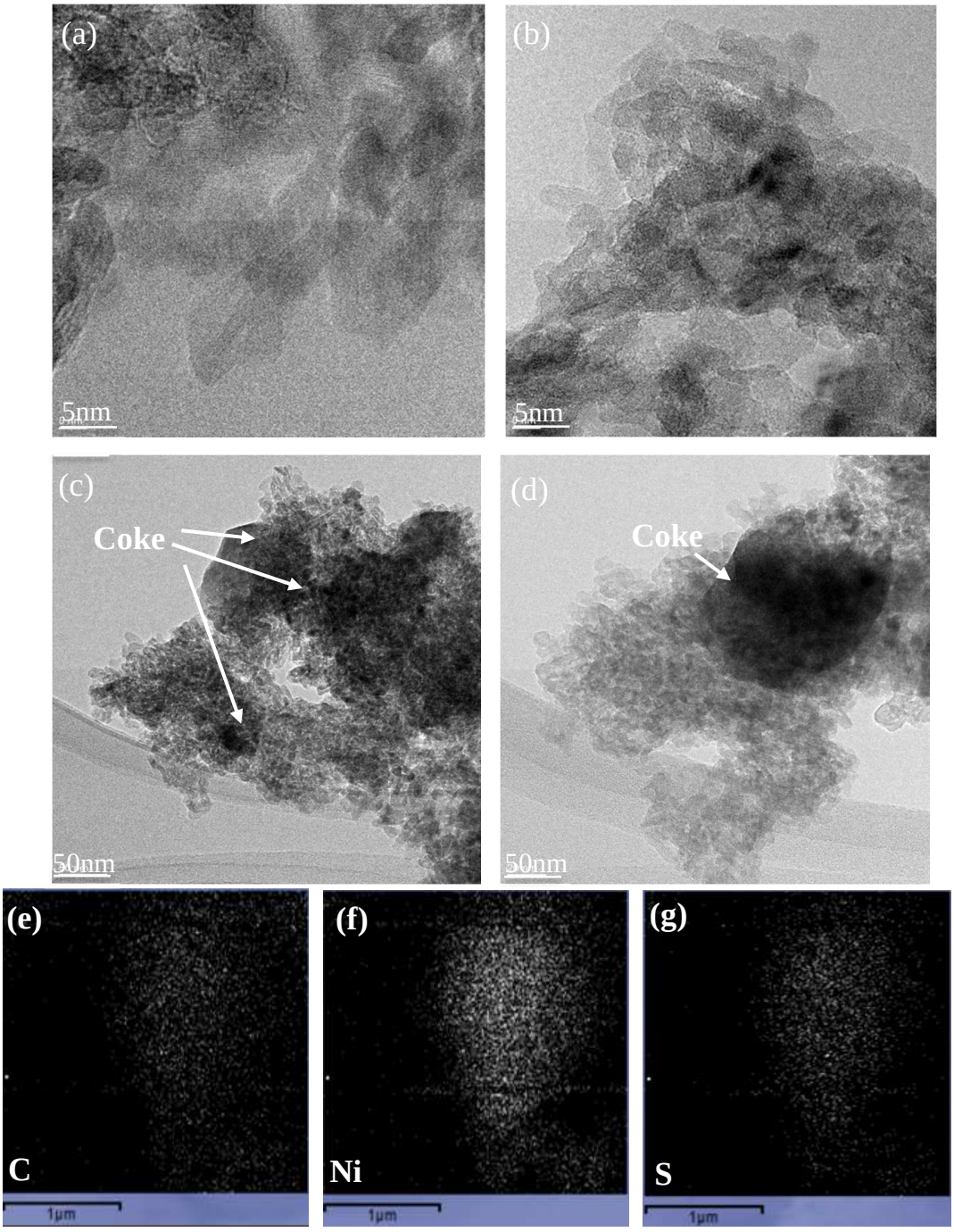

Figure 6: HRTEM images of (a) fresh γ-Al_2O_3 in a hydrate state, (b) fresh 8-NiS in a hydrate state, (c-d) deactivated 8-NiS after reactivation at 673K under a mixture of oxygen (21%) and nitrogen (79%); mappings of C (C), Ni (D) and S (E) elements.

4 Conclusion

We have previously reported a $NiSO_4$-ReO_x/γ-Al_2O_3 catalyst which catalyzes conversion of ethylene to propylene by a dimerization-metathesis tandem reaction at mild conditions.[21] However, the catalyst deactivates quite fast by coking which is due to the $NiSO_4$ based ethylene dimerization function. For $NiSO_4/\gamma$-Al_2O_3 catalysts, little is known about the deactivation and regeneration mechanism, although these catalysts have been reported to exhibit high ethylene dimerization activity.[12, 13] To the best of our knowledge, we report for the first time an attempt to regenerate spent $NiSO_4/\gamma$-Al_2O_3 ethylene dimerization catalyst by coke burn-off.

During catalyst regeneration using synthetic air, the long-chain hydrocarbons adsorbed on the catalyst surface evolve to highly unsaturated species or graphite-like residues with the increasing re-activation temperatures. The highly condensed species or graphite-like residues require a high combustion temperature. TG-MS data shows that the evolved coke on the deactivated catalyst starts to burn above 723 K and the burning rate increases with temperature. It seems that the coke deposited on the 8-NiS catalyst needs to be burned at higher temperature, e.g. >673 K, which may either damage the surface texture of the catalyst or cause decomposition of nickel sulfate. It appears that the failure of catalyst regeneration could also be due to the destruction of the active nickel dimerization site.

REFERENCES

(1) Argyle, M., Bartholomew, C., *Catalysts* **2015**, 5, 145-269.
(2) Mol, J.C., *Catal. Today* **1999**, 51, 289-299.
(3) Mol, J.C., *J. Mol. Catal. A: Chem.* **2004**, 213, 39-45.
(4) Banks, R.L., Bailey, G.C., *I&EC Product Research and Development* **1964**, 3, 170-173.
(5) Wittcoff, H.A., Reuben, B.G., Ploktin, J.S. In *Industrial Organic Chemicals.* 3rd ed.; John Wiley & Sons Ltd: Chicester, 2012, p 224.
(6) Sumner, C., US Patent 7525007 B2, April 2009
(7) K.Morikawa, *Kogyo Kagaku Zasshi* **1938**, 41, 694.

(8) Finiels, A., Fajula, F., Hulea, V., *Catal. Sci. Technol.* **2014**, 4, 2412-2426.
(9) Sohn, J.R., *Catal. Today* **2002**, 73, 197-209.
(10) Sohn, J.R., Lee, M.H., Shin, D.C., *J. Ind. Eng. Chem. (Seoul, Repub. Korea)* **2006**, 12, 710-719.
(11) Wendt, G., Fritsch, E., Deininger, D., Schoellner, R., *React. Kinet. Catal. Lett.* **1981**, 16, 137-141.
(12) Wendt, G., Hentschel, D., Finster, J., Schollner, R., Hanafi, S., Mikhail, R.S., *J. Chem. Soc., Faraday Tran. 1* **1983**, 79, 2013-2025.
(13) Royo, C., Ibarra, J.V., Monzon, A., Santamaria, J., *Ind. Eng. Chem. Res.* **1994**, 33, 2563-2570.
(14) Figueiredo, J.L., In *Progress in Catalyst Deactivation: Proceedings of the NATO Advanced Study Institute on Catalyst Deactivation*, Springer Netherlands, Dordrecht, 1982, p45.
(15) Bauer, F., Karge, H.G. In *Characterization of Coke on Zeolites.* Springer Berlin Heidelberg: Heidelberg, 2007, Vol. 5, p 249.
(16) Cai, T., Cao, D., Song, Z., Li, L., *Appl. Catal. A- Gen* **1993**, 95, L1-L7.
(17) Sohn, J.R., Park, W.C., *Appl. Catal., A* **2003**, 239, 269-278.
(18) Unpublished experiments.
(19) Andrei, R.D., Popa, M.I., Fajula, F., Hulea, V., *J. Catal.* **2015**, 323, 76-84.
(20) Klusáček, K., Davidová, H., Fott, P., Schneider, P., *Chem. Eng. Sci.* **1985**, 40, 1717-1721.
(21) Li, L., Palcheva, R., Jens, K.-J., *Top. Catal.* **2013**, 56, 783-788.
(22) Maneva, M., Rizova, D., Genov, L., Liptay, G., *J. Therm. Anal.* **1990**, 36, 915-922.
(23) Chang, C.C., Conner, W.C., Kokes, R.J., *J. Phys. Chem.* **1973**, 77, 1957-1964.
(24) Kokes, R.J., Dent, A.L., *J. Phys. Chem.* **1971**, 75, 487-491.
(25) Trombetta, M., Busca, G., Rossini, S., Piccoli, V., Cornaro, U., Guercio, A., Catani, R., Willey, R.J., *J. Catal.* **1998**, 179, 581-596.
(26) Meunier, F.C., Domokos, L., Seshan, K., Lercher, J.A., *J. Catal.* **2002**, 211, 366-378.
(27) Rozwadowski, M., Lezanska, M., Wloch, J., Erdmann, K., Golembiewski, R., Kornatowski, J., *Chem. Mater.* **2001**, 13, 1609-1616.
(28) Eberly, P.E., *J. Phys. Chem.* **1967**, 71, 1717-1722.
(29) Eisenbach, D., Gallei, E., *J. Catal.* **1979**, 56, 377-389.

Doctoral dissertation no. 4
2016

—

One-step Conversion of Ethylene to Propylene by a $NiSO_4$-ReO_x/γ-$A1_2O_3$ Catalyst

A PhD dissertation in Process, Energy and Automation Engineering

—

Lu Li

—

ISSN: 2464-2770
ISBN: 978-82-7206-413-5

usn.no